Development of High Performance Microwaves, Millimetres and Terahertz Antennas Based on Negative/Gradient Refractive Index, and Anisotropic Metatronics

By

Adel A. A. Abdelrehim

Supervisors:

Prof. Peter Gardner

Dr. Hooshang Ghafouri-Shiraz,

Dr. Alexandros Feresidis

A thesis submitted to the University of Birmingham for the degree of DOCTOR OF PHILOSOPHY

Department of Electronic, Electrical and System Engineering

College of Engineering and Physical Sciences

University of Birmingham

September 2018

Abstract

In this thesis, Metatronics have been applied to develop high performance antennas. This thesis added five new achievements to the scientific world. Firstly, a volumetric Negative Refractive Index (NRI) medium composed of Split Ring Resonators and Thin Wires (SRRs/TWs) is designed and incorporated with patch antenna operating at 10 GHz and 300 GHz. The gain is improved by 1.5dB. Secondly, a double sided NRI composed of Circular Split Ring Resonators and Thin Wires (CSRRs/TWs) employing a lens is proposed and characterized. The measured gain is improved from 6.5dB to 11.4dB. Thirdly, a new slotted waveguide antenna incorporated with Electrically Split Ring Resonator (ESRR) Metasurface (MTS) exhibiting NRI is proposed. The measured gain of the 10 GHz proposed antenna is improved from 6.7 dB to 10.5 dB. Furthermore, an anisotropic Low Epsilon Medium (LEM) ESRR-MTS is designed to focus the *E*-plane beam of the slotted antenna. The measured gain is improved by 4dB. Fourthly, high fabrication tolerance non-resonance and resonance GRIN MTS are proposed and characterized up to THz. The gain is improved from 6.7 to 11.3dB for 10 and 60 GHz antennas. Finally, a semi-analytical model based on transfer function is proposed to model THz Photoconductive antenna (PCA) excited by a femtosecond pulsed laser beam.

Acknowledgement

I would like to thank my God to help me in completing such nice piece of research work. Also, I would like to thank my supervisor Dr. H. Ghafouri-Shiraz on his great guides and his patient in reading and following my research. I would like to thank Prof. Peter Gardner who is my co-supervisor on his gaudiness and his periodically assessment of my work. I would like to thank the active technicians Alan Yates and Jag Sangha on their help in fabricating our proposed high performance antennas presented in this thesis. I would like to thank Prof. Costas Constantinou to allow us to use his facilities to measure the performance of millimetre wave antennas. Furthermore, I would like to thank my relatives, my parents, my brothers and my sisters on their supporting to me to complete my postgraduate studies.

Table of Contents

List of Figures

List of Tables

Chapter 1 Introduction

1.1. Motivations

1.1.1. Development of THz Antennas for Useful Applications

The interest of the THz region dates back to the 1920s [1] and during the last 40 years it has seen fantastic development due to the exceptional properties of the THz waves as well as its various possible applications. Since the THz region is the frequency gap located between 0.1 THz and 10 THz, i.e. it is located between the millimetre waves and the infrared, so it borrows characteristics from the two neighbouring regions which can be summarized as follows:

1- Penetration: because the THz waves are longer in wavelength (in mm) compared to the infrared waves (in μm), therefore THz wave's penetration depth is low compared to the infrared waves. The required penetration depth of the waves in the different objects is controlled by the materials of objects wanted to be scanned and the application. For example, the non-metallic materials are opaque for visible light waves and transparent for THz ones waves.

2- Resolution: since the THz waves are shorter in wavelength compared to microwaves, they provide a high spatial imaging resolution.

3- Spectral fingerprint: since most of molecules intra and inter vibration modes lie in the THz regime, so THz radiation can be applied in many applications such as imaging, spectroscopy and wireless communications [2-4].

4- Safety: since the photon energy of the THz waves is lower in energy compared with the X-rays, the THz waves are non-ionization radiation and hence more safe compared with X-rays.

There are many researchers investigated the features of the THz waves. The authors in [5] have shown that, active and enhanced resonant GaN high electron mobility transistor (HEMT) array metamaterials can be used to develop an efficient phase modulation of the THz wave. In [6], a silicon based integrated circuit is developed to enable a chip scale THz system for new sensing, imaging and wireless communication applications. Tadao Nagatsuma et al. have developed a 300-GHz-band wireless communications system that described real-time error-free transmissions at 50 Gbit/s and beyond [7]. In addition, a precise and stable THz measurement platform with displacement and angle precisions of the platform of 0.02 mm and 1°, respectively is proposed in [8].

In this thesis, a 0.3 THz high performance slotted waveguide antenna incorporated with anisotropic low epsilon medium is proposed, designed and simulated for phasic heartbeat measurement application which will be presented in chapter 6. Also a 200 GHz high performance slotted waveguide antenna incorporated with Gradient Index of Refraction Metasurface is proposed, designed and simulated which will be presented in chapter 7.

1.1.2. Continuous Demand for High Processing Speed Computation Units

The development of integrated antennas (on chip antennas) opened the door for construction of a System-on-Chip (SoC). The SoC is more efficient compared to the System-in-Package (SiP) and the parasitic cross coupling due to wiring connections are absent, since bod wire are used to connect the different components of the SiP while on chip antennas can be used to connect the different components of the SoC. Due to the increased transmission speed of the SoC, there is need for achieving higher system bandwidth. To overcome such challenge, the German Research Foundation [9] has installed “Wireless a 100 Gbps and beyond” program.

Also, another group has developed 100 Gbps wireless communication system presented in [10]. However, a broadband amplifier can be incorporated with on chip antennas to achieve a higher system bandwidth [11] and as a result there will be no restriction on system bandwidth caused by low noise and limited bandwidth amplifier.

Due to the rapid progress in information technology and the electronic devices, there is a huge amount of data generated in High Performance Computing (HPC) units [12] and IP traffic [13]. Furthermore, although the HPC becomes more efficient and offering a higher performance compared with the previous generations, the problem of energy consumption dramatically increasing. To solve such problem of energy efficiency of the HPC system from the different hardware and software levels, the Collaborative Research Centre Highly Adaptive Energy- Efficient Computing (HAEC) was established at TU Dresden in 2011 and extended in 2015 [14]. The HAEC had replaced the lossy copper wires used for inter board connection by adaptive wireless connections based on chip antennas as shown in Fig. 1.1 [15].

Although, the problem of energy efficiency can be solved by using adaptive beam splitters, unfortunately this method requires complicated active adaptive phase shifters. On the other hand, by using board to board communication scenario as shown in Fig. 1.1, the optimal placement of communication nodes among specific boards can be achieved under specific constraints controlled by using the control circuitry of the processing unit [16] which can be considered as a radical solution for the energy efficiency problem. Also, the switching capability of the communication nodes of board to board wireless communication can be improved by replacing the beam steering with beam switching. Butler Matrices [17] are well-known circuits that are used widely for antenna beam switching applications. Chapter 7 of this thesis presents a 200 GHz high performance slotted waveguide antenna incorporated with

Gradient Index of Refraction MTS to be used as a basic component for constructing an SoC system.

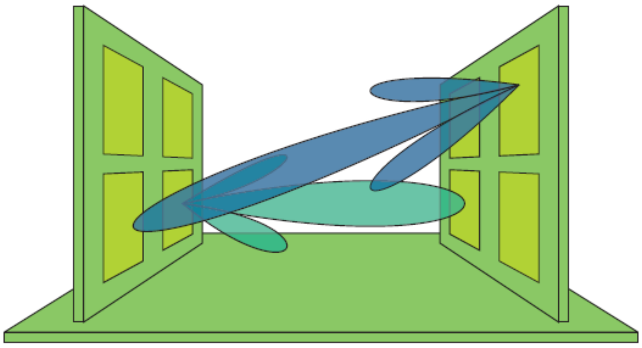

Fig. 1.1. Board to board communication in High Performance Computing (HPC) system. It illustrates two boards with four chips on each board. The shown wireless links are a few examples for connecting the different chips by beam steering or beam switching techniques [15].

1.1.3. Demand for High Bit Rate Wireless Communication Networks

During the last decades, 60 GHz millimetre-waves have seen tremendous researchers' activity and have become the best candidate for many commercial applications [18, 19]. The 60 GHz waves provide many features such as large penetration and propagation losses, so 60 GHz Wireless Local Area Networks (WLANs) are intended to be used in a single room environment and for short range communication. Furthermore, due to the development in Information Technologies (ITs), there are increasing demands in the markets for high speed multimedia data communications including transmission of huge data file, real time video streaming in the modern electronic devices such as laptops and Android mobile phones,...etc. Thus, one of the most promising solutions to achieve such demand of high speed communication is to develop a Gigabit wireless link which uses millimetre waves as a carrier signal. There are vast studies for proposing Wireless Personal Area Network (WPAN) under IEEE 802.15.3c standards which uses millimetre waves as a communication link [20]. The availability of unlicensed 5 to 7 GHz wide bandwidth sources cantered around 60 GHz has opened the door for many 60 GHz front-end technology applications. Also, the progress in electronic devices and the availability of microwave equipment measurement equipment creates new opportunities to operate at data rates up to several Gbps [21, 22].

By looking into the history of mobile and wireless technology, it can be noted that it has been evolved a lot during a short period of time; it has developed from analogy by the transmission to digital to GSM or 2G and then to 3G, 3.5G and 4G or LTE technology which has a high data rate and it is available now through the world. However, 4G technology still suffers from power consumption and spectrum scarcity problems, therefor it was necessary to develop a 5G wireless communication system and it is expected to be available in 2020 [23]. The major advantages of 5G over 4G is the high data rate and low power consumption with better area coverage. The 5G wireless communication system will use high frequency carrier signals which range from 30 GHz up to 300 GHz and reduce the wavelength from centimetres to millimetres. This will create opportunity for huge amount of bandwidth and may be applied in solving the traffic congestion problem as a real life application. On the other hand, the 5G will cause major challenges for the designer. The first challenge is related to the high frequency, since as the frequency increases, the range of data transmission becomes shorter as the waves cannot penetrate in the walls and barrier easily. The second challenge is the attenuation when sight communication is not available between the transmitter and the receiver. The millimetre wave can take the advantage of microcells, nanocells and picocells technologies and are suited for short distance wireless communications [24-26]. The third challenge is related to the fabrication of millimetre wave antennas, since as the frequency increases, the antenna size decreases and it is difficult to fabricate such tiny antennas and this is one of the major problems which has been investigated which is a role of this thesis (see chapter 7, in which 60, 100 and 200 GHz slotted waveguide antennas have been proposed, designed, and simulated).

1.2. Objectives and Contributions

Due to the high demand on the high bit rate communication systems to match the fast progress in the commercial, military, medical and industrial sites, it was necessary to design and implement high performance antennas to transmit and receive data with a high data bit rate. In this thesis, high performance antennas in three different frequency regimes will be considered which include microwave, millimetre and terahertz waves. The new proposed antennas use the technology of Metamaterials, Plasmonics, Photonic, Magnetic and Electronics which is named as Metatronics. Here we will focus on the Negative Refractive Index (NRI), Gradient Refractive Index (GRIN) materials and Low Epsilon Anisotropic Medium to develop high performance antennas. The proposed new antennas with their significant performance improvements can be summarized as follow:

- A new 10 GHz Patch antenna incorporated with double sided Metasurface based on Complementary Split Ring Resonator (CSRR) and Thin Wires (TWs) employing Negative Index of Refraction (NRI). The gain is improved from 6.5 dB to 10.9 dB and the beam area is reduced from 75 degrees to 41 degrees without significant reduction in the bandwidth.
- A new 10 GHz slotted waveguide Antenna incorporated with single sided Metasurface based on electrically Split Ring Resonator (eSRR) employing Anisotropic LEM medium is proposed, designed, fabricated and measured. The results showed that, the gain is improved from 6.5 dB to 13 dB and the beam width is reduced from 94.1 degrees to about 50 degrees.
- A new 303 GHz slotted waveguide antenna incorporated with eSRR single sided employing Anisotropic LEM medium is proposed, designed and simulated. The results showed that, the gain is improved from 6.7 dB to 10.1 dB while the beam width is reduced from 94.1 degrees to about 47 degrees.

- Novel 10 GHz, 60 GHz, 100 GHz, and 200 GHz slotted waveguide antennas incorporated with GRIN Metasurface based on rectangle and circular patch 2D periodic structure is proposed, designed, simulated and fabricated. The results showed that the gain is improved by about 4.5 dB mostly for all antennas while the beam is reduced by about 60 degrees due to beam calumniation caused by the surface impedance gradient of the GRIN structure.
- Novel 10 GHz, 60 GHz and 100 GHz slotted waveguide antennas incorporated with a 2D periodic structure of slotted ring resonators employing GRIN Metasurface is proposed, designed, simulated and fabricated. The results showed that, the antenna gain is improved by 4 dB mostly for all antennas while the beam width is reduced by about 55 degrees. The improvement in the gain is due to the spatial distribution of the refractive index and the transmission phase in the antenna radiation aperture.
- A novel THz photoconductive antenna incorporated with GRIN Metasurface is proposed, modelled and characterized. The antenna is modelled by the help of the transfer function model which integrate both the optoelectronic response and the EM response of the Photoconductive Antenna (PCA) antenna. The main purpose of using the GRIN structure is to improve the radiation efficiency of the PCA and hence improve the received power. The antenna is excited by 800 nm pulsed laser of 80 MHz repetition frequency and 120 fs pulse duration. The PCA antenna is a dipole antenna mounted on LT-GaAs semiconductor substrate and its electrode is biased by a DC voltage.

This thesis contributes the following subjects to the scientific world;

1- Propose, design and implementation of high performance X-band antennas based on volumetric and Metasurface NRI medium.

2- Propose, design and implementation of Microwave and THz high performance antenna based on eSRR MTS employing negative Index of refraction for high bite rate WLAN and WPAN wireless communication networks.

3- Suggestion, design and implementation of new high performance THz slotted waveguide antennas based on GRIN metasurface for on chip antennas.

4- Propose and design a new high performance THz antennas based on eSRR Metasurface employing anisotropic Low Epsilon Medium in the direction of wave propagation for beam culmination for Heart Beat Measurement applications.

5- Semi analytical model for the Photoconductive Antenna (PCA) based on transfer function approach is proposed and verified. Also, a 0.3 THz lens based on GRIN MTS is proposed, designed and simulated to focus the radiated THz waves from the PCA.

1.3. Challenges and Limitations

Two major challenges faced us during implementation and measurement of millimetre and THz wave antennas for WPAN, WLAN, SoC and phasic heartbeat applications which are given as follows:

1- The sensitivity between theoretical, simulation and measurements of the proposed mms and THz antennas resulted in considerable deviation between the expected and the measurement results. To mitigate such deviation, the designer of the antennas should repeat the design, fabrication, and measurement results much time to take into account random errors causes by cables, connectors and noise.

2- Fabrication and mechanical assembly variation of the proposed antennas working at mms and THz waves: The proposed mms and THz waves antennas presented in this thesis are constructed by integrating the slotted waveguide antenna with Metatronics particles. Metatronics particles proposed in this thesis are Negative Index of

Refraction (NRI) Metamaterials, Gradient Index of Refraction volumetric Metamaterials or Metasurface, and 3D anisotropic Low Epsilon Medium (LEM). Such proposed slotted antennas incorporated with Metatronics particles need two technologies for fabrication which are milling and wet etching of Printed Circuit Board (PCB). The milling technology is used to fabricate slotted waveguide antenna at 60, 100, and 200 GHz, while the PCB technology are used to fabricate Metatronics particles at the aforementioned frequencies. The PCB is based on Roger substrates of thicknesses 0.57 mm, and 0.25 mm are used to fabricate 10, and 60 GHz antenna, respectively. While PCB based on Roger substrates of thicknesses 0.125 mm are used to fabricate 100 and 200 GHz. The milling technology available in University of Birmingham (UoB) limits the minimum line/gap width to 0.2 mm which is competitive for fabricating such antennas. Also, the available low cost laboratory based PCB wet etching at the UoB limits the line gap/width to more than 0.3 mm with acceptable tolerance of 5% [27]. Furthermore, mechanical assembly of the mms and THz waves' antenna when connecting different parts such as adaptors and testing equipment affects the overall antenna performance.

1.4. Thesis Organizations

Chapter 1 presents the thesis subject, motivation, objectives and contributions, challenges and limitations as well as thesis organization.

Chapter 2 provides the literature review about the relevant research relevant to our thesis including metamaterials, antennas incorporated with NRI and GRIN and Anisotropic medium.

Chapter 3 presents patch antenna improvement using the NRI medium composed of SRR/TW volumetric metamaterials (MTM) structure. The proposed antenna is designed and simulated for 10 and 300 GHz and fabricated and measured at only 10 GHz.

Chapter 4 includes Design, and Implementation of High Performance patch antenna Incorporated with Complementary Split Ring Resonators and TWs Double sided Metasurface employing negative index of refraction. The proposed antenna is designed and simulated, fabricated and measured at 10 GHz.

Chapter 5 presents a new slotted waveguide antenna incorporated with electrically Split Ring Resonator single sided metasurface employing negative index of refraction. The antenna is designed, fabricated and measured at 10 GHz.

Chapter 6 provides new High Performance X-band and THz waves slotted waveguide antenna incorporated with anisotropic low epsilon medium in the direction of wave propagation, 10 GHz proposed antenna is fabricated and measured. The proposed antenna is designed and simulated for 10 and 300 GHz and fabricated and measured at only 10 GHz.

Chapter 7 presents High performance X-band, mms, and THz slotted antennas incorporated with Gradient Index of Refraction (GRIN) Metasurface for beam culmination purposes. The GRIN is designed and fabricated based on two concepts; the first one uses surface impedance method and the second one uses transmission phases' variation. The proposed antennas are designed, simulated, fabricated and measured for 10, 60, 100 and 200 GHz.

Chapter 8 provides the conclusion and the relevant future work.

1.5. References

[1] E. Nichols and J. Tear, "Joining the infra-red and electric wave spectra," Astrophysical Journal, vol. 61, pp. 17-37, 1925.

[2] M. Tonouchi, "Cutting-edge terahertz technology," Nat Photon, vol. 1, pp. 97-105, 2007.

[3] P. U. Jepsen, D. G. Cooke, and M. Koch, "Terahertz spectroscopy and imaging – Modern techniques and applications," Laser & Photonics Reviews, vol. 5, pp. 124-166, 2011.

[4] D. L. Woolard, R. Brown, M. Pepper, and M. Kemp, "Terahertz Frequency Sensing and Imaging: A Time of Reckoning Future Applications?," Proceedings of the IEEE, vol. 93, pp. 1722-1743, 2005.

[5] Zhao, Y., Zhang, Y., Liang, S., Feng, Z. and Yang, Z., 2017, August. "Terahertz wave phase modulator based on GaN HEMT-Metamaterial". In Infrared, Millimeter, and Terahertz Waves (IRMMW-THz), 2017 42nd International Conference on (pp. 1-2). IEEE.

[6] Sengupta, K. and Wu, X., 2017, August. "THz silicon systems on chip: EM-Circuits-Systems codesign approach". In Infrared, Millimeter, and Terahertz Waves (IRMMW-THz), 2017 42nd International Conference on (pp. 1-3). IEEE.

[7] Nagatsuma, T., Hisatake, S., Fujita, M., Pham, H.H.N., Tsuruda, K., Kuwano, S. and Terada, J., 2016. "Millimeter-wave and terahertz-wave applications enabled by photonics". IEEE Journal of Quantum Electronics, 52(1), pp.1-12.

[8] Zhu, H. and Xue, Q., 2015, August. "A THz measurement platform design for 0.2–1.1 THz". In Infrared, Millimeter, and Terahertz waves (IRMMW-THz), 2015 40th International Conference on (pp. 1-2). IEEE.

[9] R. Kraemer, “Wireless 100Gb/s and Beyond: A Special Focus Program of the German Scientific Foundation,” in IEEE Conference ICC 2013, Budapest, Hungary, 2013.

[10] KrishneGowda, K., Messinger, T., Wolf, A.C., Kraemer, R., Kallfass, I. and Scheytt, J.C., 2015, October. "Towards 100 Gbps wireless communication in THz Band with PSSS modulation: A promising hardware in the lobe experiment"s. In Ubiquitous Wireless Broadband (ICUWB), 2015 IEEE International Conference on (pp. 1-5). IEEE.

[11] F. Ellinger, D. Fritsche, J. Leufker, M. Laabs, and P. D., “Distributed Amplifier & Antenna Systems in SiGe BiCMOS for Ultra Large Bandwidth,” in European Microwave Week 2013, Nuremberg, Germany, 2013.

[12] Miller, R., 2013. "Google's infrastructure boom continues: Expansion ahead in Oregon". Data Center Knowledge.

[13] Cisco, V.N.I., 2014. "The zettabyte era: trends and analysis". Updated (29/05/2013).

[14] Van Dam, T. and Langendoen, K., 2003, November. "An adaptive energy-efficient MAC protocol for wireless sensor networks". In Proceedings of the 1st international conference on Embedded networked sensor systems (pp. 171-180). ACM.

[15] Jenning, M. and Plettemeier, D., 2016, March. "200 GHz 1× 4 antenna array based on planar Butler Matrix". In Microwave Conference (GeMiC), 2016 German (pp. 337-340). IEEE.

[16] J. Israel, J. Martinovic, A. Fischer, M. Jenning, and L. Landau, “Optimal Antenna Positioning for Wireless Board-To-Board Communication Using a Butler Matrix Beamforming Network,” in Proceedings of the International ITG Workshop on Smart Antennas, 2013.

[17] J. Butler and R. Lowe, “Beam-Forming Matrix Simplifies Design of Electronically Scanned Antennas,” Electronic Design, vol. 9, pp. 170–173, 1961.

[18] P. Smulders “Exploiting the 60 GHz Band for Local Wireless Multimedia Access: Prospects and Future Directions”, Eindhoven University of Technology, IEEE Communications Magazine, January 2002.

[19] N. Guo, R. C. Qiu, S. S. Mo, and K. Takahashi, “60-GHz Millimeter-Wave Radio: Principle, Technology, and New Results”, EURASIP Journal on Wireless Communications and Networking, ID 68253, Sept. 2006.

[20] IEEE 802.15. WPAN Millimeter Wave Alternative PHY Task Group 3c (TG3c), www.ieee802.org/15/pub/TG3c.html

[21] S. Guillouard, G. El Zein, J. Citerne, "Wideband Propagation Measurements and Doppler Analysis for the 60 GHz Indoor Channel", Proceedings of The IEEE MTT-S International Microwave Symposium, Anaheim - CA, USA, June 13-19, 1999, pp. 1751-1754.

[22] L. Rakotondrainibe, G. Zaharia, G. El Zein, Y.Lostanlen. “Indoor channel measurements and communication system design at 60 GHz”, XXIX URSRI General Assembly, Chicago, 7-16 August 2008

[23] M. M. M. Ali, O. M. Haraz, S. Alshebeili, A.-R. Sebak, "Design of a 28/32 Ghz dual-band printed slot antenna for the future 5G mobile and wireless communications", 32nd National Radio Science Conference NRSC 2015, 6th of October city, Egypt.

[24] T. S. Rappaport., “Millimeter wave mobile communications for 5G cellular: It will work, IEEE Access, vol.1, pp. 335–349, May 30, 2013.

[25] M. Ali, O. M. Haraz, S. Alshebeili, A.-R. Sebak, "Four-element dualband printed slot antennas array for the future 5G mobile communications network", 32nd National Radio Science Conference NRSC 2015, 6th of October city, Egypt.

[26] Yong Niu, Yong Li, Li Su, and Athanasios V. Vasilakos, “A survey of millimeter wave (mmWave) communications for 5G: opportunities and challenges”, Springer Science Business Media New York published online, April 2015.

[27] Shen, T.M., Kao, T.Y.J., Huang, T.Y., Tu, J., Lin, J. and Wu, R.B., 2012. "Antenna design of 60-GHz micro-radar system-in-package for noncontact vital sign detection". IEEE Antennas and Wireless Propagation Letters, 11, pp.1702-1705.

Chapter 2 Literature Review

2.1. Metamaterials

Metamaterials are artificial materials which have exotic properties which often are not found in nature. The properties of metamaterials can be controlled by the geometric shape, dimensionality and its orientation with respect to the excited EM waves rather than chemical composition. The materials can be classified according to their relative electrical permittivity ε_r and relative magnetic permeability μ_r as shown in Fig. 2.1 and are divided into the following classes; (i) most of the natural materials have ($\mu_r \geq 1$, $\varepsilon_r \geq 1$), (ii) metals in optical frequency regime exhibit negative effective permittivity ($\mu_r \geq 1$, $\varepsilon_r \leq -1$), (iii) Ferro-magnetic materials which have negative magnetic permeability ($\mu_r \leq -1$, $\varepsilon_r \geq 1$), and (iv) materials with simultaneous negative permittivity and permeability. The design, modelling and fabrication of materials with extraordinary properties when ($|\mu_{eff}| \geq 1$, $|\varepsilon_{eff}| \geq 1$) hqw resulted in great development in electromagnetic, material science and mechanical engineering and their applications [1].

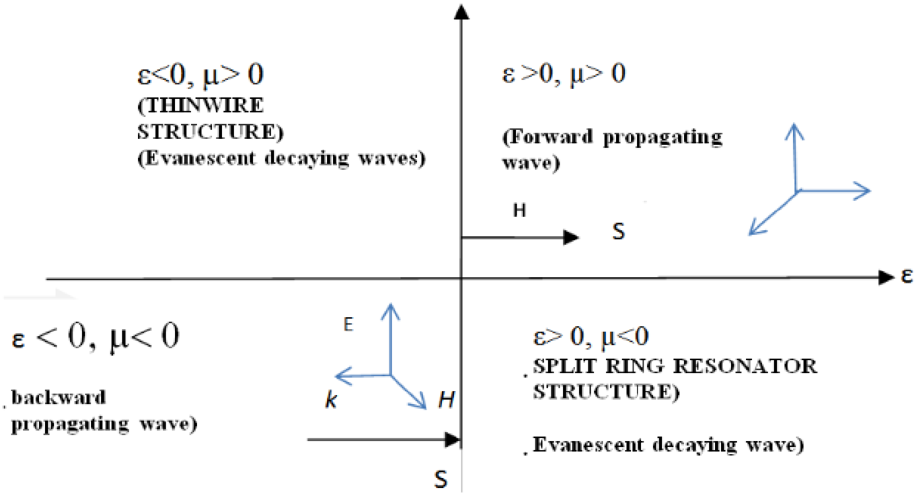

Fig. 2.1. Classification of the materials according to their electrical properties [1].

Metamaterials can be designed to exhibit simultaneously negative effective permittivity (ε_{eff} < 0) and magnetic permeability (μ_{eff}< 0) over a specific range of frequencies which is denoted as metamaterials. Metamaterials (MTM) with simultaneously negative effective permittivity and negative effective permeability were first proposed by Victor Veselago in 1968 and he displayed that the electric field vector *E*, the magnetic field vector *H* and the Poynting vector *S* of such materials form a left handed group with the wave propagation anti-parallel to the energy flow [2]. Until 1999 there is was practical demonstration of metamaterial performance. In 2000, Smith et al. [3] were the first to physically demonstrate and practically implement such artificial materials with simultaneous negative effective permittivity and permeability and they are denoted as a Left Handed Metamaterial (LHM). Metamaterials which exhibit both negative effective permittivity and negative effective permeability are called Double Negative Materials (DNG) materials. Metamaterials which exhibit either negative effective permittivity or negative effective permeability are called Single Negative materials (SNG), Epsilon Negative (ENG) or Mu negative (MNG). There are many applications for ENG, MNG and DNG such as SAR reduction [4-6], high performance antenna design [7-9], cloaking invisibility [10, 11], polarization rotation [12], compact size and/or high performance filters and other applications [13-20].

Recently, multi band metamaterials or arrays of metamaterials with Negative Refractive Index (NRI) or Near to Zero Refractive Index (NZI) are used to design high gain, and multiband antennas [21, 22]. Also, multi-band metamaterials have promising applications in the thermal detectors, explosive detection and bolometers [23]. Many researchers proposed various alphabetic metamaterial structures for various applications; for example an S-shaped metamaterial was proposed by Hayet Benosman et al. [24, 25] in the microwave regime which exhibit simultaneously negative permittivity and permeability between 15.67 and 17.43 GHz. Anik Mallik *et al.* [26] have proposed a U-shaped metamaterial that exhibits NRI around 5, 6 and 11 GHz. Evren Ekmekçi *et al.* have demonstrated a V-Shaped metamaterial which exhibits NRI around 8.10 GHz [27]. Abdallah Dhouibi *et al.* [28] have presented a Z-shaped metamaterial that is applicable for 4.5 GHz applications which exhibits negative permittivity only.

2.2. Antennas Based on Negative Index of Refraction Metamaterials

During the last decade, great attention has been given to metamaterials in many wireless communication applications because of their ability to miniaturize microwave devices such as filters, resonators and antennas [29, 30]. Multi layered metamaterials separated by a quarter wavelength have been used to improve the performance of microwave radiation sources when they are used as absorbers [31]. The metamaterial absorber can be used as a protection layer against external risk as well as to improve the performance of the radiation source [32].

There are various metamaterial configurations which can guide the wave for a specific purpose such as Electromagnetic Band Gap (EBG) structures [33], Frequency Selective Surfaces (FSS) [34], and Left Handed Metamaterials (LHM) [35]. LHM are used to improve the performance of patch antennas as it is reported in many articles [36-40]. All the metamaterials proposed in refs. [36-40] are in the low microwave frequency regime such as 1.7 GHz to 2 GHz [36], 1.5 GHz to 2.1 GHz [37], 3.5 GHz to 5 GHz [38], 1.7 GHz to 3 GHz [39] and 8.5 GHz to 9.5 GHz [40]. A large amount of research has been carried out to reduce the size and improve the performance of patch antenna [41-44] such as metamaterials based on Complementary Split Ring Resonators (CSRR) [41], MTM based on a mushroom like structure [42], reactive impedance surfaces [43] or by creating slots/gaps at the edge of the patch [44]. The metamaterial parameters can be extracted by the theoretical techniques presented in [45]. Pendry proposed NRI MTM to be used as a focusing lens [46] and then Grbic and Eleftheriades worked on developing a NRI MTM as a focusing lens [47]. It should be noted that printed Split Ring Resonators (SRRs) and Thin Wires (TWs) structures integrated together are used to construct Double Negative DNG volumetric materials [2], also printed Transmission Line (TL) can be used to construct Left Handed TL [48]. Both volumetric NRI and LHTL unit cells can be repeated in a plane perpendicular on the wave propagation to construct metamaterial medium.

In this thesis, Adel A. A. Abdelrehim and Hooshang Ghafouri-Shiraz proposed high performance patch antenna incorporated with Circular Split Ring Resonators and Thin Wires (CSRR/TW) employing NRI MTM lens [49]. The antenna operating at 10 GHz and the gain was improved by 4.6 dB, while the beam width was reduced from 75 to 41 degrees without affecting significantly the bandwidth and impedance matching. Also, the aforementioned authors proposed a high performance 0.3 THz patch antenna based on beam focusing using SRR/TW NRI MTM for Heartbeat (HB) Measurement applications [50]. Bala, *et al.* proposed a patch antenna based on graphene operating at 13 THz with 12.3% impedance matching and -27.57 dB return loss with reasonable good gain [51]. In [52], a THz antenna operating around 1.3 THz was designed based on a graphene plasmonic resonance; the antenna was excited by a Continuous Wave (CW) laser beam, the antenna provides size miniaturization and high performance in terms of return loss and radiation efficiency point of views. Wongkasem, N. et al. proposed, designed, fabricated and tested a novel Y-shaped chiral negative index of refraction metamaterials in the microwave and terahertz frequency regime [53]. Many researchers have proved that, NRI volumetric metamaterials suffer from narrow bandwidth and high loss challenges; some other research has overcome this problem. For example, in [54], a broadband low profile negative index of refraction metamaterial lens was designed and simulated based on a fishnet metamaterial structure. The lens operates in a broadband regime from 54 GHz to 58 GHz, and provides a fractional bandwidth of ~7%. Also, in [55], active NRI metamaterial operating at sub THz frequencies was designed and simulated. Such active NRI MTM is constructed from passive NRI MTM on a quartz substrate and tunnelling diode to provide gain which works as a compensator to the loss coming from the passive MTM. All of the volumetric NRI MTMs have to overcome the challenge in terms of mechanical assembly and fabrication which becomes increasingly different at THz frequencies. This problem can be solve by using NRI Metasurface (MTS) structures, Adel A. A. Abdelrehim and Hooshang Ghafouri-Shiraz proposed, designed, fabricated and tested X-band high performance slotted waveguide antenna based on an Electrically Split Ring Resonator (ESRR) NRI MTS structure, the antenna provides high gain and it is scalable up to 900 GHz since it uses waveguide connectors for excitation and an MTS single side NRI MTS lens for beam focusing [56].

2.3. Impact of 3-D Anisotropic ZIM, LEM and LMM Metamaterials on Antenna Performance

In recent years, MTM has resulted tremendous attention in the field of materials and electromagnetics because of their exotic properties [57]. Metamaterials are a good candidate for miniaturizing the size while maintaining high performance microwave and terahertz devices [58-61] and microwave antennas [62-64]. In addition to the tremendous isotropic volumetric and metasurface NRI structures (provided in the last section), metamaterials can be designed to exhibit three dimension (3D) anisotropic properties. The 3D anisotropic MTM was developed for the first time in 2002 when Enoch et al. displayed that Zero Index Metamaterials (ZIM) can provide an antenna system with directive emission [65] and then Ziolkowski characterized the propagation and scattering of electromagnetic (EM) waves in the ZIM MTM [66]. The Zero Index Metamaterial has been applied by many researchers to employ a ZIM Lens [67-74]. The ZIM can be implemented by electrical resonators which exhibit near zero permittivity [65, 67, 68, 70, 75] or by magnetic resonators which exhibit near zero permeability [72]. In case of ZIM which is implemented by Epsilon Near to Zero (ENZ) or Mu Near to Zero (MNZ), the wave impedance of such ZIM cannot be matched with free space impedance. As a result the radiation efficiency of the antenna decreases and hence the impedance match of the ZIM layer with the free space is placed inside the aperture of the horn [67, 70] or it can be placed as part of the ground plan as in the case of the patch antenna [69, 71, 75, 76] in which case it works due to a Fabry-Perot resonance [77-79], or the ZIM can cover the whole space around the radiating element [65, 72].

In 2009, Ma, et al. had investigated the problem of impedance matching of homogenous ZIM with the free space when he theoretically displayed that anisotropic Zero Index Metamaterial Lens (ZIML) with convenient constitutive tensor had good impedance matching with free space [73]. As a result, the anisotropic ZIML can efficiently improve the antenna gain and has a good impedance matching with free space. According to the theory presented in [73], Cheng et al. proposed and implemented anisotropic ZIML composed of Split Ring Resonator (SRR) to improve the line source antenna directivity [72], but unfortunately the proposed ZIML was large and had limited in bandwidth. In [80], broadband anisotropic ZIML was proposed and implemented to enhance the performance of the Vivaldi antenna. Furthermore, Turpin et al. in [82] proposed, designed and numerically investigated a new anisotropic ZIML based on the Transformation Optics (TO) method according to the theory presented in [81]. The anisotropic ZIML presented in [82] suffers from fabrication difficulty and assembly because it is a 3D structure. By comparing the aforementioned anisotropic ZIML with the metamaterial based Gradient Refractive Index (GRIN) lenses presented in [83-85], it is clear that, ZIMLs are small in size.

In [86], the antenna directivity is improved by applying Near to Zero Refractive Index (NZRI) as a superstrate. The proposed NZRI is applied to two types of antennas which are parabolic and very large array antenna, but the bulk and the curved surface of the parabolic antenna limit its application, and also the large array patch antenna incorporated with NZRI suffers from having a complex feeding network [87]. One of the interesting solutions to the fabrication difficulty of the antenna incorporated with NZRI is to use planar metasurface embedded with a patch antenna [88]. The NZRI has been developed for different applications [89, 90]. One of the major electromagnetic characteristics of the NZRI is it’s near to zero phase variation. As a result, it is considered as the best candidate to be used for different applications from microwave to optical frequency including controllable surface, novel waveguide structure, miniaturized cavity resonator, absorbers and for other components. However, the major advantages of NZRI MTS are its low profile, ease in integration with the other microwave components, cavity less structure and reduction in mutual coupling between the array antenna elements [90]. Abdelrehim, A.A. and Ghafouri-Shiraz, H. have proposed a new anisotropic Low Epsilon Medium (LEM) which exhibits a near to zero epsilon in direction of wave propagation and has a unity effective permittivity in the other two directions. The proposed anisotropic LEM is composed of Electrically Split Ring Resonator (ESRR) MTS structure. Then the anisotropic LEM MTS is incorporated with a slotted wave guide antenna operating in the X-band 10 and sub-THz frequency of 300 GH. The results showed that the *E*-plane beam of the antenna is significantly improved, the gain, and directivity are also improved, and beam is reduced without significantly affecting the bandwidth and impedance matching. The proposed novel antenna was fabricated and tested at 10 GHz [91, 92].

2.4. Beam Focusing of Radiated waves by using Gradient Index of Refraction Lenses

Recently, lens antennas have resulted considerable interest for microwave and millimetre wave applications, since they achieve a broadband and high gain performance due to beam focusing in the quiescent direction. The conventional lenses are implemented from dielectric materials and they suffer from heavy and bulky profile and require expensive machining processes [93]. The sub wavelength resonance and non-resonance periodic structures have been considered as alternatives for dielectric lenses [94-96], also metamaterials are used to implement a lens to focus the radiated spherical waves [97-108]. Various types of lenses have been implemented by controlling the effective parameters of metamaterials such as negative index of refraction lenses [97], zero index of refraction lenses [98, 99] and Gradient Index of Refraction (GRIN) lenses [100-107].

The lenses constructed from ZIM, and NRI suffer from narrow bandwidth and large transmission loss problems and GRIN lenses overcome such challenges. GRIN lens operates in the non-resonance region of the index of refraction and the index of refraction is gradually changed with the lens aperture. There are some famous GRIN lens configurations presented in the literature such as Maxwell fisheye and Luneburg lenses [105-107]. For example, the Luneburg lens presented in [105] is a 3-D half sphere with index of refraction n of spatially distribution function given by $n = \left(2 - \frac{r^2}{R^2}\right)^{0.5}$ which has been designed at 15 GHz, where R is the radius of the lens aperture and r is the radius of the unit cell measured from the centre of the lens. The index of refraction is gradually changed by 0.8 through the whole lens aperture. This 3-D Luneburg lens is bulky since it is constructed from 35 spherical shells. In this thesis, non-resonance and resonance GRIN MTS structures for beam focusing are proposed, designed, simulated and implemented. The no-resonance GRIN MTS is constructed from a 2D periodic metallic patch structure mounted on a grounded dielectric substrate. The resonance GRIN MTS was constructed from an annular slot 2D periodic structure. The GRIN MTS was then incorporated with the slotted waveguide antenna to construct high gain microwave, millimetre, and terahertz antennas.

2.5. References

[1] Gangwar, K., & Gangwar, R. P. S. (2014)." Metamaterials: characteristics, process and applications". Advances in Electronic and Electric Engineering, 4, 97-106.

[2] Veselago, V.G. "The electrodynamics of substances with simultaneously negative values of ε and μ'. Sov. Phys. Uspekhi **1968**, 10, 509–514.

[3] Smith, D.R.; Padilla, W.J.; Vier, D.C.; Nemat-Nasser, S.C.; Schultz, S. "Composite medium with simultaneously negative permeability and permittivity". Phys. Rev. Lett. **2000**, 84, 4184–4187.

[4] Faruque, M.R.I.; Islam, M.T.; Misran, N. "Design analysis of new metamaterial for EM absorption reduction". Prog. Electromagn. Res. **2012**, 124, 119–135.

[5] Faruque, M.R.I.; Islam, M.T.; Misran, N. "Evaluation of EM absorption in human head with metamaterial attachment". Appl. Comput. Electromagn. Soc. J. **2010**, 25, 1097–1107.

[6] Islam, M.T.; Faruque, M.R.I.; Misran, N. "Study of specific absorption rate (SAR) in the human head by metamaterial attachment". IEICE Electron. Express **2010**, 7, 240–246.

[7] Li, L.; Li, Y.; Yeo, T.S.; Mosig, J.R.; Martin, O.J.F. "A broadband and high-gain metamaterial microstrip antenna". Appl. Phys. Lett. **2010**, 96, 164101:1–164101:3.

[8] Wu, B.-I.; Wang, W.; Pacheco, J.; Chen, X.; Grzegorczyk, T.; Kong, J.A. "A study of using metamaterials as antenna substrate to enhance gain". Prog. Electromagn. Res. **2005**, 51, 295–328.

[9] Yang, Y.; Singh, R.; Zhang, W. "Anomalous terahertz transmission in bow-tie plasmonic antenna apertures". Opt. Lett. **2011**, 36, 2901–2903.

[10] Schurig, D.; Mock, J.J.; Justice, B.J.; Cummer, S.A.; Pendry, J.B.; Starr, A.F.; Smith, D.R. "Metamaterial Electromagnetic Cloak at Microwave Frequencies". Science **2006**, 314, 977–980.

[11] Landy, N.; Smith, D.R. "A full-parameter unidirectional metamaterial cloak for microwaves". Nat. Mater. **2013**, 12, 25–28.

[12] Cong, L.; Cao, W.; Zhang, X.; Tian, Z.; Gu, J.; Singh, R.; Han, J.; Zhang, W. "A perfect metamaterial polarization rotator". Appl. Phys. Lett. **2013**, 103, 171107:1–171107:4.

[13] Al-Naib, I.; Jansen, C.; Singh, R.; Walther, M.; Koch, M. "Novel THz metamaterial designs: From near- and far-field coupling to high-q resonances". IEEE Trans. Terahertz Sci. Technol. **2013**, 3, 772–782.

[14] Singh, R.; Al-Naib, I.; Cao, W.; Rockstuhl, C.; Koch, M.; Zhang, W. "The fano resonance in symmetry broken terahertz Metamaterials". IEEE Trans. Terahertz Sci. Technol. **2013**, 3, 1–7.

[15] Chowdhury, D.R.; Azad, A.K.; Zhang, W.; Singh, R. "Near field coupling in passive and active terahertz metamaterial devices". IEEE Trans. Terahertz Sci. Technol. **2013**, 3, 783–789.

[16] Chowdhury, D.R.; Singh, R.; Reiten, M.; Zhou, J.; Taylor, A.J.; O'Hara, J.F. Tailored resonator coupling for modifying the terahertz metamaterial response. Opt. Express **2011**, 19, 10679–10685.

[17] Chowdhury, D.R.; Singh, R.; O'Hara, J.F.; Chen, H.T.; Taylor, A.J.; Azad, A.K. "Dynamically reconfigurable terahertz metamaterial through photo-doped semiconductor". Appl. Phys. Lett. **2011**, 99, 231101:1–231101:3.

[18] Cao, W.; Singh, R.; Zhang, C.; Han, J.; Tonouchi, M.; Zhang, W. "Plasmon-induced transparency in metamaterials: Active near field coupling between bright superconducting and dark metallic mode resonators". Appl. Phys. Lett. **2011**, 103, 101106:1–101106:5.

[19] Gu, J.; Singh, R.; Azad, A.K.; Han, J.; Taylor, A.J.; O'Hara, J.F.; Zhang, W. "An active hybrid plasmonic metamaterial". Opt. Mater. Express **2012**, 2, 31–37.

[20] Menzel, C.; Singh, R.; Rockstuhl, C.; Zhang, W.; Lederer, F. "Effective properties of terahertz double split-ring resonators at oblique incidence". J. Opt. Soc. Am. B **2009**, 26, B143–B147.

[21] Ullah, M.H.; Islam, M.T.; Faruque, M.R.I. "A Near-Zero Refractive Index Meta-Surface Structure for Antenna Performance Improvement". Materials **2013**, 6, 5058–5068.

[22] Islam, M.T.; Ullah, M.H.; Singh, M.J.; Faruque, M.R.I. "A new metasurface superstrate structure for antenna performance enhancement". Materials **2013**, 6, 3226–3240.

[23] Shen, X.; Cui, T.J.; Zhao, J.; Ma, H.F.; Jiang, W.X.; Li, H. "Polarization-independent wide-angle triple-band metamaterial absorber". Opt. Express **2011**, 19, 9401–9407.

[24] Benosman, H.; Hacene, N.B. "Design and simulation of double "S" shaped metamaterial". Int. J. Comput. Sci. Issues **2012**, 9, 534–537.

[25] Chen, H.; Ran, L.; Huangfu, J.; Zhang, "X. Left-handed materials composed of only S-shaped resonators". Phys. Rev. E **2004**, 70, 940–942.

[26] Mallik, A.; Kundu, A.S.; Goni, M.O. "Design of a novel two-rectangular U-shaped double negative metamaterial". In Proceedings of the International Conference on Informatics, Electronics & Vision (ICIEV), Dhaka, Bangladesh, 17–18 May 2013.

[27] Ekmekci, E.; Sayan, G.T. 'Investigation of effective permittivity and permeability for a novel V-shaped metamaterial using S-parameters". In Proceedings of the 5th International Conference on Electrical and Electronics Engineering, Bursa, Turkey, 5–9 December 2007.

[28] Dhouibi, A.; Burokur, S.N.; Lustrac, A.; Priou, A. "Study and analysis of an electric Z-shaped meta-atom". Adv. Electromagn. **2012**, 1, 64–70.

[29] A. Lio, and T. Itoh, “Composit right/left – handed transmission line metamaterials,” IEEE microwave magazine, pp. 34–50, September 2004.

[30] S. N. BUrokur, M. Latrach, and S. Toutain, “Theoretical investigation of a circular patch antenna in presence of a left – handed medium,” IEEE antenna and wirless propagation letters, vol. 4, pp.183–186, April, 2005.

[31] C. M. Watts, X. Liu,and W. J. Padilla,“Metamaterial electromagnetic wave absorbers,” Adv. mater, vol. 24, pp. 98 – 120, 2012.

[32] H. Attia, O. Siddiqui, L. Yousefi, and O. M. Ramahi, “Metamaterials for gain enhancement of printed antenna : Theory, measurement and optimization,”IEEE electronics, communication and photonics conference (SIECPC) Saudi international, pp.1 – 6, 2011.

[33] A. Kumar, “A microstrip patch antenna with metamaterial and EBG structures,” IEEE signal processing and communication (ICSE), International Conference,pp. 27-32, 12-14 December.2013 .

[34] S. Narayan and R. M. Jha, “Electromagnetic techniques and design strategies for FSS structure application,”IEEE Antenna and Propagation Magazine, vol. 57,issue 5, pp. 135- 158, October 2015.

[35] B. Garg and D. Saleem, “Experimental verification of double negative property of LHM with significant improvement in microstrip transceiver paramerers in S band,” International Journal of Practical Research (IJEPR), vol. 2, issue 2, pp. 64–70, May 2013.

[36] R. K. Bagari and S. Meena, “Design and analysis of rectangular microstrip patch antenna using metamaterial for better efficiency,” JMEIT , vol.2, issue 2,pp. 15-20, Apr. 2015.

[37] A. Tomar, “Design of square split ring resonator shaped metamaterials structure for enhancing the microstrip patch antenna parameter,” IJRECT, vol.1,issue 3, pp. 21-24, September 2014.

[38] S. Chaimool, K. L. Chung and P. Akkaraekthalin, “Simulataneous gain and bandwidths enhancement of a single feed circularly polarized microstrip patch antenna using a metamaterials reflective surfface,” Progress In Electromagnetics Research B, vol.22,pp.23-37, 2010.

[39] P. K Singhal and B. Garg, “A novel approach for size reduction for rectangular microstrip patch antenna, ” IJECCT, vol.3(1), pp. 35-39,2012.

[40] P.Paswan, V. Mishra, P.N. Patel, and S. Dwivedi, “Performance enhancement of coaxial feed microstrip paatch antennausing left- handed metamaterial cover,” IEEE Student Conference on Electrical, Electronics and Computer Science, pp. 1 – 4, 2014.

[41] M. Selvanayagam, “A compact printed antenna with an embedded double tuned metamaterial matching network,” IEEE Transactions on Antennas and Propagation, vol.58,pp, 2354-2361, 2010.

[42] A. Lai, K. Leong, and T. Itoh, “Infinite wavelength resonant antennas with monopolar radiation pattern based on periodic structures,” IEEE Transactions On Antennas and Propagation, vol. 55,pp. 868-876, 2007.

[43] K. Sarabandi, G. Palafox, “Reducing antenna visual signature using metamaterials,” The 25th Army Science Conference, Orlando, Fl. , Nov. 2006.

[44] D.T. Notris, C. Phaedra, P. Dimitris, “Dual polarized microstrip patch antenna, reduced in size by use of peripheral slits,” The 7th European Conference on Wireless Technology, Amsterdam, The Netherlands, pp. 273–276, Oct. 2004.

[45] M. S. Sharawi and A. B. Numan, “Extraction of meterial parameters for metamaterials using a full wave simulator” IEEE Antenna and Propagation Magazine, vol.55,no. 5. October 2013.

[46] J.B. Pendry, “Negative Refraction Makes a Perfect Lens,” Physical Review Letters, Vol. 85, No. 18, pp.3966-3969, 30 October 2000.

[47] A. Grbic and G.V. Eleftheriades, “Subwavelength Focusing Using a Negative-Refractive-Index Transmission Line Lens,” IEEE Antennas and Wireless Propagation Letters, Vol. 2, pp.186-189, 2003.

[48] L. Markley and G.V. Eleftheriades, “A Negative-Refractive-Index Metamaterial for Incident Plane Waves of Arbitrary Polarization,” IEEE Antennas and Wireless Propagation Letters, Vol. 6, pp.28-32, 2007.

[49] Abdelrehim, A.A. and Ghafouri-Shiraz, H. "Performance Improvement of Patch Antenna Using Circular Split Ring Resonators and Thin Wires Employing

Metamaterials Lens". Progress in Electromagnetics Research B, 69, pp.137-155, 2016.

[50] Abdelrehim, A.A. and Ghafouri-Shiraz, H. "High performance terahertz antennas based on split ring resonator and thin wire metamaterial structures". Microwave and Optical Technology Letters, 58(2), pp.382-389, 2016.

[51] Bala, R., Marwaha, A. and Marwaha, S. "Performance Enhancement of Patch Antenna in Terahertz Region Using Graphene". Current Nanoscience, 12(2), pp.237-243, 2016.

[52] Tamagnone, M., Gomez-Diaz, J.S., Mosig, J.R. and Perruisseau-Carrier, J. "Analysis and design of terahertz antennas based on plasmonic resonant graphene sheets". Journal of Applied Physics, 112(11), p.114915, 2012.

[53] Wongkasem, N., Akyurtlu, A., Marx, K.A., Dong, Q., Li, J. and Goodhue, W.D." Development of chiral negative refractive index metamaterials for the terahertz frequency regime". IEEE Transactions on Antennas and Propagation, 55(11), pp.3052-3062, 2007.

[54] Orazbayev, B., Pacheco-Peña, V., Beruete, M. and Navarro-Cía, M." Exploiting the dispersion of the double-negative-index fishnet metamaterial to create a broadband low-profile metallic lens". Optics express, 23(7), pp.8555-8564, 2015.

[55] Kantemur, A., Tang, Q. and Xin, H. "Design of volumetric sub-THz negative refractive index metamaterial with gain". In Antennas and Propagation (APSURSI), 2016 IEEE International Symposium on (pp. 269-270). IEEE, 2016.

[56] Abdelrehim, A.A. and Ghafouri-Shiraz, H."High gain slotted waveguide antenna based on beam focusing using electrically split ring resonator metasurface

employing negative refractive index medium". Submitted to Progress In Electromagnetics Research, 2017

[57] Pendry, J.B. "A chiral route to negative refraction". Science, 306(5700), pp.1353-1355, 2004.

[58] Andres-Garcia, B., Garcia-Munoz, L.E., Gonzalez-Posadas, V., Herraiz-Martinez, F.J. and Segovia-Vargas, D. "Filtering lens structure based on SRRs in the low THz band". Progress In Electromagnetics Research, 93, pp.71-90, 2009.

[59] Huang, L. and Chen, H. "Multi-band and polarization insensitive metamaterial absorber". Progress In Electromagnetics Research, 113, pp.103-110, 2011.

[60] Torres, V., Sánchez, N., Etayo, D., Ortuño, R., Navarro-Cía, M., Martínez, A. and Beruete, M. "Compact quarter-wave plate metasurface at 1 and 2.2 THz". In Antennas and Propagation (EuCAP), 2015 9th European Conference on (pp. 1-2). IEEE, 2015.

[61] Chen, H., Hou, B., Chen, S., Ao, X., Wen, W. and Chan, C.T. "Design and experimental realization of a broadband transformation media field rotator at microwave frequencies". Physical review letters, 102(18), p.183903, 2009.

[62] Lim, S., Caloz, C. and Itoh, T. "A reflectodirective system using a composite right/left-handed (CRLH) leaky-wave antenna and heterodyne mixing". IEEE Microwave and Wireless Components Letters, 14(4), pp.183-185, 2004.

[63] Attia, H., Bait-Suwailam, M.M. and Ramahi, O.M. "Enhanced gain planar inverted-F antenna with metamaterial superstrate for UMTS applications". PIERS online, 6(6), pp.585-588, 2010.

[64] Bahrami, H., Hakkak, M. and Pirhadi, A. "Analysis and design of highly compact bandpass waveguide filter using complementary split ring resonators (CSRR)". Progress In Electromagnetics Research, 80, pp.107-122, 2008.

[65] Enoch, S., Tayeb, G., Sabouroux, P., Guérin, N. and Vincent, P. "A metamaterial for directive emission". Physical Review Letters, 89(21), p.213902, 2008.

[66] Ziolkowski, Richard W. "Propagation in and scattering from a matched metamaterial having a zero index of refraction." Physical Review E 70, no. 4 (2004): 046608.

[67] Wu, Qun, Pan Pan, F-Y. Meng, L-W. Li, and J. Wu. "A novel flat lens horn antenna designed based on zero refraction principle of metamaterials." Applied Physics A 87, no. 2 (2007): 151-156.

[68] Xiao, Zhigang, and Huiliang Xu. "Low refractive metamaterials for gain enhancement of horn antenna." Journal of Infrared, Millimeter, and Terahertz Waves 30, no. 3 (2009): 225-232.

[69] Kim, D. and Choi, J., 2010. Analysis of antenna gain enhancement with a new planar metamaterial superstrate: An effective medium and a Fabry-Pérot resonance approach. Journal of Infrared, Millimeter, and Terahertz Waves, 31(11), pp.1289-1303.

[70] Hrabar, Silvio, Davor Bonefacic, and Damir Muha. "ENZ-based shortened horn antenna-An experimental study." In Antennas and Propagation Society International Symposium, 2008. AP-S 2008. IEEE, pp. 1-4. IEEE, 2008.

[71] Ju, Jeongho, Dongho Kim, Wangjoo J. Lee, and Jaeick I. Choi. "Wideband high-gain antenna using metamaterial superstrate with the zero refractive index." Microwave and Optical Technology Letters 51, no. 8 (2009): 1973-1976.

[72] Cheng, Qiang, Wei Xiang Jiang, and Tie Jun Cui. "Radiation of planar electromagnetic waves by a line source in anisotropic metamaterials." Journal of Physics D: Applied Physics 43, no. 33 (2010): 335406.

[73] Ma, Y. G., P. Wang, X. Chen, and C. K. Ong. "Near-field plane-wave-like beam emitting antenna fabricated by anisotropic metamaterial." Applied Physics Letters 94, no. 4 (2009): 044107.

[74] Jiang, Zhi Hao, and Douglas H. Werner. "Anisotropic metamaterial lens with a monopole feed for high-gain multi-beam radiation." In Antennas and Propagation (APSURSI), 2011 IEEE International Symposium on, pp. 1346-1349. IEEE, 2011.

[75] Weng, Zi-Bin, Yong-Chang Jiao, Gang Zhao, and Fu-Shun Zhang. "Design and experiment of one dimension and two dimension metamaterial structures for directive emission." Progress In Electromagnetics Research 70 (2007): 199-209.

[76] Weng, Z-B., X-M. Wang, Y. Song, Y-C. Jiao, and F-S. Zhang. "A directive patch antenna with arbitrary ring aperture lattice metamaterial structure." Journal of Electromagnetic Waves and Applications 22, no. 8-9 (2008): 1283-1291.

[77] Sauleau, Ronan, Philippe Coquet, Toshiaki Matsui, and J-P. Daniel. "A new concept of focusing antennas using plane-parallel Fabry-Perot cavities with nonuniform mirrors." IEEE Transactions on Antennas and Propagation 51, no. 11 (2003): 3171-3175.

[78] Smith, D. R., S. Schultz, S. L. McCall, and P. M. Platzmann. "Defect studies in a two-dimensional periodic photonic lattice." Journal of Modern Optics 41, no. 2 (1994): 395-404.

[79] Kaklamani, D. I. "Full-wave analysis of a Fabry-Perot type resonator." Progress In Electromagnetics Research 24 (1999): 279-310.

[80] Zhou, Bin, Hui Li, Xiaying Zou, and Tie-Jun Cui. "Broadband and high-gain planar Vivaldi antennas based on inhomogeneous anisotropic zero-index metamaterials." Progress In Electromagnetics Research 120 (2011): 235-247.

[81] Wu, Qi, Jeremiah P. Turpin, Douglas H. Werner, and Erik Lier. "Thin metamaterial lens for directive radiation." In Antennas and Propagation (APSURSI), 2011 IEEE International Symposium on, pp. 2890-2893. IEEE, 2011.

[82] Turpin, J.P., Wu, Q., Werner, D.H., Lier, E., Martin, B. and Bray, M. "Anisotropic metamaterial realization of a flat gain-enhancing lens for antenna applications". In Antennas and Propagation (APSURSI), 2011 IEEE International Symposium on (pp. 2886-2889). IEEE, 2011.

[83] Mei, Zhong Lei, Jing Bai, Tiao Ming Niu, and Tie Jun Cui. "A half Maxwell fish-eye lens antenna based on gradient-index metamaterials." IEEE Transactions on Antennas and Propagation 60, no. 1 (2012): 398-401.

[84] Zhang, Y., R. Mittra, and W. Hong. "On the synthesis of a flat lens using a wideband low-reflection gradient-index metamaterial." Journal of Electromagnetic Waves and Applications 25, no. 16 (2011): 2178-2187.

[85] Neu, Jens, Bernd Krolla, Oliver Paul, Benjamin Reinhard, René Beigang, and Marco Rahm. "Metamaterial-based gradient index lens with strong focusing in the THz frequency range." Optics express 18, no. 26 (2010): 27748-27757.

[86] Yang, G.M., Xing, X., Daigle, A., Obi, O., Liu, M., Lou, J., Stoute, S., Naishadham, K. and Sun, N.X. "Planar annular ring antennas with multilayer self-biased NiCo-ferrite films loading". IEEE, 2010

[87] Zhou, H., Z. Pei, S. Qu, S. Zhang, J. Wang, Q. Li, and Z. Xu. "A planar zero-index metamaterial for directive emission." Journal of Electromagnetic Waves and Applications 23, no. 7 (2009): 953-962.

[88] Enoch, Stefan, Gérard Tayeb, Pierre Sabouroux, Nicolas Guérin, and Patrick Vincent. "A metamaterial for directive emission." Physical Review Letters 89, no. 21 (2002): 213902.

[89] Valentine, Jason, Shuang Zhang, Thomas Zentgraf, Erick Ulin-Avila, Dentcho A. Genov, Guy Bartal, and Xiang Zhang. "Three-dimensional optical metamaterial with a negative refractive index." nature 455, no. 7211 (2008): 376.

[90] Zhu, Ning, and Richard W. Ziolkowski. "Photoconductive THz antenna designs with high radiation efficiency, high directivity, and high aperture efficiency." IEEE Transactions on terahertz science and technology 3, no. 6 (2013): 721-730.

[91] Abdelrehim, A.A. and Ghafouri-Shiraz, H. "Design of High Performance Slotted Waveguide Antenna Based on Electrically Split Ring Resonator Metasurface Employing Anisotropic Low Epsilon Medium for E-Plane Beam Focusing". submitted to IET journal, 2017

[92] Abdelrehim, A.A. and Ghafouri-Shiraz, H. "High performance terahertz slotted waveguide antenna based on electrically split ring resonator metasurface employing low epsilon medium for E-plane beam focusing". Microwave and Optical Technology Letters, 59(7), pp.1507-1517, 2017.

[93] T. L. A. Rhys, “The design of radially symmetric lenses,” IEEE Trans. Antennas Propag., vol. 18, no. 4, pp. 497–506, Jul. 1970.

[94] A. Petosa and D. A. McNamara, “Research and development on phase shifting surfaces (PSSs),” IEEE Antennas Propag. Mag., vol. 55, no. 2, pp. 29–48, Jun. 2013.

[95] M. Niroo-Jazi, A. R. Sebak, M. Chaharmir, and J. Shaker, “Applications of polarization-independent frequency selective filters for transmit array antennas,” in Proc. IEEE Int. Symp. Antennas Propag., Jul. 2014.

[96] S. M. A. M. H. Abadi and N. Behdad, “Design of wideband, FSS-based multi beam antennas using the effective medium approach,” IEEE Trans. Antennas Propag., vol. 62, no. 11, pp. 5557–64, Nov. 2014.

[97] R. B. Greegor, C. Parazzoli, J. Nielse, M. A Thompson, M. H. Tanielian, and D. R. Smith, “Simulation and testing of a graded negative index of refraction lens,” Appl. Phys. Lett., vol. 87, pp. 091114-1–091114-3, Aug. 2005.

[98] H. Xu, G. Wang, and T. Cai, “Miniaturization of 3-D anistropic zerorefractive- index metamaterials with application to directive emissions,” IEEE Trans. Antennas Propag., vol. 62, no. 6, pp. 3141–9, Jun. 2014.

[99] J. Turpin, Q. Wu, D. Werner, B. Martin, M. Bray, and E. Lier, “Low cost and broadband dual-polarization metamaterial lens for directivity enhancement,” IEEE Trans. Antennas Propag., vol. 60, no. 12, pp. 5717– 26, Dec. 2012.

[100] D. R. Smith, J. J. Mock, and D. Schurig, “A gradient index metamaterials,” Phys. Rev. E, vol. 71, no. 3, pp. 036609-1–036609-5, Mar. 2005.

[101] X. Q. Lin, T. J. Cui, J. Y. Chin, X.M. Yang, and R. Liu, “Controlling electromagnetic waves using tunable gradient dielectric metamaterial lens,” Appl. Phys. Lett., vol. 92, pp. 131904-1–131904-3, Apr. 2008.

[102] O. Paul, B. Reinhard, B. Krolla, R. Beigang, and M. Rahm, “Gradient index metamaterial based on slot elements,” Appl. Phys. Lett., vol. 96, no. 24, pp. 241110-1–241110-3, Jun. 2010.

[103] X. Chen, H. F. Ma, X. Y. Zou, W. X. Jiang, and T. J. Cui, “Three dimensional broadband and high- directivity lens antenna made of metamaterials,” J. Appl. Phys., vol. 110, pp. 044904-1–044904-8, Aug. 2011.

[104] H. Ma, X. Chen, X. Yang, W. Jiang, and T. Cui, “Design of multi-beam scanning antennas with high gains and low side lobes using gradient index metamaterials,” J. Appl. Phys., vol. 107, pp. 014902-1–014902-9, Jan. 2010.

[105] H. F. Ma, B. G. Cai, T. X. Zhang, Y. Yang, W. X. Jiang, and T. J. Cui, “Three-dimensional gradient-index materials and their applications in microwave lens antennas,” IEEE Trans. Antennas Propag., vol. 61, no. 5, pp. 2561–9, May 2013.

[106] A. Dhouibi, S. N. Burokur, A. Lustrac, and A. Priou, “Compact metamaterial-based substrate-integrated luneburg lens antenna,” IEEE Antennas Wireless Propag. Lett., vol. 11, pp. 1504–07, Jan. 2012.

[107] H. X. Xu, G. M. Wang, Z. Tao, and T. Cai, “An octave-bandwidth half Maxwell fish-eye lens antenna using three-dimensional gradient-index fractal metamaterials,” IEEE Trans. Antennas Propag., vol. 62, no. 9, pp. 4823–28, Sep. 2014.

[108] C. Pfeiffer and A. Grbic, “Planar lens antennas of subwavelength thickness: Collimating leaky-waves with metasurfaces,” IEEE Trans. Antennas Propag., vol. 63, no. 7, pp. 3248–3253, Jul. 2015.

Chapter 3 High Performance Terahertz Antenna Based on Split Ring Resonator and Thin Wire Metamaterial Structure

This chapter is reproduced from the authors published work reported in [1], the author of this thesis was the first author and the second author was acting purely in a supervision capacity. In this Chapter, the left-handed metamaterial (LH-MTM) which has a negative refractive index (NRI) is employed to improve the performance of microstrip patch antenna. The LH-MTM used in this work is a 3-D periodic structure which consists of split ring resonators and thin wires (SRR/TW). The LH-MTM is placed in front of the microstrip patch antenna and due to the negative refractive index property of the LH-MTM; the radiated electromagnetic beam size reduces which results in a highly focused beam. The proposed antenna has been designed and simulated using CST microwave studio and the MTM effective parameters are extracted from the *S-parameters* by using Nicolson-Ross-Weir (NRW) algorithm. A parametric analysis has been performed to study the effects of the patch antenna and LH-MTM lens separation and the size of the 3-D LH-MTM structure on the radiating properties and the impedance matching of the proposed antenna. For the experimental verification, the proposed antenna operating at 10 GHz was fabricated; the return loss and the gain for the proposed antenna with and without MTM were measured. Furthermore, the results show the antenna gain improved by 1.5 dB which validate the concept of beam focusing using NRI MTM structure, while the return loss and the bandwidth are slightly reduced. However, the idea has been extended to the terahertz frequency range by designing and simulating a 303 GHz antenna for Heartbeat Rate (HR) measurement. For 303 GHz patch antenna, the results demonstrate an improvement in the gain by 1.1 dB, in the bandwidth by 14.73 GHz, and in the return loss by 12.62 dB over their original values without the MTM lens, while the beam size is slightly reduced. The simulation and experimental results investigated the idea of the beam focusing using NRI MTM for wide frequency ranges including microwave and terahertz part of electromagnetic spectrum.

3.1. Introduction

Microstrip patch antennas offer an attractive solution to compact, conformal and low-cost designs of many wireless application systems [2]. It is well known that the gain of a single patch antenna is generally low and it can be increased by using an array of patches or by reducing the surface wave, which can create ripples in the radiation pattern and hence reduce the main lobe gain. Several methods have been proposed to reduce the effects of surface waves [3]. During the last decade a metamaterial layer with negative refractive index has been developed to act as a lens [4]. This metamaterial (MTM) lens can be placed in front of the patch antenna and due to the negative refractive index property of the MTM, the radiated electromagnetic beam size reduces which results in a highly focused beam and hence the gain, directivity and radiation efficiency can be significantly improved [5,6]. Metamaterials can be designed for many purposes, for example, it is used to design a binary coded terahertz logic gates as it has been addressed in [7].

Recently, several structures have been proposed which exhibit the LH-MTM properties such as omega shape, spiral multi-split, fishnet, and S-shape structures [8-10]. After publication of these initial findings, many researchers have been interested in investigating this artificial material, and several of them used the LH-MTM to improve the properties of the microwave devices such as antennas and filters. Although other metamaterials such as frequency selective surface (FSS) and electromagnetic band gap (EBG) have been used to enhance the gain of an antenna [11], the NRI property of the LH-MTM was exploited to improve the directivity and gain of the antennas [12]. In addition a metamaterial structure composed of copper grids with a lattice was given by Stefan Enoch et al. for directive emission [13]. It was shown that the electromagnetic waves in the media can be congregated in a narrow rectangular area when applied to a monopole antenna; this structure can greatly improve the directivity of the antenna. Also, metamaterials have been designed and investigated in the THz frequency range for developing new THz devices such as antennas, filters, sensors, and absorbers [14].

In this chapter, the left-handed metamaterial (LH-MTM) which has a NRI is employed to improve the performance of a terahertz microstrip patch antenna operating at 303GHz. The LH-MTM used in this work is a 3-D periodic structure which consists of split ring resonators and thin wires (SRR/TW) [15]. The LH-MTM is placed in front of the microstrip patch antenna and due to the negative refractive index property of the LH-MTM, the radiated electromagnetic beam size reduces which results in a highly focused beam and hence the radiation parameters of the antenna such as gain, directivity, and radiation efficiency will be improved.

This chapter is organized as follows: Section 3.2 provides the design and simulation of a 10 GHz patch antenna based on metamaterials then the idea of beam focusing using LH-MTM is extended to the THz frequency range as will be illustrated in section 3.3, particularly the 303 GHz antenna for Heartbeat Rate (HR) measurement [16]. The experimental validation of the proposed antenna is illustrated in section 3.4. Finally, the conclusion is given in section 3.5.

3.2. Analysis and Design of the Proposed Antenna

In order to investigate the idea of beam focusing using NRI MTM structure, a microstrip patch antenna operating at 10 GHz and a Split Ring Resonator and Thin Wires (SRR/TW) LH-MTM unit cell resonating at the same frequency as that of the patch antenna are designed and simulated using CST microwave studio, then the proposed idea is extended to the THz frequency range at 303 GHz in particular for heartbeat measurement application.

Furthermore the LH-MTM unit cell is used to construct a 3-D LH-MTM periodic structure which is then placed in front of the conventional patch antenna with specific separation S as shown in Fig. 3.1 (a). The conventional patch antenna has a length, L, and width, W, of 8.6 mm and 11.86 mm, respectively, and is printed on a RT/Duroid 5880 substrate with a relative permittivity of $\varepsilon_r = 2.2$ and a thickness of h= 1.57 mm. The patch is fed by a 50 Ω microstrip line and is matched with quarter wavelength transformer which has a line length, L_T, and width,W_T, of 7mm and 0.3 mm, respectively. The quarter wavelength transformer length and/or the patch width were optimized to give good impedance matching. The size of the substrate a×b was calculated from the formula $(W + 6h) \times (L + 1.5\, L_T)$. The maximum gain of the conventional patch antenna is about 7 dB. However, the detailed SRR/TW MTM unit cell is shown in Fig. 3.1 (b), also the front and the back views of the 2-D SRR/TW MTM periodic structure enabling construction of the 3-D structure are shown in Figs. 3.1 (c) and 3.1 (d), respectively. In the simulation process, convergence and minimization of numerical errors were obtained by ensuring that the mesh was sufficiently fine. However, the 3-D LH-MTM structure is designed with a specific periodicity which satisfies the homogeneity condition of the LH-MTM. The following two subsections illustrate the design and simulation analysis of 10 GHz and 303 GHz proposed antennas, respectively.

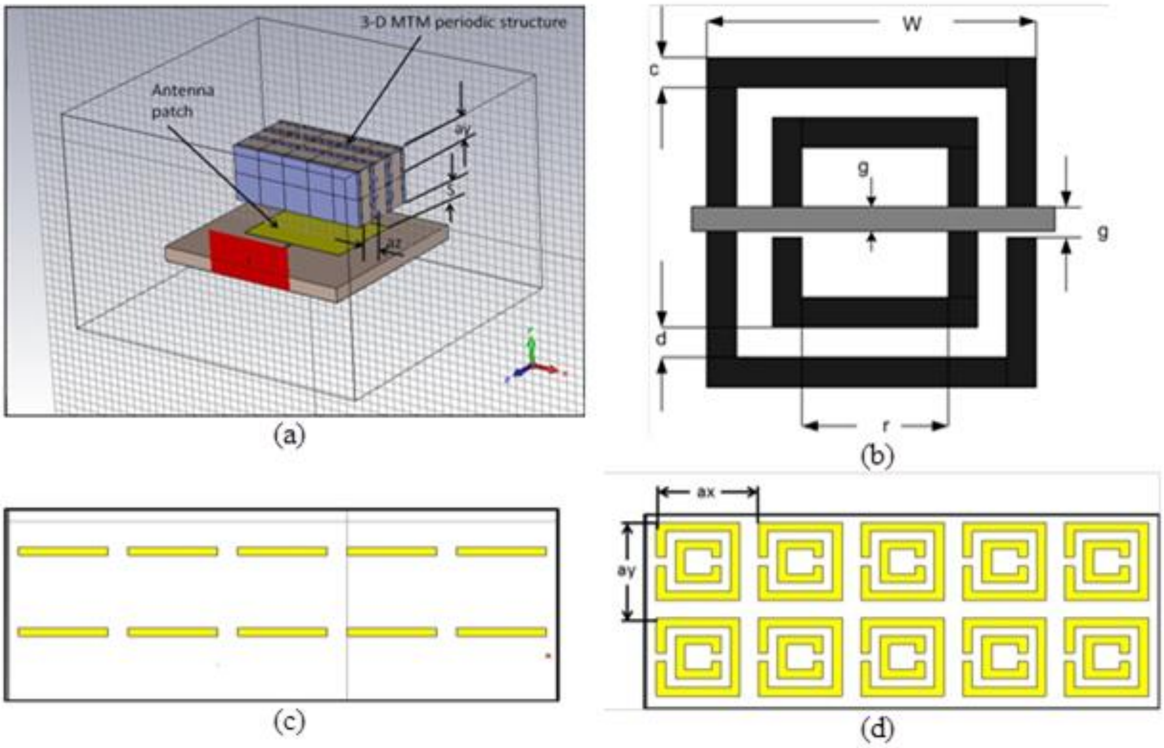

Fig. 3.1. The structure of the proposed antenna, (a) 3D view, (b) the SRR/TW MTM unit cell, (c) 2D TW periodic structure, and (d) 2D SRR periodic

3.2.1. Design of a SRR/TW MTM Unit Cell Resonates at 10 GHz

Here, a unit cell of SRR/TW with negative effective permittivity (ε_r) and negative effective permeability (μ_r) was designed. The dimensions of the SRR/TW unit cell are designed and optimized in order to give a simultaneous negative permittivity and negative permeability in a frequency range to be matched with the bandwidth of the patch antenna designed in the last subsection [14], to achieve an optimal beam focusing when it is integrated with the patch antenna. The SRR is a copper layer with thickness t of 35 µm mounted on the top side of a RT/Duriod 5880 dielectric substrate with relative dielectric permittivity εr of 2.2 and height h = 1.57 mm, and the TW is mounted on the other side, i.e. the MTM structure is a double-sided process structure. The SRR/TW unit cell depicted in Fig. 3.1(b) was designed using the CST Microwave Studio to resonate at 10 GHz with parameters d = 0.3 mm, g = 0.3 mm, and w=2.64 mm. The effective parameters of the SRRs/TWs unit cell including effective permittivity ε_r, effective permeability μ_r, and refractive index n, have been extracted from the S-parameters using the Nicolson-Ross-Weir (NRW) approach [17]. The details of the NRW algorithm are given in Appendix A. Figure 3.2 (a) shows that the SRR/TW unit cell has a high pass frequency response with a cut-off frequency of 10 GHz. However, for the SRR/TW MTM unit cell, the real part of the effective permittivity, effective permeability, and refractive index are negative around 10 GHz as shown in Figs. 3.2 (b), (c) and (d), respectively. The MTM unit cell effective parameters can be obtained by using boundary conditions of the magnetic walls at the back and front sides since the magnetic field is polarized in the x-direction and also electric walls on the left and right sides as the electric field is polarized in the y-direction. The theoretical resonant frequency of the SRR/TW unit cell is 10 GHz, according to the theories developed in [14], which is matched with the operating frequency of the patch antenna. The transversal periodicity is a = 3.5 mm, which is less than 1/8 of the free space wave length at resonance, which is used to construct the 2-D MTM periodic structure to employ the MTM lens as will be illustrated in the next section.

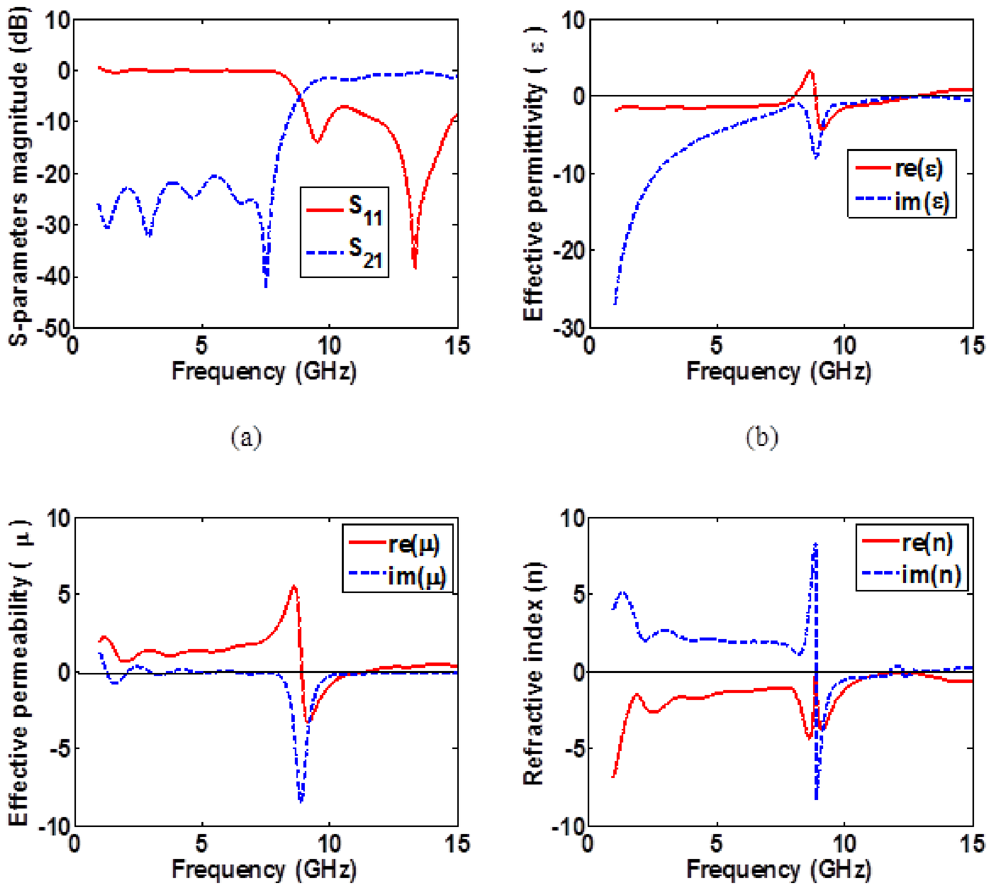

(a) (b)

(c) (d)

Fig. 3.2. The SRR/TW MTM unit cell parameters designed at 10 GHz, (a) S-parameters magnitude, (b) effective permittivity, (c) effective permeability and (d) refractive index.

3.2.2. Integration of 10 GHz Patch Antenna with the SRR/TW 3-D MTM Structure

The pre-designed MTM unit cell here is used to construct a 3-D MTM periodic structure with transversal periodicities a_x and a_y in x and y directions, respectively, and longitudinal periodicity a_z in z direction. Then the 3-D MTM structure is integrated with or placed in front of the patch antenna to construct the proposed antenna as depicted in Fig. 3.1. To obtain the optimal radiation properties and impedance matching; the 3-D MTM periodic structure dimensions of (N × M × K) and the patch-MTM structure separation ‘*S*’ are justified. Figure

3.3 shows the return loss and gain simulation results of the proposed antenna at different ‘S’ separations between the patch antenna and the 3-D MTM structure of 5×4×2 dimensions. It is clear that, the antenna gain is significantly improved by 0.91 dB when the conventional patch antenna is integrated with a 3-D MTM structure of size 5×4×2 at 1 mm separation distance between the patch and the MTM structure, while the bandwidth and radiation efficiency approximately remain the same and the beam area is slightly reduced. The increase in the antenna gain comes from the fact that radiated electromagnetic waves from the patch are focused by the negative refractive index metamaterial.

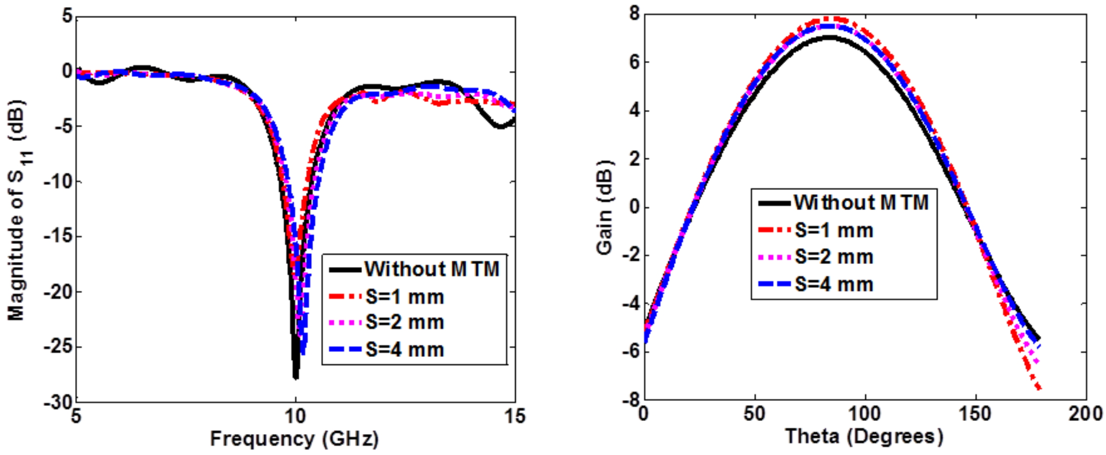

(a) (b)

Fig. 3.3. The return loss (a) and the gain (b) of the proposed antenna without MTM and with 3D MTM periodic structure dimensions of 5× 4 ×2

Furthermore, the effect of the 3-D MTM structure dimensions on the antenna parameters have been studied as shown in Fig. 3.4. The results show that the antenna gain is increased as the 3-D MTM structure size increases while the return loss; the bandwidth and the angular width are slightly decreased. The maximum improvement in the gain is approximately 1.5 dB which occurs when the 3-D MTM structure dimensions are of the form 5×4×4 and at a separation of 3 mm.

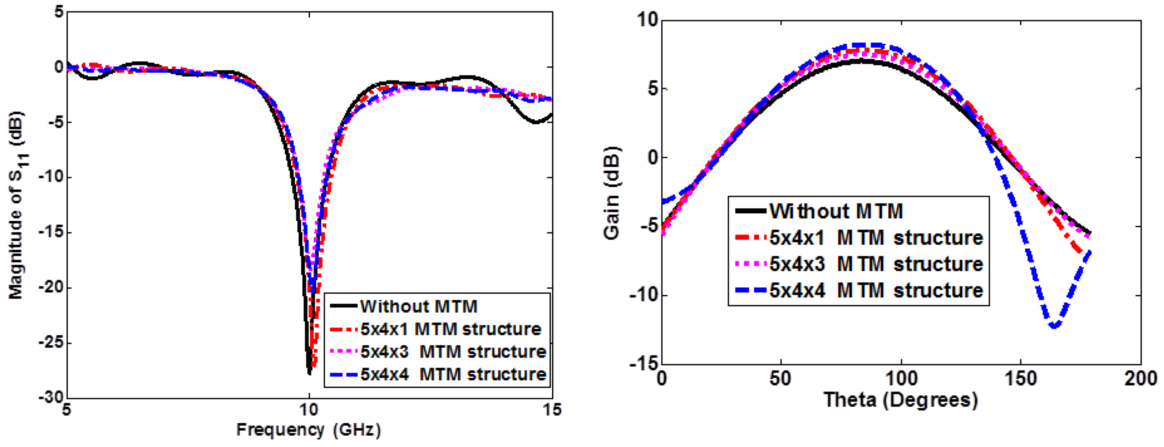

(a)

(b)

Fig. 3.4. The return loss (a) and the gain (b) of the proposed antenna without MTM and with MTM 3D periodic structure of different sizes

3.2.3. Design and Simulation of 303 GHz MTM Based Patch Antenna

The main goal of this section is to investigate the beam focusing property of electromagnetic waves radiated from the proposed antenna composed of conventional patch antenna and SRR/TW MTM structure in the THz frequency range. In doing so, based on the following procedure a 303 GHz antenna was designed and simulated using CST microwave studio commercial software. Firstly, a conventional 303 GHz patch antenna was designed which has a patch length L and width W of 254 μm, and 420 μm, respectively. The antenna is printed on a RT/Duroid 5880 substrate with a relative permittivity of εr = 2.2 and a thickness h=125 μm. The patch antenna is fed by a 50 Ω microstrip line and is matched with a quarter wavelength transformer which has the length and width of 194.7 μm and 8.24 μm, respectively. The length and width of the quarter wavelength transformers were optimized to provide a good impedance matching. Secondly, a SRR/TW MTM unit cell resonating at 303 GHz was designed and simulated. Then from its S-parameters (i.e. S_{11} and S_{21}) the MTM effective permittivity ε_r, permeability μ_r and refractive index n are extracted by using the NRW algorithm. The SRR is a gold layer with thickness t= 10 μm mounted on the top side of a polyimide substrate with a relative dielectric constant of 3.5, a loss tangent of 0.003 as it is mentioned in the data sheet of the Roger substrates and height h = 6 μm. The TW is mounted on the other side, i.e. the MTM structure is a double-sided process structure. The SRR/TW unit cell shown in Fig. 3.1(b) was designed to resonate at 303 GHz with parameters: c = 12 μm, d = 10 μm, g = 10 μm, w=98 μm and with transversal periodicity a=113 μm. Figure 3.5 (a) shows both s_{11} and s_{21} parameters of the SRRs/TWs MTM unit cell and Fig. 3.5 (b) to 3.5 (d) show variations of ε_r, μ_r and n with frequency which have been extracted using NRW algorithm from the MTM unit cell scattering parameters shown in Fig. 3.5 (a).

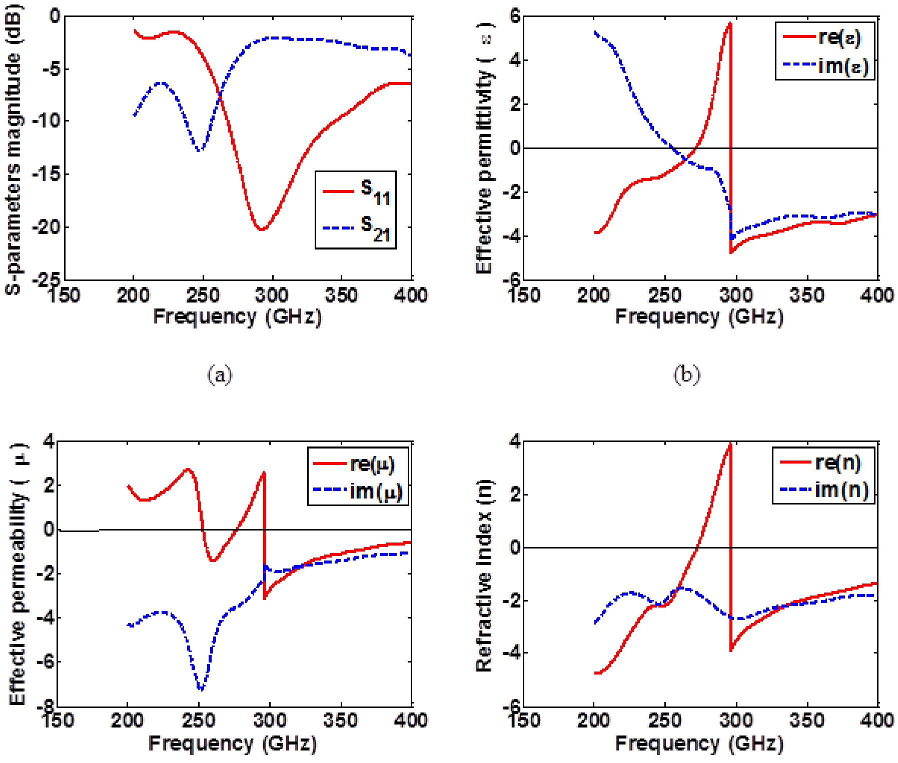

(a)

(b)

(c)

(d)

Fig. 3.5. SRR/TW MTM unit cell parameters resonating at 303 GHz, (a) S-parameters magnitude, (b) effective permittivity (ε), (c) effective permeability (μ), and (d) refractive index (n).

Thirdly, the MTM unit cell is used to construct a 3-D MTM periodic structure which is then placed in front of the designed 303 GHz patch antenna to construct the proposed antenna shown in Fig. 3.1. The distance between the antenna and the 3-D MTM structure have been optimized to obtain the optimum antenna return loss and gain as shown in Figs. 3. 6 (a) and 3.6 (b). Also, the effect of MTM size on the overall antenna parameters s_{11} and gain have been analysed as shown in Figs. 3.6 (c) and 3.6 (d). The reason behind the impacts of the 3-D MTM structure on the antenna matching can be explained through the capacitive and inductive couplings between the SRR and TW periodic structures which have a significant effect on the antenna input impedance and hence change the antenna bandwidth and return loss. However due the NRI property of the MTM layers, the radiated EM waves from the patch antenna are focused and the beam becomes more directive so the antenna gain and directivity have been improved and the antenna radiated power is managed with a small reduction in the beam area. The new improvement in the MTM is that instead of having the trade-off between the antenna gain and bandwidth, now by using the MTM, a new trade-off is evident between three parameters which are the antenna gain, antenna bandwidth, and the beam area would be obtained. For example, the antenna gain and bandwidth can be improved simultaneously while the beam area is reduced or the antenna gain and beam area can be improved while the antenna bandwidth is reduced.

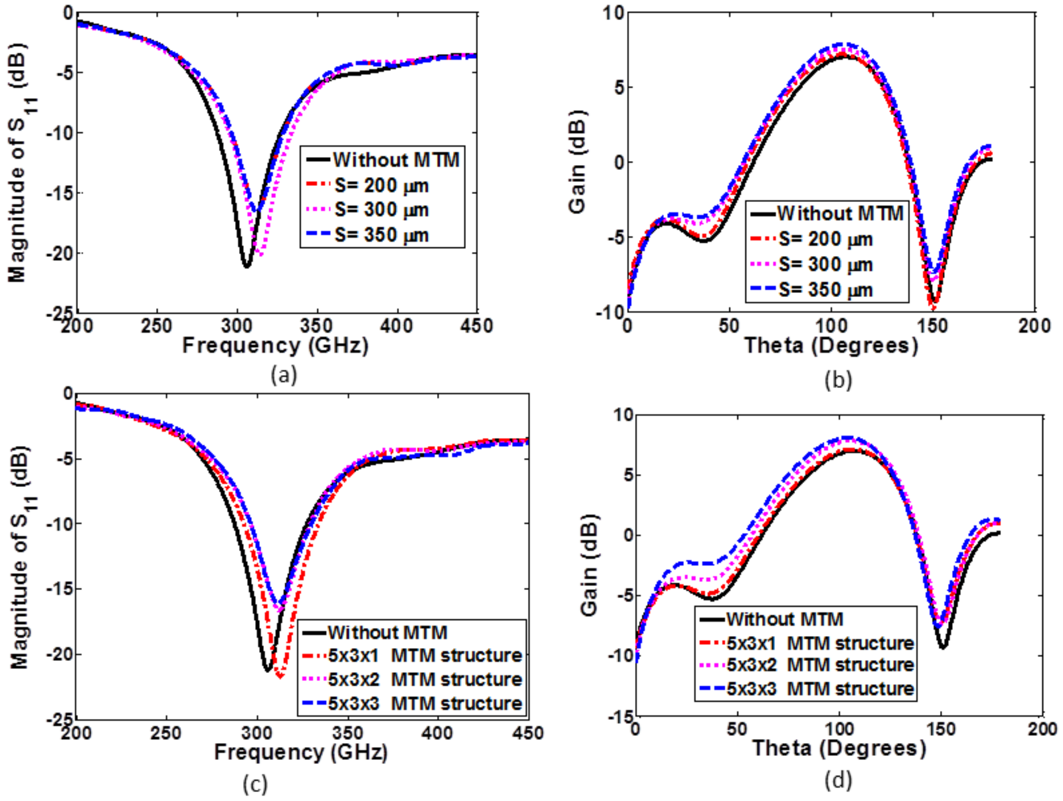

Fig. 3.6. The return loss (a) and the gain (b) of the proposed antenna without MTM and with 3D MTM periodic structure of size 5×3×2 at different separations between the patch antenna and the MTM 3D periodic structure. The return loss (c) and the gain (d) of the proposed antenna operating at 303 GHz with and without MTM 3D periodic structure of different sizes and fixed separation of 350 mm between the patch antenna and the MTM.

However, there is an optimal separation of 200 µm at which the bandwidth is maximum (i.e. 55.53 GHz). Furthermore, the minimum return loss of -33.80dB is achieved when the optimal separation is 250 µm. The results illustrated that by using a 3-D MTM structure of size 5×4×2 and optimizing the separation '*S*' the bandwidth, gain and the return loss are improved by 14.73 GHz, 0.84 dB and 12.62dB, respectively, while the beam width remains approximately the same. It is clear from the results that, the antenna gain is increased as the size of the 3-D MTM structure increases while the return loss and the bandwidth are decreased and the angular angle remains approximately the same. The gain is improved by 1.08 dB.

3.3. Fabrication and Measurements

For experimental validation, the proposed antenna resonating at 10 GHz as well as the SRR/TW 2-D MTM structure have been fabricated as shown in Fig 3.7 The fabrication is done using wet etching technique on a RT/Duroid 5880 substrate for both the patch antenna and the MTM with a relative permittivity of ε_r = 2.2 and a thickness of h= 1.57 mm. The return loss, S_{11} for the simulated and the fabricated antenna with and without MTM structure is shown in Fig. 3.8 (a). The measured bandwidth of the patch antenna with and without MTM is approximately the same which is around 700 MHz

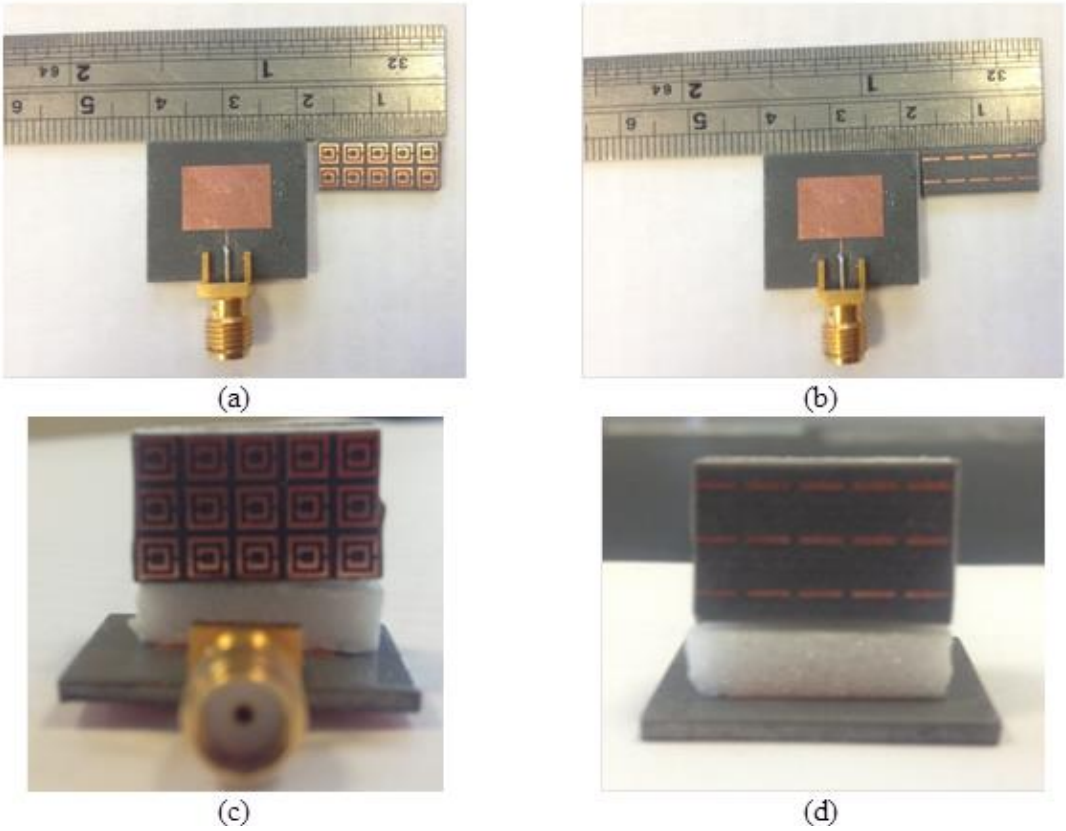

Fig. 3.7. The 10 GHz fabricated antenna: (a) patch antenna and 2D array of SRRs, (b) patch antenna and 2D array of TWs, (c, d) antenna front and back views.

Figures 8 (b) and 8 (c) show the radiation patterns of the antenna with and without MTM structure in both *E* and *H*- planes. From the measured results it has been found that (i) the gain of the antenna with 5×4×3 3-D MTM has improved by 1.2 dB, (ii) the side lobes become smaller and (iii) the main lobe become more focused in both *E* and *H* planes.

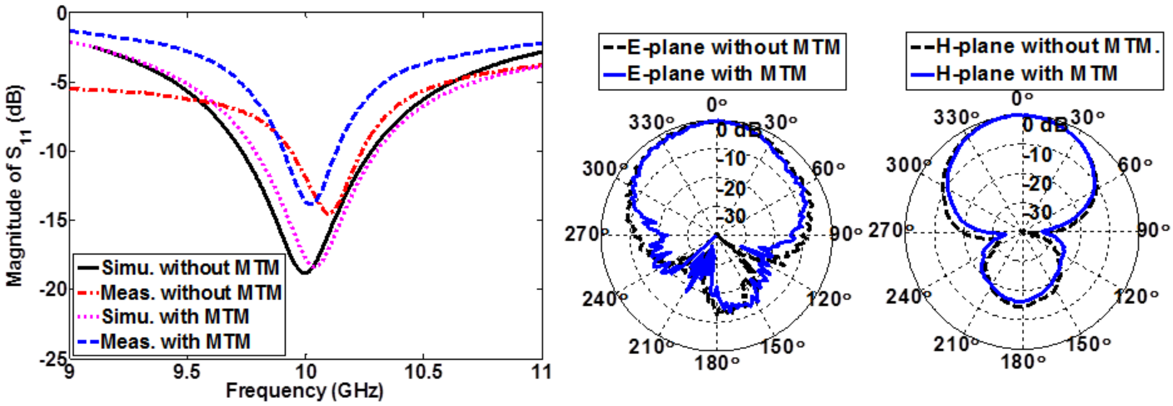

(a) (b) (c)

Fig. 3.8. Simulation and measured return loss (a) of the 10 GHz proposed antenna both with 5×4×3 3D MTM and without the MTM structure. Measured radiation patterns of the proposed antenna both with 5×4×3 3D MTM and without the MTM structure, (b) E-plane co-polarized, and (c) H-plane co-polarized.

3.4. Summary

In this chapter, the performance of a patch antenna is greatly improved by beam focusing when it is integrated with a 3-D SRRs/TWs periodic structure employing an MTM lens. The MTM lens was suspended above the patch antenna through Foam spacers; the MTM lens focused the radiated EM waves of the patch antenna in a narrow area. As a result, the antenna gain and directivity have improved. Also it has been found that by carefully design of the MTM structure and the separation between the patch antenna and the MTM structure are designed properly, the antenna return loss, bandwidth, and radiation efficiency can be improved. This is because MTM structures have both capacitive and inductive coupling properties which changes the antenna input impedance and hence affect the above mentioned antenna parameters.

The optimized radiation properties of the proposed patch antenna have been obtained through the justification of the patch-MTM lens separation and the dimensions of the 3-D

MTM periodic structure employing the MTM lens. As an example for terahertz applications, the proposed antenna has been designed to operate at 303 GHz which can be used for heart beat rate measurement [36]. The terahertz antenna simulation results demonstrated enhancements of 1.1dB, 14.73GHz and 12.62dB in the antenna gain, bandwidth and return loss as compared with the patch antenna without the MTM lens. These improvements in the antenna parameters validate the proposed concept of beam focusing using a 3-D periodic structure of SRRs/TWs, which employ the MTM lens, without modifying significantly the matching methodology of the patch antenna. Furthermore, we have demonstrated the validity of the above properties experimentally at 10 GHz and showed that at this frequency the antenna gain, bandwidth and return loss have improved by 1.5 dB, 10.15 MHz and 2 dB, respectively with minimal change in the antenna beam width. The results presented in this chapter investigated the idea of beam focusing using the NRI MTM structure; Future work will be to optimize the MTM structure to increase the gain. Also, the angular response of the MTM structure will be studied to prove that the MTM structure with an NRI can act as a lens.

3.5. References

[1] Abdelrehim, A.A. and Ghafouri-Shiraz, H. High performance terahertz antennas based on split ring resonator and thin wire metamaterial structures. Microwave and Optical Technology Letters, 58(2), pp.382-389, 2016.

[2] R. Collin, Field theory of guided waves. New York: McGraw-Hill, 1960.

[3] J. Colburn and Y. Rahmat-Samii, Patch antennas on externally perforated high dielectric constant substrates, IEEE Transactions on Antennas and Propagation, 1999, vol. 47, no. 12, pp. 1785-1794.

[4] J. Pendry, Negative Refraction Makes a Perfect Lens, Phys. Rev. Lett. , 2000, vol. 85, no. 18, pp. 3966-3969.

[5] Z. Weng, N. Wang, Y. Jiao and F. Zhang, A directive patch antenna with metamaterial structure, Microwave Opt Technol Lett 49 (2006), 456-459.

[6] Y. Liu and X. Zhao, Enhanced patch antenna performances using dendritic structure metamaterials, Microwave Opt Technol Lett 51 (2009), 1732-1738.

[7] Ho, C.P., Pitchappa, P. and Lee, C., 2016. Digitally reconfigurable binary coded terahertz metamaterial with output analogous to NOR and AND. Journal of Applied Physics, 119(15), p.153104.

[8] W. Bae-Ian, W. Wang, J. Pacheco, X. Chen, T. M. Grzegorczyk, and J. A. Kong, A study of using metamaterials as antenna substrate to enhance gain, Progress In Electromagnetics Research 51 (2005): 295-328.

[9] K. Alici, F. Bilotti, L. Vegni and E. Ozbay, Optimization and tunability of deep subwavelength resonators for metamaterial applications: complete enhanced transmission through a subwavelength aperture, Opt. Express, vol. 17, no. 8, p. 5933, 2009.

[10] K. Alici and E. Ozbay, Characterization and tilted response of a fishnet metamaterial operating at 100 GHz, Journal of Physics D: Applied Physics, 2008, vol. 41, no. 13, p. 135011.

[11] Pirhadi, F. Keshmiri, M. Hakkak and M. Tayarani, Analysis and design of dual band high directive EBG resonator antenna using square lobe FSS as superstrate, 2007, PIER, vol. 70, pp. 1-20.

[12] Erentok, P. Luljak and R. Ziolkowski, Characterization of a volumetric metamaterial realization of an artificial magnetic conductor for antenna applications, IEEE Transactions on Antennas and Propagation, 2005, vol. 53, no. 1, pp. 160-172.

[13] S. Enoch, G. Tayeb, P. Sabouroux, N. Guérin and P. Vincent, A Metamaterial for Directive Emission, 2002, Phys. Rev. Lett., vol. 89, no. 21.

[14] M. El-Nawawy, A. A. Allam and A. Korzec, The Design of a 0.35THz Microstrip Patch Antenna on LTCC Substrate, EEE, 2011, vol. 1, no. 1, pp. 1-4.

[15] J. Woodley, M. Wheeler and M. Mojahedi, Left-handed and right-handed metamaterials composed of split ring resonators and strip wires, Physical Review E, 2005, vol. 71, no. 6.

[16] Y. Kurzweil-Segev, M. Brodsky, A. Polsman, E. Safrai, Y. Feldman, S. Einav and P. Ben Ishai, Remote Monitoring of Phasic Heart Rate Changes From the Palm, IEEE Transactions on Terahertz Science and Technology, 2014, vol. 4, no. 5, pp. 618-623.

[17] X. Chen, T. Grzegorczyk, B. Wu, J. Pacheco and J. Kong, Robust method to retrieve the constitutive effective parameters of metamaterials, Physical Review E, 2004, vol. 70, no. 1.

Chapter 4 Performance Improvement of Patch Antenna using Circular Split Ring Resonators and Thin Wires Employing Metamaterials Lens

This chapter is reproduced from the author's published work reported in [1]. The author of this thesis was the first author and the second author was acting purely in a supervision capacity. In this chapter, the left-handed metamaterial which acts as a lens is employed to improve the performance of a microstrip patch antenna. The left-handed metamaterial used in this work is a three dimensional periodic structure which consists of Circular split ring resonators and thin wires. The metamaterials three dimensional periodic structure shows angular independency characteristics over wide range angles, so it acts as a metamaterial lens. However, the MTM structure infinite periodicity truncation has no impact on the MTM lens scattering, effective parameters and homogeneity. The left-handed metamaterial is placed in front of the microstrip patch antenna and due to the negative refractive index property of the left-handed metamaterial; the radiated electromagnetic beam size reduces which results in a highly focused beam. The proposed antenna has been designed and simulated using CST microwave studio and the metamaterial effective parameters are extracted from the s parameters by using the Nicolson-Ross-Weir algorithm and by selecting the appropriate ambiguity branch parameter. Furthermore, the angular independency of the metamaterial lens has been verified by rotating the metamaterial structure with respect to the excitation probe of the transverse electromagnetic waves and extracting the S-parameters and the effective parameters for each rotation angle. A parametric analysis has been performed to study the effects of the patch antenna and left-handed metamaterial lens separation and the size of the three dimensional left-handed metamaterial structure on the radiating properties and the impedance matching of the proposed antenna. For the experimental verification, the proposed antenna operating at 10 GHz is fabricated; the return loss, radiation pattern and the gain for the proposed antenna with and without metamaterial are measured. Furthermore, the results show that, the antenna gain is improved by 4.6 dB which validate the concept of beam focusing using negative refractive index metamaterial structure, while the return loss and the bandwidth are slightly reduced. The simulation and experimental results investigated the idea of the beam focusing using negative refractive index metamaterial lens in the microwave regime.

4.1. Introduction

Metamaterials are artificial materials which exhibit their non-natural properties such as negative permittivity, negative permeability and negative refractive index (NRI) from physical dimensions and geometrical shapes rather that chemical composition [2-6]. Metamaterials which have simultaneous negative permittivity and negative permeability are called left-handed materials (LH-MTM), in which the electric field *E*, the magnetic field *H*, and the wave vector *k* form a left-handed system.

Recently, several structures have been proposed which exhibit the LH-MTM properties such as omega shape, spiral multi-split, fishnet, and S-shape structures [7-9]. Based on this interest in artificial materials increased, and several of researchers used the LH-MTM to improve the properties of the microwave devices such as antennas and filters [10]. However, many papers have been published regarding the LH-MTM integrated with antennas, and their properties have been analyzed [11-13]. Although other metamaterials such as frequency selective surface (FSS) and electromagnetic band gap (EBG) have been used to enhance the gain of an antenna [14-15], the NRI property of the LH-MTM was exploited to improve the directivity and gain of the antennas [16-18]. In addition a metamaterial structure composed of wire medium was given by Burghignoli, P. et al. for Directive leaky-wave radiation from a dipole source [19]. It was shown that the electromagnetic waves in the media can be congregated in a narrow rectangle area properly when applied to a monopole antenna; this structure can greatly improve the directivity of the antenna. Also, metamaterials have been designed and investigated in the THz frequency range for developing new THz devices such as antennas, filters, sensors, and absorbers [20-23]. Furthermore, metamaterial structures composed of 3-D metal grid superstrate have been used to improve the directivity of the antenna [24-25]. It should be noted that, the aperture size of the metamaterial superstrate is much created as compared with the size of the patch which makes the antenna bulky. Also, zero index medium metamaterial superstrate are used to develop a high gain and wideband antenna [26]. It is clear from the structure of the antenna that, the metamaterial superstrate uses metallic via to resemble shunt inductance, which makes it difficult to fabricate. A photonic crystal-based resonant antenna presented in [27] is a high directive antenna, but it is bulky and has a narrow bandwidth.

Nader Engheta et al. proved numerically and theoretically that a perfect Electric Conductor (PEC) screen with a small hole covered by two sub wavelength metamaterial structure can be used to improve the directivity of the antenna [28]. A planar metamaterial with NRI has been developed using a split ring resonator (SRR) in [29]. In this work, a planar double-sided structure composed of CSRR s/TWs with NRI was used as a cover for the patch antenna to improve the antenna directivity. The novelty of using such a structure to improve the antenna gain is that it is easy to fabricate and has a small size compared to the published work in Refs. [24-27]. However, the CSRR/TWs have strong electric and magnetic couplings compared with the SRR (of Ref. 29) due to the double sided structure, as a result the patch antenna incorporated with NRI cover composed of CSRRs/TWs may have a higher gain than that when covered by a SRR only.

Here, the left-handed metamaterial (LH-MTM) which acts as a lens is employed to improve the performance of a microstrip patch antenna operating at 10 GHz. The LH-MTM used in this work is a 3-D periodic structure which consists of circular split ring resonators and thin wires (CSRR/TWs) [30]. The LH-MTM is placed in front of the microstrip patch antenna and due to the negative refractive index property of the LH-MTM, the radiated electromagnetic beam size reduces which results in a highly focused beam and hence the radiation parameters of the antenna such as gain, and directivity will be improved.

This chapter is organized as follows: Section 4.2 provides the design and simulation of the 10 GHz proposed patch antenna. Furthermore, this section includes; designs of a conventional line fed patch antenna at 10 GHz, frequency response and the angular independency of the CSRR/TWs MTM structure, and parametric analysis of a 10 GHz patch antenna incorporated with a CSRR/TWs MTM lens. The experimental validation of the proposed antenna is illustrated in section 4.3. Finally, the chapter summary is given in section 4.4.

4.2. Analysis and Design of the Proposed Antenna

In order to investigate the idea of beam focusing using NRI MTM Lens, a microstrip patch antenna operating at 10 GHz and a CSRR/TW LH-MTM unit cell resonating at the same frequency as that of the patch antenna were designed and simulated using CST microwave studio. The conventional patch antenna has a length, L, and width, W, of 8.6mm and 11.86 mm, respectively, and is printed on a RT/Duroid 5880 substrate with a relative permittivity of ε_r = 2.2 and a thickness of h= 1.57 mm. The patch is fed by a 50 Ω microstrip line and is matched with quarter wavelength transformer which has a line length, L_T , and width,W_T , of 7mm and 0.3mm, respectively. The quarter wavelength transformer length and/or the patch width were optimized to give a good impedance matching. The size of the substrate $a \times b$ was calculated from the formula $(W + 6h\,) \times (L + 6h)$ [31]. The conventional microstrip patch antenna (MSA) parameters such as gain, bandwidth, and directivity and radiation efficiency are calculated theoretically using cavity model [32]. The Directivity (D) is calculated as follows

$$D = \frac{2\left(\frac{4b^2\pi^2}{I_1\lambda_0}\right)}{1 + g_{12}} \tag{4.1}$$

$$I_1 = \int_0^{\pi} \sin^2\left(\frac{k_0 b\cos(\theta)}{2}\right)\tan^2(\theta)\sin(\theta)\,d\theta \tag{4.2}$$

$$g_{21} = \frac{1}{120\pi^2}\int_0^{\pi} \frac{\sin^2\left(\frac{\pi b cos(\theta)}{\lambda_0}\right)\tan^2\theta sin\theta\, J_0(\frac{2\pi a}{\lambda_0} sin\theta)}{G}\,d\theta \tag{4.3}$$

Where $J_o(x)$ is the zeroth-order Bessel function, k_o is the free space wave number which equals $\lambda_0/2\pi$, a is the substrate length which equals $W + 6h$, b is the substrate width which equals $W + 6h$, and G is the radiation inductance $G = 1/R_r$ and R_r is the radiation resistance and is given by [32]

$$R_r = \frac{120\pi^2}{I_1} \tag{4.4}$$

The bandwidth BW of the MSA can also be inversely proportional to its total quality factor Q_T and is given by [27]

$$BW = \frac{VSWR - 1}{Q_T\sqrt{VSWR}} \tag{4.5}$$

The total quality factor Q_T is given by [26]

$$\frac{1}{Q_T} = \frac{1}{Q_r} + \frac{1}{Q_c} + \frac{1}{Q_{sw}} + \frac{1}{Q_d} \tag{4.6}$$

Where Q_r Q_c, Q_{sw} and Q_d are the radiation, conductor, surface wave and dielectric quality factors, respectively. The relationship between $VSWR$ and return loss S_{11} is as follows [33].

$$S_{11}(dB) = 20\log_{10}\left(\frac{VSWR}{VSWR-1}\right) \tag{4.7}$$

The MSA radiation efficiency is given by [32]

$$e = \frac{Q_T}{Q_r} = \frac{Q_d Q_c Q_{sw}}{Q_{sw}Q_c Q_d + Q_{sw}Q_c Q_r + Q_{sw}Q_r Q_d + Q_r Q_d Q_c} \tag{4.8}$$

The gain G of the MSA is given by [32]

$$G = eD \tag{4.9}$$

The maximum gain of the conventional patch antenna is about 7 dB. Furthermore, the CSRR/TW LH-MTM unit cell is used to construct a 3-D LH-MTM periodic structure which is then placed in front of the patch antenna with specific separation h_S as shown in Figs. 4.1 (a), 4.1 (b), 4.1 (c), and 4.1 (d) which illustrate the 3-D view, bottom view, top view and side view of the propose antenna, respectively. However, the 3-D CSRR/TW LH-MTM structure is designed with specific periodicities of a_x, a_y, and a_z in *x, y,* and *z*, respectively, which satisfies the homogeneity condition of the LH-MTM as shown in Figs. 4.1 (b) and 4.1 (c). The different layers of the MTM structure are attached to the conventional patch antenna by using a foam spacer, since it has effective parameters close to air, so it will have no impacts on the antenna performance. The detailed dimensions, the frequency response and angular response of the CSRR/TW MTM unit cell constructing the MTM lens will be given in subsections 4*.2.1*, and 4*.2.2*. After that, the proposed antenna is simulated in CST for different sizes of the 3-D CSRR/TW structure employing the MTM lens at different separation h_S between the patch and the MTM lens; as a result the optimized structure of the proposed antenna can be obtained.

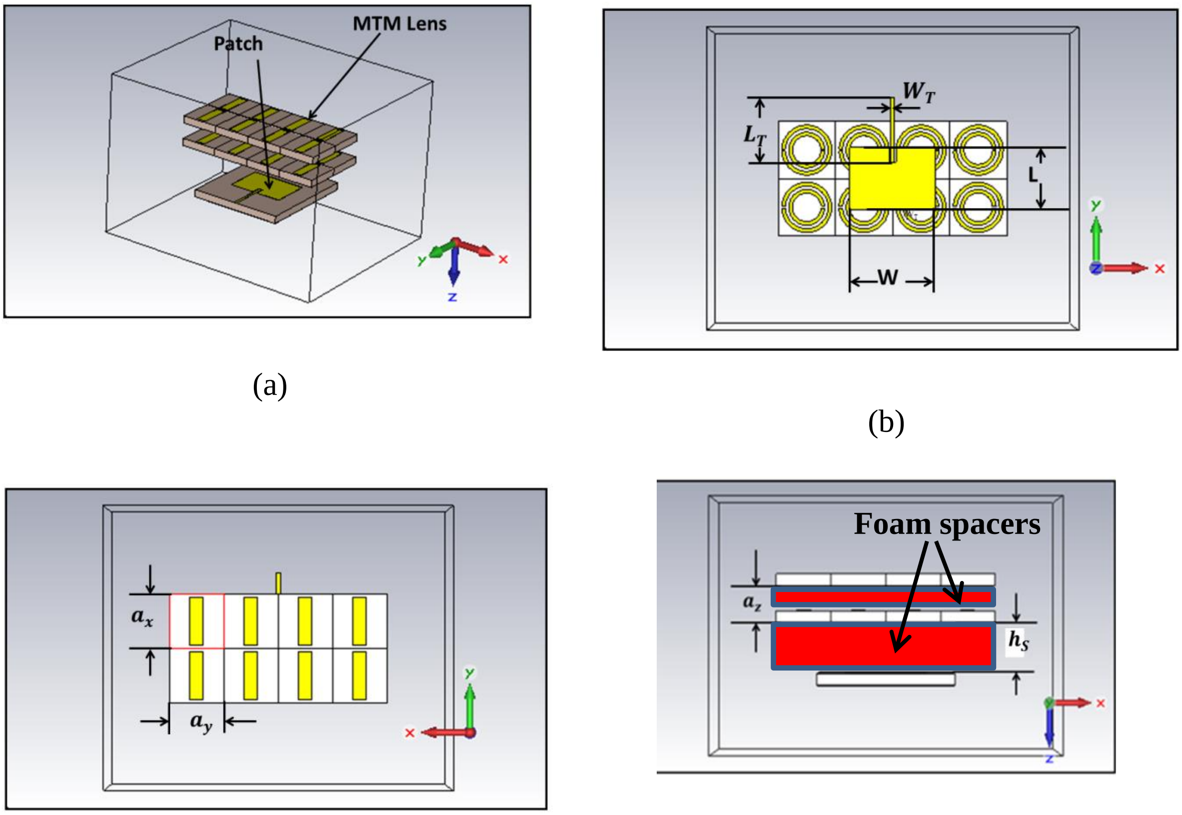

(a)

(b)

(c)

(d)

Fig. 4.1. The structure of the proposed antenna, (a) 3-D view, with hidden foam spacer located between the patch and the MTM lens and between the different layers of the MTM lens, (b) bottom view, (c) top view and (d) side view with foam spacer.

4.2.1. Frequency Response of CSRR/TW MTM unit cell resonating at 10 GHz

Here, a unit cell of CSRR/TW was designed and simulated using CST which was when repeated in two dimension, it may give a negative effective permittivity (ε), negative effective permeability (μ) and hence a negative refractive index (*n*) around the interesting frequency of 10 GHz [21,35]. The dimensions of the 2-D CSRR/TW MTM structure were optimized in order to give a simultaneous negative permittivity and negative permeability in a frequency range to be matched with the bandwidth of the patch antenna designed in the last subsection, to achieve an optimal beam focusing when it is integrated with the patch antenna. The CSRR consisted of a copper layer with thickness t of 35 µm mounted on the top side of a RT/Duriod 5880 dielectric substrate with relative dielectric permittivity εr of 2.2 and height h = 1.57 mm, and the TW is mounted on the other side, i.e. the MTM structure is a double-sided process structure. The CSRR/TW unit cell depicted in Fig. 4.2 was designed using the CST Microwave Studio to resonate at 10 GHz. The CSRR/TW parameters are: a=4.5 mm, g=0.3 mm, $r1i$=1 mm, $r1o$=1.4 mm, $r2i$=1.8 mm, $r2o$=2.1 mm, L_{TW}= 4.2 mm. W_{TW}= 1 mm and t= 17 µm.

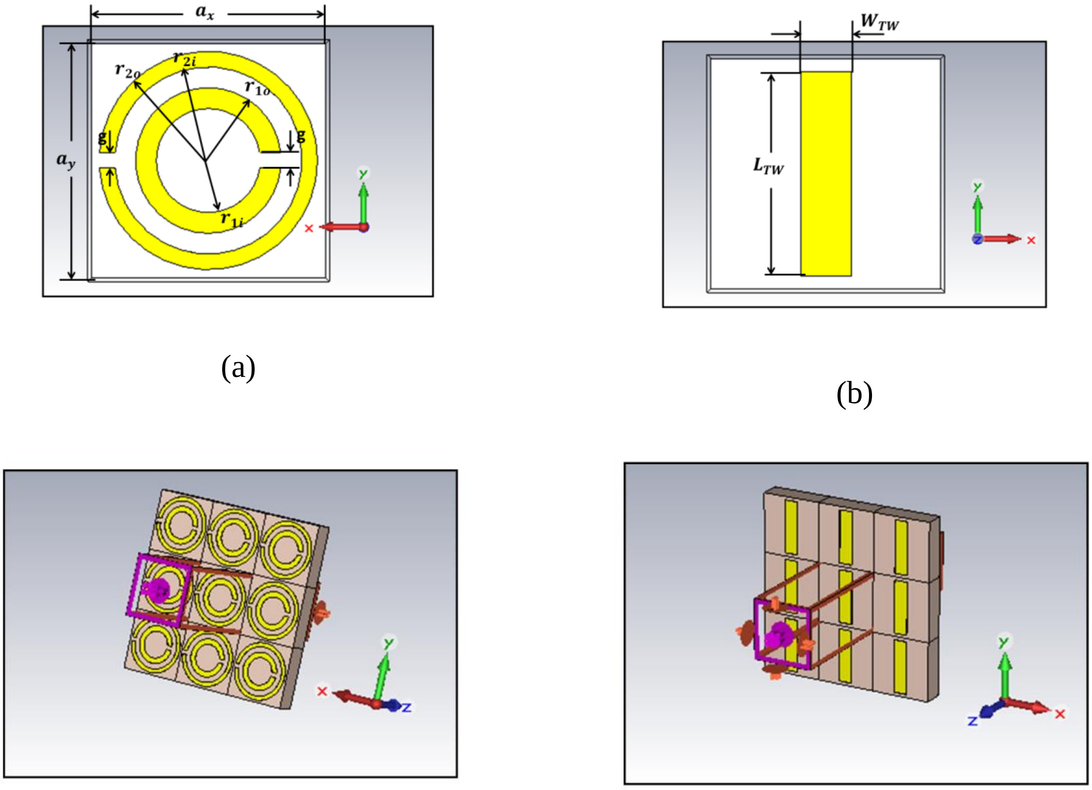

(a)

(b)

(c)

(d)

Fig. 4.2. The MTM Structure composed of CSRR/TW MTM unit cell with infinite periodicity in x and y directions (a) front view, (b) back view, (c) and (d) indicate 3-D view with boundary conditions of unit cells in x and y directions and the feeding source in the x-y plane.

After the MTM structure was designed and simulated using the CST software, the scattering parameters were traced as shown in Fig. 4.3 (a). Figure 4.3 (a) shows that the

MTM structure has a band pass frequency response with a transmission peak center frequency of 10 GHz. The scattering parameters of the MTM unit cell with infinite periodicity in the x and y directions are obtained by using the boundary conditions of magnetic walls at the back and front sides since the magnetic field is polarized in the x-direction and also the electric walls on the left and right sides as the electric field is polarized in the y-direction. The theoretical resonant frequency of the CSRR/TW unit cell is 10 GHz, according to the theories developed in [10, 24], which is matched with the operating frequency of the patch antenna. The transversal periodicity is a = 4.5 mm, which is less than 1/8 of the free space wave length at resonance, which is used to construct the 3-D MTM periodic structure to employ the MTM lens as will be illustrated in the next subsection.

Then, the effective parameters of the MTM unit cell with infinite periodicity in the x and y directions, including effective permittivity ε, effective permeability μ, and refractive index n, have been extracted from the *S-parameters* using the Nicolson-Ross-Weir (NRW) approach [34-38] and the results are plotted as shown in (b), (c) and (d), respectively for two different branch ambiguity factor p of 0 and 1 values. According to the theory developed in [46], the correct branch ambiguity factor for this MTM structure is p=0 since it is a thin MTM slab. Figures 3 (b), (c) and (d) illustrates that, the real parts of the effective permittivity ε', the effective permeability μ' and effective refractive index n', respectively are negative around the resonance frequency of 10 GHz at p=0. In [35], the authors proved that, the MTM effective parameters extraction based on the *S-parameters* method has no ambiguity related to the sign of the wavenumber $k_S$and the intrinsic impedance η_S of the metamaterials layer, while it has ambiguities related to the branch of the complex logarithm. Based on this method, the effective permittivity ε_S and the effective permeability μ_S are computed by using NRW algorithm given in Appendix A

It is clear from equation A.6 that, he term $2\pi p$ (where p is an integer number) defines the branches of log Z, there is a specific value of p which gives the branch ambiguity in the real part of k_s which is k_s' it has been noticed that, there is no branch ambiguity in the imaginary part of k_s which is k_s''. The branch ambiguity factor p is determined based on the geometry of the MTM slab, whether it is thin, thick or multi-layered. In our case the MTM slab is thin, since the relation between the wavelength λ_s of 30 mm at the predefined interesting frequency which is 10 GHz and the thickness d of the MTM slab which is 1.6 mm is $\lambda_s > 2d$. As a result $|k_s'|d < \pi$ and therefore, Arg (Z) is limited to the interval $[-\pi, \pi]$, so p is set to 0 in equation A.6. Thus, the material parameters can be extracted unambiguously for an electrically thin slab which is the case of the proposed MTM structure presented in this chapter.

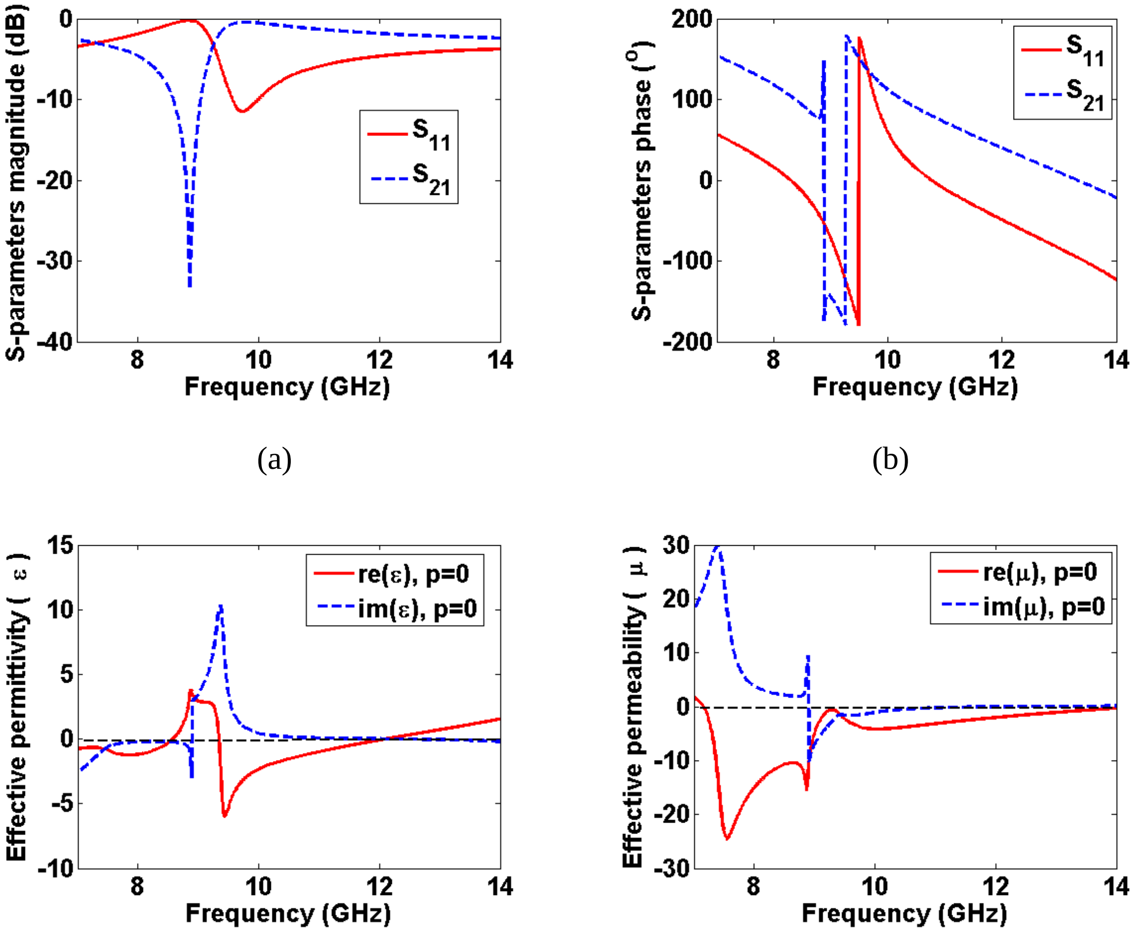
(a) (b)

(c) (d)

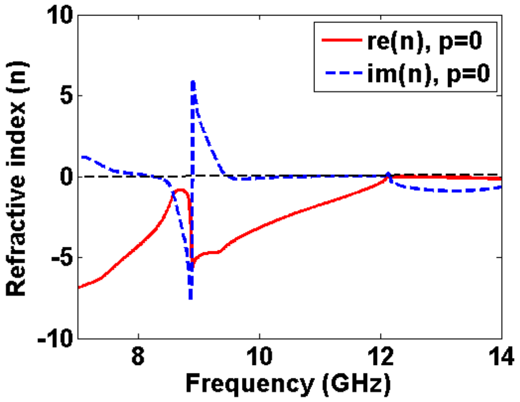

(e)

Fig. 4.3. The CSRR/TWs infinite 2-D periodicity MTM structure with negative effective parameters around the fundamental resonance frequency of 10 GHz, extracted at unambiguity branch parameter p=0 [35] (a) *S-parameters* magnitude, (b) *S-parameters* phase, (c) Effective permittivity (ε), (d) Effective permeability (μ) and (e) refractive index (n).

Figures 4.3 (a) and 4.3 (b) shows that, the CSRR/TWs MTM unit cell with infinite 2D periodicity resonates at a fundamental frequency of 10 GHz and has a negative effective parameters around 10 GHz as shown in Figs. 4.3 (c), 4.3 (d) and 4.3 (e). However, the bandwidths of the negative effective parameters of the CSRR/TWs MTM unit cell with infinite 2-D periodicity can be widened if the unit cell dimensions are increased and the first harmonic resonance of the CSRR/TWs unit cell is chosen instead of the fundamental resonator. To do so, the dimensions of the CSRR/TWs MTM unit cell shown in Fig. 4.2 are redesigned to have a first harmonic resonance around 10 GHz with a wider bandwidth. The CSRR/TWs MTM unit cell parameters are: a=8 mm, g=0.3 mm, r_{1i}=2 mm, r_{1o}=2.5 mm, r_{2i}=3 mm, r_{2o}=3.5 mm, L_{TW}= 7 mm. W_{TW}= 1 mm and t= 17 μm. The effective parameters of the CSRRs/TWs unit cell with infinite 2-D periodicity including effective permittivity ε, effective permeability μ, and refractive index n, have been extracted from the *S-parameters* using the method presented in [46] for unambiguity branch parameter p of 0. Figures 4.4 (a) and 4.4 (b) show that the infinite 2-D periodicity CSRR/TWs unit cell has band pass frequency response with a center frequency of 10 GHz. However, the real part of the effective permittivity, effective permeability, and refractive index are negative around 10 GHz as shown in Figs. 4.4 (c), 4.4 (d) and 4.4 (e), respectively. Furthermore, according to the theory developed in [35], the selected ambiguity branch parameter is p=0 since the structure is a thin MTM slab. It is important to notice that, as the ambiguity branch parameter is chosen properly, the non-Lorentzian response is minimized. By comparing the scattering parameters shown in Figs. 4.3 (a) and 4.3 (b) with the effective parameters shown in Figs. 4.4 (c) to 4.4 (e), it is clear that, far away from resonance the effective parameters has DC offset values and it has negative real effective parameters after resonance. However, the MTM structure exhibits simultaneous negative effective parameters.

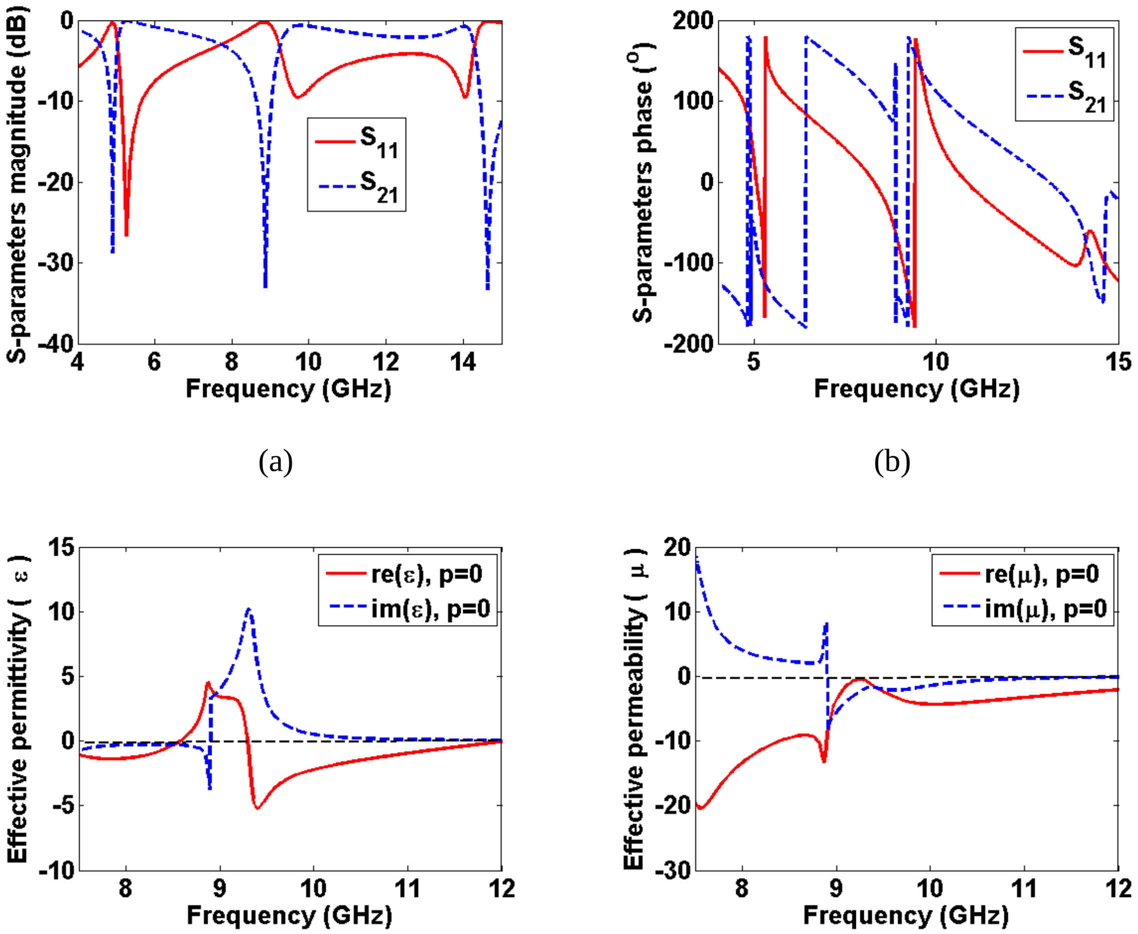

(a)

(b)

(c)

(d)

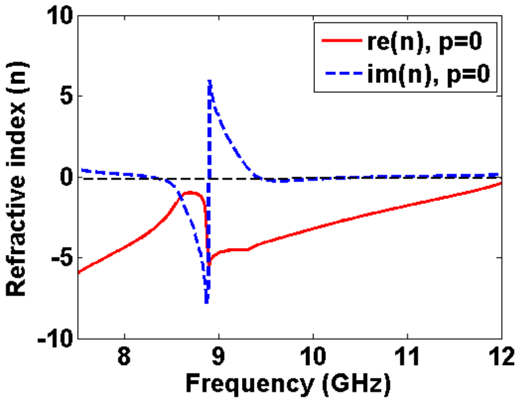

(e)

Fig. 4.4. The 2-D infinite periodicity CSRR/TWs MTM structure with negative effective parameters around the first harmonic resonance frequency of 10 GHz, extracted at unambiguity branch parameter p of 0 [35] (a) S-parameters magnitude, (b) S-parameters phase, (c) Effective permittivity (ε), (d) Effective permeability (μ) and (e) refractive index (n).

4.2.2. Angular Response, infinite periodicity truncation impacts and lens verifications of the CSRR/TWs NRI MTM structure

In this section, the angular response of the CSRR/TWs structure with 2-D infinite periodicity was studied to verify the angular independency of the CSRR/TWs NRI MTM structure to ensure that the MTM structure designed in the previous section has a negative refractive index (NRI) and good reflection and transmission characteristics in a wide band of angles, and hence the MTM structure can be used to act as a lens to focus the EM waves, as a result the radiation parameters of the patch antenna such as gain, directivity and radiation efficiency will be improved, if the MTM structure is placed in the front of the patch antenna. Also, the infinite periodicity truncation impacts of the MTM structure on the effective parameters of the MTM structure were studied.

Firstly, to verify the angular independency characteristics of the CSRR/TWs MTM structure, the MTM structure was rotated from 0 degree to 180 degrees with respect to the excitation probe of the Transverse Electromagnetic Waves (TEM) waves. Due to the symmetry of the MTM structure, it will reach its initial orientation angle of 0 degree if it is rotated by 180 degrees, so no need to rotate the structure by 360 degrees to check the angular independency of its characteristics. For each orientation angle of the MTM structure from 0 to 180 degrees, the transmission, reflection and effective parameters were traced and then compared for all the rotation angles. If the MTM structure has good transmission and reflection characteristics as well as simultaneous negative effective permittivity, negative effective permeability and NRI for all rotation angles from 0 to 180 degrees, then it can be said that the structure has angular independency and can act as a MTM lens. This task has been achieved by fixing the direction of the excitation TEM wave and rotating the CSRR/TWs MTM structure with respect to the source. Then, for selected rotational angles of 0, 45, and 180 degrees, the scattering parameters of the structure are traced as shown in Fig. 4.5. Then the effective parameters of the structure are extracted and plotted as shown in Fig. 4.6 based on the method presented in [35] and choosing ambiguity branch parameter *p* of 0 since the MTM structure is a thin MTM slab as it proven in section 4.*2.1* of this chapter. It is clear from Fig. 4.5 that, although there are significant variations for S_{11} and S_{21} by rotating the MTM structure with respect to the TEM wave excitation source, the real effective permittivity ε', real effective permeability μ' and real refractive index n', all have negative values around 10 GHz for all rotation angles.

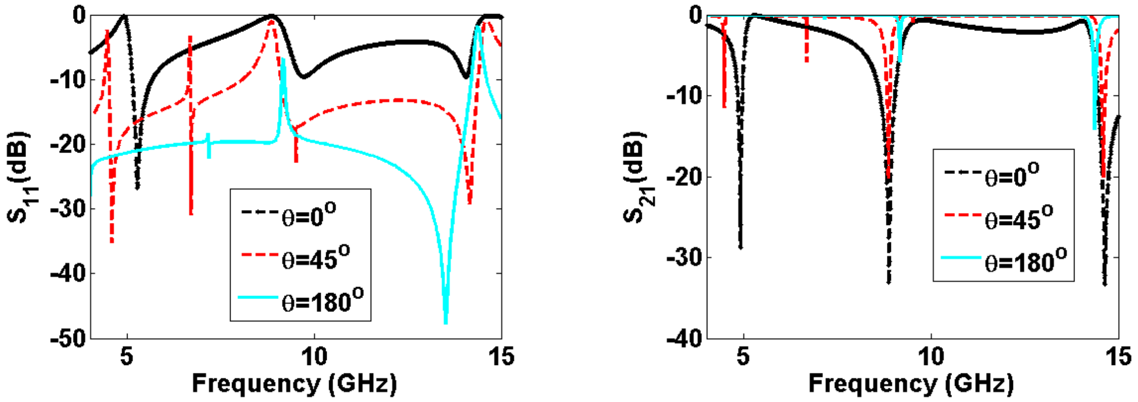

(a) (b)

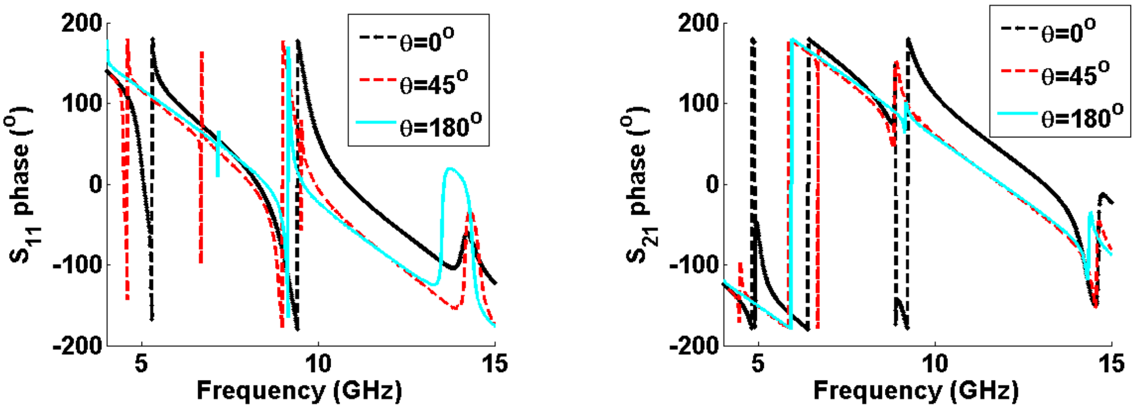

(c) (d)

Fig. 4.5. Magnitude of the scattering parameters of the infinite 2-D CSRR/TWs MTM structure at different rotational angles of 0, 45, and 180 degrees with respect to the excitation TEM wave direction, (a) S11, (b) S21,(c) S11 phase, and (d) S21 phase.

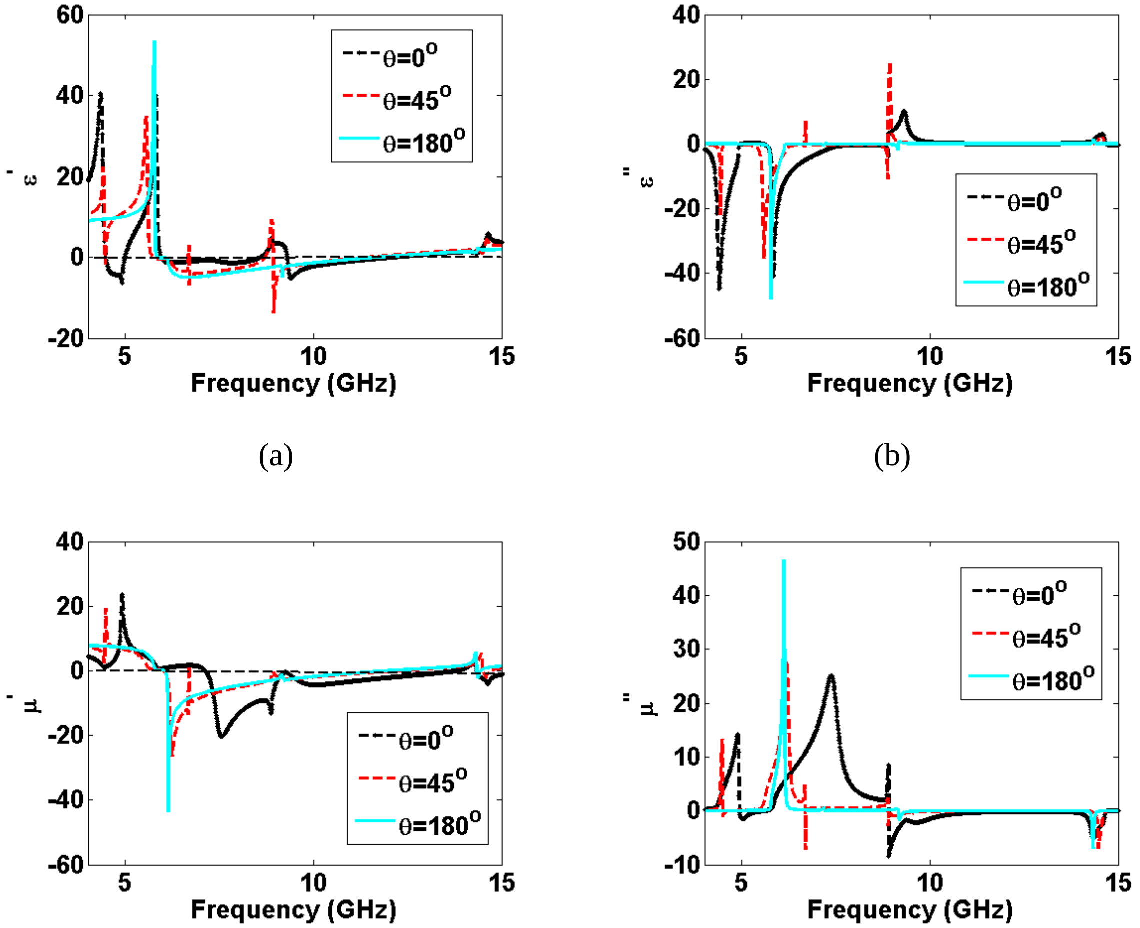

(a) (b)

(c) (d)

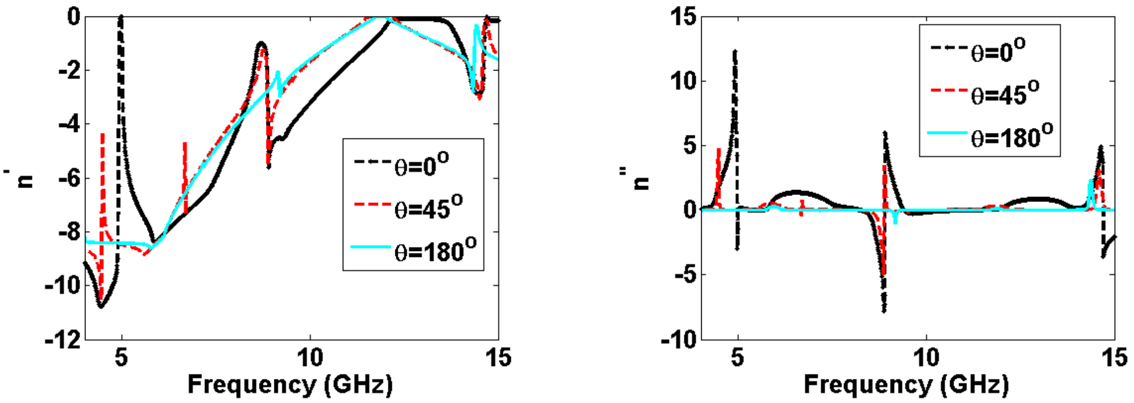

(d) (e)

Fig. 4.6. The 2-D infinite periodicity CSRR/TWs MTM structure with negative effective parameters around the first harmonic resonance frequency of 10 GHz, extracted with ambiguity branch parameter p of 0 [35] and at different rotational angles of 0, 45, and 180 degrees with respect to the excitation TEM wave direction, (a) real part of effective permittivity (ε′), (b) imaginary part of effective permittivity (ε″), (c) real part of effective permeability (μ′), (d) imaginary part of effective permeability (μ″), (e) real part of refractive index (n′), and (f) imaginary part of refractive index (n″).

Secondly, the effect of the MTM infinite periodic structure truncation on the MTM lens effective parameters and the metamaterial homogeneity is considered. It is impossible to use infinite MTM periodic structure in our application of incorporating the patch antenna with the MTM lens, since the patch antenna has a patch length of $\lambda/2$ and a patch width which determines the antenna impedance matching. This means that we have a finite MTM lens size which can be identified as function of the patch dimensions and the resonance wavelength to make sure that the antenna impedance matching occurs and at the same time the MTM structure has negative real part effective parameters around the resonance frequency and the MTM homogeneity is still satisfied. For example in the direction of the antenna patch length L which is the y- axis as shown in Fig. 4.1, the infinite periodicity is truncated at two unit cells of cell size a=8 mm, and this number of cells satisfies the MTM homogeneity at the operating wavelength which is 30 mm at 10 GHz, since at this frequency, the ratio λ/a will be approximately 4, which means that, two unit cells are required to cover the patch of effective length $L = \lambda/2$ of 15 mm in the direction of the patch length. This means that, there will be approximately $\lambda/4$ wave propagating across each MTM unit cell which is not bad related to the MTM homogeneity condition. Furthermore, it is good if we can increase the number of MTM unit cells per wavelength greater than 8, and this can be done by taking a MTM unit cell of a unit cell size of 4.5 mm and has a fundamental resonance frequency of 10 GHz, this approach was suggested but unfortunately a less gain improvement was achieved (the results not shown here). So to tackle the tradeoff between the MTM homogeneity and the antenna performance improvement, a consistent homogeneity factor of 4 is chosen. However, if the number of cells in the direction of the patch length is increased, it will affect the impedance matching of the antenna and the return loss is increased as will be illustrated in the next section (see Fig. 4.9 (a) for a MTM size of $3 \times 3 \times 2$), so two unit cells are the optimum number in the *y*-direction. For the number of cells in *x*-direction aligned to the patch width for different sizes of 2, 3 and 4 were used which fully covered the patch and even the whole antenna substrate. While in the *z*-direction, the periodicity of the MTM structure is truncated at two unit cells, since more cells in such a direction will cause impedance mismatching.

To verify the above explanation of the infinite periodicity truncation of the MTM structure, three different 3-D MTM structures with truncated periodicity of sizes $2 \times 2 \times 2$, $3 \times 3 \times 2$, and $4 \times 2 \times 2$, in addition to one 2-D MTM structure with infinite periodicity are designed and simulated in CST software. The scattering parameters of the MTM structures with infinite and truncated periodicities are traced as shown in Fig. 4.7. It is clear that the return loss and the transmission characteristics of the 3-D truncated MTM structures are better than their counterparts of the 2-D infinite periodicity MTM structure, these improvements are because of the multilayer used in case of the truncated MTM structure, while in the case of the infinite periodicity, one layer of 2-D infinite periodicity was used. Then the effective parameters of all the MTM structures are extracted and plotted for ambiguity branch parameter *p* of 0 [35] as shown in Fig. 4.8. Figure 4.8 illustrates that, the infinite periodicity truncation of the MTM structure do not destroy the negative effective parameters of the MTM structure and the structure still has negative values for real effective permittivity, real effective permeability and real refractive index as shown in Fig. 4.8 (a), 4.8 (c) and 4.8 (e), respectively, around 10 GHz. Also, the imaginary part of the effective permittivity and permeability they have a DC offset at values far away from resonance and peak at resonance which show that the structure has a physical Lorentzian response. Furthermore, the optimum dimensions of the MTM lens structure will be chosen such that the return loss of the antenna is not destroyed as a result of the capacitive and inductive coupling presented by the MTM lens to the conventional antenna. This will be studied in the coming section

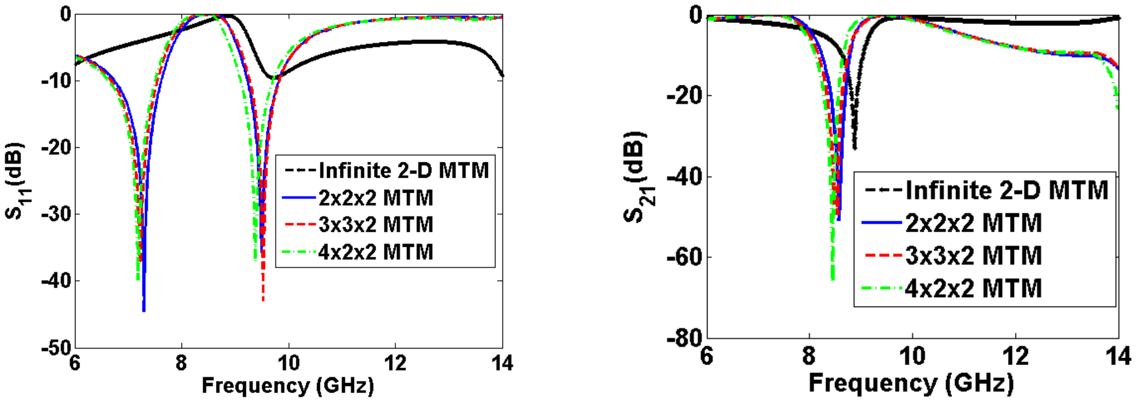

(a) (b)

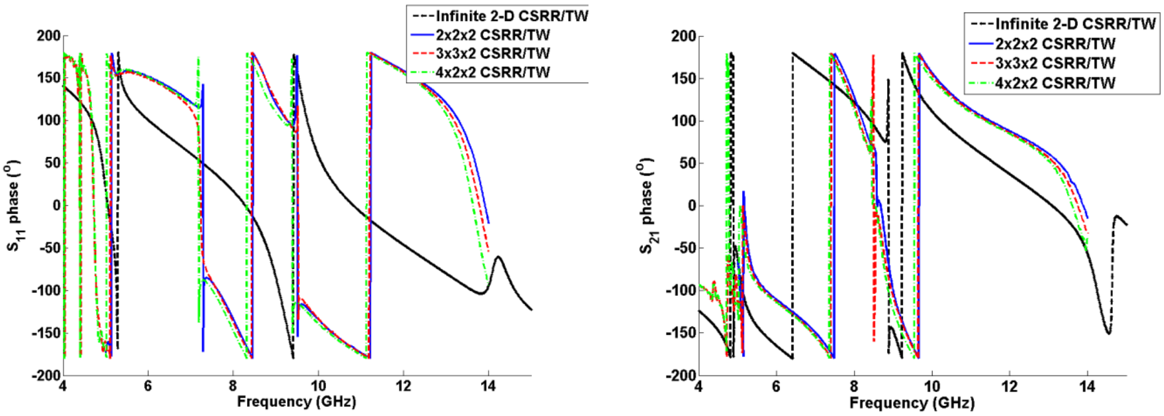

(c)

(d)

Fig. 4.7. Magnitude of the scattering parameters of the MTM structure with truncated periodicity by building the MTM lens from 3-D structure with finite sizes of 2 × 2 × 2 , 3 × 3 × 2 and4 × 2 × 2 (a) S_{11}, and (b) S_{21}, (c) S_{11} phase, and (d) S_{21} phase.

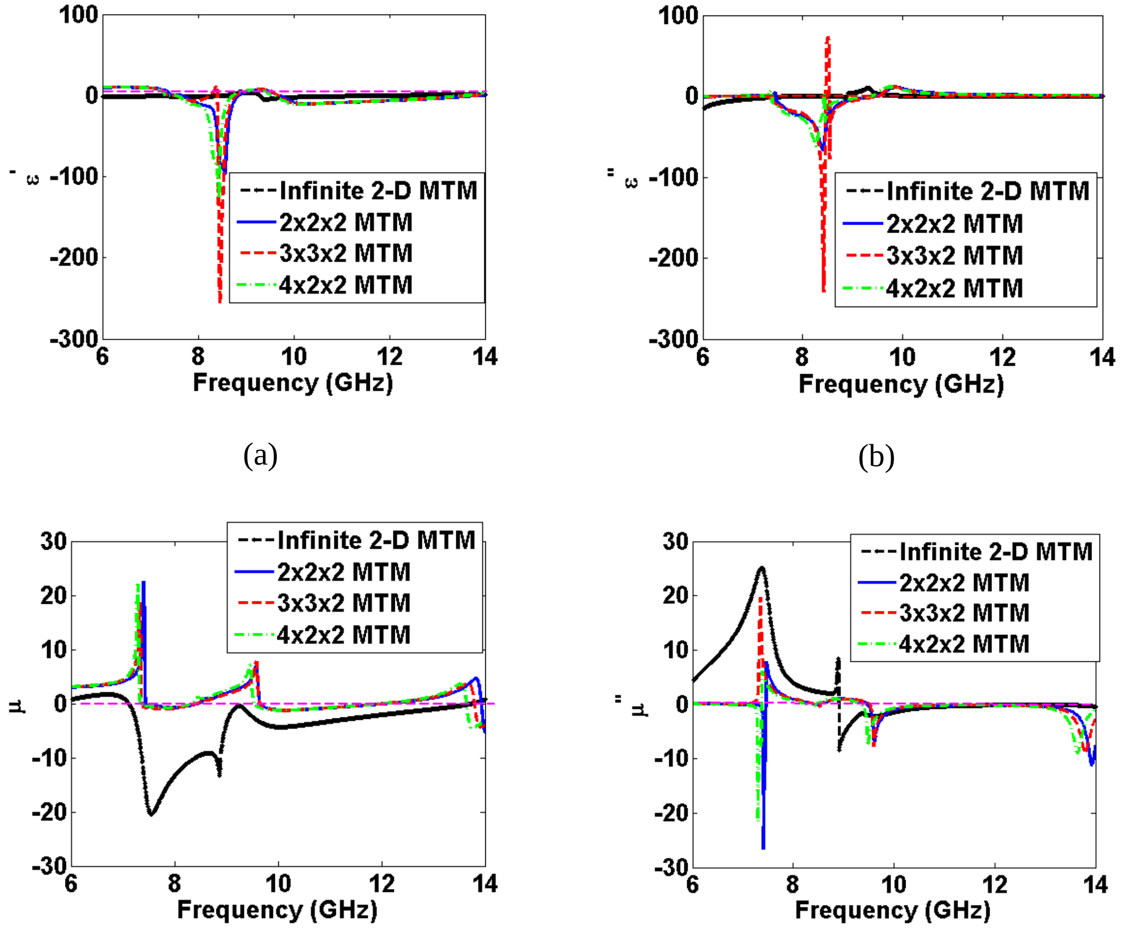

(a)

(b)

(c)

(d)

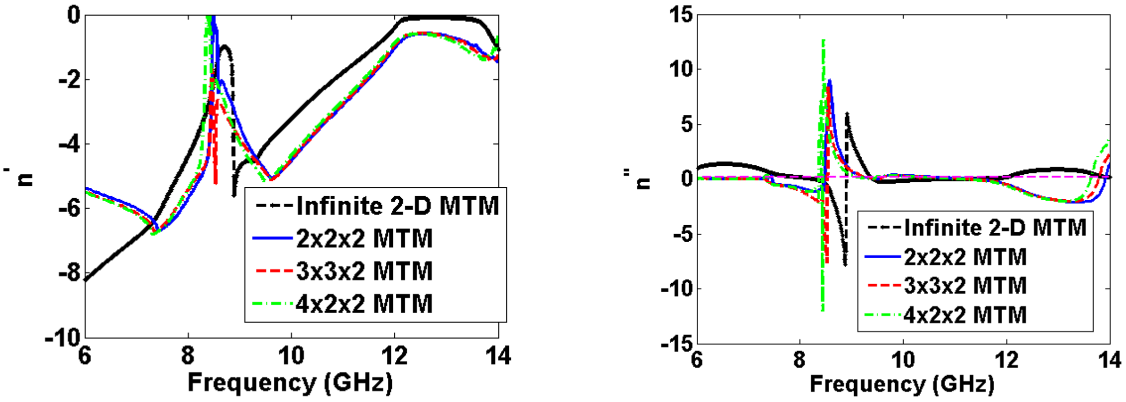

(e) (f)

Fig. 4.8. The extracted effective parameters of the MTM structure truncated periodicity by building the MTM lens from 3-D structure with finite sizes of $2 \times 2 \times 2$, $3 \times 3 \times 2$ and$4 \times 2 \times 2$ with ambiguity branch parameter p of 0 [35], (a) real part of effective permittivity (ε′), (b) imaginary part of effective permittivity (ε′′), (c) real part of effective permeability (μ′), (d) imaginary part of effective permeability (μ′′), (e) real part of refractive index (n′), and (f) imaginary part of refractive index (n′′).

4.2.3. Design and Simulation of 10 GHz Patch Antenna incorporated with CSRR/TW MTM lens in Front of the Patch

Here, the proposed patch antenna incorporated with the MTM is analyzed, simulated and optimized using CST software. The MTM lens of the proposed antenna shown in Fig. 2.4 was optimized to have a negative permeability, negative permittivity and negative refractive index in a wideband around 10 GHz. The antenna was optimized by changing the size of the MTM lens and the separation between the MTM lens and the patch. Figures 4.9 (a) and 4.9 (b) show the return loss and the radiation gain at 10 GHz of the proposed antenna at 10 mm separation distance h_s between the patch and the MTM lens bottom side and at different MTM lens sizes. The separation distance between each two 2D MTM layers was 2 mm.

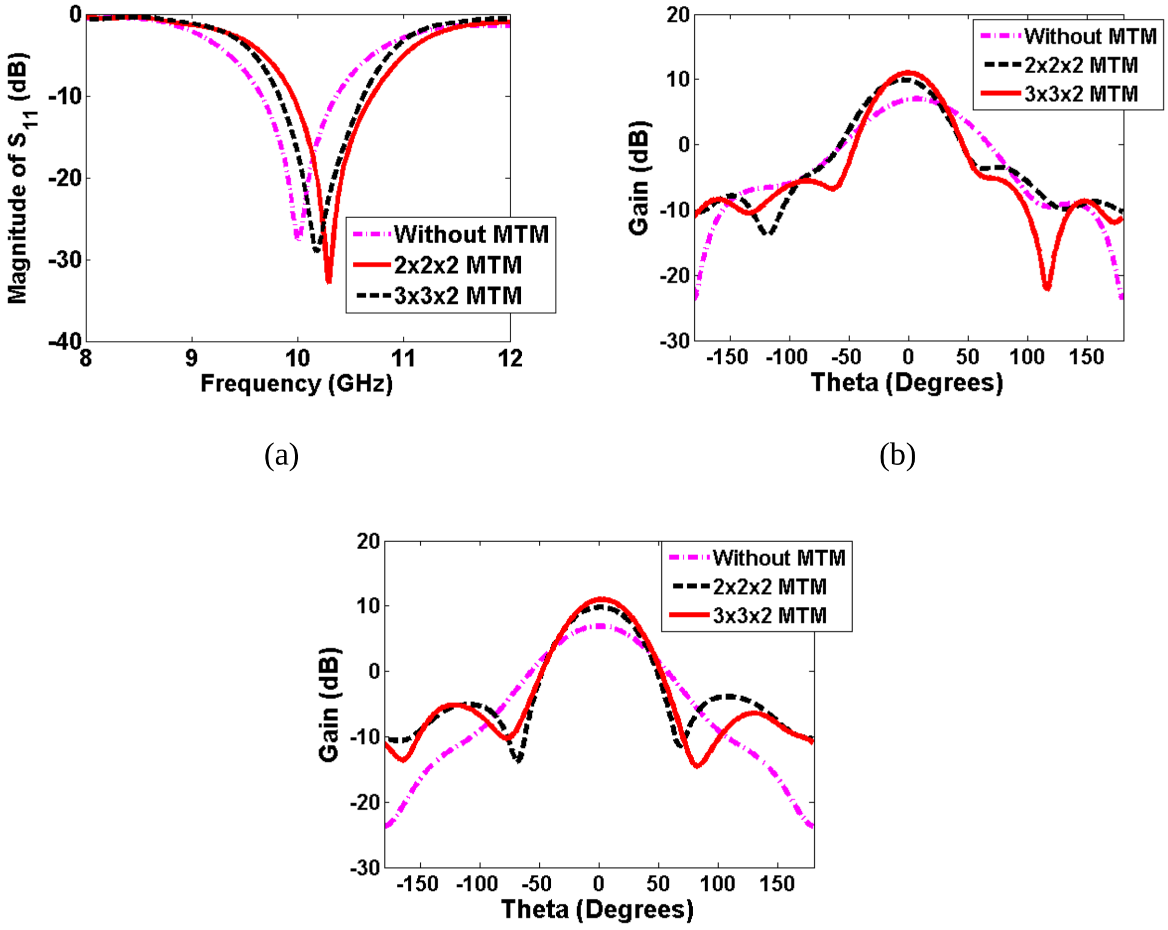

(a) (b)

(c)

Fig. 4.9. The simulated return loss (a) and the simulated E-plane (b) and H-plane (c) gain at 10 GHz of the proposed antenna with and without MTM lens of different sizes and at 10 mm separation distance h_s between the patch and the MTM lens.

Furthermore, the effect of the patch and MTM lens separation on the radiation and impedance matching parameters were studied by fixing the size of the MTM lens at 3×3×2 in *x*, *y* and *z* direction, respectively and changing the separation distance h_s from 6 mm to 12 mm by a step size of 2 mm. It is important to notice that, the separation distance between the patch antenna and the MTM lens as well as the size of the MTM lens plays an important role in optimizing the antenna parameters. The results show that, the proposed antenna is optimized at a separation distance of 10 mm. The return loss and the radiation gain for the proposed antenna at different patch and MTM lens separation and at a 3×3×2 MTM lens size is plotted as shown in Figs. 4.10 (a) and 4.10 (b). However, the magnitude of the near electric and magnetic fields of the proposed antenna with and without MTM lens at 10 GHz are plotted as shown in Fig. 4.11. It is clear that, by placing the MTM lens of size 3×3×2 and identifying the convergence mesh criteria in the CST, the electric field *E* magnitude is improved from 29788 v/m to 37996 v/m and the magnetic field *H* strength is slightly improved from 76.4 A/m to 77.1 A/m and the field is focused above the patch around the center of the MTM lens which claim lays that the NRI CSRR/TWs MTM structure is acting as a lens. It is important to notice that, the shown number for the *E* and *H* fields are just to clarify the improvement in the near field of the patch antenna which occurs due to the MTM lens and these numbers may be changed slightly if the numbers of meshes in the CST simulation are changed.

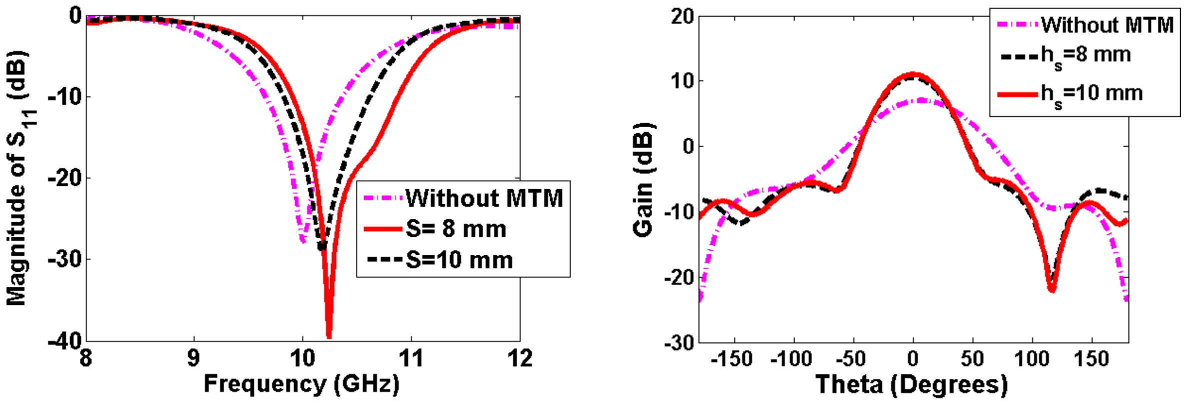

(a) (b)

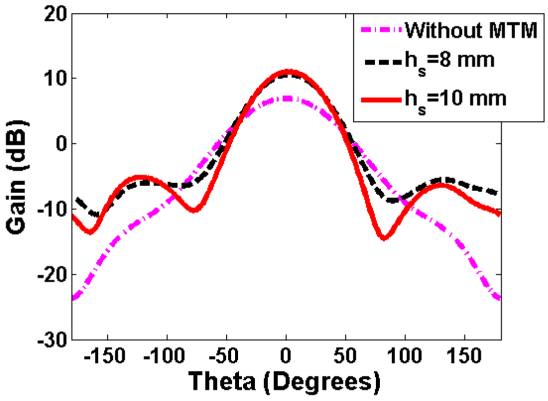

(c)

Fig. 4.10. The simulated return loss (a) and the simulated E-plane (b) and H-plane (c) gain at 10 GHz of the proposed antenna with and without MTM lens of size 3x3x2 and different separation distances h_s between the patch and the MTM lens.

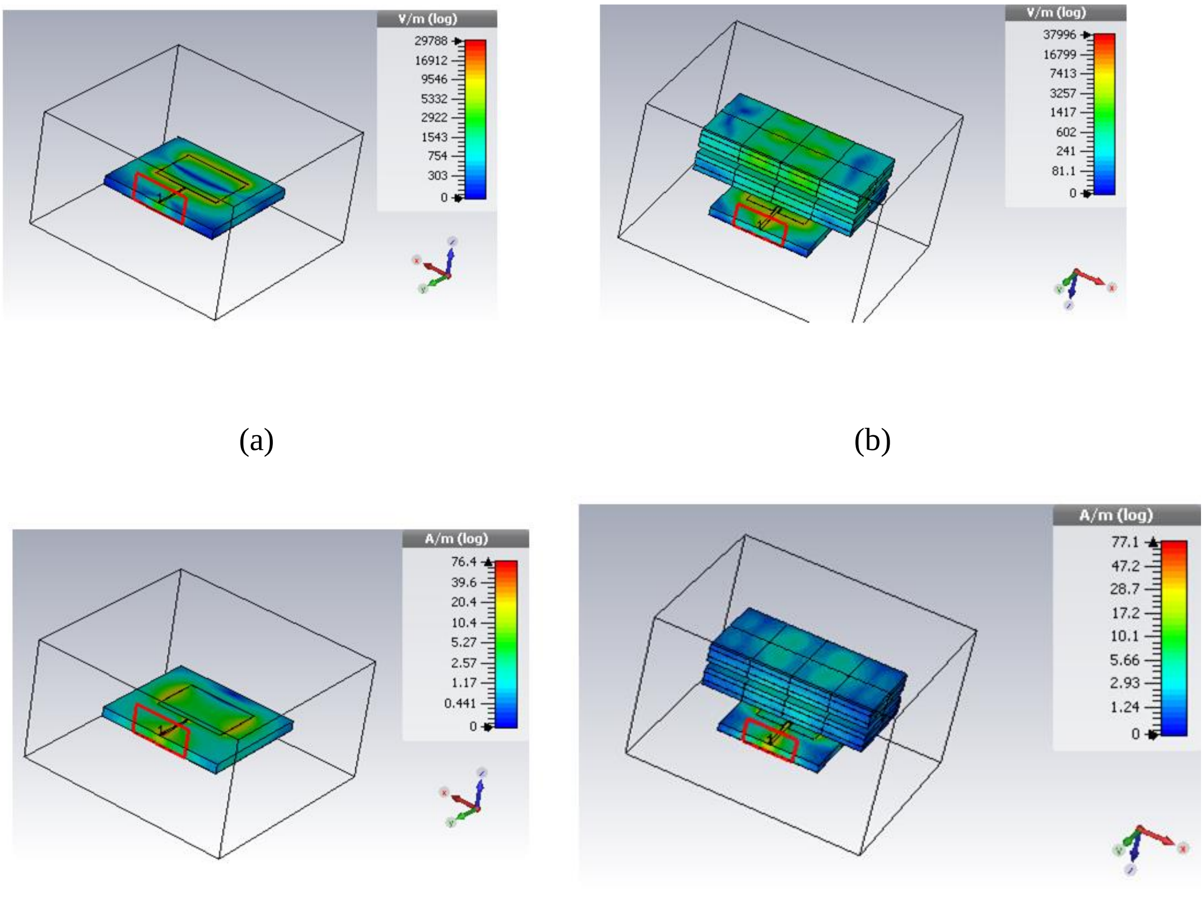

(a)

(b)

(c)

(d)

Fig. 4.11. Near field of the proposed antenna without and with MTM lens at 10 GHz, (a) E-field without MTM lens, (b) E-field with MTM lens, (c) H-field without MTM lens and (d) H-field with MTM lens.

It is clear from Figs. 4.9 that, as the size of the MTM lens increases, the gain increases, and the beam area is reduced, while the return loss increases (decreases with negative values), and the bandwidth is increased. As the MTM lens is added the losses of the antenna increases, so the total quality factor decreases and hence according to equation (4.5) given above, the bandwidth increases. Furthermore, according to equations (4.6, 4.8 and 4.9), the gain improves for the antenna with an MTM lens although the losses increases, because the beam becomes more directive due to the NRI of the MTM lens and hence the directivity *D* increases. The increase in directivity *D* is more than the reduction in the antenna efficiency due to the losses presented by the MTM lens, so the antenna gain increases. Furthermore, according to equation 4.7, the reason behind the reduction in the return loss of the proposed antenna comes from the change in input impedance which determines the *VSWR* of the antenna. The antenna input impedance is changed due to the magnetic and the electric coupling between the patch and the MTM lens which result in adding a reactance term to the antenna input impedances, as a result the resistive part of the antenna input impedance may become more dominant and hence impedance matching occurs and the return loss is improved as in the case of MTM lens of 2×2×2 size the opposite situation may happen such as in the remaining sizes of the MTM lens as shown in Fig. 9 (a).

The optimum dimensions of the MTN lens is chosen to achieve a compromise between good impedance matching and high gain. It can be said that, the input impedance and hence the return loss of the antenna is affected dramatically when the MTM lens is added, since the MTM lens adding a new terms for the input impedance of the antenna. However, it is obvious that, the optimum MTM lens has a size of 3×3×2 and the optimum separation distance between the patch and the MTM lens is 8 mm. For the optimized proposed antenna, the simulated gain is improved from 7 dB to 11.6 dB; the band width is improved from 700 MHz to 900 MHz, while the return loss improved from -27 dB to -39 dB. In addition, for a patch antenna with a MTM lens of size 2×2×2 separated from the patch at a distance h_S of 10 mm, the return loss is improved from -27 dB to about -35 dB as shown in Fig. 4.9 (a), while the beam area is reduced from 75 degrees to 41 degree as shown in Fig. 9 (b). However, it should be noticed from Fig. 4.9 and 4.10 that, as the size of the 3-D MTM structure employing the MTM lens increases, the return loss increases and the antenna matching becomes worst due the loading effect of the MTM lens which affects directly the input impedance of the antenna, so to avoid this problem a compromise between the return loss and the gain of the antenna should be carried out to obtain a good match and a high gain at the same time.

4.3. Fabrication and Measurement

For experimental validation, the proposed antenna resonating at 10 GHz as well as the CSRR/TW MTM lens have been fabricated as shown in Fig. 4.12. The fabrication is done using a wet etching technique on a RT/Duroid 5880 substrate for both the patch antenna and the MTM with a relative permittivity of ε_r = 2.2 and a thickness of h= 1.57 mm. The return loss, S_{11} for the simulated and the fabricated antenna with and without MTM structure is shown in Fig. 4.13. Furthermore, the effect of the separation distance between the patch and the MTM lens of size 3x3x2, and the effect of the MTM lens size at fixed separation h_S of 8 mm, on the impedance matching of the antenna are illustrated as shown in Fig. 4.13 (a) and Fig 4.13 (b), respectively. The measured bandwidth of the patch antenna with and without MTM is approximately the same which is around 400 MHz. However, the measured return loss of the 10 GHz proposed antenna incorporated with an MTM lens placed on the patch at a separation distance of 8 mm and of size 3×3×2 improved the return loos from -13 dB to -30 dB. The separation distance between each two 2D MTM layers was 2 mm. By comparing Figures 4.9 (a), 4.9 (b) and 4.13, it is clear that the simulated and the measured results proved that the antenna return loss is improved by adding the MTM lens. The minor difference between the simulated and the measured results is due to the soldering of the SMA connector and the misalignment of the MTM lens at the top of the patch.

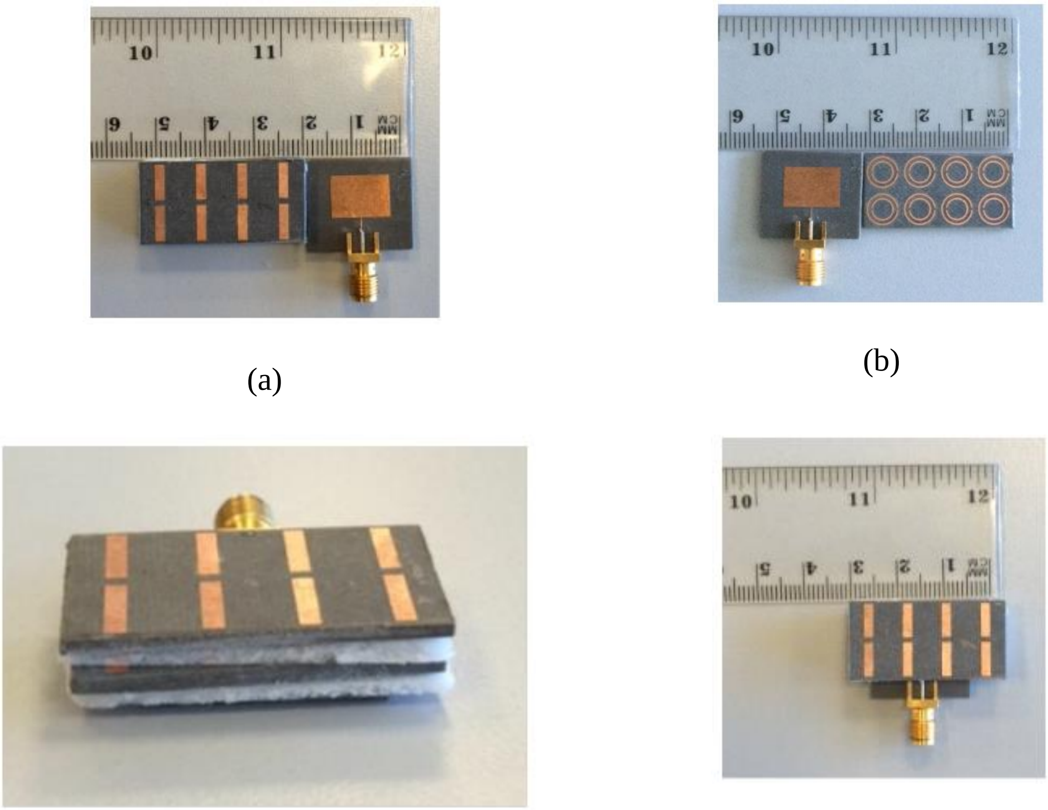

(a)

(b)

(c)

(d)

Fig. 4.12. The fabricated antenna, (a) conventional patch and top view of CSRR/TW 2-D periodic structure of size 4×4×2, (b) conventional patch and bottom view of CSRR/TW 2-D periodic structure, 3-D view of the proposed antenna, and (d) top view of the proposed antenna incorporated with MTM lens.

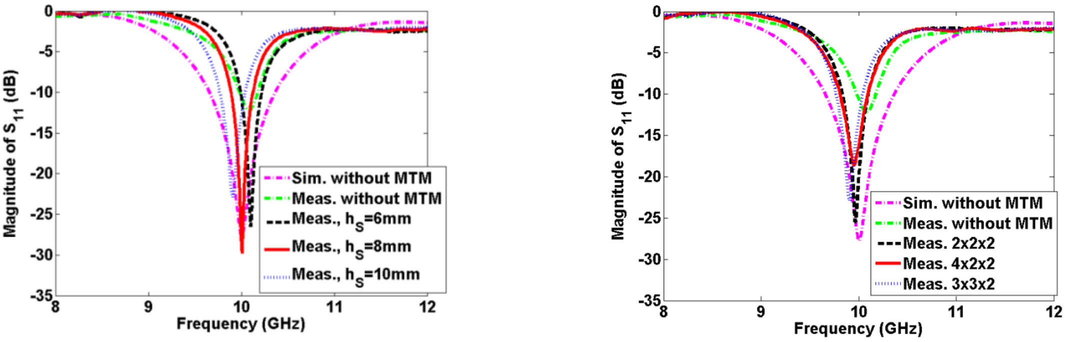

(a)

(b)

Fig. 4.13. The measured and simulated return loss of the proposed antenna with and without MTM lens (conventional): (a) at different separation between the MTM lens and the patch and 3x3x2 MTM lens size, and (b) at different MTM lens sizes and separation distance of 10 mm between the patch and the MTM lens.

Furthermore, both *E*-plane and *H*-plane radiation patterns at 10 GHz proposed antenna with and without MTM are measured for different MTM lenses of sizes 4×2×2 and 3×3×2 and fixed separation h_S of 10 mm between the patch and the bottom side of the MTM lens as shown in Fig. 4.14. However, the simulated *E*-plane and *H*-plane radiation patterns at 10 GHz proposed antenna with and without MTM are plotted on the same figure. It is clear from Fig. 4.14 that, the measured results proved that the radiation pattern of the antenna with MTM is more focused than that withoutthe MTM lens, although there is a deviation between the conventional measured and simulated H-plane radiation pattern which may be due to the soldering of the SMA connector which may distort the radiation pattern.

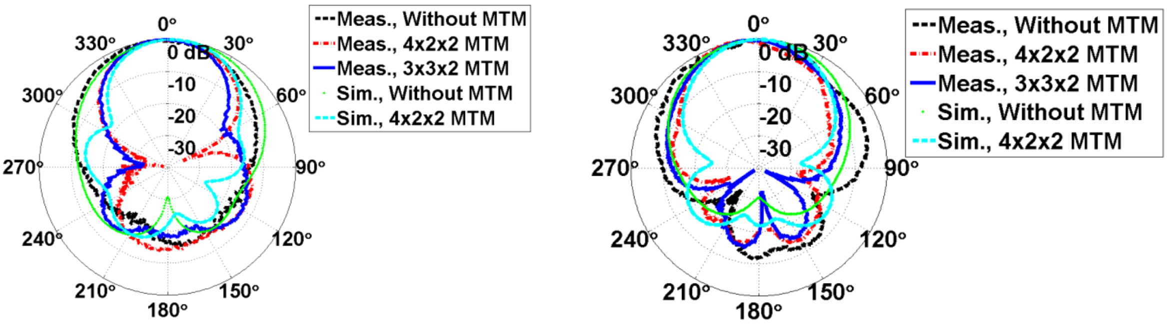

(a)

(b)

Fig. 4.14. Measured and simulated radiation pattern at 10 GHz of the proposed antenna with and without MTM lens for different MTM lens sizes, (a) E-plane and (b) H-plane and fixed separation h_S of 10 mm between the patch and the MTM lens

The results showed a good agreement between the simulated and the measured results and that the radiation beam in both *E*-plane and *H*-plane become more focused as the MTM lens is placed at the top of the patch. To verify the idea that as the beam becomes more focused and hence the gain of the antenna is improved, the gain versus frequency for the proposed antenna with and without the MTM lens for different MTM lens sizes of 3×3×2 and 4×2×2 and fixed separation of 10 mm between the patch and the MTM lens bottom side is plotted as shown in Fig. 4.15.

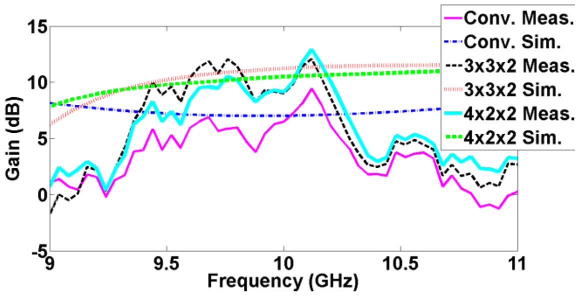

Fig. 4.15. Comparison between the measured and the simulated gains of the proposed antenna with and with MTM lens of different sizes and fixed separation h_s of 10 mm between the patch and the MTM lens.

It is clear from Fig. 4.15 that, the simulated gain of the proposed antenna incorporated with a MTM lens of 3×3×2 size is improved from 7 dB to 11.6 dB inside the bandwidth of the antenna, at the same time the measured gain is also improved approximately with the same figures. The gain versus frequency graph of Fig. 4.15 shows that the measured and the simulated gain of the proposed antenna are roughly closed inside the antenna bandwidth but with a little bit of fluctuation due to the measurement errors and the misalignment of the placement of the MTM lens above the patch. However, as the MTM lens size increases, the gain of the proposed antenna increases, because the MTM lens congregates more EM waves from the patch radiated waves and the beam becomes more focus. With regard to the antenna efficiency, it is important to notice that, due to the added MTM lens, the dielectric and the conductor losses increase which for sure degrade the antenna overall efficiency, but due to the beam focusing of the radiated wave caused by the MTM lens, the directivity of the antenna increase significantly. The increase of the directivity becomes dominant compared with the decrease in the antenna radiation efficiency; as a result, the antenna gain being improved.

4.4. Major Contribution of This Work

There are two main reasons behind the proposed antenna presented in this chapter. Firstly, the published papers which used the MTM as a cover to improve the performance of the patch antenna such as [7, 39] suffer from two problems of mechanical stability and large size. With regard to the mechanical stability problem, in [7] the MTM layers are placed vertically on the patch substrate which causes difficulty in the alignment and low mechanical stability. In terms of the large size problem, in [39] a large size and bulky MTM structure consists of a 3-D array of thin wires which is used to focus the radiated waves. Furthermore, the two mentioned literature papers didn't focus on neither the NRI extraction nor the oblique response of the MTM structure and didn't show the transmission and the reflection coefficients of the structure at different orientation angles of the MTM structure with respect to the excitation source. Because in order for the NRI MTM structure to be as a lens, it should have good transmission and reflection coefficients as well as employed NRI around the frequency of interest which is 10 GHz in this chapter. In this chapter, the two mentioned problems are solved. For example, in terms of a mechanical stability point of view, the MTM structure is composed of a NRI CSRR/TWs MTM layers, placed at the top of the patch in a parallel arrangement to the patch substrate with foam spacers which results in rigid and mechanically stable antennas. However, it is not necessary to stack many layers of the CSRR/TWs MTM in front of the patch to improve the gain, two layers is enough to improve the gain from 7 dB to 11.6 dB. Thus, the proposed antenna is rigid, light weight and mechanically stable and easier to fabricate, since the MTM lens consists of one layer or multi layers of 2-D CSRR/TWs structure rather than a 3-D array of thin wires [39].

Secondly, this work will service our future plan of proposing a THz optical antenna incorporated with an MTM lens for Heart beat measurement [40] and high resolution imaging systems. Here, i thas been illustrated that in the microwave regime, if the NRI CSRR/TWs MTM structure is excited obliquely, it will have a good transmission and reflection as well as NRI for all angles. So, if the structure is scaled down in dimension and up in frequency in order to develop a MTM lens in the THz regime, it can focus the radiated THz waves from the optical THz antenna instead of using a bulky silicon lens [41]. However, the proposed antenna can be optically tuned by rotating the optical antenna as well as the lens with respect to the excitation laser beam, the MTM structure will still have NRI for all angles and by this way, it is possible to propose an efficient THz optically-tuned optical antenna incorporated with MTM lens. Furthermore, by study the MTM structures through their oblique response, it is possible to optimize and propose novel MTM lenses for the THz optical antennas.

4.5. Summary

In this chapter, the performance of a 10 GHz patch antenna is greatly improved by beam focusing when it is integrated with a 3-D CSRRs/TWs periodic structure employing a MTM lens. The MTM lens was suspended above the patch antenna through bears made of foam; the MTM lens focused the radiated EM waves of the patch antenna in a narrow area. The 2-D infinite periodicity CSRR/TWs MTM structure was designed and simulated using CST software and the effective parameters extracted, the results illustrated that the MTM structure has negative values for the real part of the effective parameters. Furthermore, the angular independency of the CSRR/TWs MTM structure with infinite 2-D periodicity has been verified by rotating the MTM structure from 0 to 180 degrees with respect to the excitation probe of the TEM waves. The results showed that the MTM structure has negative effective parameters and good reflection and transmission characteristics in a wide band of angles around 10 GHz which proved that, the MTM acts as a lens. In addition, the infinite periodicity truncation of the MTM structure was also studied by designing and simulating 3-D MTM structures with finite sizes of 2×2×2, 3×3×2, and 4×2×2. The results showed that, the MTM structure truncation has no impact on both the MTM lens negative effective parameters and homogeneity.

The proposed antenna has been designed and optimized using CST software, the antenna bandwidth was improved and the return loss generally increased, although it might be further improved by optimizing the size of the MTM lens size is chosen properly. The results showed that, as the MTM lens is added the losses of the antenna increases, so the total quality factor decreases and hence the bandwidth increases. The change in the impedance matching and hence the return loss is because of the capacitive and inductive coupling between the patch and the MTM lens. The optimized radiation properties of the proposed patch antenna have been obtained through the justification of the patch-MTM lens separation and the dimensions of the 3-D MTM periodic structure employing the MTM lens. These improvements in the antenna parameters validate the proposed concept of beam focusing using the 3-D periodic structure of CSRRs/TWs, which employing the MTM lens, without modifying significantly the matching methodology of the patch antenna.

Furthermore, we have demonstrated the validity of the above properties using CST software EM simulator and experimentally at 10 GHz and showed that at this frequency the antenna gain, has improved by 4.6 dB, while the beam width is reduced from 75 degrees to 41 degrees which validate the concept of beam focusing using CSRR/TWs MTM lens. The measured and the simulated results showed an improvement in the return loss by about -20 dB for the antenna incorporated with MTM lens of size 2×2×2 although it increases when 3×3×2 and 4×2×2 MTM lens sizes are used. This improvement due to the reactance coming out from the electric and the magnetic coupling between the patch and the MTM lens and the coupling between the different parts of the MTM lens itself which result in a reactance term added to the antenna input impedance. As a future work, the idea of gain improvement of the patch antenna incorporated with the NRI MTM lens will be extended to the THz frequency range to be used for short distance wireless communication link, particularly in the biomedical application and inside the satellite to reduce the wiring complexity of the satellite system. However, the MTM lens can replace the bulky silicon lens used in the THz optical antennas to focus the radiated beam and improve the antenna gain.

4.6. References

[1] Abdelrehim, Adel AA, and H. Ghafouri-Shiraz. "High performance patch antenna using circular split ring resonators and thin wires employing electromagnetic coupling improvement." Photonics and Nanostructures-Fundamentals and Applications 21 (2016): 19-31.

[2] D. Smith and N. Kroll, 'Negative Refractive Index in Left-Handed Materials', Phys. Rev. Lett., vol. 85, no. 14, pp. 2933-2936, 2000.

[3] R. Shelby, 'Experimental Verification of a Negative Index of Refraction', Science, vol. 292, no. 5514, pp. 77-79, 2001.

[4] A. Grbic and G. Eleftheriades, 'Periodic analysis of a 2-D negative refractive index transmission line structure', IEEE Transactions on Antennas and Propagation, vol. 51, no. 10, pp. 2604-2611, 2003.

[5] L. Chen, S. He and L. Shen, 'Finite-Size Effects of a Left-Handed Material Slab on the Image Quality', Phys. Rev. Lett., vol. 92, no. 10, 2004.

[6] Veselago, Viktor G. "The electrodynamics of substances with simultaneously negative values of and μ." Soviet physics uspekhi 10, no. 4 (1968): 509.

[7] Majid, Huda Abdul, Mohamad Kamal Abd Rahim, and Thelaha Masri. "Microstrip antenna's gain enhancement using left-handed metamaterial structure." Progress in Electromagnetics Research 8 (2009): 235-247.

[8] K. Alici, F. Bilotti, L. Vegni and E. Ozbay, 'Optimization and tunability of deep subwavelength resonators for metamaterial applications: complete enhanced transmission through a subwavelength aperture', Opt. Express, vol. 17, no. 8, p. 5933, 2009.

[9] K. Alici and E. Ozbay, 'Characterization and tilted response of a fishnet metamaterial operating at 100 GHz', Journal of Physics D: Applied Physics, vol. 41, no. 13, p. 135011, 2008.

[10] M. Gil, J. Bonache, J. Selga, J. Garcia-Garcia and F. Martin, 'High-pass Filters Implemented by Composite Right/Left Handed (CRLH) Transmission Lines Based on Complementary Split Rings Resonators (CSRRs)', PIERS Online, vol. 3, no. 3, pp. 251-253, 2007.

[11] K. Buell, H. Mosallaei and K. Sarabandi, 'A substrate for small patch antennas providing tunable miniaturization factors', IEEE Transactions on Microwave Theory and Techniques, vol. 54, no. 1, pp. 135-146, 2006.

[12] K. Alici and E. Ozbay, 'Electrically small split ring resonator antennas', J. Appl. Phys., vol. 101, no. 8, p. 083104, 2007.

[13] A. Alu, F. Bilotti, N. Engheta and L. Vegni, 'Subwavelength, Compact, Resonant Patch Antennas Loaded With Metamaterials', IEEE Transactions on Antennas and Propagation, vol. 55, no. 1, pp. 13-25, 2007.

[14] Pirhadi, A., Keshmiri, F., Hakkak, M. and Tayarani, M., 2007. Analysis and design of dual band high directive EBG resonator antenna using square lobe FSS as superstrate layer. Progress In Electromagnetics Research, 70, pp.1-20.

[15] Y. Lee, J. Yeo, K. Ko, R. Mittra, Y. Lee and W. Park, 'A novel design technique for control of defect frequencies of an electromagnetic bandgap (EBG) superstrate for dual-band directivity enhancement', Microwave and Optical Technology Letters, vol. 42, no. 1, pp. 25-31, 2004.

[16] A. Erentok, P. Luljak and R. Ziolkowski, 'Characterization of a volumetric metamaterial realization of an artificial magnetic conductor for antenna applications', IEEE Transactions on Antennas and Propagation, vol. 53, no. 1, pp. 160-172, 2005.

[17] S. Burokur, M. Latrach and S. Toutain, 'Theoretical Investigation of a Circular Patch Antenna in the Presence of a Left-Handed Medium', Antennas and Wireless Propagation Letters, vol. 4, no. 1, pp. 183-186, 2005.

[18] Li, B., Wu, B. and Liang, C.H., 2006. Study on high gain circular waveguide array antenna with metamaterial structure. Progress In Electromagnetics Research, 60, pp.207-219.

[19] Burghignoli, P., Lovat, G., Capolino, F., Jackson, D. R., & Wilton, D. R. (2008). Directive leaky-wave radiation from a dipole source in a wire-medium slab. Antennas and Propagation, IEEE Transactions on, 56(5), 1329-1339

[20] M. El-Nawawy, A. A. Allam and A. Korzec, 'The Design of a 0.35THz Microstrip Patch Antenna on LTCC Substrate', EEE, vol. 1, no. 1, pp. 1-4, 2011.

[21] J. Turpin, J. Bossard, K. Morgan, D. Werner and P. Werner, 'Reconfigurable and Tunable Metamaterials: A Review of the Theory and Applications', International Journal of Antennas and Propagation, vol. 2014, pp. 1-18, 2014.

[22] I. Vendik, O. Vendik, M. Odit, D. Kholodnyak, S. Zubko, M. Sitnikova, P. Turalchuk, K. Zemlyakov, I. Munina, D. Kozlov, V. Turgaliev, A. Ustinov, Yeonsang Park, Jinyun Kihm and Chang-Won Lee, 'Tunable Metamaterials for Controlling THz Radiation', IEEE Transactions on Terahertz Science and Technology, vol. 2, no. 5, pp. 540-549, 2012.

[23] Ziolkowski, R.W., 2006. Metamaterial-based antennas: Research and developments. IEICE transactions on electronics, 89(9), pp.1267-1275.

[24] S. Enoch, G. Tayeb , P. Sabouroux, N. Guérin, and P. Vincent, “A Metamaterial for Directive Emission,” Physical Review Letters 89, 213902 (2002).

[25] H. Xu, Z. Zhao, Y. Lv, C. Du and X. Luo, “Metamaterial Superstrate and Electromagnetic Band-Gap Substrate for High Directive Antenna, ” Int J Infrared Milli Waves, (2008) 29:493–498.

[26] J. Ju, D. kim, W. J. Lee, and J. I. Choi “Wideband High-Gain Antenna Using Metamaterial Superstrate with the Zero Refractive Index,” Microwave and Optical Tech. Lett., vol. 51, no. 8, 1973–1976, 2009.

[27] B. Temelkuaran, M. Bayindir, E. Ozbay, R. Biswas, M. Sigalas, G. Tuttle, and K. M. Ho, “Photonic Crystal-Based Resonant Antenna with a Very High Directivity,” Journal of Applied Physics 87, 603–605(2000).

[28] A. Alù, F. Bilotti, N. Engheta and L. Vegni “Metamaterial Covers Over a Small Aperture,” IEEE Trans. Antennas Propag., vol. AP-54, no. 6, pp. 1632–1643, June. 2006.

[29] M. Tang, S. Xiao, D. Wang, J. Xiong, K. Chen, B. Wang, “Negative Index of Reflection in Planar Metamaterial Composed of Single Split-Ring Resonators,” Applied Computational Electromagnetics Society (ACES) Journal, vol. 26, no. 3, pp. 250–258, March 2011.

[30] J. Woodley, M. Wheeler and M. Mojahedi, 'Left-handed and right-handed metamaterials composed of split ring resonators and strip wires', Physical Review E, vol. 71, no. 6, 2005.

[31] Kamtongdee, C., & Wongkasem, N. (2009, May). A novel design of compact 2.4 GHz microstrip antennas. In Electrical Engineering/Electronics, Computer, Telecommunications and Information Technology, 2009. ECTI-CON 2009. 6th International Conference on (Vol. 2, pp. 766-769). IEEE.

[32] Bancroft, Randy. Microstrip and printed antenna design. The Institution of Engineering and Technology, 2009.

[33] H. Pues and A. V Capelle, “Accurate transmission-line model for the rectangular microstrip antenna, “Proc. IEEE, vol. 131, no.6, pp. 334-340, December 1984.

[34] X. Chen, T. Grzegorczyk, B. Wu, J. Pacheco and J. Kong, 'Robust method to retrieve the constitutive effective parameters of metamaterials', Physical Review E, vol. 70, no. 1, 2004.

[35] Arslanagić, S., Troels Vejle Hansen, N. Asger Mortensen, Anders Heidemann Gregersen, Ole Sigmund, Richard W. Ziolkowski, and Olav Breinbjerg. "A review of the

scattering-parameter extraction method with clarification of ambiguity issues in relation to metamaterial homogenization." IEEE Antennas and Propagation Magazine 55, no. 2 (2013): 91-106.

[36] Nicolson, A. M., & Ross, G. F. Measurement of the intrinsic properties of materials by time-domain techniques. Instrumentation and Measurement, IEEE Transactions on, 19(4), 377-382, 1970.

[37] Boughriet, A-H., Christian Legrand, and Alain Chapoton. "Noniterative stable transmission/reflection method for low-loss material complex permittivity determination." IEEE Transactions on Microwave Theory and Techniques 45, no. 1 (1997): 52-57.

[38] Campione, Salvatore, Sergiy Steshenko, Matteo Albani, and Filippo Capolino. "Complex modes and effective refractive index in 3D periodic arrays of plasmonic nanospheres." Optics express 19, no. 27 (2011): 26027-26043.

[39] Hu, Jun, Chun-sheng Yan, and Qing-chun Lin. "A new patch antenna with metamaterial cover." Journal of Zhejiang University-SCIENCE A 7, no. 1 (2006): 89-94.

[40] Y. Kurzweil-Segev, M. Brodsky, A. Polsman, E. Safrai, Y. Feldman, S. Einav and P. Ben Ishai, 'Remote Monitoring of Phasic Heart Rate Changes From the Palm', IEEE Transactions on Terahertz Science and Technology, vol. 4, no. 5, pp. 618-623, 2014.

Sun, M., Z. N. Chen, H. Tanoto, Q. Y. Wu, J. H. Teng, and S. B. Yeap. "Design of continuous-wave photomixer driven terahertz dipole lens antennas." In APSIPA Annual Summit and Conference, pp. 14-17. 2010.

Chapter 5 High Gain Slotted Waveguide Antenna Based on Beam Focusing using Electrically Split Ring Resonator Metasurface Employing negative Refractive Index Medium

This chapter is reproduced from the author's published work reported in [1]. The author of this thesis was the first author and the second author was acting purely in a supervision capacity. In this chapter, a new high performance slotted waveguide antenna incorporated with negative refractive index metamaterial structure is proposed, designed and experimentally demonstrated. The metamaterial structure is constructed from multilayer two directional structure of electrically split ring resonator which exhibits negative refractive index in direction of the radiated wave propagation when it is placed in front of the slotted waveguide antenna. As a result, the radiation beams of the slotted waveguide antenna are focused in both *E* and *H* planes, and hence the directivity and the gain are improved, while the beam area is reduced. The proposed antenna was designed, optimized and numerically simulated by using the CST software. The effective parameters of the eSRR structure were extracted using the Nicolson Ross Weir (NRW) algorithm from the s-parameters. For experimental verification, a proposed antenna operating at 10 GHz was fabricated using both a wet etching microwave integrated circuit technique (for the metamaterial structure) and a milling technique (for the slotted waveguide antenna). The measurements were carried out an anechoic chamber. The measured results showed that, the *E*-plane gain of the proposed slotted waveguide antenna was improved from 6.5 dB to 11 dB as compared to the conventional slotted waveguide antenna. Also, the E plane beam width was reduced from 94.1 degrees to about 50 degrees. The antenna return loss and the bandwidth were slightly changed. Furthermore, the proposed antenna offered easier fabrication processes with a high gain compared with the horn antenna, particularly if the proposed antenna was scaled down in dimensionality to work in the THz regime.

5.1. Introduction

During the last two decades, Metamaterials (MTMs) have received great attention due to their fascinating electromagnetic (EM) properties. MTMs are artificial atoms which exhibit exotic EM properties that cannot be achieved by natural materials. MTMs can provide negative, zero or positive electric permittivity and magnetic permeability by inserting inclusion with specific geometrical shape and dimensionality in a host medium, both the inclusions and the host medium are constructed from metals and dielectrics [2]. There are two main categories for the MTMs which are resonance and non-resonance and each group has its own advantages and disadvantages and can be used to develop practical applications, here resonance MTM was used [3]. Recently, MTM with simultaneously negative permittivity, permeability and negative index of refraction are used to design perfect lenses [4, 5] for high resolution imaging system and to design many antennas [6, 7]. Also, MTMs are proposed to design gradient index of refraction lenses [8], absorbing, cloaking [9, 10], and polarization transformers [11]. By using MTMs with negative or gradient index of refraction, compact size high directive antennas can be designed [12, 13]. It is well known that, high directive antennas play an important role for many practical applications. Many conventional efforts have been done to improve the antenna directivity such as parasitic patches, array of patch antennas, parabolic reflectors [14-16]. Unfortunately, the aforementioned approaches suffer from the large sizes, design methodology, complex feeding network and fabrication processes, particularly when optimizing at high frequencies. As John Pendry investigated the first negative refractive index perfect lens (i.e. double negative MTMs with simultaneously negative permittivity, permeability and negative index of refraction) in 2000 [17], it is possible to design a compact size and high directive antennas [18, 19]. Furthermore, metamaterial structures composed of 3-D metal grid superstrate have been used to improve the directivity of the antenna [20, 21]. It should be noted that, the aperture size of the metamaterial superstrate is much larger compared with the size of the patch which makes the antenna bulky. Also, zero index medium metamaterial superstrate are used to develop a high gain and wideband antenna [22]. It is clear from the structure of the antenna that, the metamaterial superstrate uses via to resemble shunt inductance, which makes it difficult to fabricate. The photonic crystal-based resonant antenna presented in [23] is a high directive antenna, but it is so bulky and has a narrow bandwidth. Nader Engheta et al. proved numerically and theoretically that a PEC screen with a small hole covered by two subwavelength metamaterial structures can be used to improve the directivity of the antenna [24]. Planar metamaterial with NRI has been developed using split ring resonators (SRR) in [25].

This work focuses on two interesting contributions. Firstly, 2D single sided metasurface structure based on electrically split ring resonator (eSRR) [26] was designed by choosing the proper dimensionality and orientation such that it exhibits NRI property in the direction of the wave propagation and hence it can be used to improve the directivity of the EM emission. This 2D metasurface structure has the advantage of being easier to fabricate and assemble over the volumetric MTMs (mentioned in Refs. [20-22]), so it can be scaled down to be fabricated for THz antennas for high resolution imaging and biomedical application (e.g. heart beat measurements). Secondly, a slotted waveguide antenna [27] was used as an EM radiator instead of a horn antenna or a patch antenna because it is difficult to design a horn antenna with flared surfaces in the THz regime. Furthermore, there are no SMA connectors for the patch antenna operating in the THz regime. Fortunately, for waveguide, there are waveguide connectors up to 900 GHz [28, 29]. Thus the only solution to design a THz antenna is to use waveguide fed or photo conductive antennas. Here, we use the waveguide to feed the slotted antenna. Due to the low gain of the single element slotted antenna (the typical gain is 6.5 dB), a NRI medium is used as a superstrate to improve the transverse electromagnetic (TEM) wave radiated from the slotted waveguide antenna and hence the E and H plane gains and directivities are improved. For experimental verification the slotted waveguide antenna incorporated with eSRR NRI medium operating at 10 GHz was designed, numerically optimized using CST software, fabricated and measured.

This chapter is organized as follow: Section 5.2 provides the design and simulation of 10 GHz conventional slotted antenna. Section 5.3 discusses the design and effective parameter extraction of the NRI medium based on the eSRR. Section 5.4 presents the design and numerical simulation of the 10 GHz slotted waveguide antenna incorporated with NRI medium. In section 5.5, experimental verifications for the proposed antenna are carried out. Finally the conclusion and the future recommendations are given in section 5.6.

5.2. Design and Simulation of 10 GHz slotted waveguide Antenna

According to Babinet's principle, in order to form aperture radiator, a slot of length L_s and width W_s can be cut in the side wall, top wall or even in the back wall of a waveguide [30]. Here, a conventional 10 GHz slotted waveguide antenna is designed and simulated using Finite Element based Electromagnetic CST simulator. Figure 5.1 illustrates the structure of the antenna; the antenna is constructed from WR-90 waveguide of standard dimensions a and b of 22.86 mm and 10.16 mm, respectively, the slot is cut in the back wall of the waveguide. The slot dimensions are designed properly such that the antenna operates at 10 GHz and have a good impedance matching with the free space; the slot length is about free space half wavelength. Three different slotted antennas of back wall slots of dimensions (L_s, W_s) of (14.5, 2), (14.7, 4), and (15.2, 6) are designed, all dimensions are in mm. The waveguide has length L_{wg} of 30 mm which equals one free space wavelength at the operating frequency of

10 GHz and thickness 3 mm to match the requirements of the fabrication, mechanical, and assembly processes. The antenna was simulated in CST software; the return loss S_{11} and the gain are extracted as shown in Fig. 5.2. It is clear from Fig. 5.2 that, when the slot width W_s increases, and the slot length L_s is changed slightly around the half the free space wavelength of 15 mm at 10 GHz to keep the operating frequency at 10 GHz the gain slightly decreases, while the bandwidth increases. Furthermore, the results illustrate that, for slotted waveguide antennas of slot widths W_s of 2, 4, and 6 mm and slot lengths L_s of 14.5, 14.7 and 15.2 mm, the bandwidths are 0.72, 1.5 and 2.88 GHz, respectively and the gain is about 6.5 dB mostly for all the three slot dimensions.

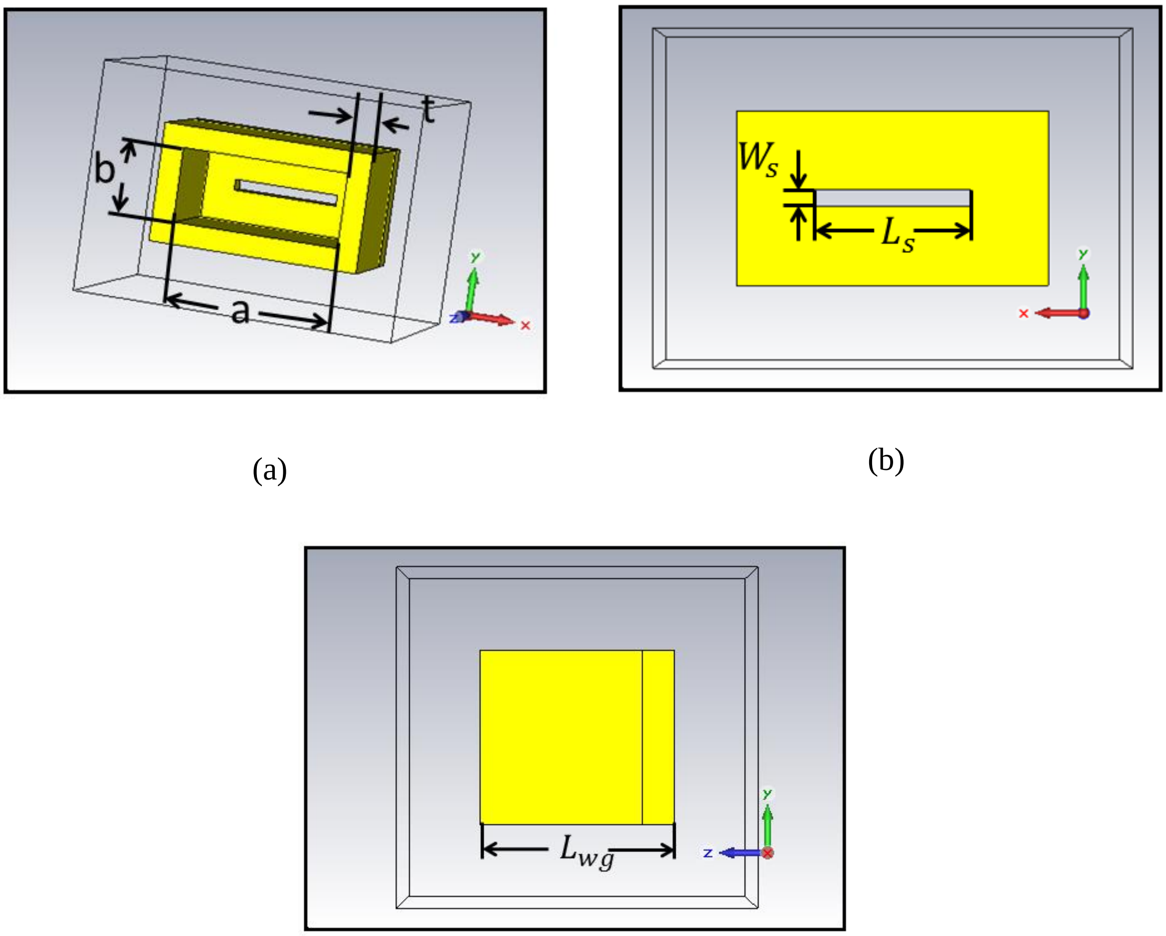

(a)

(b)

(c)

Fig. 5.1. Conventional waveguide slotted antenna, (a) 3-D view, (b) back view and (c) side view

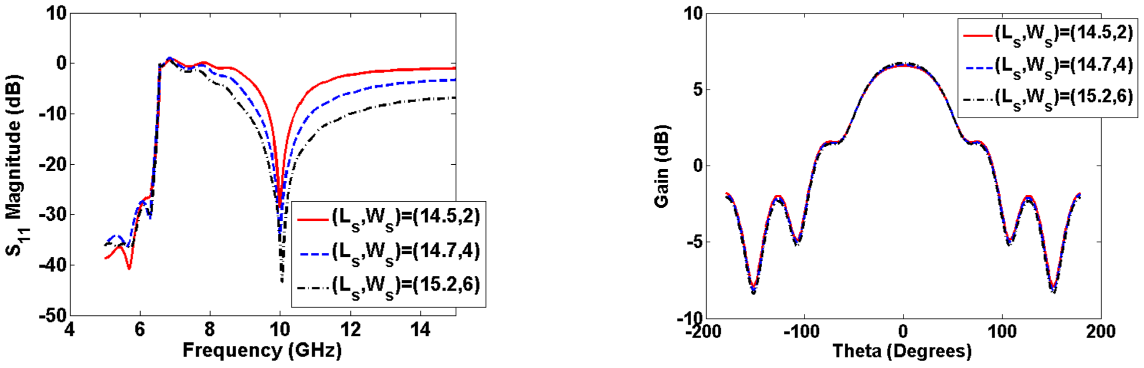

(a) (b)

Fig. 5.2. Conventional 10 GHz slotted waveguide antenna performance at different slot dimensions of length L_s and width W_s, all dimensions are in mm, (a) return loss S_{11} in dB and (b) E-plane Gain in dB.

5.3. Design and Simulation of 10 GHz Negative Refractive Index layer Based on ESRR

Here, a unit cell of Electrically Split Ring Resonator (eSRR) metasurface structure is designed and simulated in CST. The eSRR unit cell is optimized and repeated in two dimensions which may provide electric and magnetic plasmonic resonances around 10 GHz and hence exhibits simultaneous negative permittivity, permeability and index of refraction. The eSRR metasurface is a copper layer with thickness t of 35 μm mounted on the top side of a RT/Duriod 5880 dielectric substrate with relative dielectric permittivity εr of 2.2 and height *h* = 1.57 mm. The eSRR is shown in Fig. 5.3 with physical dimensions; *a, L, d, g* and *w* of 5.5, 5.3, 2.8, 0.3 and 0.62, respectively. All dimensions are in mm. Then, the eSRR unit cell is simulated in CST software using Floquet's boundaries conditions of unit cells in the *x* and *y* directions. The structure is excited by a TEM plane wave propagating in the z-direction, with incident electric field polarized in the *x* direction and incident magnetic field polarized in the *y* direction as shown in Fig. 5.3 (b). The scattering parameters of the metasurface structure are calculated, extracted and plotted as shown in Fig. 5.4 (a). Figure 5.4 (a) shows that the eSRR metasurface infinite periodicity unit cell has a band pass response with center frequency around 10 GHz.

Then the effective parameters of the metasurface unit cell with infinite periodicity have been extracted from the S-parameters using the Nicolson-Ross-Weir (NRW) approach [31-35] and the results are plotted as shown in Figs. 4 (b), (c) and (d), respectively for two different branch ambiguity factors *p* of 0 and 1. According to the theory developed in [32], the correct branch ambiguity factor for this MTM structure is *p*=0 since it is a thin MTM slab. The NRW algorithm is described by equations 4.10 to 4.16 and in Appendix A.

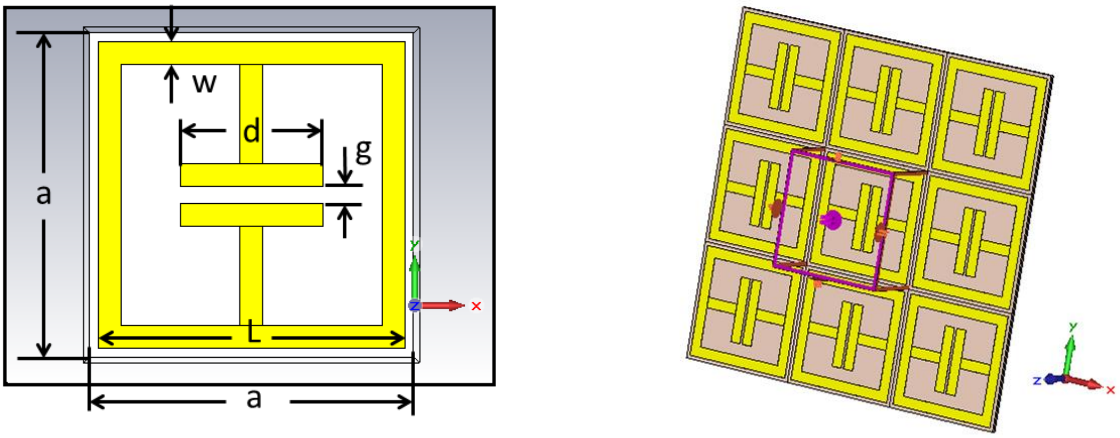

(a)

(b)

Fig. 5.3. The eSRR metasurface structure, (a) 3-D view with unit cell boundary conditions in x-y plane and the excitation in z direction, and (b) front view of MTM unit cell with unit cells infinite periodicities in x and y directions.

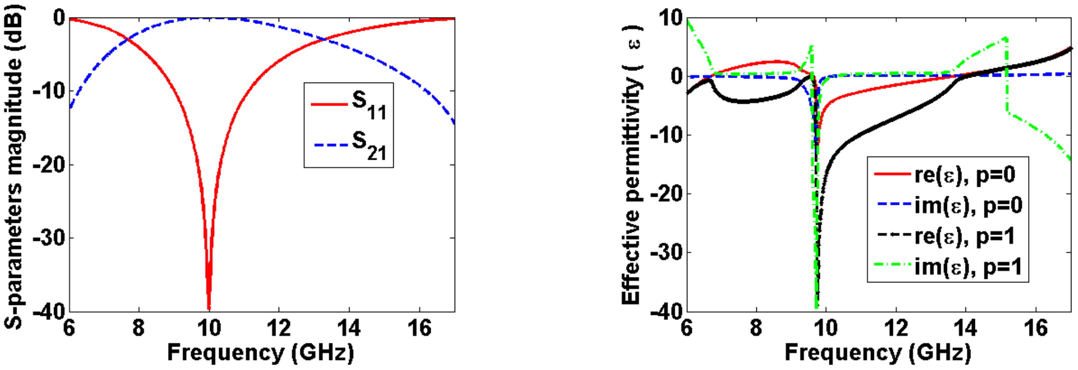

(a)

(b)

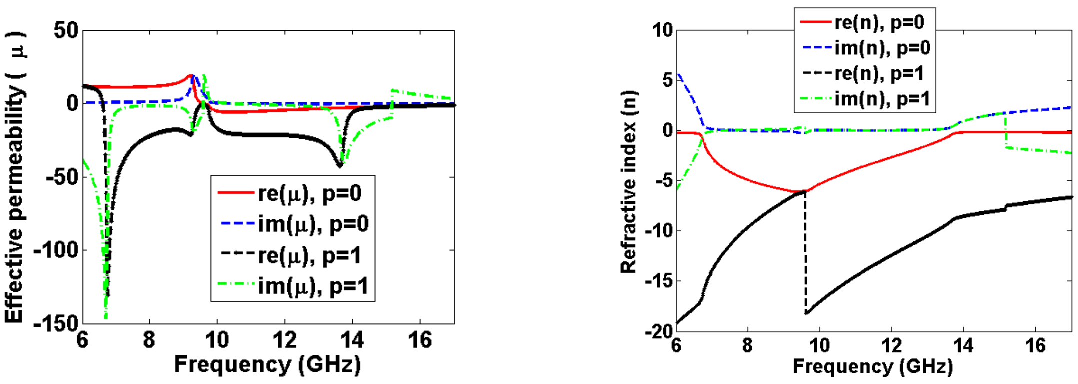

(c) (d)

Fig. 5.4. The eSRRs infinite 2-D periodicity metasurface structure with negative effective parameters around 10 GHz, extracted at two different unambiguity branch parameter p of 0 and 1 [32] (a) S-parameters magnitude, (b) Effective permittivity (ε), Effective permeability (μ) and refractive index (n). The real part of effective parameters at p=1 are plotted with dotted lines.

Figure 5.4 (b), (c) and (d) show that, the real parts of the effective permittivity ε', the effective permeability μ' and effective refractive index n', respectively are negative around the resonance frequency of 10 GHz at p=0. In [32], the authors proved that, the MTM effective parameters extraction based on the S-parameters method has no ambiguity related to the sign of the wavenumber $k_s$and the intrinsic impedance η_s of the metamaterials layer, while it has ambiguities related to the branch of the complex logarithm.

The impact of the infinite periodicity truncation of the metasurface structure on the effective parameters is studied by designing an eSRR metasurface structure of size 3×6×2 with negative effective parameters around 10 GHz. After truncation, the dimensions of the eSRR unit cell is optimized such that the structure still has a negative effective parameters around 10 GHz. The dimensions of the truncated periodicity eSRR metasurface are; a=3.75 mm, *L*=3.525 mm, *d*=1.75 mm, *g*=0.3 mm and *w*=0.496 mm. The truncated periodicity eSRR metasurface structure was designed and simulated in CST; the S- parameters were extracted and plotted as shown in Fig. 5.5 (a). The S-parameters shows that, the structure still has a band pass response at 10 GHz. Then the effective parameters are extracted and plotted as shown in Figs. 5 (b) to (d) from the S-parameters using the NRW algorithm at different non ambiguity branches of p=0 and =1. It is clear from Fig. 5.5 that, at p=0 which is the correct branch according to the theory developed in [32], the structure still has simultaneous negative real effective parameters around 10 GHz. This means that the eSRR structure of size 3×6×2 exhibits NRI, so it can focus the radiated EM waves from the slotted waveguide antenna.

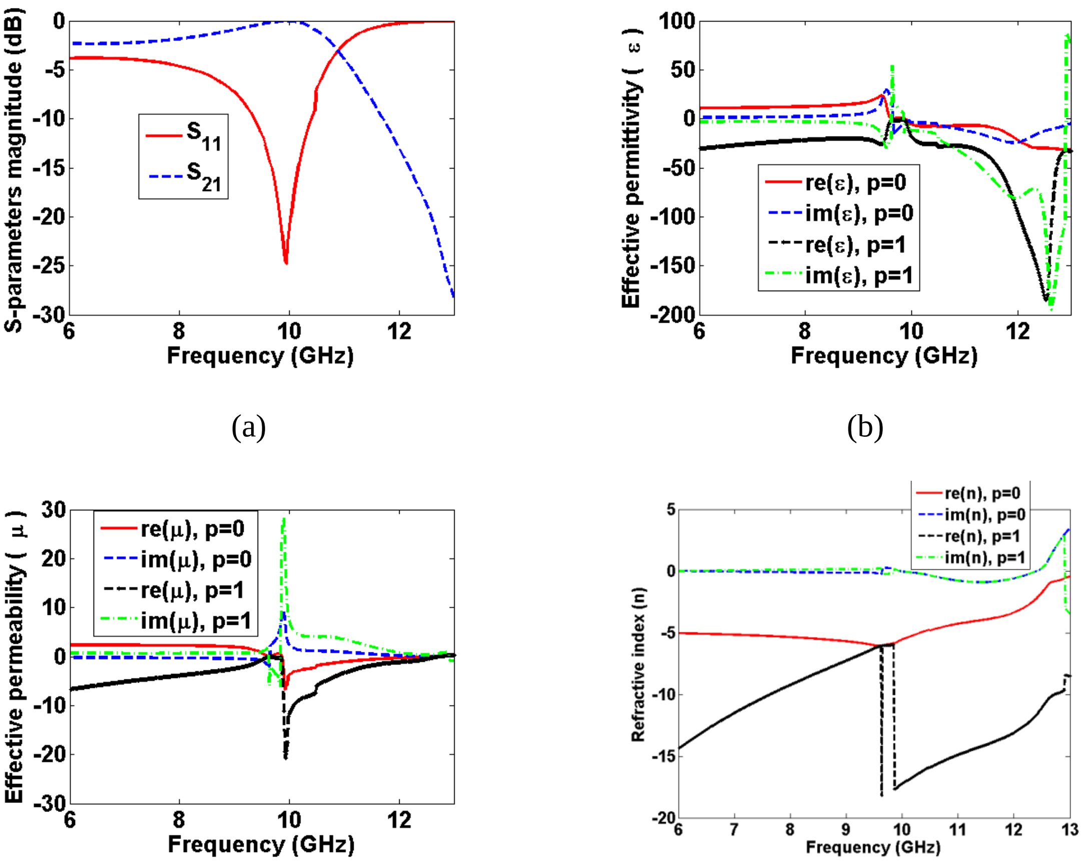

(a) (b)

(c) (d)

Fig. 5.5. The eSRR metasurface structure with truncated periodicity with finite sizes of 3×6×2 with negative effective parameters around 10 GHz, extracted at two different unambiguity branch parameter p of 0 and 1 [32] (a) Magnitude of the scattering parameters, (b) Effective permittivity (ε), Effective permeability (μ) and refractive index (n).

5.4. Design and Simulation of 10 GHz slotted waveguide antenna incorporated with MTM lens

Here, the proposed slotted waveguide antenna incorporated with eSRR Metasurface employing MTM lens is analyzed, simulated and optimized using CST software. The proposed antenna is operating at 10 GHz and the metasurface structure is optimized to have a negative permeability, negative permittivity and negative refractive index in a wideband around 10 GHz. Among high microwave frequencies X-band (8–12 GHz) makes a significant contribution to various applied and emerging wireless services [36–39]. X-band is mostly devoted to point to point wireless applications like on-road traffic control [36], air traffic control [37], imaging radar [36–38] and satellite communications [39] where low profile and highly directive antennas are appropriated as a reliable and economical solution for the transmission systems.

The antenna is optimized by changing the size of the metasurface and the separation between the metasurface and the slotted waveguide antenna. Figures 5.7 (a) and 5.7 (b) show the return loss and the radiation gain at 10 GHz of the proposed antenna at 18.5 mm separation distance h_s between the slot and the metasurface bottom side and with different slot sizes (L_s, W_s) of (14.5,2), (14.7,4),and (15.2, 6). The size of metasurface is 6×6×2 in x, y and z direction, respectively However, the proposed antennas are compared with a conventional antenna of a slot size (L_s, W_s) of (15.2, 6), all dimensional are given in mm.

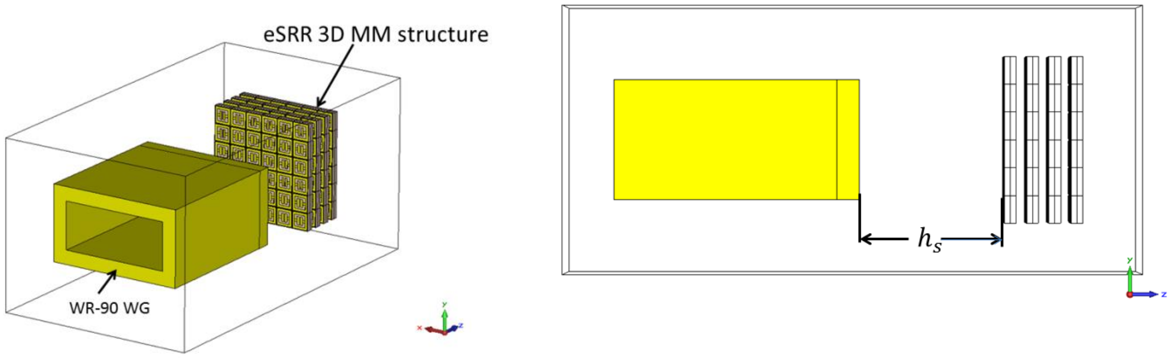

(a) (b)

Fig. 5.6. 10 GHz slotted waveguide antenna incorporated with eSRR NRI metasurface structure (a) 3D view, and (b) side view.

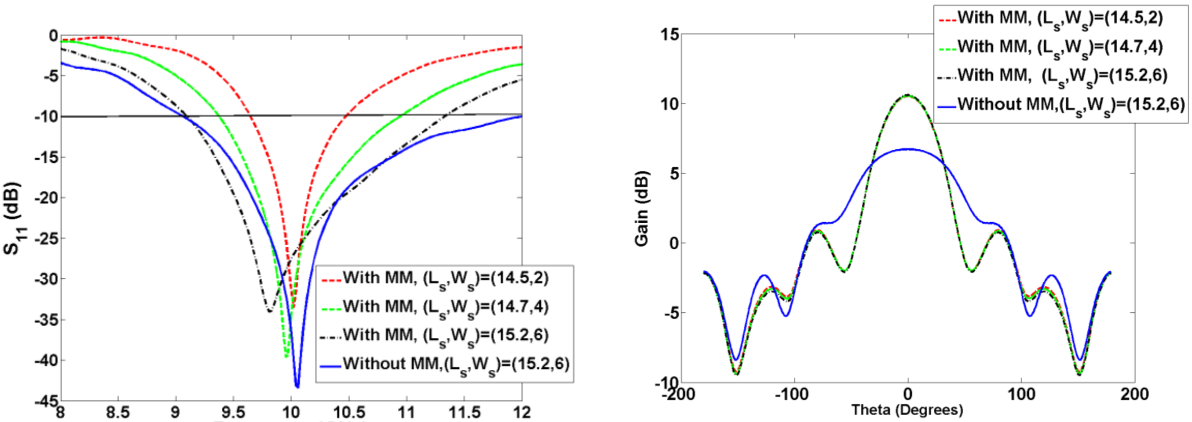

(a)

(b)

Fig. 5.7. The simulated return loss (a) and the simulated E plane gain at 10 GHz of the proposed slotted waveguide antenna with and without eSRR metasurface with different slot sizes (L_S, W_S) of (14.5,2), (14.7,4),and (15.2,6) and at 18.5 mm separation distance between the slot and the metasurface, the NRI metasurface is 3-D eSRR of 6×6×2 size in x, y and z direction, respectively.

It is clear from Fig. 5.7 (a) that, the radiated slot size plays an important role in widening the bandwidth of the proposed antenna. For example, the bandwidth of the proposed antenna increases from 0.854 GHz to 1.567 GHz and 2.22 GHz as the radiated slot size (L_S, W_S) is changed from (14.5,2) to (14.7,4), and (15.2,6), respectively. Furthermore, as it is shown in Fig. 5.7 (b), the gain of the proposed slotted waveguide antenna incorporated with NRI metasurface has been increased from 6.5 dB to 10.6 dB, i.e., the *E* plane gain is improved by 4.1 dB, while the beam width reduces from 94.1 degrees to about 50 degrees, mostly for all the different three slots compared with their conventional slotted waveguide antenna counterparts, mostly for all slot sizes. However, the bandwidth of the proposed antenna is decreased from 2.88 GHz to 2.22 GHz compared with the conventional slotted waveguide antenna for a slot dimensions (L_S, W_S) of (15.2, 6).

In addition, the effect of the MM structure (eSRR metasurface) size on the impedance matching, bandwidth, beam width and the gain of the proposed antenna was studied as shown in Fig. 5.8 which shows the return loss and the gain of the proposed slotted waveguide antenna with and without eSRR metasurface layers. By using CST, the MM was designed with different sizes of 3×6×2, 3×6×4 and 6×6×2 sizes in the *x*, *y* and *z* directions and then the separation distance h_s between the slot and the MM was changed slightly around half the free space wavelength of 15 mm at 10 GHz until the optimum impedance matching and gain were obtained. The radiated slot is of dimensions (L_s, W_s) of (14.5 mm, 2 mm) and for each MM structure size the crossponding separation h_s between the slot and the MM structure was 21.5 mm, 22.5 mm and 18.5 mm for the MM structure of sizes of 3×6×2, 3×6×4 and 6×6×2, respectively.

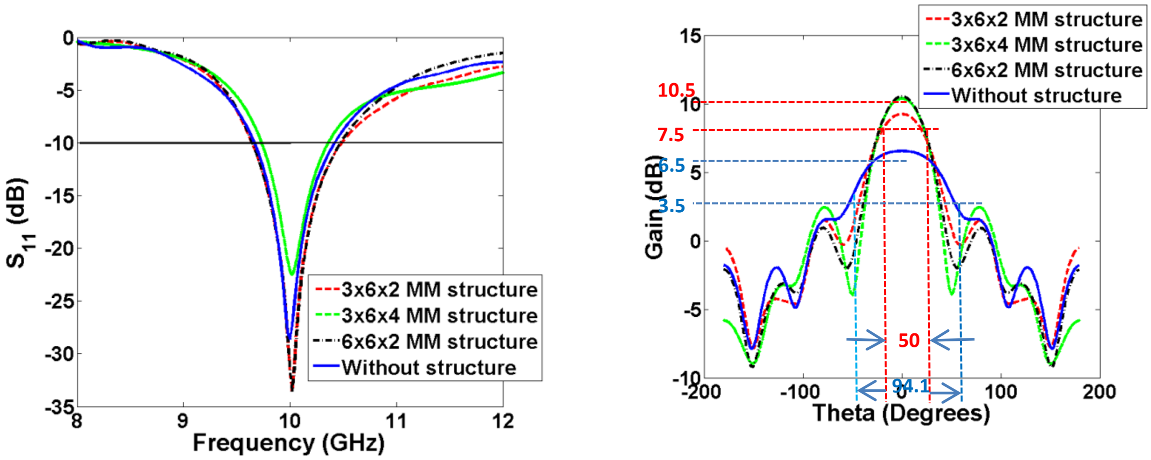

(a)

(b)

Fig. 5.8. The simulated return loss (a) and the simulated E plane gain at 10 GHz of the proposed slotted waveguide antenna with and without MM of slot sizes (W_s, L_s) of (2mm, 14.5 mm) and at 18.5 mm separation distance between the slot and the MM, the MM is 3-D eSRR metasurface of different sizes of 3×6×2, 3×6×4 and 6×6×2 sizes in the x, y and z directions.

Figure 5.8 (a) shows that, the size of the MM structure and the separation distance between the slot and the MM structure play important roles in optimizing the impedance matching of the antenna. For example, the return loss was improved from -30 dB to about -34 dB when the size of the MM was 6×6×2 and the separation distance h_s was 18.5 mm, while it becomes worst when the size of the MM size was 3×6×4. However, as shown in Fig. 5.8 (b), the E plane gain improved from 6.5 dB to 10.5 dB when the slotted waveguide antenna was incorporated with a MM structure of size 6×6×2. It is clear that, as the transverse size of the MM increases with the same number of unit cells in both the *x* and *y* directions while keeping the longitudinal size the same both the return loss and the gain are improved.

5.5. Fabrication and Measurement

For experimental verification, the proposed antenna resonating at 10 GHz as well as the eSRR metasurface structure have been fabricated as shown in Fig. 5.9. The eSRR metasurface structure was fabricated using a wet etching technique on a RT/Duroid 5880 substrate with a relative permittivity of $\varepsilon r = 2.2$ and a thickness of $h = 1.57$ mm. The slotted waveguide antenna was fabricated using milling technology with the same dimensions mentioned in the previous section. Furthermore, the effect of the MM structure size on the antenna performance was studied using eSRR metasurface of sizes 6×6×4 and 7×7×4, placed in front of the slotted waveguide antenna at a separation distance of 18 mm. The separation distance was 5 mm from the center to the center of each two adjacent eSRR layers. The slot dimensions (W_s, L_s) was (6mm, 15.2mm). The return loss, S_{11} for the simulated and the fabricated antenna with and without the eSRR metasurface/MM is shown in Fig. 5.10. The measured and the simulated return loss the proposed antenna without the eSRR metasurface agreed and the bandwidth was about 2.88 GHz. It is important to notice that, there is a shift in the center frequency and some losses for the measured proposed antenna with a MM over the simulated one due to the SMA connector, the nylon screws, and the misalignment of the eSRR stacked layers constructing the MM structure. Furthermore, the bandwidth of the proposed antenna with eSRR MM of size 7×7×4 is more than that of size 6×6×4. This means that as the size of the MM structure increases, the bandwidth of the antenna increases, due to decreasing of the quality factor as a result of the added conductor and dielectric losses. The bandwidth of the 10 GHz slotted wave guide antenna incorporated with an MTM is increased from 22.8 % to 28.8%. This increase in the bandwidth is useful for applications such as airport surveillance radar antennas which can send and receive with different frequencies in different directions [37]. It is clear from Fig. 5.10 that, there is about 1 GHz bandwidth deviation between the simulated and the measured results for the antenna incorporated with a 6×6×4 MTM structure due to the misalignment of the MTM layers with respect to the slotted antenna.

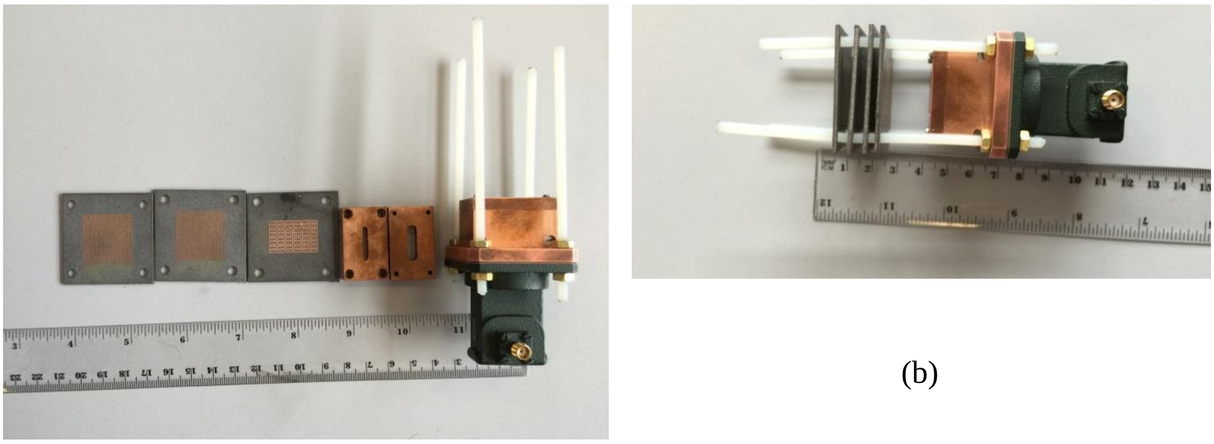

(a)

(b)

Fig. 5.9. The fabricated antenna, (a) conventional slotted waveguide antenna on the right, other two slots in the center and eSRR metasurface of sizes 6×4×1, 6×6×1 and 7×7×1 from right to left, and (b) slotted waveguide antenna incorporated with eSRR 3D structure of size 6×6×4 located at a distance h_s of 18 mm from the slot and the separation distance is 5 mm from the centre to the centre of each two adjacent eSRR layers.

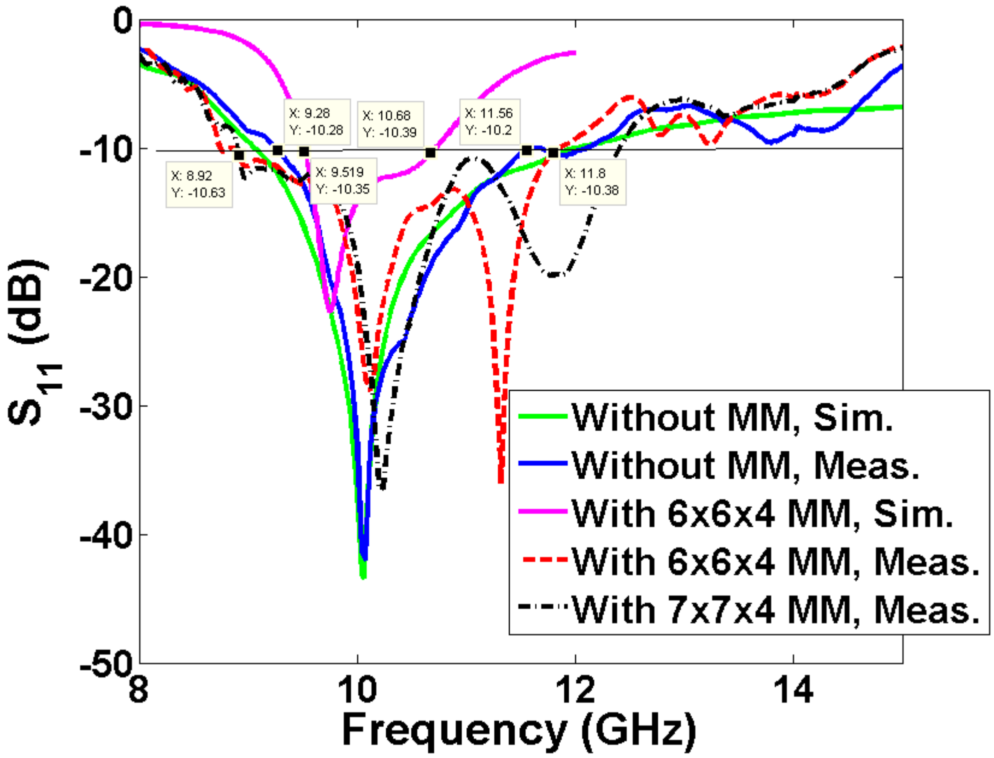

Fig. 5.10. Simulated and measured s-parameter magnitudes of the slotted waveguide antenna with and without eSRR MM of sizes 6×6×4 and 7×7×4, located at a distance h_s of 18 mm from the slot and the separation distance is 5 mm from the centre to the centre of each two adjacent eSRR layers.

The simulated and the measured gain versus frequency of the proposed antenna with and without MM are then plotted as shown in Fig. 5.11. The results show that, as the size of the MM structure increases, the radiated wave becomes more focused due to the NRI property and hence the antenna directivity increases. Although the MM structure adds more loss to the antenna which degrades the radiation efficiency, the overall gain of the antenna increase due to the significant increase in the antenna directivity over its efficiency. The antenna gain increase from about 6 dB to 11 dB at 10 GHz. There is a deviation between the measured and the simulated results due to the losses presented by the connectors, the nylon spacers, metal nuts and miss alignment of the eSRR layers.

It is clear that, although the MTM has a good transmission around 10 GHz and the allotted waveguide antenna has a good impedance matching at 10 GHz, the slotted waveguide antenna peak gain does not occur at 10 GHz as shown in Fig. 5.11. The main reason behind shifting the gain peak away from 10 GHz for the measured proposed antenna was because the reference antenna used in measuring the S_{21} from which we can calculate the gain is linearly polarized and at the same time the MTM layers placed in front of the slotted antenna can slightly change the polarization of the antenna due to the misalignments between the different layers of the MTM and/or between the MTM layers and the slotted antenna. The mismatching between the polarization of the measured antenna and the reference antenna may cause a shift in the transmission peak between the two antennas as shown in Fig. 5.11. As a future work, this problem can be solved by using a more precise alignment tools in the construction of the prototyped antenna.

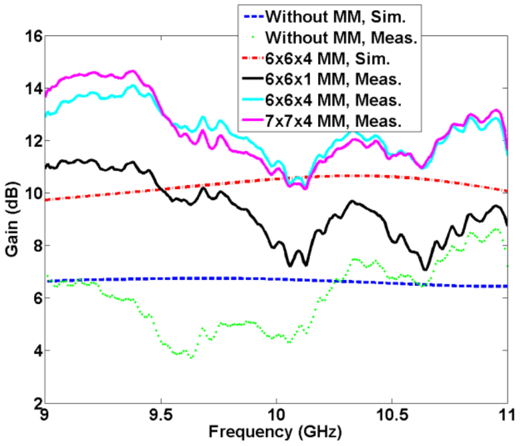

Fig. 5.11. Comparison between the measured and the simulated gains of the proposed antenna with and without eSRR MM of sizes 6×6×4 and 7×7×4, located at a distance $h_s$of 18 mm from the slot and the separation distance is 5 mm from the centre to the centre of each two adjacent eSRR layers.

Furthermore, E and H planes radiation patterns at 10 GHz of the simulated and the measured proposed antenna with and without MM structure are plotted as shown in Fig. 5.12 for different MM structure sizes and at a separation distance of 18 mm between the MM structure and the slot edge. It is clear that, as the MM structure size is increased from 6×6×1 to 7×7×4, the radiation pattern becomes more focused and the beam width reduces in both E and H planes. However, there is a nice agreement between the measured and the simulated results.

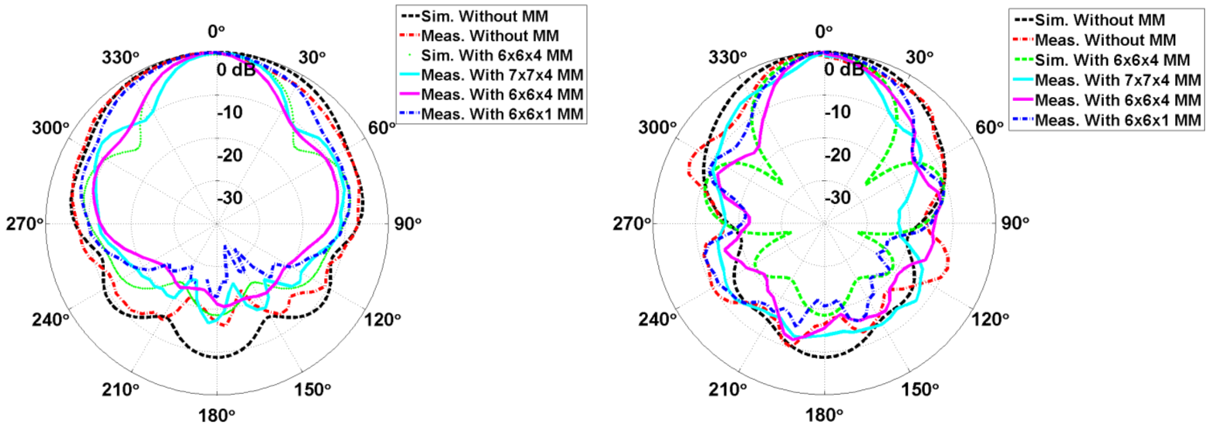

(a) (b)

Fig. 5.12. Measured and simulated radiation pattern at 10 GHz of the proposed with and without eSRR MM of sizes 6×6×1, 6×6×4 and 7×7×4, located at a distance $h_s$of 18 mm from the slot and the separation distance is 5 mm from the centre to the centre of each two adjacent eSRR layers, (a) E-plane and (b) H-plane.

5.6. Summary

In this chapter, a new slotted waveguide antenna incorporated with eSRR MM structure employing a NRI medium is proposed, designed, simulated in CST, fabricated and measured. The major advantage of the proposed slotted waveguide antenna over the high gain conventional horn antennas is that it is uses planner metasurface structure with NRI property for beam focusing purposes of the radiated EM waves and hence antenna gain can be improved. The proposed MTM structure in this chapter can be designed at THz frequencies by using different materials.

The proposed antenna was constructed from back side slotted waveguide antenna incorporated with 2-D eSRR metasurface structure arranged as sacked layers with 5 mm separation distance between each two layers, then the 3D MM structure was placed in front of the slotted antenna with a separation distance about half the free space wavelength. The proposed antenna was designed and optimized in CST, the impact of the MM size and the separation distance between the MM structure and the slotted antenna on the antenna performance was studied. The slotted waveguide antenna was fabricated using milling technology and the MM structure fabricated using the wet etching technology. The return loss, the gain and radiation pattern in both *E* and *H* planes were measured. The simulated and the measured results are compared. The result showed a good agreement between the simulation and the measurement. The antenna gain was improved from 6.5 dB to 11 dB; the beam reduced from 94.1 degrees to about 50 degrees in the E plane, while the bandwidth and the return loss were slightly changed.

As a future work, the idea of gain improvement of the slotted waveguide incorporated with the eSRR metasurface structure can be extended to THz frequency range to be used for short distance wireless communication links, particularly in the biomedical application and inside the satellite to reduce the wiring complexity of the satellite system. Also, eSRR metasurface structure can replace the bulky silicon lens used in the THz photoconductive and photo mixer optical antennas to focus the radiated beam and improve the antenna gain for medical applications [40, 41].

5.7. References

[1] Abdelrehim, A.A. and Ghafouri-Shiraz, H.,"High Gain Slotted Waveguide Antenna Based on Beam Focusing Using Electrically Split Ring Resonator Metasurface Employing Negative Refractive Index Medium". Progress In Electromagnetics Research, 79, pp.115-126,2017.

[2] Kang, Ming, Nian-Hai Shen, Jing Chen, Jian Chen, Ya-Xian Fan, Jianping Ding, Hui-Tian Wang, and Peiheng Wu. "A new planar left-handed metamaterial composed of metal-dielectric-metal structure." Optics Express 16, no. 12 (2008): 8617-8622.

[3] Luk'yanchuk, Boris, Nikolay I. Zheludev, Stefan A. Maier, Naomi J. Halas, Peter Nordlander, Harald Giessen, and Chong Tow Chong. "The Fano resonance in plasmonic nanostructures and metamaterials." Nature materials 9, no. 9 (2010): 707.

[4] Pendry, John Brian. "Negative refraction makes a perfect lens." Physical review letters 85, no. 18 (2000): 3966.

[5] Zharov, Alexander A., Nina A. Zharova, Roman E. Noskov, Ilya V. Shadrivov, and Yuri S. Kivshar. "Birefringent left-handed metamaterials and perfect lenses for vectorial fields." New Journal of Physics 7, no. 1 (2005): 220.

[6] Grbic, A., & Eleftheriades, G. V. (2002). A backward-wave antenna based on negative refractive index LC networks. In Antennas and Propagation Society International Symposium, 2002. IEEE (Vol. 4, pp. 340-343). IEEE.

[7] Grbic, Anthony, and George V. Eleftheriades. "Experimental verification of backward-wave radiation from a negative refractive index metamaterial." Journal of Applied Physics 92, no. 10 (2002): 5930-5935.

[8] X. Chen, H. F. Ma, X. M. Yang, Q. Cheng, W. X. Jiang, and T. J. Cui, “X-band high directivity lens antenna realized by gradient index metamaterials,” in Proc. Asia Pac. Microw. Conf. (APMC), 2009, vol. 1–5, pp. 793–797.

[9] Y.Yuan, C. Bingham, T. Tyler, S. Palit, T. H. Hand,W. J. Padilla, N.M. Jokerst, and S. A. Cummer, “A dual-resonant terahertz metamaterial based on single-particle electric-field-coupled resonators,” Appl. Phys. Lett., vol. 93, no. 19, p. 191110, 2008.

[10] N. I. Landy, S. Sajuyigbe, J. J. Mock, D. R. Smith, andW. J. Padilla, “Perfect metamaterial absorber,” Phys. Rev. Lett., vol. 100, no. 20, p. 207402, 2008.

[11] J.Y. Chin, J.N.Gollub, J. J.Mock, R. P. Liu, C.Harrison,D.R. Smith, and T. J. Cui, “An efficient broadband metamaterial wave retarder,” Opt. Express, vol. 17, no. 9, pp. 7640–7647, 2009.

[12] X. Chen, H. F. Ma, X. M. Yang, Q. Cheng, W. X. Jiang, and T. J. Cui, “X-band high directivity lens antenna realized by gradient index metamaterials,” in Proc. Asia Pac. Microw. Conf. (APMC), 2009, vol. 1–5, pp. 793–797.

[13] Z.G. Xiao and H. L. Xu, “Low refractiveMTMs for gain enhancement of horn antenna,” J. Infrared Millimeter Terahertz Waves, vol. 30, no. 3, pp. 225–232, 2009.

[14] Vaidya, Avinash R., Rajiv Kumar Gupta, Sanjeev Kumar Mishra, and Jayanta Mukherjee. "High-gain low side lobe level Fabry Perot cavity antenna with feed patch array." Progress In Electromagnetics Research 28 (2012): 223-238.

[15] Choi, Wonkyu, Yong Heui Cho, Cheol-Sik Pyo, and Jae-Ick Choi. "A high-gain microstrip patch array antenna using a superstrate layer." ETRI journal 25, no. 5 (2003): 407-411.

[16] "Parabolic reflector antennas." U.S. Patent 3,572,071, issued March 23, 1971.

[17] J. Pendry, 'Negative Refraction Makes a Perfect Lens', Phys. Rev. Lett., vol. 85, no. 18, pp. 4166-4169, 2000.

[18] Islam, Md Moinul, Mohammad Tariqul Islam, Md Samsuzzaman, Mohammad Rashed Iqbal Faruque, Norbahiah Misran, and Mohd Fais Mansor. "A miniaturized

antenna with negative index metamaterial based on modified SRR and CLS unit cell for UWB microwave imaging applications." Materials 8, no. 2 (2015): 392-407.

[19] Alibakhshi-Kenari, M., & Naser-Moghadasi, M. (2015). Novel UWB miniaturized integrated antenna based on CRLH metamaterial transmission lines. AEU-International Journal of Electronics and Communications, 69(8), 1143-1149.

[20] S. Enoch, G. Tayeb , P. Sabouroux, N. Guérin, and P. Vincent, “A Metamaterial for Directive Emission,” Physical Review Letters 89, 213902 (2002).

[21] H. Xu, Z. Zhao, Y. Lv, C. Du and X. Luo, “Metamaterial Superstrate and Electromagnetic Band-Gap Substrate for High Directive Antenna, ” Int J Infrared Milli Waves, (2008) 29:493–498.

[22] J. Ju, D. kim, W. J. Lee, and J. I. Choi “Wideband High-Gain Antenna Using Metamaterial Superstrate with the Zero Refractive Index,” Microwave and Optical Tech. Lett., vol. 51, no. 8, 1973–1976, 2009.

[23] B. Temelkuaran, M. Bayindir, E. Ozbay, R. Biswas, M. Sigalas, G. Tuttle, and K. M. Ho, “Photonic Crystal-Based Resonant Antenna with a Very High Directivity,” Journal of Applied Physics 87, 603–605(2000).

[24] A. Alù, F. Bilotti, N. Engheta and L. Vegni “Metamaterial Covers Over a Small Aperture,” IEEE Trans. Antennas Propag., vol. AP-54, no. 6, pp. 1632–1643, June. 2006.

[25] M. Tang, S. Xiao, D. Wang, J. Xiong, K. Chen, B. Wang, “Negative Index of Reflection in Planar Metamaterial Composed of Single Split-Ring Resonators,” Applied Computational Electromagnetics Society (ACES) Journal, vol. 26, no. 3, pp. 250–258, March 2011.

[26] Averitt, R. D., Padilla, W. J., Chen, H. T., O'Hara, J. F., Taylor, A. J., Highstrete, C., ... & Gossard, A. C. (2007, September). Terahertz metamaterial devices. In Optics East 2007 (pp. 677209-677209). International Society for Optics and Photonics.

[27] Maritz, Andries Johannes Nicolaas. "Investigation and design of a slotted waveguide antenna with low 3D sidelobes." PhD diss., Stellenbosch: University of Stellenbosch, 2010.

[28] Mahmud, Rashad, Tianhao He, Micahel Lancaster, Yi Wang, and Xiaobang Shang. "Micromachined travelling wave slotted waveguide antenna array for beam-scanning applications." In 10th Loughborough Antennas and Propagation Conference, LAPC. 2014.

[29] Abdelrehim, A. A., & Ghafouri-Shiraz, H. (2017). High Gain Slotted Waveguide Antenna Based on Beam Focusing Using Electrically Split Ring Resonator Metasurface Employing Negative Refractive Index Medium. Progress In Electromagnetics Research, 79, 115-126.

[30] Grabowski, M. Non-Resonant Slotted Waveguide Antenna Design Method.

[31] X. Chen, T. Grzegorczyk, B. Wu, J. Pacheco and J. Kong, 'Robust method to retrieve the constitutive effective parameters of metamaterials', Physical Review E, vol. 70, no. 1, 2004.

[32] Arslanagic, S., Hansen, T. V., Mortensen, N. A., Gregersen, A. H., Sigmund, O., Ziolkowski, R. W., & Breinbjerg, O. (2013). A review of the scattering-parameter extraction method with clarification of ambiguity issues in relation to metamaterial homogenization. Antennas and Propagation Magazine, IEEE, 55(2), 91-106.

[33] Nicolson, A. M., & Ross, G. F. Measurement of the intrinsic properties of materials by time-domain techniques. Instrumentation and Measurement, IEEE Transactions on, 19(4), 377-382,1970.

[34] Boughriet, A-H., Christian Legrand, and Alain Chapoton. "Noniterative stable transmission/reflection method for low-loss material complex permittivity determination." IEEE Transactions on Microwave Theory and Techniques 45, no. 1 (1997): 52-57.

[35] Campione, Salvatore, Sergiy Steshenko, Matteo Albani, and Filippo Capolino. "Complex modes and effective refractive index in 3D periodic arrays of plasmonic nanospheres." Optics express 19, no. 27 (2011): 26027-26043.

[36] Carrasco, Eduardo, Mariano Barba, and José A. Encinar. "X-band reflectarray antenna with switching-beam using PIN diodes and gathered elements." IEEE Transactions on Antennas and Propagation 60, no. 12 (2012): 5700-5708.

[37] Vallecchi, A., Gentili, G.B.: ‘A shaped-beam hybrid coupling microstrip planar array antenna for X-band dual polarization airport surveillance radars’. The Second European Conf. on Antennas and Propagation, 2007. EuCAP 2007. November 2007, pp. 1–7

[38] Kuo, F.Y., Hwang, R.B.: ‘High-Isolation X-band marine radar antenna design’, IEEE Trans. Antennas Propag., 2014, 62, (5), pp. 2331–2337

[39] Jung, E.Y., Lee, J.W., Lee, T.K., et al.: ‘SIW-based array antennas with sequential feeding for X-band satellite communication’, IEEE Trans. Antennas Propag., 2012, 60, (8), pp. 3632–3639

[40] Y. Kurzweil-Segev, M. Brodsky, A. Polsman, E. Safrai, Y. Feldman, S. Einav and P. Ben Ishai, 'Remote Monitoring of Phasic Heart Rate Changes From the Palm', IEEE Transactions on Terahertz Science and Technology, vol. 4, no. 5, pp. 618-623, 2014.

Sun, M., Z. N. Chen, H. Tanoto, Q. Y. Wu, J. H. Teng, and S. B. Yeap. "Design of continuous-wave photomixer driven terahertz dipole lens antennas." In APSIPA Annual Summit and Conference, pp. 14-17. 2010.

Chapter 6 X-band and THz Slotted Waveguide Antenna Incorporated with Electrically Split Ring Resonator Metasurface Employing Anisotropic Low Epsilon Medium for E-Plane Beam Focusing

This chapter is reproduced from the authors published work reported in [1, 2], the author of this thesis was the first author and the second author was acting purely in a supervision capacity. In this chapter, a high performance slotted waveguide antenna incorporated with three dimension anisotropic low epsilon medium is proposed, designed and experimentally demonstrated. The low epsilon medium (LEM) is constructed from multilayer two dimension structure of electrically split ring resonator (eSRR) metasurface which exhibits anisotropic LEM medium in the direction of propagation when it is placed in front of the slotted waveguide antenna at optimum distance. As a result, the *E*- plane radiation beam of the slotted waveguide antenna is focused, and hence the directivity and the gain are improved, while the beam area is reduced. The proposed antenna as well as the LEM structure operating at 10 GHz were designed, optimized and numerically simulated by using CST software. The effective parameters of the eSRR structure are extracted by the Nicolson Ross Weir (NRW) algorithm from the s-parameters. For experimental verification, a proposed antenna operating at 10 GHz is fabricated using both a wet etching microwave integrated circuit technique (for the LEM structure) and a milling technique (for the slotted waveguide antenna). The measurements were carried out in an anechoic chamber. The measured results showed that, the *E*-plane gain of the proposed slotted waveguide antenna is improved from 6.5 dB to 9.5 dB compared with the conventional slotted waveguide antenna. Also, the *E*-plane beam width is reduced from 94.1 degrees to about 45.1 degrees. The antenna return loss and the bandwidth are slightly changed. Furthermore, the proposed antenna offered easier fabrication processes with a high gain compared with the horn antenna of the same size, particularly if the proposed antenna is scaled down in dimensionality to work in the THz regime.

However, the proposed antenna is redesigned to work at 303 GHz for Heart beat rate measurement applications. As a result, the *E*- plane radiation beam of the slotted waveguide antenna is focused, and hence the directivity and the gain are improved, while the beam area is reduced. The proposed antenna as well as the LEM structure operating at 303 GHz are designed, optimized and numerically simulated by using CST software. The effective parameters of the eSRR structure are extracted by the Nicolson Ross Weir (NRW) algorithm from the S-parameters. The simulated results showed that, the E-plane gain of the proposed slotted waveguide antenna is improved from 6.7 dB to 10.1 dB compared with the conventional slotted waveguide antenna. Also, the E-plane beam width is reduced from 94.1 degrees to about 47 degrees. The antenna return loss and the bandwidth are slightly changed. Furthermore, the proposed THz antenna offered easier fabrication processes with a high gain as compared to a horn antenna of the same size.

6.1. Introduction

During the last two decades, Metamaterials (MTMs) have received great attention due to their fascinating electromagnetic (EM) properties. MTMs are artificial atoms which exhibit exotic EM properties that cannot be achieved by the natural materials. MTMs can provide negative, zero or positive electric permittivity and magnetic permeability by inserting inclusion with specific geometrical shape and dimensionality in a host medium, both of the inclusions and the host medium are constructed from metals and dielectrics [3]. Recently, MTM with simultaneously negative permittivity, permeability and negative index of refraction are used to design perfect lenses [4, 5] for high resolution imaging system and to design many antennas [6, 7]. Also, MTMs are proposed to design gradient index of refraction lenses [8], absorbing, cloaking [9, 10], polarization transformer [11]. By using MTMs with negative or gradient index of refraction, compact size high directive antennas can be designed [12, 13]. It is well know that, high directive antennas play an important role for many practical applications. Many conventional efforts have been done to improve the antenna directivity such as parasitic patches, array of patch antennas, parabolic reflectors [14-16]. Unfortunately, the aforementioned approaches suffer from the large sizes, design methodology, complex feeding network and fabrication processes, particularly in the high frequencies. As John Pendry investigated the first negative refractive index perfect lens (i.e. double negative MTMs with simultaneously negative permittivity, permeability and negative index of refraction) in 2000 [17], it is possible to design a compact size and high directive antennas [18, 19]. One of the tremendous properties of MTMs are epsilon near zero (ENZ) or low epsilon medium (LEM), Mu near zero (MNZ) and index of refraction near zero (INZ) are fantastic ways to improve the directivity of the antenna. Enoch et al. proposed ENZ medium to improve the directivity of the EM radiation of a source embedded in the centre of the ENZ medium [20]. Many researchers have developed the performance of different types of antennas (i.e. patch, horn, etc.) [21] using zero index medium (ZIM). Unfortunately, due to the impedance mismatch between the free space and the ZIM, the antenna radiation efficiency is degraded. Ma et al. overcame this problem in 2009 and proposed a theoretical model for a 2D anisotropic MTM structure with single near zero component of the effective parameters tensor [22]. This idea is experimentally verified in 2010 by Cheng et al. [23]. Furthermore, Jiang et al. proposed transformation lens with good impedance matching and with ENZ and achieved high gain and broad bandwidth antenna [24].

This work focuses on two interesting contributions. Firstly, 2D, single sided metasurface (MS) structure based on electrically split ring resonator (eSRR) was designed with proper dimensionality such that it exhibits anisotropic LEM property in the direction of propagation and hence it can be used to improve the directivity of the EM emission as well as it exhibits a unity effective permittivity and permeability in the transverse directions. As a result the effective impedance of the LEM in the direction of wave propagation is matched with the free space intrinsic impedance and also the *E*-plane radiation pattern will be focused and the gain is improved. This 2D MS structure has advantages of easier in fabrication and assembly processes as compared to volumetric MTMs, so it can be scaled down to be fabricated for THz antennas for high resolution imaging and biomedical application for heart beat measurements. Secondly, a slotted waveguide antenna [25] is used as an EM radiator instead of a horn antenna or a patch antenna because it is difficult to design a horn antenna with flared surfaces in the THz regime. Furthermore, there are no SMA connectors for the patch antenna operating in the THz regime. Fortunately, for waveguide, there are waveguide connectors up to 900 GHz [26, 27]. Also the slotted waveguide antenna can handle high power particularly in the THz range and has low loss. Thus one of the sophisticated methods to design a THz antenna powered by microwave sources is to use slotted waveguide antennas. Due to the low gain of the single element slotted antenna (the typical gain is 6.5 dB), anisotropic LEM is used as a superstrate to improve the transverse magnetic (TM) wave radiated from the slotted waveguide antenna and hence the *E* plane gain and directivity are improved. For experimental verification the slotted waveguide antenna incorporated with eSRR anisotropic LEM medium operating at 10 GHz was designed, numerically optimized using CST software, fabricated and measured.

This chapter is organized as follow: in section 6.2, the theory of wave propagation in LEM is presented. Section 6.3 discusses the design and effective parameter extraction of anisotropic LEM medium based on eSRR metasurface. Section 6.4 presents the design and numerical simulation of the 10 GHz slotted waveguide antenna incorporated with the anisotropic LEM medium. In section 6.5, experimental verifications for the proposed antenna are carried out. Finally the conclusion and the future recommendations are given in section 6.6. Section 6.7 provides the design and simulation of a 303 GHz conventional slotted antenna. Section 6.8 discusses the design and effective parameter extraction of anisotropic

LEM medium based on eSRR metasurface. Section 6.9 presents the design and numerical simulation of the 303 GHz slotted waveguide antenna incorporated with anisotropic LEM medium. Finally the conclusion and the future recommendations are given in section 6.10.

6.2. Theoretical analysis of wave propagation in anisotropic ENZ medium for TM modes

Here the theoretical verification of the anisotropic ENZ layer has on the impedance matching and the beam area of the E plane radiated pattern are studied. Figure 6.1 shows the propagation of TM modes in anisotropic ENZ medium. Assume medium 1 is free space and medium 2 is anisotropic ENZ medium. Refereeing to the field components of the TM mode, the wave propagation in the ENZ layer satisfies the following dispersion equation

$$\frac{k_y^2}{\varepsilon_{2z}} + \frac{k_z^2}{\varepsilon_{2y}} = \frac{\omega^2}{c^2}\mu_{2x} \tag{6.1}$$

Where ε_{2y}, ε_{2z} and μ_{2x} are the components of the permittivity and permeability tensors in the anisotropic layer.

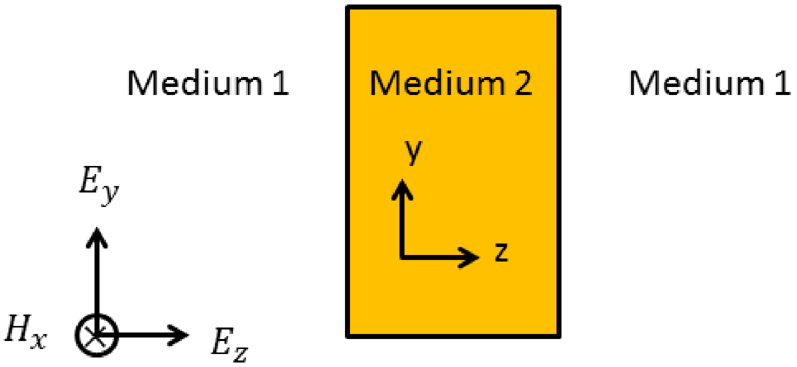

Fig. 6.1. TM modes wave propagation in anisotropic ENZ medium.

If the anisotropic medium is designed such that $\varepsilon_{2z} \rightarrow 0$, $\varepsilon_{2y} \neq 0$ and $\mu_{2x} \neq 0$, so k_y should be zero. As a result the wave propagates only in the z direction and thus the directivity is increased. Consequently, the wave vector k_z and the intrinsic impedance η_z can be calculated using Eqs. 6.2 and 6.3, respectively.

$$k_z = \frac{\omega}{c}\sqrt{\varepsilon_{2y}\mu_{2x}} \tag{6.2}$$

$$\eta_{2z} = \eta_0\sqrt{\frac{\varepsilon_{2y}}{\mu_{2x}}} \tag{6.3}$$

Where η_0 is the free space wave impedance. Using the boundary conditions at the interface between low epsilon medium (LEM, i.e. meduim2) and the free space (i.e. medium 1), the filed components can be given as follow

Since

$$D_{1n} = D_{2n}, H_{1t} = H_{2t} \; and \; E_{1t} = E_{2t} \tag{6.4}$$

So

$$\varepsilon_1 E_{1z} = \varepsilon_{2z} E_{2z} \tag{6.5}$$

$$H_{1x} = H_{2x} \tag{6.6}$$

$$E_{1y} = E_{2y} \tag{6.7}$$

It is clear from Eq. (6.5) that, since $\varepsilon_{2z} \rightarrow 0$, the electric field in medium 1 $E_{1z} \rightarrow 0$, so there is no electric field in the direction of propagation. However, there is design degree of freedom for the values of ε_{2y} and μ_{2x}, the values of such two parameters to match the wave impedance η_{2z} with the free space wave impedance η_0. According to Eq. (6.3), the wave impedance of the LEM is matched with the free space wave impedance, when the values of ε_{2y} and μ_{2x} are close to each other.

6.3. **Design and Simulation of 10 GHz Anisotropic LEM MS Based on ESRR**

Here, the electrically Split Ring Resonator (eSRR) metasurface structure with 2-D infinite periodicities is designed such that it exhibits anisotropic LEM at 10 GHz. The geometry of the eSRR metasurface is shown in Fig. 6.2. The orientation and the dimensionality of the eSRR are specified such that the structure exhibits $\varepsilon_{2z} \to 0$, $\varepsilon_{2y} \cong 1$ and $\mu_{2x} \cong 1$ according to the theory presented in the previous section to make sure that the radiated *TM* waves from the slotted waveguide antenna can be focused. To achieve such 3-D anisotropic properties, the eSRR metasurface is excited by *a TEM* wave propagated in the *y*-direction with the *E*-field polarized in the *z*-direction and *H*-field polarized in the *x*-direction as shown in Fig. 6.3. The dimensions of the eSRR metasurface employing anisotropic low epsilon medium around 10 GHz are shown in Table 6.1.

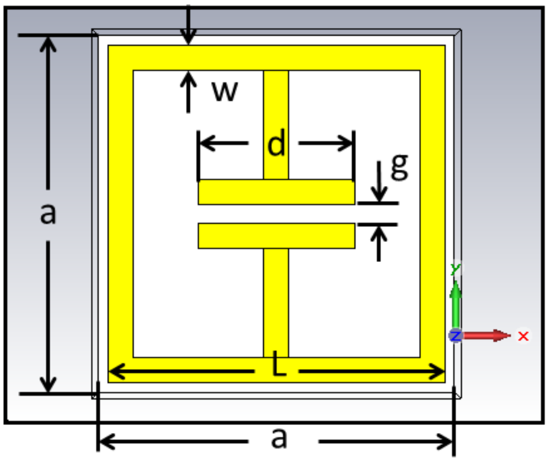

Fig. 6.2. Front view of eSRR metasurface unit cell with all dimensions indicated

Table 6.1 Dimensions of 10 GHZ eSRR metasurface structure employing anisotropic low epsilon medium

Parameter	*a*	*L*	*d*	*g*	*w*
Dimension (mm)	5.5	5.3	2.8	0.3	0.62

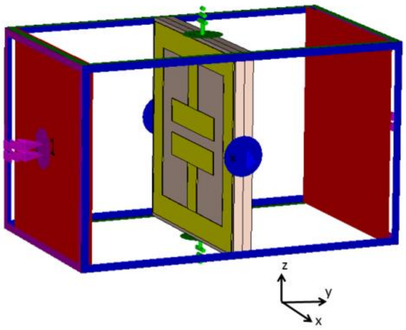

Fig. 6.3. The 3-D view of eSRR metasurface unit cell, the excitation is by a TEM wave propagated in the y-direction with the *E*-field polarized in *z*-direction and *H*-field polarized in the x-direction.

To verify the anisotropic properties of the eSRR metasurface structure and extract its effective parameters in the other directions, the eSRR is rotated and excited by a *TEM* wave propagated in the *z*-direction with the *E*-field polarized in *y*-direction and the *H*-field polarized in the *x*-direction as shown in Fig. 6.4.

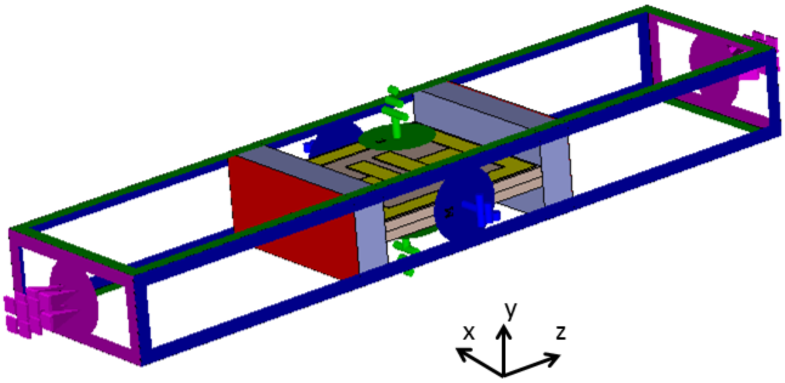

Fig. 6.4. The 3-D view of eSRR unit cell, the excitation is by a TEM wave propagated in the *z*-direction with *E*-field polarized in the *y*-direction and *H*-field polarized in the *x*-direction.

The eSRR is then simulated in CST with a unit cell boundary condition in the *x* and *z* directions. The S-parameters are calculated and plotted as shown in Fig. 6.5 (a). The effective permittivity, permeability and index of refraction are extracted from the *S-parameters* as shown in Figs. 6.5 (b), (c) and (d), respectively using the NRW algorithm taking the unambiguity branching into account [29]. It is clear from Fig. 6.5 (a), that, the eSRR has a band pass response around 10 GHz. Furthermore, at 10 GHz, the effective permittivity is 0.147 which is less than 1, the effective permeability is close to 1, and the effective index of refraction is less than 1 as shown in Figs. 6.5 (b), (c) and (d), respectively.

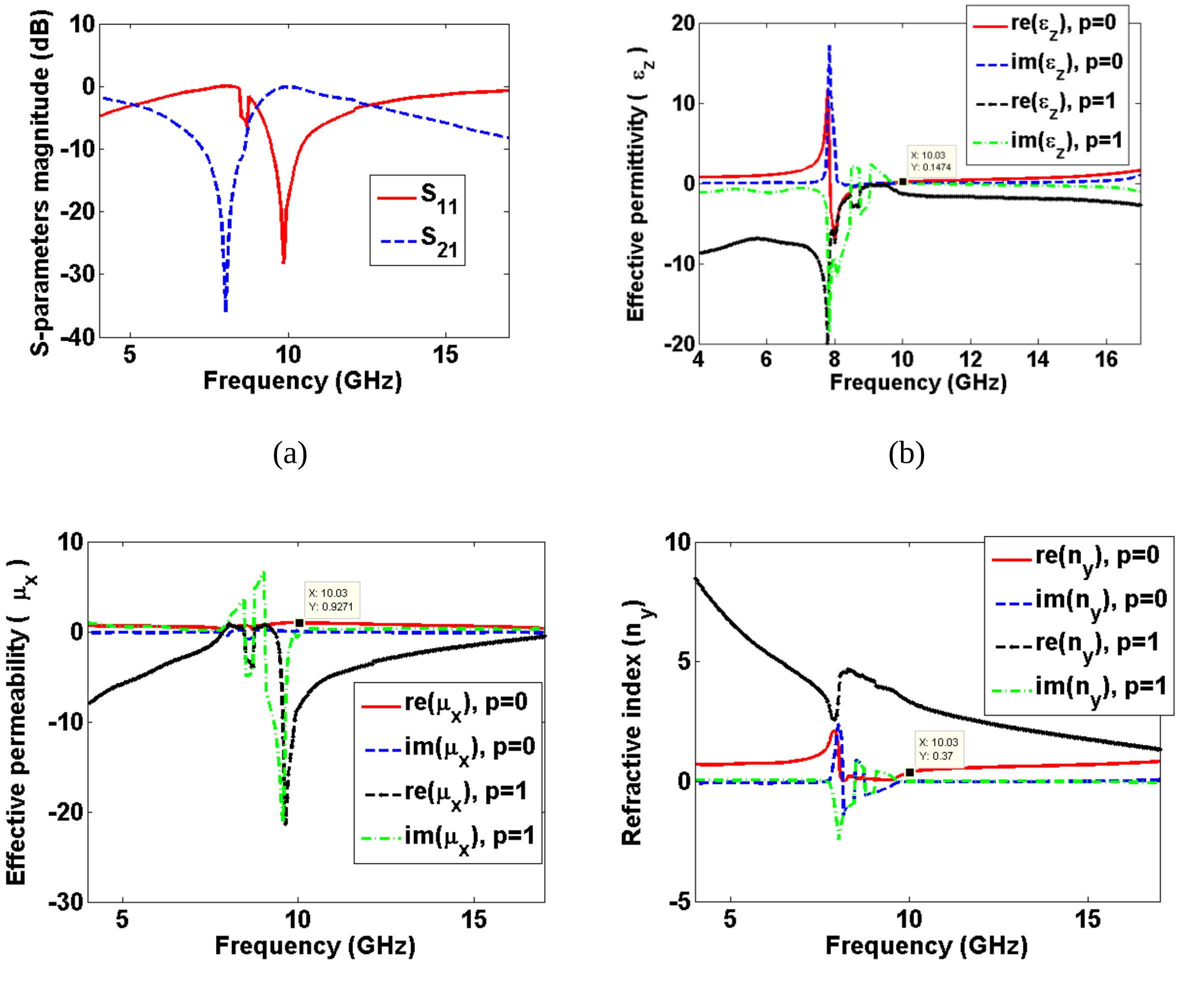

(a) (b)

(c) (d)

Fig. 6.5. The scattering and the effective parameters of eSRR metasurface with 2-D infinite periodicity excited with TEM wave propagated in the y-direction with the E-field polarized in the z-direction and the H-field polarized in the x-direction, extracted at two different unambiguity branch parameters p of 0 and 1 [29] (a) S-parameters magnitude, (b) Effective permittivity (ε_z), Effective permeability (μ_x) and refractive index (n_y).

The anisotropic LEM structure shown in Fig. 6.3 is simulated in CST with unit cell boundary conditions shown in the *x* and *y* directions. The scattering parameters are calculated and plotted as in Fig. 6.6 (a), and then the effective parameters are extracted from the *S*-

parameters and plotted as shown in Fig. 6.6 (b), (c), and (d) for the effective permittivity, permeability and index of refraction, respectively. It is clear from Fig. 6.6 (a) that, the structure has all pass response with good reflection and transmission coefficients for such excitation scenario. However, Figs. 6.6 (b), (c) and (d) illustrate that, the effective permittivity ε_y, permeability μ_x and index n of refraction are all close to unity. By substituting with ε_y and μ_x into equation (3), the wave impedance inside the anisotropic LEM equals the free space wave impedance, so the input impedance of the slotted waveguide antenna will not be affected by the eSRR 3-D structure if it is placed in front of the slot at specific separation distance as will be discussed in the coming section.

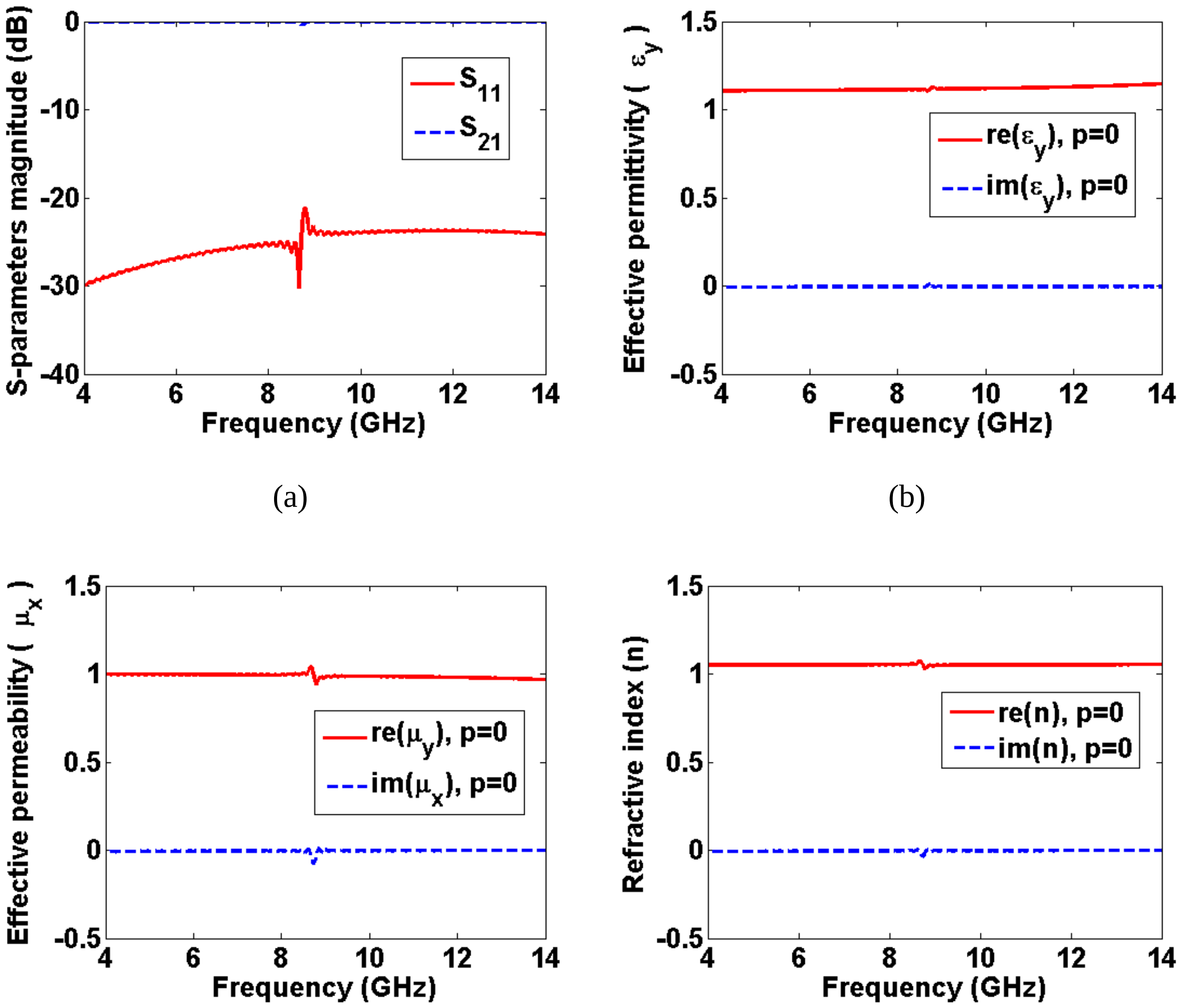

(a)

(b)

(c) (d)

Fig. 6.6. The scattering and the effective parameters of eSRR metasurface with 2-D infinite periodicity excited with the TEM wave propagated in the z-direction with the E-field polarized in the y-direction and the H-field polarized in the x-direction, extracted at unambiguity branch parameters p of 0 [29] (a) S-parameters magnitude, (b) Effective permittivity (ε_y), Effective permeability (μ_x) and refractive index (n_z).

The impact of infinite periodicity truncation effect of the eSRR metasurface on the effective parameters of the anisotropic medium is studied. Two eSRR metasurface structures of sizes 6×3×1 and 6×3×2 were designed and simulated in CST. The metasurface structure is excited by a *TEM* wave propagated in the *y*-direction with the *E*-field polarized in *z*-direction and the *H*-field polarized in *x*-direction. The scattering parameters are calculated and then the effective parameters are extracted and plotted for unambiguity branch parameter *p* of 0 as shown in Fig. 6.7. Figure 6.7 illustrates that; the eSRR metasurface structures with and without 2-D infinite periodicity exhibit approximately the same *S-parameters* and effective parameters around 10 GHz. However, the metasurface structure with and without infinite periodicity still has a low epsilon medium in *z*-direction and approximately unity effective permeability in the *x*-direction as shown in Figs. 6.7 (b) and (c), respectively.

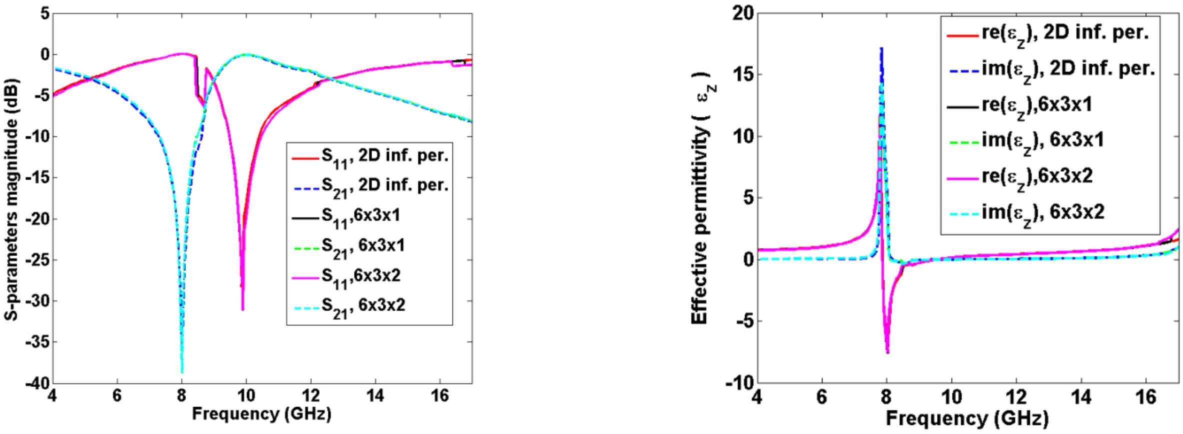

(a) (b)

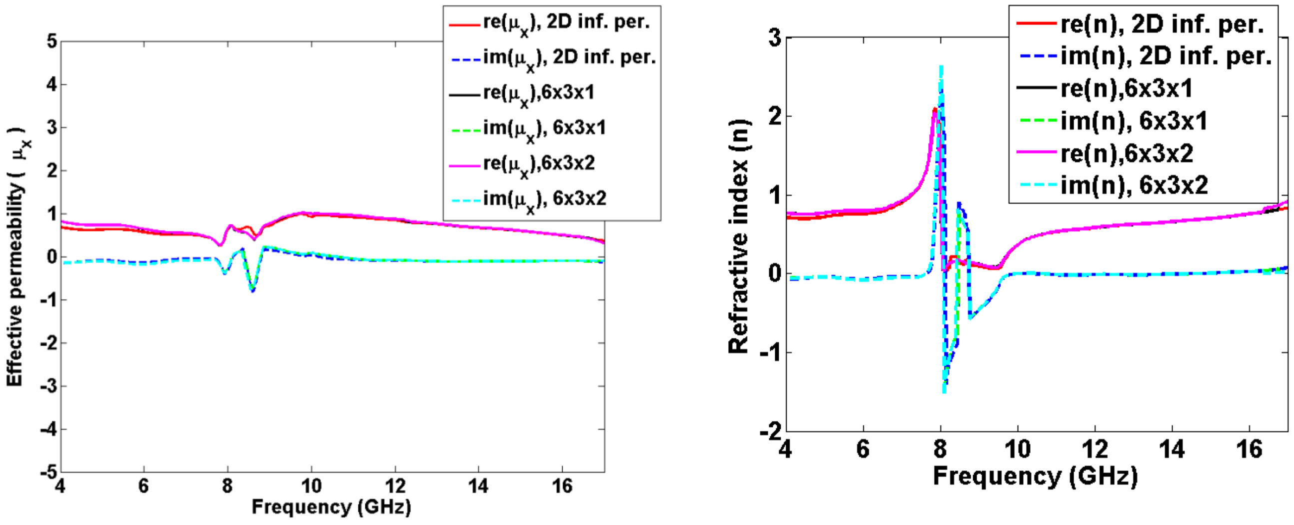

(c)

(d)

Fig. 6.7. The scattering and the effective parameters of eSRR metasurface with and without 2-D infinite periodicity (inf. per.) excited with the TEM wave propagated in the y-direction with the E-field polarized in the z-direction and the H-field polarized in the x-direction, extracted at unambiguity branch parameter p of 0, (a) S-parameters magnitude, (b) Effective permittivity (ε_z), Effective permeability (μ_x) and refractive index (n).

6.4. Design and Simulation of 10 GHz slotted waveguide antenna incorporated with Anisotropic LEM MS structure

Here, the proposed slotted waveguide antenna incorporated with eSRR metasurface structure employing anisotropic low epsilon medium (LEM) as shown in Fig. 6.8 was simulated and optimized using CST software. The proposed antenna is composed of slotted waveguide antenna as shown in Fig. 5.1 and an isotropic 3D LEM eSRR structure. The proposed antenna operated at 10 GHz and the eSRR metasurface structure was optimized to exhibit anisotropic LEM around 10 GHz. The antenna was optimized by changing the size of the eSRR metasurface structure and the separation between the eSRR metasurface structure and the slotted waveguide antenna. Figures 6.9 (a) and 6.9 (b) show the return loss and the gain versus frequency in the main lobe direction of $\varphi = 0^o$ and $\theta = 0^o$ of the proposed antenna with and without anisotropic LEM MS at different separation distance h_s between the slot and the MS bottom side and with slot size (L_s, W_s) of (15.2, 6). The size of LEM MS structure is 6×6×12. Also both E and H planes radiation gains are plotted as shown in Fig. 6.10

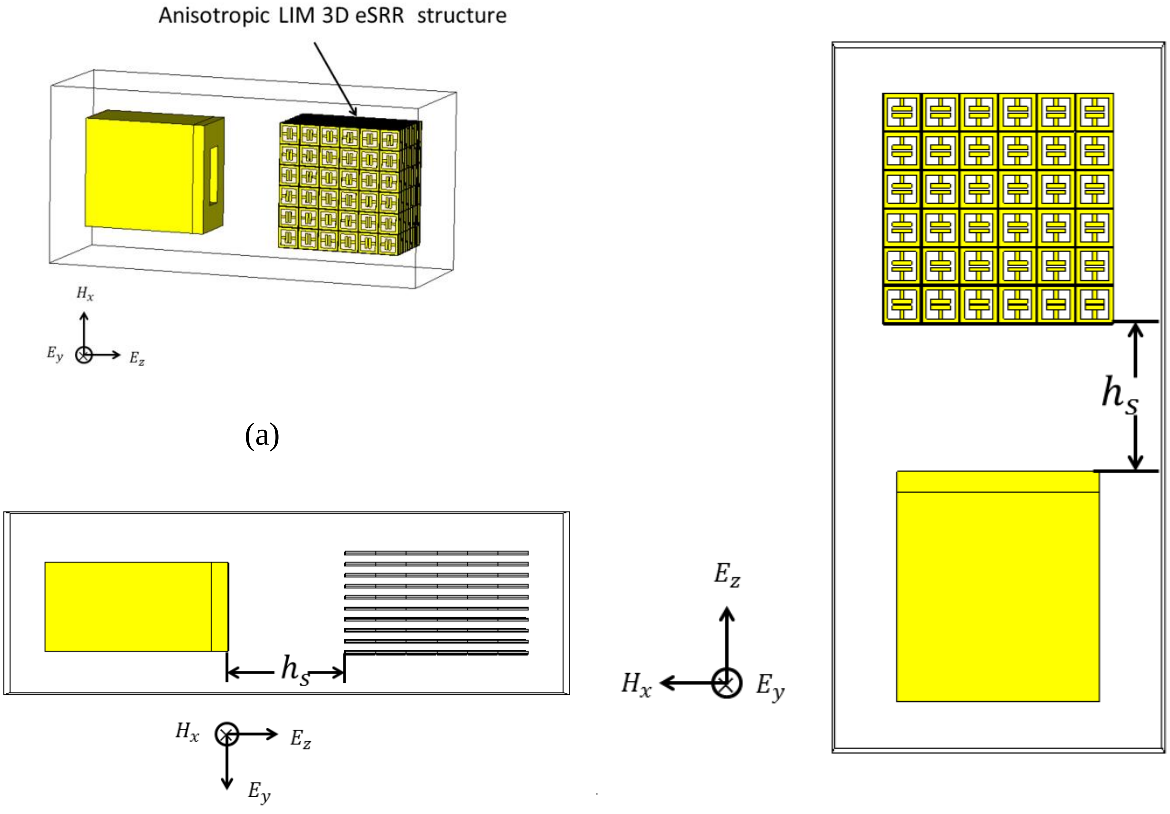

(a)

(b)

(c)

Fig. 6.8. 10 GHz slotted waveguide antenna incorporated with ESRR an Isotropic LEM, (a) 3D view, (b) side view, and (c) top view.

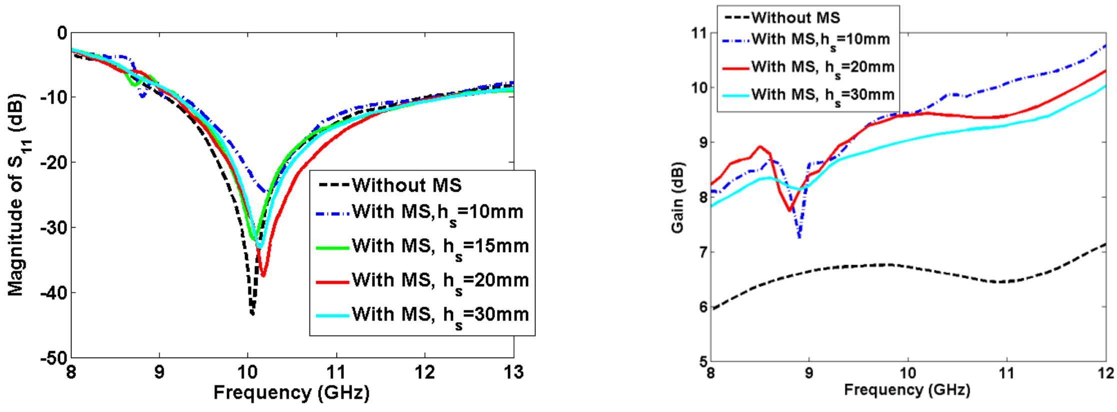

(a)

(b)

Fig. 6.9. The simulated return loss (a) and the simulated gain versus frequency at main lobe direction of $\varphi = 0^o$ and $\theta = 0^o$ (b) for the proposed antenna with and without MS at different separation distance between the slot

and the MS structure size of 6×6×12 in the x, y and z direction, respectively with 1 mm separation distance between each two MS layers.

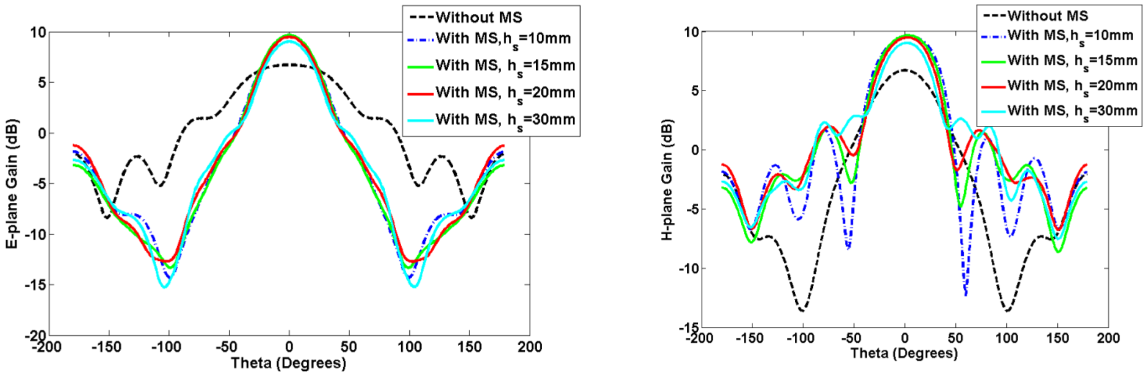

(a) (b)

Fig. 6.10. E-plane gain (a) and H-plane gain (b) for the proposed antenna with and without anisotropic LEM MS of size 6×6×12 and at different separation distance between the slot and the MS structure with 1 mm separation distance between each two MS layers.

It is clear from Fig. 6.9 (a) that the separation distance h_s plays an important role in the impedance matching of the proposed antenna. The optimum separation distance h_s is 20 mm. Figure 6.9 (b) illustrates that as the separation distance h_s increases the gain decreases. However, the radiation gain increase for the proposed antenna with anisotropic LEM MS and the beam area decreases in both the E and H planes as shown in Fig. 6.10. At the optimum separation distance h_s of 20 mm, the *H*-plane gain is increased from 6.7 to 9.48 dB, the *E*-plane gain is increased from 6.7 to 9.47 dB, while the beam area in the *H*-plane is reduced from 67.6 to 56.1 degrees and in the *E*-plane it is decreased from 94.1 to 45.1 degrees. It is clear that the BW is slightly changed.

In addition, the effect of the anisotropic LEM MS sizes on return loss, gain versus frequency, *and E*- and *H*-plane gains of the proposed antenna was studied and plotted as shown in Figs. 6.11 and 6.12. Figure 6.11 (a) and (b) shows the return loss and the gain versus frequency of the proposed antenna with and without anisotropic LEM MS of different sizes and at a separation distance $h_s$of 20 mm. it is clear from Fig. 6.11 (a) that the MS of size 6×6×6 has better return loss than 6×6×12. In contrast the gain increases as the MS size increases as shown in Figs. 6.11 (b) and 12.

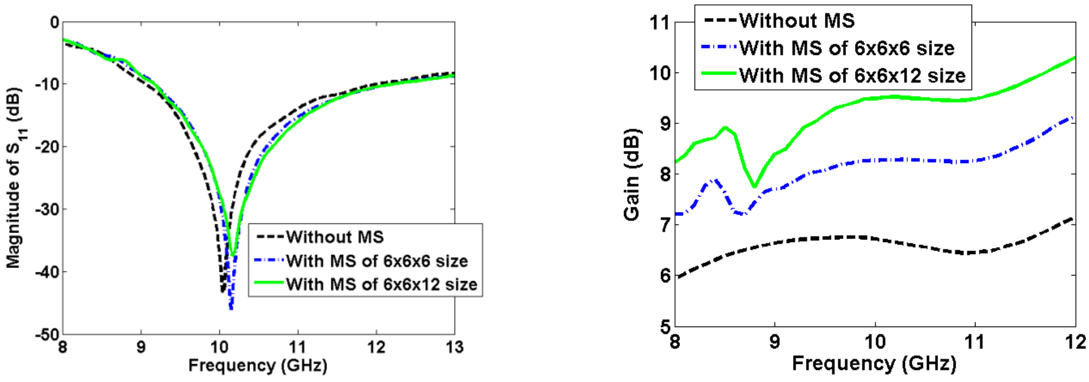

(a)

(b)

Fig. 6.11**.** The simulated return loss (a) and the simulated gain versus frequency in the main lobe direction of $\varphi = 0^o$ and $\theta = 0^o$ (b) for the proposed antenna with and without MS at fixed separation distance h_S of 20 mm and different MS structure sizes with 1 mm separation distance between each two MS layers.

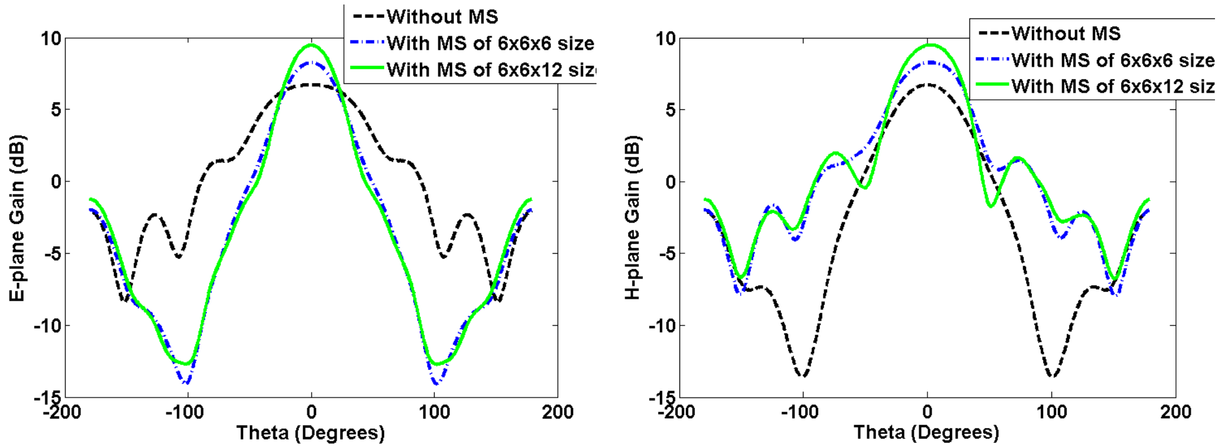

(a)

(b)

Fig. 6.12. E-plane gain (a) and H-plane gain (b) for the proposed antenna with and without MS at fixed separation distance h_S of 20 mm and different MS structure sizes with 1 mm separation distance between each two MS layers.

6.5. Fabrication and Measurement of the Proposed Slotted Waveguide Antenna Operating at 10 GHz

For experimental verification, the proposed antenna resonating at 10 GHz as well as the eSRR anisotropic LEM MS structure have been fabricated as shown in Fig. 6.13. The MS structure is fabricated using wet etching technique on a RT/Duroid 5880 substrate with a relative permittivity of εr = 2.2 and a thickness of h= 0.57 mm. the slotted waveguide antenna is fabricated using milling technology with the same dimensions mentioned in the previous section. The slot dimensions (W_S, L_S) is (6mm, 15.2mm). The return loss, S_{11} and the gain versus frequency for the simulated and the fabricated antenna with and without eSRR anisotropic LEM MS of size 6×6×12 and separation distance h_s of 20 mm is shown in Fig. 6.14. The measured and the simulated return loss of the proposed antenna without eSRR MS agreed and the bandwidth was about 2.88 GHz. It is important to notice that, there is a shift in the centre frequency and some losses for the measured proposed antenna with MS over the simulated one due to the SMA connector, the nylon screws, and the misalignment of the eSRR stacked layers constructing the MS structure. Furthermore, the bandwidth of the proposed antenna with eSRR MS is slightly changed over the conventional one. It is clear from Fig. 6.14 (b) that the proposed antenna measured gain with anisotropic LEM MS was increased by about 3 dB over the conventional one.

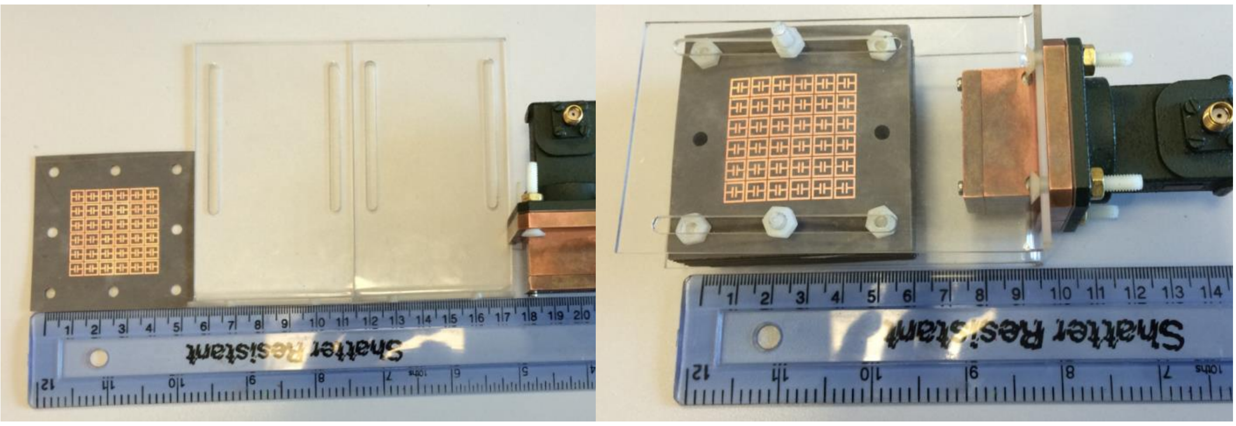

(a) (b)

Fig. 6.13. The fabricated antenna, (a) conventional slotted waveguide antenna on the right, two plastic bears on the middle and eSRR MS of sizes 6×6×6, on the left, and (b) slotted waveguide antenna incorporated with eSRR 3D structure of size 6×6×12 located at a distance h_s of 20 mm from the slot and the separation distance is 1 mm from the centre to the centre of each two adjacent eSRR layers.

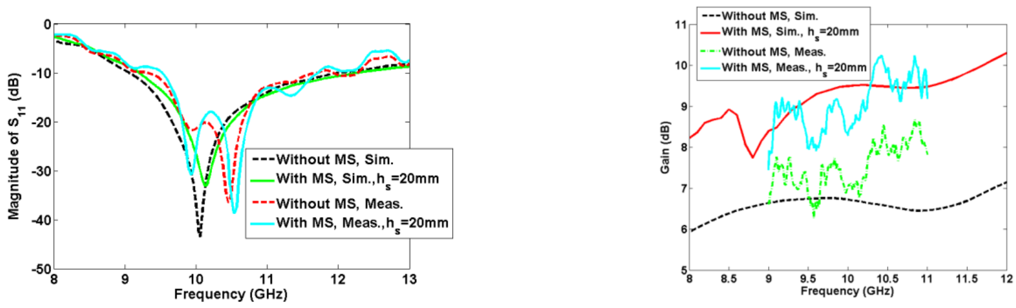

(a) (b)

Fig. 6.14. The simulated and the measured return loss (a) and the simulated gain versus frequency in the main lobe direction of $\varphi = 0^{o}$ and $\theta = 0^{o}$ (b) for the proposed antenna with and without MS at fixed separation distance of 20 mm between the slot and the MS structure size of 6×6×12 in the x, y and z direction, respectively with 1 mm separation distance between each two MS layers.

Furthermore, the *E*- and *H*- plane radiation patterns of the simulated and the measured proposed antenna with and without anisotropic LEM MS are plotted as shown in Fig. 6.15 for fixed MS size of 6×6×12 and different separation distance h_s. It is clear that, there are deviations between the measured and the simulated results due to the plastic bears which are added to suspend the MS structure in front of the slotted waveguide antenna in the measurement. Fortunately the impact of the MS in beam focusing still working even after adding the plastic beard as shown in Fig. 6.15 which shows that both *E* and *H* plane radiation patterns of the proposed antenna have narrower beam widths as compared with the conventional ones.

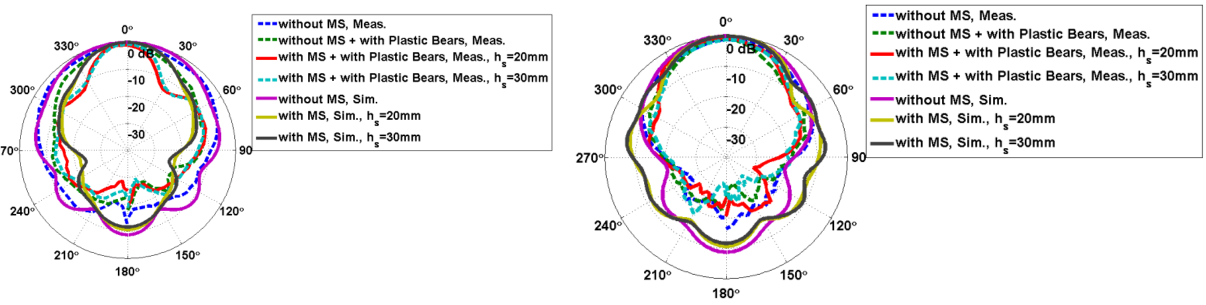

(a) (b)

Fig. 6.15. Simulated and measured E-plane gain (a) and H-plane gain (b) for the proposed antenna with and without MS at different separation distance h_s and with MS structure size of 6×6×12 with 1 mm separation distance between each two MS layers.

6.6. Design and Simulation of 303 GHz Conventional Slotted Waveguide Antenna

Here, the dimensions of the conventional slotted waveguide antenna shown in Fig. 6.2 are designed properly such that the antenna operates at 303 GHz and has a good impedance matching with the free space; the slot length is about half wavelength. Three different slotted antennas of back wall slots of dimensions (L_s, W_s) of (460, 100), (480, 150), and (490, 200) were designed, all dimensions are in µm. The waveguide has length L_{wg} of 1.5 mm which equals one and half of the free space wavelength at the operating frequency of 303 GHz and thickness 50 µm to match requirements of the fabrication, mechanical, and assembly processes. The antenna is simulated in CST software and the return loss S_{11} as well as both E and H planes gains are extracted as shown in Fig. 6.16. It is clear from Fig. 6.16 (a) that, as the slot width W_s increases, and the slot length L_s is changed slightly around the free space half wavelength of 15 mm at 10 GHz to keep the operating frequency at 303 GHz the gain slightly decreases, while the bandwidth increases. Furthermore, the results illustrate that, for slotted waveguide antennas of slot widths W_s of 100, 150, and 200 µm and slot lengths L_s of 460, 480 and 490 µm, the bandwidths are 34.35, 50 and 72 GHz, respectively and the gain is about 6.5 dB mostly for all the three slot dimensions.

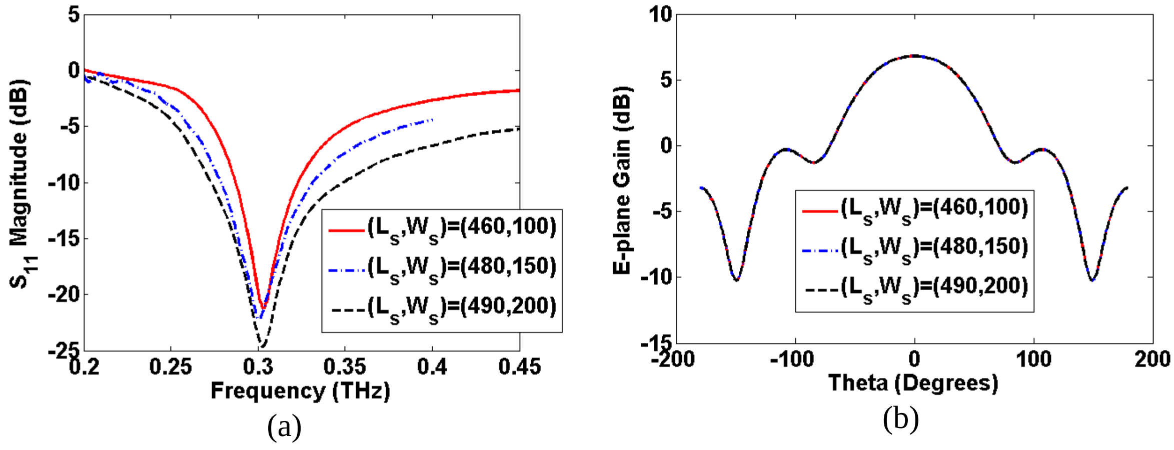

(a) (b)

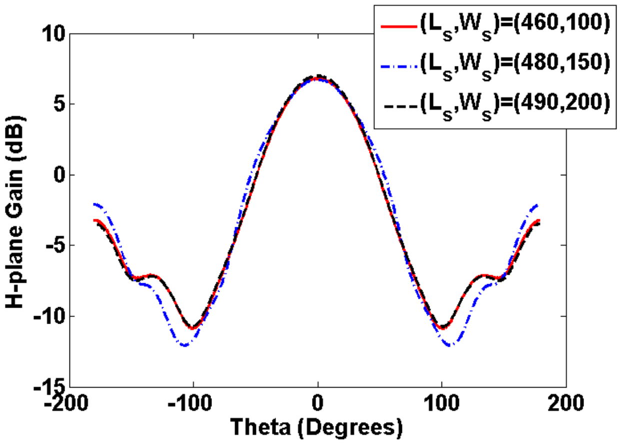

(c)

Fig. 6.16. Conventional 303 GHz slotted waveguide antenna performance at different slot dimensions of length L_s and widthW_s, all dimensions are in mm, (a) return loss S_{11} in dB, (b) E-plane Gain in dB, and (c) H-plane Gain in dB.

6.7. Design and Simulation of 303 GHz eSRR Metasurface Employing LEM Medium

Here, the electrically Split Ring Resonator (eSRR) metasurface structure with 2-D infinite periodicities is designed such that it exhibits anisotropic LEM at 303 GHz. The eSRR MS is a 0.2 µm gold layer which is mounted on the top surface of a 2 µm silicon layer which is placed at the top of a 2 µm silicon dioxide layer. The geometry of the eSRR metasurface employing anisotropic low epsilon medium around 303 GHz is shown in Fig. 6.17 (a) and the dimensions are given in Table 6.2. The orientation and the dimensionality of the eSRR are specified such that the structure exhibits $\varepsilon_{2z} \rightarrow 0$, $\varepsilon_{2y} \cong 1$ and $\mu_{2x} \cong 1$ to satisfy the theory anisotropic low epsilon medium presented in section 6.2 to make sure that the radiated TM waves from the slotted waveguide antenna can be focused. To achieve such 3-D anisotropic properties, the eSRR metasurface is excited by a TEM wave propagated in the y-direction with *E*-field polarized in the *z*-direction and the *H*-field polarized in the *x*-direction as shown in Fig. 6.17 (b). The eSRR is then simulated in CST with unit cell boundary condition in the *x* and *z* directions. The *S-parameters* are calculated and plotted as shown in Fig. 6.18 (a). The effective permittivity, permeability and index of refraction are extracted from the *S-parameters* as shown in Figs. 6.18 (b), (c) and (d), respectively using the NRW algorithm taking the unambiguity branching into account [30]. It is clear from Fig. 6.18 (a), that, the eSRR has a band pass response around 303 GHz. Furthermore, at 303 GHz, the effective permittivity is 0.1309 which is less than 1, the effective permeability is close to 1, and the effective index of refraction is less than 1 as shown in Figs. 6.18 (b), (c) and (d), respectively.

To verify the anisotropic properties of the eSRR metasurface structure and extract its effective parameters in the other directions, the eSRR is rotated and excited by TEM wave propagated in the *z*-direction with the *E*-field polarized in the *y*-direction and the *H*-field polarized in the *x*-direction as shown in Fig. 6.17 (c). The structure is simulated in CST with unit cell boundary conditions in *x* and *y* directions. The scattering parameters are calculated and plotted as shown in Fig. 6.19 (a), and then the effective parameters are extracted from the S-parameters and plotted as shown in Fig. 6.19 (b), (c), and (d) for the effective permittivity, permeability and index of refraction, respectively. It is clear from Fig. 6.19 (a) that, the structure has all pass response with good reflection and transmission coefficients for such excitation scenario. However, Figs. 6.19 (b), (c) and (d) illustrate that, the effective permittivity ε_{yy}, permeability μ_{xx} and index n of refraction are all close to unity. By substituting with ε_{yy} and μ_{xx} into equation (3), the wave impedance inside the anisotropic LEM equals the free space wave impedance, so the input impedance of the slotted waveguide antenna will not be affected by the eSRR 3-D structure if it is placed in front of the slot at a specific separation distance as will be discussed in the coming section.

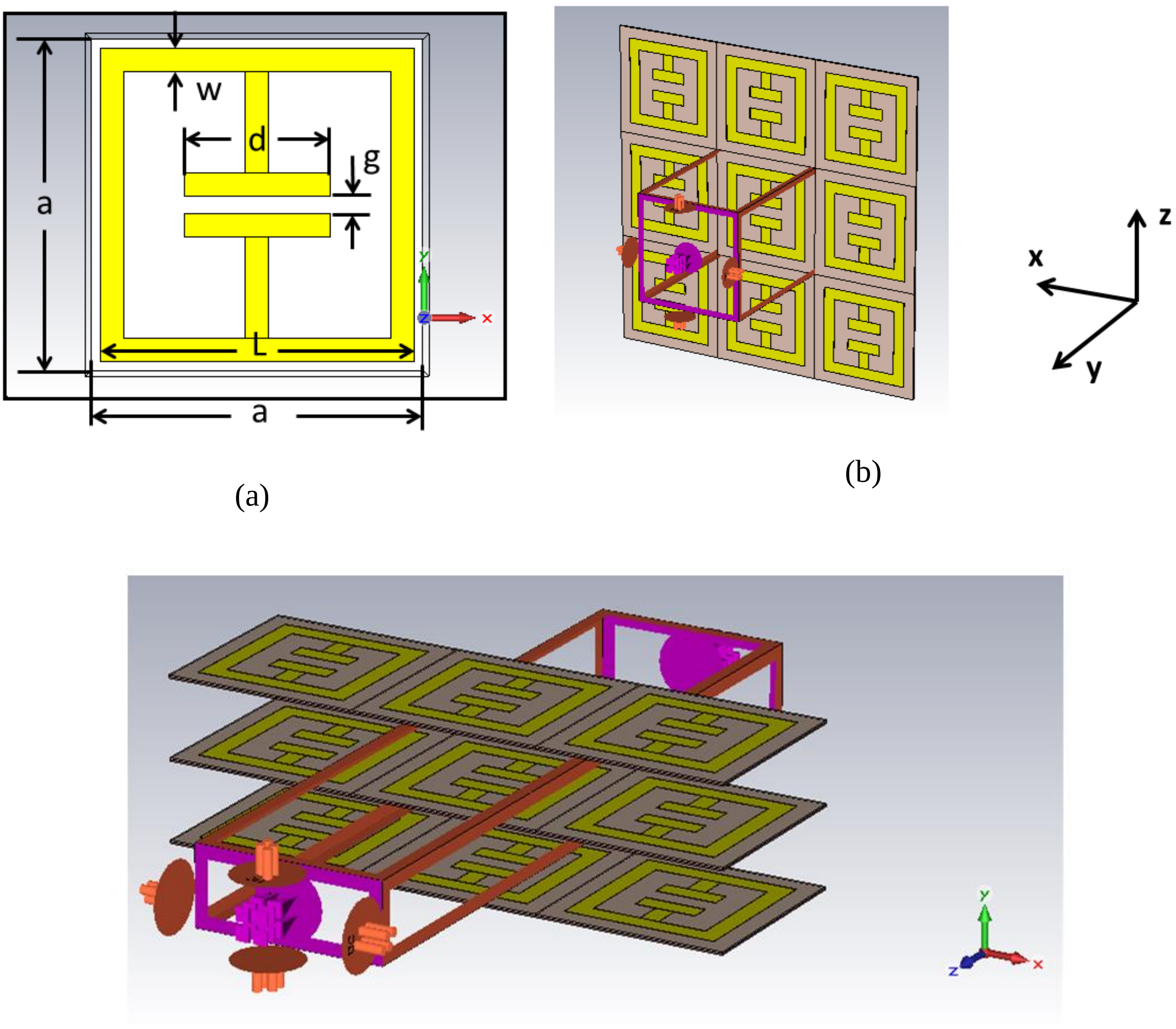

(a)

(b)

(c)

Fig. 6.17. 303 GHz eSRR metasurface excited in different directions, (a) front view of eSRR unit cell with all dimensions indicated, (b) 3-D view of eSRR unit cell, the excitation is by a TEM wave propagated in the y-direction with the E-field polarized in the z-direction and the H-field polarized in the x-direction and (c) 3-D view of eSRR unit cell, the excitation is by a TEM wave propagated in the z-direction with the E-field polarized in the y-direction and the H-field polarized in the x-direction.

Table 6.2: Dimensions of 303 GHz eSRR metasurface employing LEM

Parameter	a	L	d	$h1$	$h2$	g	W	t
Dimension (μm)	250	200	80	2	2	25	25	0.2

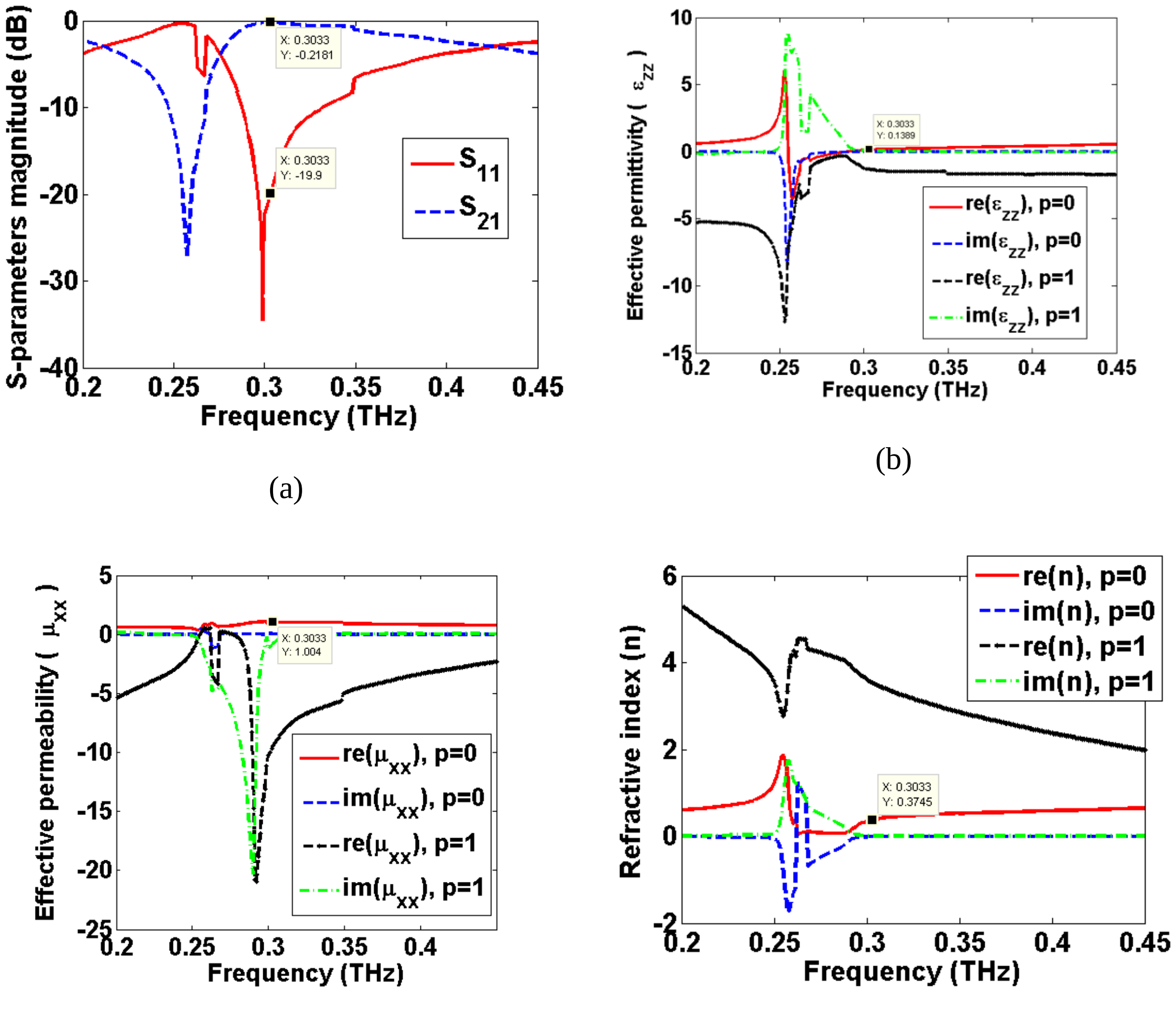

(a)

(b)

(c)

(d)

Fig. 6.18. The scattering and the effective parameters of eSRR metasurface with 2-D infinite periodicity excited with the TEM wave propagated in the y-direction with the E-field polarized in the z-direction and the H-field polarized in the x-direction, extracted at two different unambiguity branch parameter p of 0 and 1 [30] (a) S-parameters magnitude, (b) Effective permittivity (ε_{zz}), Effective permeability (μ_{xx}) and refractive index (n).

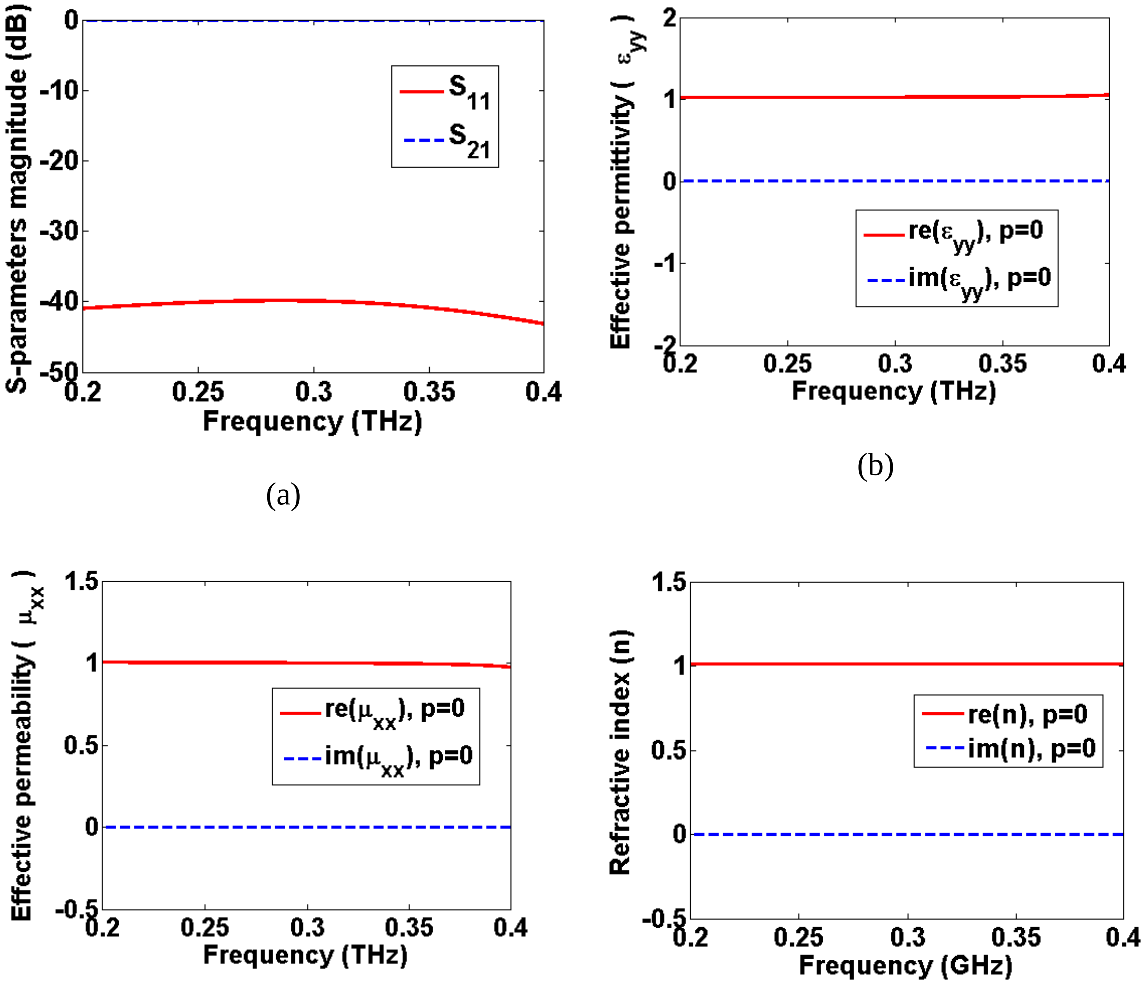

(a)

(b)

(c)

(d)

Fig. 6.19. The scattering and the effective parameters of eSRR metasurface with 2-D infinite periodicity excited with the TEM wave propagated in the z-direction with the E-field polarized in the y-direction and the H-field polarized in the x-direction, extracted at unambiguity branch parameter p of 0 [30] (a) S-parameters magnitude, (b) Effective permittivity (ε_{yy}), Effective permeability (μ_{xx}) and refractive index (n).

Furthermore, the dimensions of the eSRR structure can be tuned in order to change its center frequency. Also, the relationship between each parameter of the eSRR metasurface structure and the operating frequency f_r at which the eSRR exhibits its fundamental transmission peak can be extracted numerically by fixing all the other parameters of the eSRR and tune such specific parameters. Then by using CST software, the scattering parameters are calculated and plotted as a function of the tuned parameter; also the resonance frequency f_r is plotted as a function of the tuned parameter. Finally linear regression curve fitting is used to find a closed form expression for the resonance frequency f_r as a function of the tuned parameter. Refer to the dimension parameter names of the eSRR shown in Fig. 6.17, the impact of each parameter on the resonance frequency of the eSRR with fixing the other parameter can be studied. Firstly, consider the impact of unit cell size a. The resonance frequency f_r, reflection coefficient and transmission coefficient the scattering parameters of the eSRR are plotted as a function of a as shown in Figs. 6.20 (a) (b), and (c), respectively. The dimensions are given in Table. 6.3. Using the linear regression, the resonance frequency can be given as a function of unit cell size a by this equation

$$f_r = -0.0025\,a + 0.5423$$

Table 6.3: dimensions of the eSRR when tuning the unit cell size a and fixing all the other dimensions

Parameter	*d*	*g*	h_1	h_2	*A*	*s*	*t*	*w*	*L*
Value (µm)	20	4	2	2	55:2.5:200	20	0.2	8	a-20

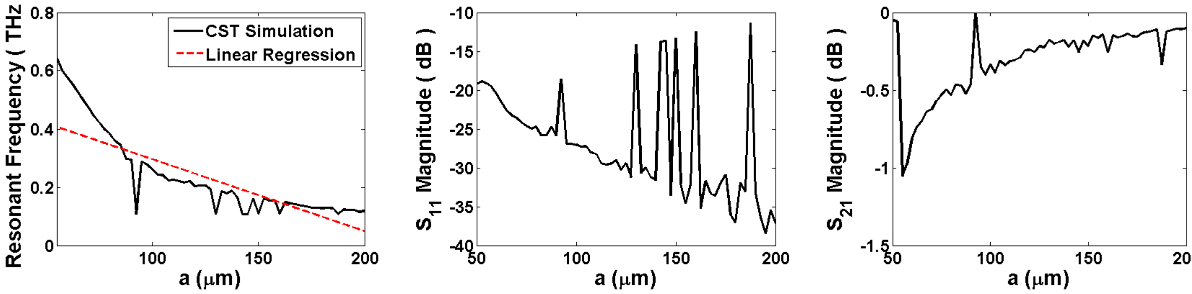

(a) (b) (c)

Fig. 6.20. Resonance frequency and scattering parameters magnitude versus unit cell size a of the eSRR, (a) resonance frequency f_r, (b) reflection coefficient S_{11} and (c) transmission coefficient S_{21}.

Secondly, consider the impact of the gap g on the resonance frequency. The resonance frequency f_r, reflection coefficient and transmission coefficient the scattering parameters of the eSRR are plotted as a function of g as shown in Figs. 6.21 (a), (b), and (c), respectively. The dimensions are given in Table. 6.4. The resonance frequency can be given as a function of g by this equation

$$f_r = 0.0146g + 0.2556$$

Table 6.4: dimensions of the eSRR when tuning the gap g and fixing all the other dimensions

Parameter	d	g	h_1	h_2	A	s	t	w	L
Value (µm)	20	1.4:0.4:30	2	2	110	20	0.2	8	90

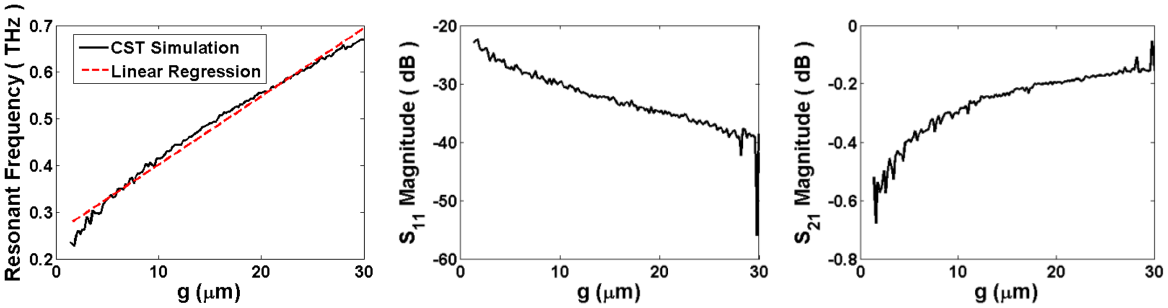

(a) (b) (c)

Fig. 6.21. Resonance frequency and scattering parameters magnitude versus gap g of the eSRR, (a) resonance frequency f_r, (b) reflection coefficient S_{11} and (c) transmission coefficient S_{21}.

Thirdly, consider the impact of the wire width “w” on the resonance frequency. The resonance frequency f_r, reflection coefficient and transmission coefficient the scattering parameters of the eSRR are plotted as a function of w as shown in Figs. 6.22 (a), (b), and (c), respectively. The dimensions are given in Table. 6.5. The resonance frequency can be given as a function of w by this equation

$$f_r = 0.0179\, w + 0.1800$$

Table 6.5: dimensions of the eSRR when tuning the wire width w and fixing all the other dimensions

Parameter	d	g	h_1	h_2	A	s	t	w	L
Value (µm)	20	4	2	2	110	20	0.2	2:2.5:20	90

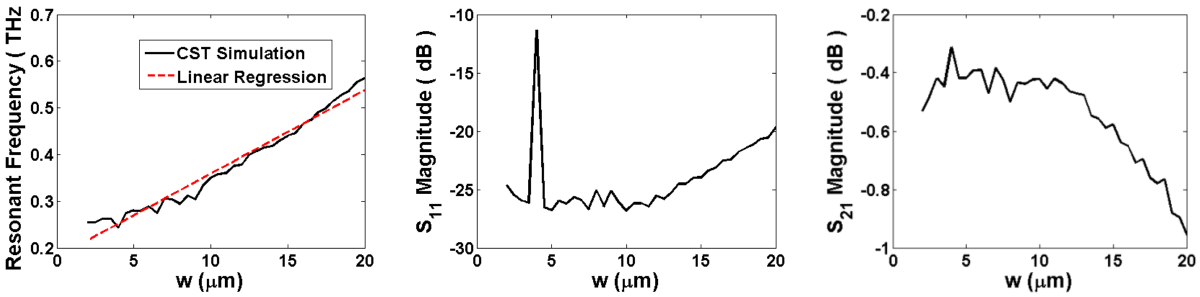

(a) (b) (c)

Fig. 6.22. Resonance frequency and scattering parameters magnitude versus wire width w of the eSRR, (a) resonance frequency f_r, (b) reflection coefficient S_{11} and (c) transmission coefficient S_{21}.

Finally, consider the impact of the gap length *d* on the resonance frequency. The resonance frequency f_r, reflection coefficient and transmission coefficient the scattering parameters of the eSRR are plotted as a function of *d* as shown in Figs. 6.23 (a), (b), and (c), respectively. The dimensions are given in Table. 6.6. The resonance frequency can be given as a function of *d* by this equation

$$f_r = -0.0025\ d + 0.3553$$

Table 6.6 dimensions of the eSRR when tuning center conduction length *d* and fixing all the other dimensions

Parameter	*d*	*g*	h_1	h_2	*A*	*s*	*t*	*w*	*L*
Value (μm)	8:0.5:70	4	2	2	110	20	0.2	8	90

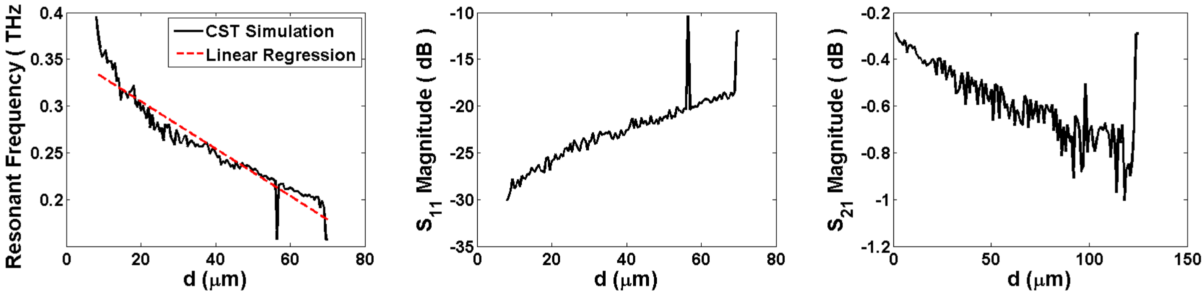

(a) (b) (c)

Fig. 6.23. Resonance frequency and scattering parameters magnitude versus gap length d of the eSRR, (a) resonance frequency f_r, (b) reflection coefficient S_{11} and (c) transmission coefficient S_{21}.

6.8. Design and Simulation of 303 GHz Antenna Incorporated with eSRR Metasurface Employing LEM Medium

Here, the proposed slotted waveguide antenna incorporated with eSRR metasurface structure employing anisotropic low epsilon medium (LEM) as shown in Fig. 6.8 is simulated and optimized using CST software. The proposed antenna dimensions are designed to operate at 303 GHz and the eSRR metasurface structure is optimized to exhibit anisotropic LEM around 303 GHz. The antenna is optimized by changing the size of the eSRR metasurface structure and the separation between the eSRR metasurface structure and the slotted waveguide antenna. Figure 6.24 (a) and 6.24 (b) show the return loss and the total efficiency versus frequency at main lobe direction of $\varphi = 0^o$ and $\theta = 0^o$ of the proposed antenna with and without anisotropic LEM MS of size 6×6×32 at different separation distance h_s between the slot and the MS bottom side and with slot size $(\mathrm{L}_s, \mathrm{W}_s)$ of (480 µm, 150 µm). Also the *E* and *H* planes radiation gains are plotted as shown in Figs. 6.24 (c) and 6.24 (d), respectively.

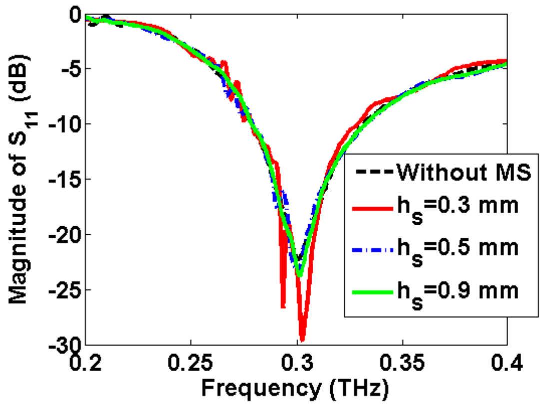

(a)

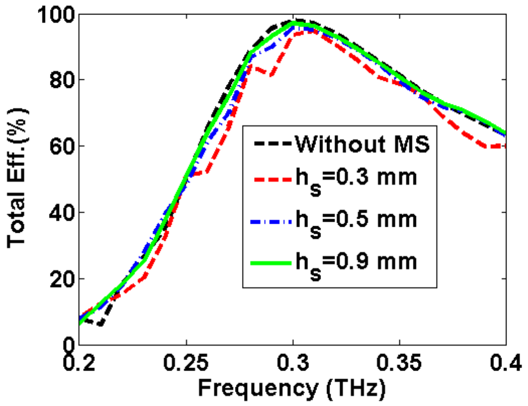

(b)

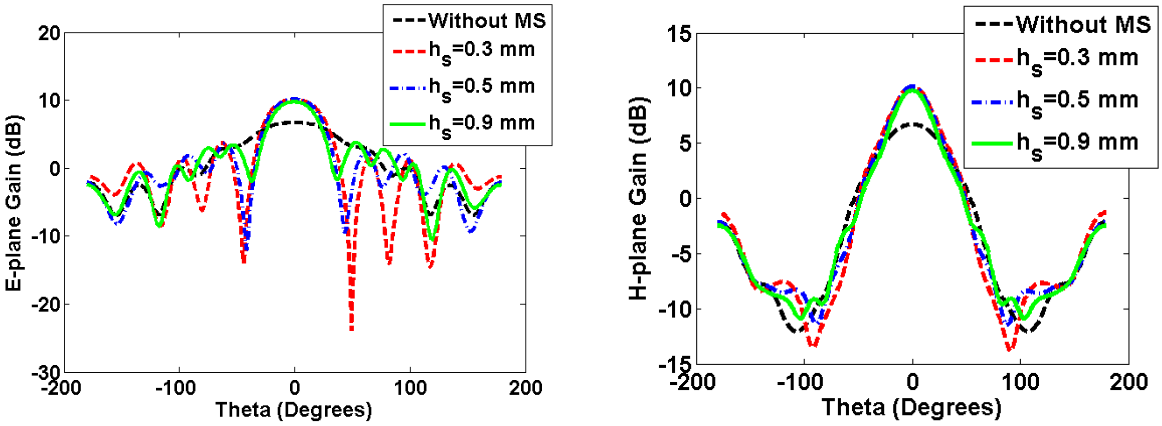

(c) (d)

Fig. 6.24. (a) The simulated return loss, (b) the simulated total efficiency versus frequency at main lobe direction of $\varphi = 0^o$ and $\theta = 0^o$, (c) E-plane gain, and (d) H-plane gain, for the proposed antenna with and without MS at different separation distance h_S between the slot and the MS structure size of 6×6×32 in x, y and z direction, respectively with 20 µm separation distance between each two MS layers.

It is clear from Fig. 6.24 that the separation distance h_s plays an important role in the impedance matching and the gain of the proposed antenna. The optimum separation distance h_s is 0.5 mm which is half wavelength. Figures 6.24 (c) and (d) illustrate that as the separation distance h_s increases the gain decreases. However, the radiation gain increase for the proposed antenna with anisotropic LEM MS and the beam area decreases in both *E* and *H* planes as shown in Figs. 6.24 (c) and 6.24 (d), respectively. At the optimum separation distance h_s of 0.5 mm, the *E*-plane and *H*-pane gains are increased from 6.7 to 10.1 dB, the *E*-plane gain is increased from 6.7 to 10.1 dB, while the beam area in the *H*-plane is reduced from 67.6 to 41.4 degrees and in the *E*-plane it is decreased from 94.1 to 47 degrees. It is clear that the BW and the total efficiency are slightly changed.

In addition, the effect of the anisotropic LEM MS sizes on return loss, total efficiency versus frequency, and *E*- and *H*-plane gains of the proposed antenna are studied and plotted as shown in Fig. 6.25. Figure 6.25 (a) and 6.25 (b) shows the return loss and the gain versus frequency of the proposed antenna with and without anisotropic LEM MS of different sizes and at a separation distance $h_s$of 0.5 mm. it is clear from Fig. 13 that the MS of size 6×6×32 has better return loss and gain than the other MS of sizes 6×6×8 and 6×6×16. In contrast the gain increases as the MS size increases, while the BW and total efficiency are slightly changed.

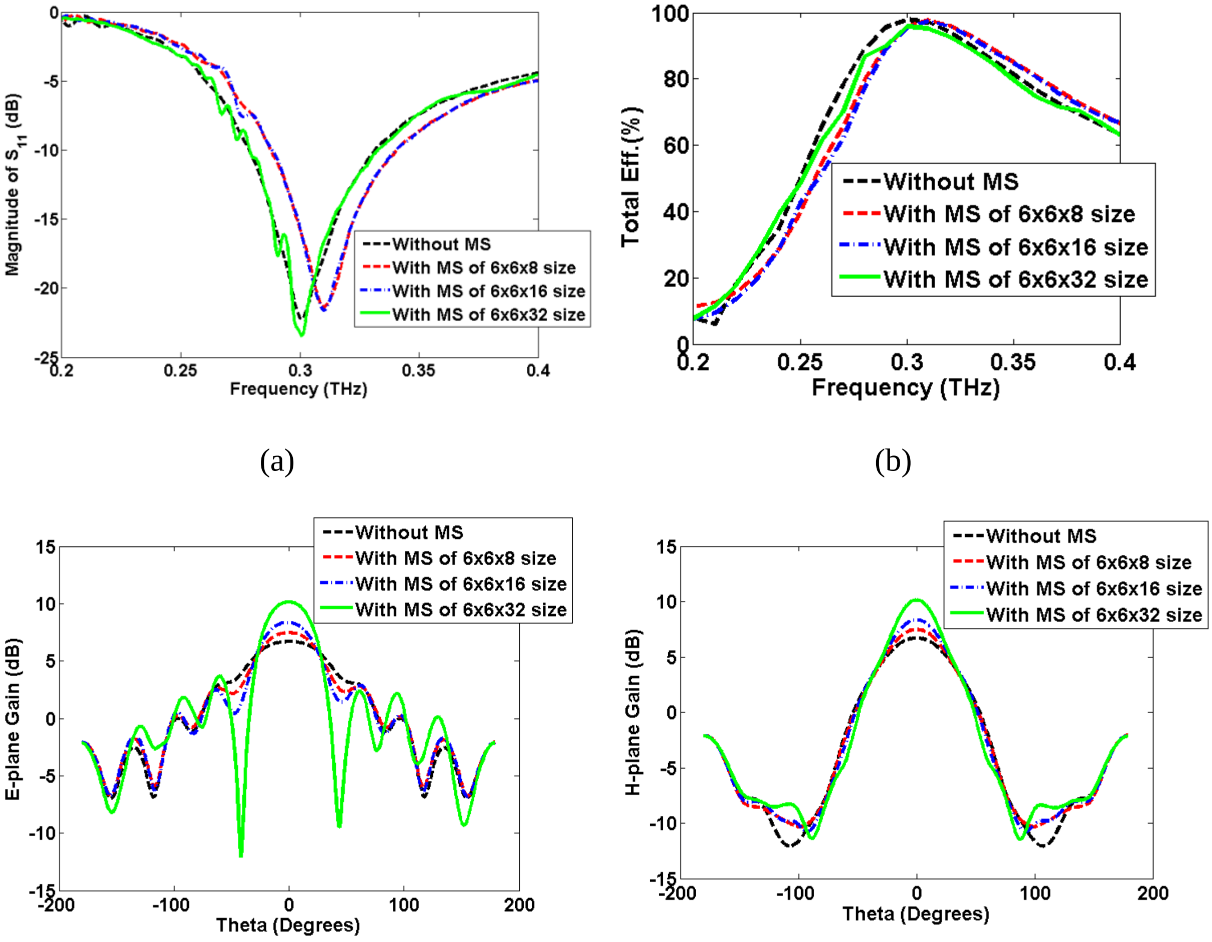

(a) (b)

(c) (d)

Fig. 6.25. (a) The simulated return loss, (b) the simulated total efficiency versus frequency at main lobe direction of $\varphi = 0^o$ and $\theta = 0^o$, (c) E-plane gain, and (d) H-plane gain, for the proposed antenna with and without MS at fixed separation distance h_s of 0.5 mm and different MS structure sizes with 20 μm separation distance between each two MS layers.

6.9. Summary

In this chapter, a slotted waveguide antenna incorporated with an eSRR metasurface structure employing anisotropic LEM medium in the direction of the radiated wave propagation was designed and fabricated. The eSRR metasurface structure was placed in front of the slotted waveguide antenna. Due to the anisotropy LEM property of the MS; the radiated spherical waves are converted to quasi-planar waves in the direction of the *E*-plane. As a result, the beam becomes more focused; the gain and the directivity of the *E*-plane are improved, while the beam area is reduced. The proposed antenna operating at 10 GHz was designed and optimized by using the CST software. The eSRR metasurface unit cell which has a transmission peak and the LEM MS around 10 GHz was designed and simulated using frequency domain solver with unit cell boundary conditions, the *S*-parameters were calculated and then the effective parameters of the metasurface are extracted from the *S*-parameters. The simulation results of the metasurface unit cell with infinite periodicity showed that, the eSRR structure exhibits LEM in the direction of the *E*-field polarization and has unity effective permittivity and permeability in the other two directions. The effect of periodicity truncation and the number of eSRR MS layers on the scattering parameters and the effective parameters of were studied. For experimental verification, the proposed antenna slotted waveguide antenna incorporated with anisotropic LEM MS eSRR structure was fabricated and measured. The measured results showed that, the *E*-plane gain of the proposed antenna improved from 6.5 dB to 9.5 dB, while the beam area reduced from 94.1 degrees to 45.1 degrees. The return loss and the bandwidth remained approximately the same. As a future work, a low mu medium (LMU) can be designed to focus the *H*-plane radiation pattern, also the proposed antenna can be scaled down and fabricated to operate in the THz frequency regime.

Hoverer, a proposed antenna operating at 303 GHz was designed and optimized by using the CST software. The eSRR metasurface unit cell which has a transmission peak and the LEM MS around 303 GHz was designed and simulated using the frequency domain solver with unit cell boundary conditions, the *S*-parameters were calculated and then the effective parameters of the metasurface extracted from the *S*-parameters. The simulation results of the metasurface unit cell with infinite periodicity showed that, the eSRR structure exhibits LEM in the direction of the *E*-field polarization and has unity effective permittivity and permeability in the other two directions. The effect of periodicity truncation and the number of eSRR MS layers on the scattering parameters and the effective parameters were studied. The simulated results showed that, the *E*-plane gain of the proposed antenna improved from 6.5 dB to 10.1 dB, while the beam area reduced from 94.1 degrees to 47 degrees. The return loss and the bandwidth and the total efficiency were slightly changed. As a future work, a low mu medium (LMU) can be designed to focus the *H*-plane radiation pattern and then proposed slotted waveguide antenna incorporated with both anisotropic low epsilon and low mu mediums to focus both the *E* and *H* planes fields such a structure can be designed, simulated, fabricated and measured.

6.10. References

[1] Abdelrehim, A.A. and Ghafouri-Shiraz, H., "Design of high performance slotted wave guide antenna based on electrically split ring resonator metasurface employing anaisotropic low epsilon meaduim for E plane beam focusing". Submitted to IET journal, 2017.

[2] Abdelrehim, A.A. and Ghafouri-Shiraz, H., "High performance terahertz slotted waveguide antenna based on electrically split ring resonator metasurface employing low epsilon medium for E-plane beam focusing". Microwave and Optical Technology Letters, 59(7), pp.1507-1517, 2017.

[3] Kang, M., Shen, N. H., Chen, J., Chen, J., Fan, Y. X., Ding, J., ... & Wu, P. (2008). A new planar left-handed metamaterial composed of metal-dielectric-metal structure. Optics Express, 16(12), 8617-8622.

[4] Pendry, J. B. (2000). Negative refraction makes a perfect lens. Physical review letters, 85(18), 3966.

[5] Zharov, A. A., Zharova, N. A., Noskov, R. E., Shadrivov, I. V., & Kivshar, Y. S. (2005). Birefringent left-handed metamaterials and perfect lenses for vectorial fields. New Journal of Physics, 7(1), 220.

[6] Grbic, A., & Eleftheriades, G. V. (2002). A backward-wave antenna based on negative refractive index LC networks. In Antennas and Propagation Society International Symposium, 2002. IEEE (Vol. 4, pp. 340-343). IEEE.

[7] Grbic, A., & Eleftheriades, G. V. (2002). Experimental verification of backward-wave radiation from a negative refractive index metamaterial. Journal of Applied Physics, 92(10), 5930-5935.

[8] X. Chen, H. F. Ma, X. M. Yang, Q. Cheng, W. X. Jiang, and T. J. Cui, “X-band high directivity lens antenna realized by gradient index metamaterials,” in Proc. Asia Pac. Microw. Conf. (APMC), 2009, vol. 1–5, pp. 793–797.

[9] Y.Yuan, C. Bingham, T. Tyler, S. Palit, T. H. Hand,W. J. Padilla, N.M. Jokerst, and S. A. Cummer, “A dual-resonant terahertz metamaterial based on single-particle electric-field-coupled resonators,” Appl. Phys. Lett., vol. 93, no. 19, p. 191110, 2008.

[10] N. I. Landy, S. Sajuyigbe, J. J. Mock, D. R. Smith, andW. J. Padilla, “Perfect metamaterial absorber,” Phys. Rev. Lett., vol. 100, no. 20, p. 207402, 2008.

[11] J.Y. Chin, J.N.Gollub, J. J.Mock, R. P. Liu, C.Harrison,D.R. Smith, and T. J. Cui, “An efficient broadband metamaterial wave retarder,” Opt. Express, vol. 17, no. 9, pp. 7640–7647, 2009.

[12] X. Chen, H. F. Ma, X. M. Yang, Q. Cheng, W. X. Jiang, and T. J. Cui, “X-band high directivity lens antenna realized by gradient index metamaterials,” in Proc. Asia Pac. Microw. Conf. (APMC), 2009, vol. 1–5, pp. 793–797.

[13] Z.G. Xiao and H. L. Xu, “Low refractiveMTMs for gain enhancement of horn antenna,” J. Infrared Millimeter Terahertz Waves, vol. 30, no. 3, pp. 225–232, 2009.

[14] Vaidya, A. R., Gupta, R. K., Mishra, S. K., & Mukherjee, J. (2012). High-gain low side lobe level Fabry Perot cavity antenna with feed patch array. Progress In Electromagnetics Research, 28, 223-238.

[15] Choi, W., Cho, Y. H., Pyo, C. S., & Choi, J. I. (2003). A high-gain microstrip patch array antenna using a superstrate layer. ETRI journal, 25(5), 407-411.

[16] "Parabolic reflector antennas." U.S. Patent 3,572,071, issued March 23, 1971.

[17] J. Pendry, 'Negative Refraction Makes a Perfect Lens', Phys. Rev. Lett., vol. 85, no. 18, pp. 4166-4169, 2000.

[18] Islam, M. M., Islam, M. T., Samsuzzaman, M., Faruque, M. R. I., Misran, N., & Mansor, M. F. (2015). A miniaturized antenna with negative index metamaterial based on modified SRR and CLS unit cell for UWB microwave imaging applications. Materials, 8(2), 392-407.

[19] Alibakhshi-Kenari, M., & Naser-Moghadasi, M. (2015). Novel UWB miniaturized integrated antenna based on CRLH metamaterial transmission lines. AEU-International Journal of Electronics and Communications, 69(8), 1143-1149.

[20] S. Enoch, G. Tayeb , P. Sabouroux, N. Guérin, and P. Vincent, “A Metamaterial for Directive Emission,” Physical Review Letters 89, 213902 (2002).

[21] H.L.Xu, Z. Y. Zhao,Y.G.Lv,C. L.Du, andX. A. Luo, “Metamaterial superstrate and electromagnetic band-gap substrate for high directive antenna,” Int. J. InfraredMillimeterWaves, vol. 29, no. 5, pp. 493–498, 2008.

[22] Y. G. Ma, P. Wang, X. Chen, and C. K. Ong, “Near-field plane-wavelike beam emitting antenna fabricated by anisotropic metamaterial,” Appl. Phys. Lett., vol. 94, no. 4, p. 044107, 2009.

[23] Q. Cheng, W. X. Jiang, and T. J. Cui, “Radiation of planar electromagnetic waves by a line source in anisotropic MTMs,” J. Phys. D—Appl. Phys., vol. 43, no. 33, p. 335406, 2010.

[24] Z. H. Jiang, M. D. Gregory, and D. H. Werner, “Experimental demonstration of a broadband transformation optics lens for highly directive multibeam emission,” Phys. Rev. B, vol. 84, p. 165111, 2011.

[25] Maritz, A. J. N. (2010). Investigation and design of a slotted waveguide antenna with low 3D sidelobes (Doctoral dissertation, Stellenbosch: University of Stellenbosch).

[26] Mahmud, R., He, T., Lancaster, M., Wang, Y., & Shang, X. (2014). Micromachined travelling wave slotted waveguide antenna array for beam-scanning applications.

[27] Li, Y., Mehdi, I., Maestrini, A., Lin, R. H., & Papapolymerou, J. (2011). A broadband 900-GHz silicon micromachined two-anode frequency tripler. IEEE Transactions on Microwave Theory and Techniques, 59(6), 1673-1681.

[28] Grabowski, Michal. "Non-Resonant Slotted Waveguide Antenna Design Method." High Frequency Electronics (2012): 32-46.

Arslanagić, S., Troels Vejle Hansen, N. Asger Mortensen, Anders Heidemann Gregersen, Ole Sigmund, Richard W. Ziolkowski, and Olav Breinbjerg. "A review of the scattering-parameter extraction method with clarification of ambiguity issues in relation to metamaterial homogenization." IEEE Antennas and Propagation Magazine 55, no. 2 (2013): 91-106.

Chapter 7 Developing High Performance X-band, millimetre waves and THz slotted waveguide antenna incorporated with GRIN Metasurface

In this chapter, X-band, mms and THz high performance slotted waveguide antennas operating at 10, 60, 100 and 200 GHz based on Gradient Refractive Index (GRIN) Metasurface (MTS) have been proposed, designed, and simulated. For verification purposes, 10 and 60 GHz are fabricated and measured. The proposed antennas are constructed by incorporating slotted waveguide antenna which can be fabricated by using the milling technology and MTS structure which can be fabricated by using the wet etching PCB technology. Two different structures of the proposed GRIN MTS has been developed; one based on the metallic patches 2D periodic structure mounted on dielectric substrate which works in the non-resonance mode and the other one is based on the annular slot 2D periodic structure which operates in the resonance mode. The metallic patch GRIN is used to construct a MTS with gradient surface impedance, consequently the phase velocity is modified and the MTS exhibits gradient index of refraction. So, a dispersion diagram can be used to design such a structure. In CST software, the Eigen mode solver was used to compute the dispersion diagram of the metallic patch GRIN MTS structure. Furthermore, the annular slot GRIN MTS was constructed from linearly or parabolic spatially distributed 2D annular slot periodic structure and it is designed based on Effective Medium Theory (EMT). The GRIN medium is placed in front of the antenna slot with an approximately half wavelength separation distance and the antenna performance parameters are computed numerically using the CST software. The proposed antennas are simulated and optimized in CST software at frequencies of 10, 60, 100 and 200 GHz. For verification purposes, 10 and 60 GHz antennas were fabricated and measured. The results showed that, the proposed antenna gain is improved from about 6.7 dB to 11.5 dB while the beam area is reduced from 107° and 67° to 40° and 25° for the *E* and *H* plane beams, respectively. The proposed antenna gain is improved by focusing the radiated beam based on the spatially distributed GRIN profile without significant influences on antenna bandwidth and impedance matching.

7.1. Introduction

Recently, metasurfaces have shared great contributions by inspiring various new antenna applications [1-2]. Metamaterial surfaces, electromagnetic bandgap (EBG) surfaces, artificial high-impedance surfaces are examples of metasurfaces. The main reason behind designing metasurfaces is to exhibit electromagnetic properties which often are not found in nature.

Metasurfaces can be realized by placing periodic metallization on a host dielectric medium with or without vias and it is denoted as a mushroom surface [3]. The mushroom surface works as an EBG surface which exhibits high-impedance for close-to-broadside plane wave reflection within the Epsilon Negative (ENG) frequency bandwidth. There are other realization methods for the metasurfaces which can exhibit soft and hard boundary conditions [4] and also it can be realized without the use of vias [5]. Since the metasurface is periodic structure, therefore it can be analysed by using Floquet mode theory for periodic structures before proceeding to a low-frequency regime homogenization process. Modulation of the surface impedance of the metasurface can be achieved by changing the geometrical parameters of the printed metallization. Surface impedance modulation has many applications in the design of microwave antennas and devices. Recently, metasurface have been applied in the holography principle where the non-directive source pattern is transformed into a pencil beam [6].

One of the more interesting methods for designing the metasurfaces is to design a surface with non-uniform surface impedance such that it mimics certain lens properties [7]. This method is gaining renewed interest under the impulse of the metasurfing concept [8]. Planar metasurface lenses have low profile and are simpler to manufacture compared to standard dielectric lenses, thus offering advantages for new communication antennas and sensor applications.

Classical dielectric lenses are very expensive due to their complex manufacturing process because they are constructed from several layers of various dielectrics with certain refractive index profiles. In addition, in order to achieve a relatively smooth refractive index profile, a large number of dielectric layers are needed [9] which causes high complexity in the whole manufacturing process. Metasurface lenses are considered as a best candidate that can overcome this problem. In Metasurface lenses, the variation of the surface impedance that corresponds to the refractive index can be made practically continuous since a large number of layers/pixels can be used. In this chapter, a planner GRIN MTS based metallic patch 2D periodic structure mounted on a dielectric substrate is proposed, designed, modelled and characterized at microwave, millimetre and terahertz frequencies for antenna applications.

7.2. Design of Metallic Patch GRIN MTS Employing Lens by Using Dispersion Diagram at 10, 60, 100 and 200 GHz

One of the interesting methods to design EM lens with high fabrication tolerance is based on GRIN MTS. The GRIN MTS can be constructed by gradually changing the boundary conditions of non-resonance MTS such as metallic patches printed on dielectric substrate. This method allows the fabrication of GRIN MTS operating at mms and THz waves by using wet etching PCB technology. The impact of changing one boundary conditions wall of the metallic patches printed on dielectric substrate is equivalent to changing the phase velocity of the propagating wave through the structure. Figure 7.1 shows 2D periodic structure of square metallic patches. The boundary conditions of the metallic patch unit cell can be changed in both *x* and *y* directions to construct GRIN MTS and hence to provide phase velocity and dispersion variations in the *x*-*y* plane and hence the propagating waves are focused. This allows variation in the macroscopic wave-front which happens in the conventional dielectric lens implemented from solid dielectric with variable index of refraction. The MTS GRIN is low profile and is easier to fabricate as compared with the conventional dielectric GRIN. As the boundary conditions of the metallic patch unit cell is changed uniformly, the index of refraction also changed uniformly and hence an inhomogeneous index of refraction is obtained. As shown in Fig. 7.1, the change in the metallic patch boundary conditions can be obtained by changing the rectangle patch sides *Lx* and *Ly* or the circular patch radius *r* or the substrate height *h*. In this work *Lx* and *Ly* are changed for the rectangular patch and *r* for the circular one.

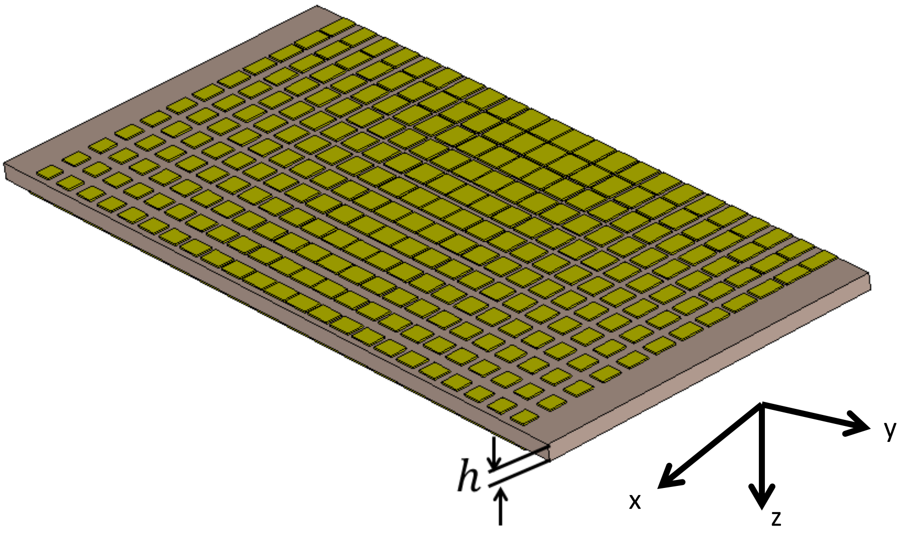

(a)

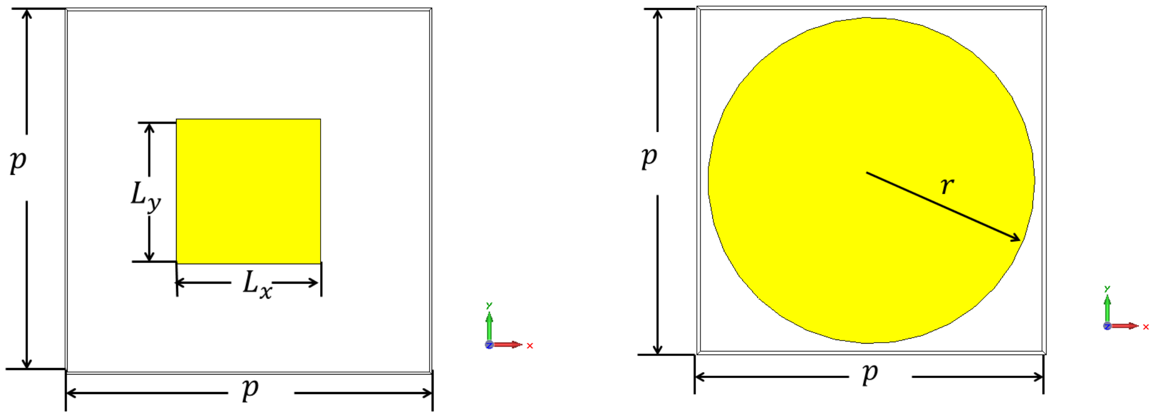

(b)

(c)

Fig. 7.1. Printed square patches on a dielectric substrate. Changing the patch sides controls the equivalent inhomogeneous surface impedance.

As it is reported in [10], when the profile of the index of refraction is parabolic spatially distributed across the aperture area, Luneburg lens can be implemented. Also, when the equivalent index of refraction n_{eq} is gradually changed with specific profile, the surface reactance X_s of the MTS is changed according to [10] as shown in Fig. 7.2

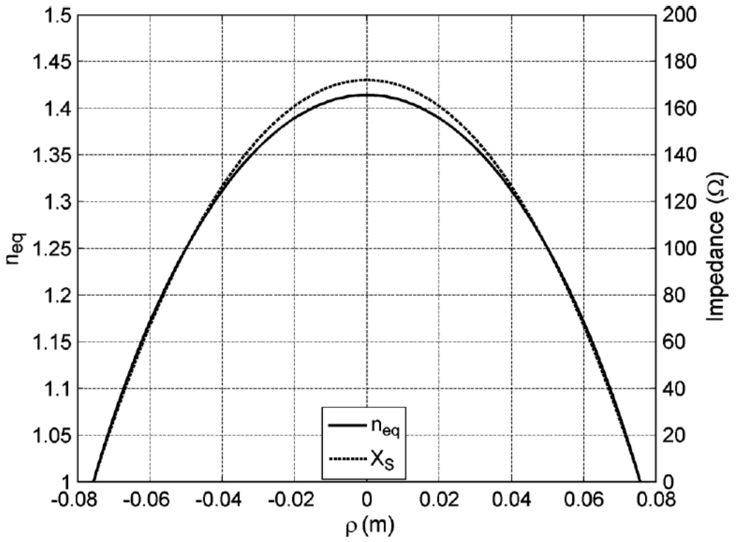

Fig. 7.2. Refractive index and reactance profile for the observed Luneburg lens case [10].

Since, as the index of refraction changed, the phase velocity, wave number, surface impedance and dispersion of the propagating wave are changed accordingly, so the dispersion diagram can be used to design GRIN MTS with the aid of CST Microwave Studio Eigen mode solver. Here, Microwaves (MWs), millimetres (mms) and THz non-resonance GRIN MTS structures operating at 10, 60, 100 and 200 GHz frequencies are designed based on dispersion diagram method. The GRIN MTS is constructed from 2D rectangular or circular patch of periodicity/unit cell size p in both x and y directions as shown in Figs 7.1(b) and 7.1(c), respectively. The rectangular patch has a length and a width of L_x and L_y, respectively while the circular patch has a radius r. The rectangular or circular metallic patch is mounted at the top of RT/Duriod 5880 substrate of relative permittivity ε_r of 2.2 and height h and the bottom side of the substrate is fully grounded.

Firstly, the metallic patch GRIN is designed at 10 GHz, modelled and simulated in CST using the Eigen mode solver. The rectangular patch GRIN is optimized using parametric analysis on the unit cell size p, and the patch dimensions and for each case the dispersion diagram is plotted. The goal is to design GRIN patch operating at 10 GHz and has a phase variation as the patch dimensions are changed at fixed unit cell size p. For the rectangular patch, two samples are designed. The first sample which is denoted as sample #1 and it has optimal unit cell size p of 9 mm and its patch length/width $L = L_x = L_y$ (setting it as a square) is changed from 8.5 to 4.1 mm. The second sample which is denoted as sample #2 and it has a unit cell size p of 9 mm and its patch length/width L is changed from 8.5 to 5.2 mm. The dispersion diagrams for samples #1 and #2 is plotted at the allowable maximum and the minimum patch side L as shown in Figs. 7.3 (a) and (b), respectively. For the circular patch GRIN, sample #3 is designed, simulated and optimized in CST software, it has optimal unit cell size p is 9.2 mm and then its patch radius r is reduced from 4.4 mm to 2 mm to get phase variation at 10 GHz. The dispersion diagram of sample #3 is plotted at the allowable maximum and the minimum patch radius as shown in Fig. 7.3 (c). All samples are mounted on RT/Duriod 5880 substrate of relative permittivity ε_r of 2.2 and height h of 0.508 mm. It is clear from Fig. 7.3 that sample #1, sample #2 and sample #3 have phase changes Δφ of 5.54°, 3.37° and 3.94°, respectively at 10 GHz.

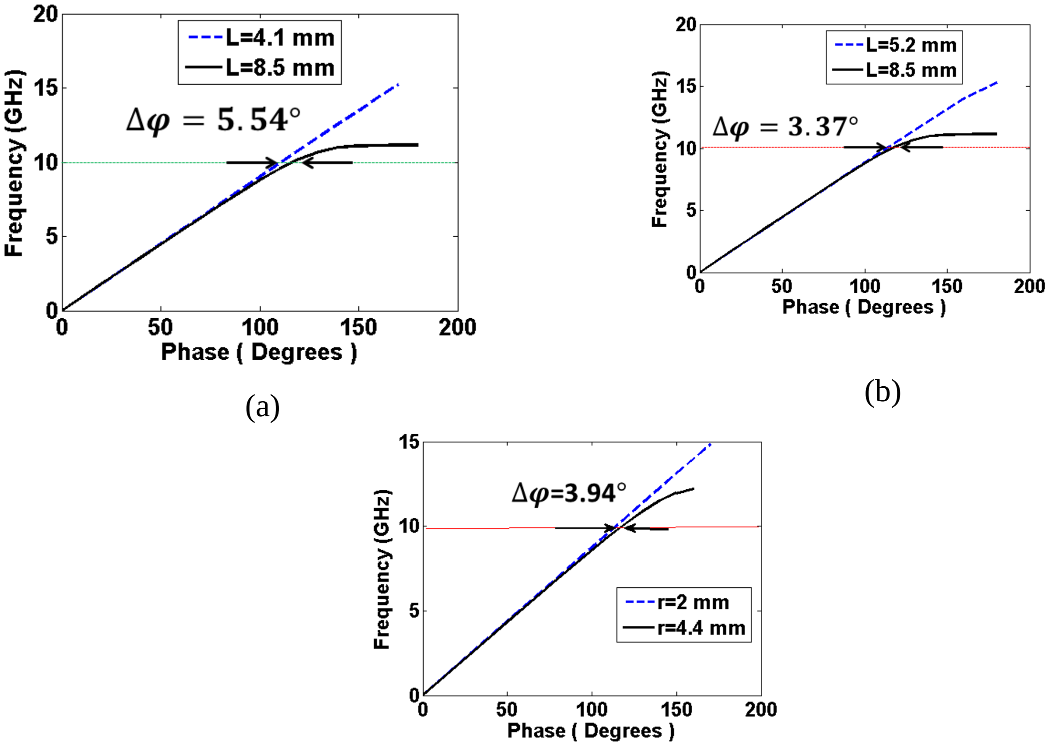

(a) (b)

(c)

Fig. 7.3. Dispersion diagram for the metallic patch GRIN MTS and its phase variation at 10 GHz for (a) sample #1 which is a rectangular patch of unit cell size p of 9 mm and patch its side L changes from 8.5 to 4.1 mm, (b) sample #2 which is a rectangular patch of unit cell size p of 9 mm and its patch side L changes from 8.5 to 5.2 mm, and (c) sample #3 which is a circular patch of unit cell size p of 9.2 mm and patch radius r changes from 4.4 to 2 mm.

Secondly, the metallic patch GRIN was designed at 60 GHz and simulated in CST using Eigen mode solver. Three different samples are designed and simulated. All samples have periodicity p of 1.5 mm. Samples #1 and #2 are rectangle patch, the patch side L is changed from 1.2 to 0.4 mm for sample #1 and from 1.2 to 0.45 mm for sample #2. Sample #3 is a circular patch and its patch radius r is changed from 1.2 to 0.45 mm. The dispersion diagrams for the three samples are plotted at the minimum and the maximum allowable patch sizes as shown in Fig. 7.4. All samples are mounted on RT/Duroid 5880 substrate of relative permittivity ε_r of 2.2 and height h of 0.127 mm. It is clear from Fig. 7.4 that, sample #1, sample #2 and sample 3 have phase variations Δφ of 28.39°, 27.13° and 35.18°, respectively at 60 GHz.

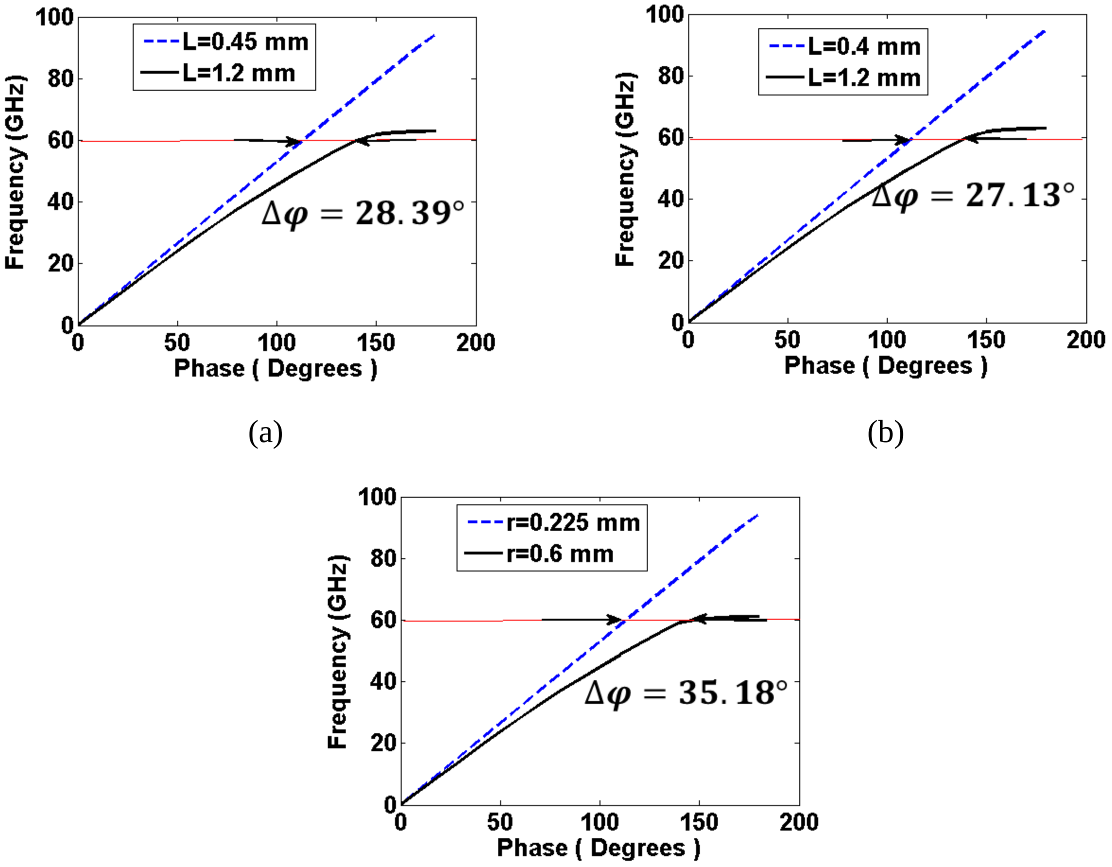

(a)

(b)

(c)

Fig. 7.4. Dispersion diagram for the metallic patch GRIN MTS and its phase variation at 60 GHz for (a) sample #1 which is a rectangular patch of patch side *L* changes from 1.2 to 0.45 mm, (b) sample #2 which is a rectangular patch of patch side *L* changes from 1.2 to 0.4 mm, and (c) sample #3 which is a circular patch of patch radius *r* changed from 1.2 to 0.45 mm. all samples have unit cell size *p* of 1.5 mm.

Thirdly, the metallic patch GRIN is designed at 100 GHz. Three different samples were designed and simulated in CST software using Eigen mode solver. All samples have periodicity *p* of 0.9 mm. Samples #1 and #2 are rectangle patch of patch side *L* changes from 0.75 to 0.425 mm for sample # 1 and from 0.75 to 0.41 mm for sample #2. Sample #3 is a circular patch of patch radius *r* changes from 0.375 to 0.21 mm. The dispersion diagrams for the three samples are plotted at the maximum and minimum allowable patch size as shown in Fig. 7.5. All samples are mounted on RT/Duriod 5880 substrate of relative permittivity ε_r of

2.2 and height *h* of 0.127 mm. It is clear from Fig. 7.5 that, sample #1, sample #2 and sample #3 have phase variations Δφ of 3.27°, 7.1° and 15.29°, respectively at 100 GHz.

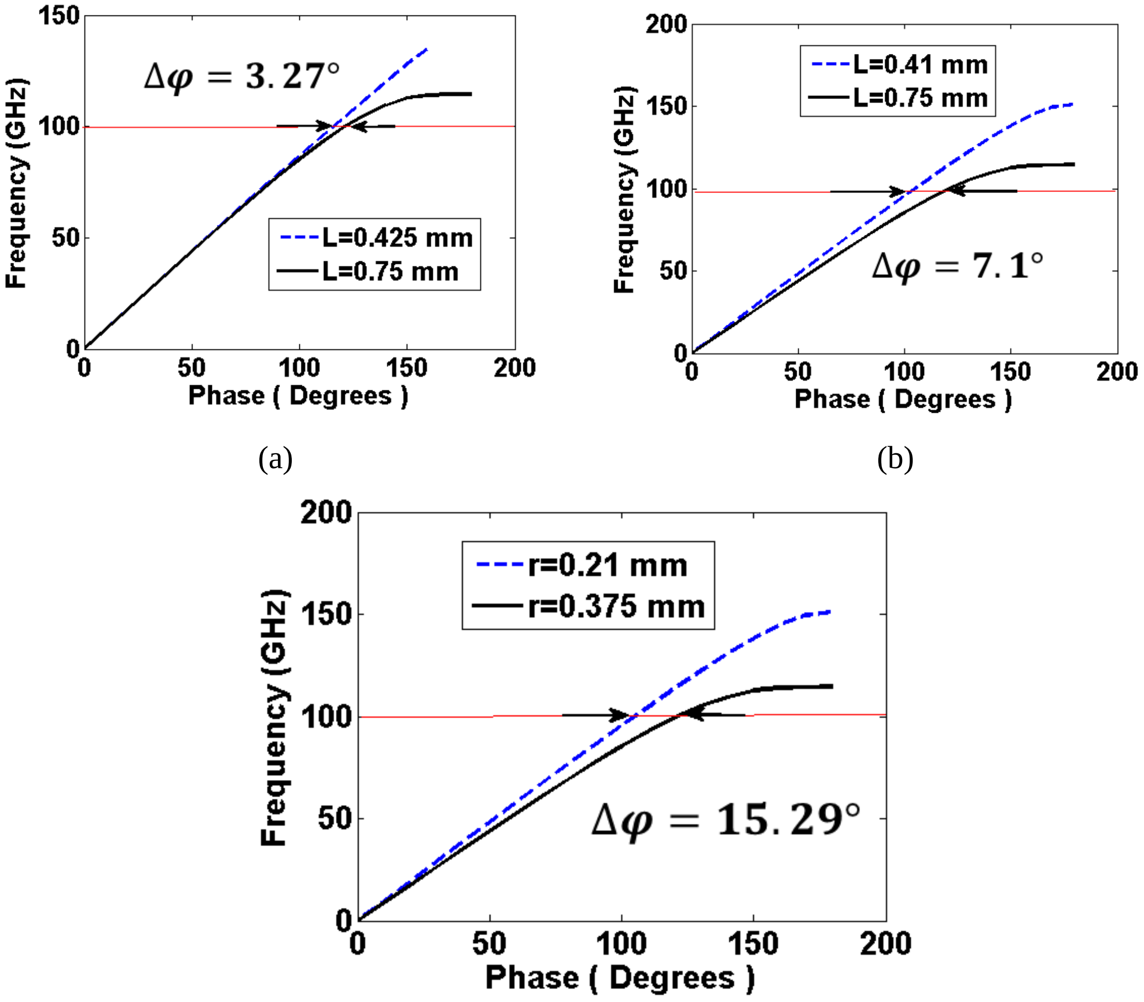

(a) (b)

(c)

Fig. 7.5. Dispersion diagram for the metallic patch GRIN MTS and its phase variations at 100 GHz for (a) sample #1 which is a rectangular patch of patch side *L* changes from 0.75 to 0.425 mm, (b) sample #2 which is a rectangular patch of patch side *L* changes from 0.75 to 0.41 mm, and (c) sample #3 which is a circular patch of patch radius *r* changes from 0.375 to 0.21 mm. all samples have unit cell size *p* of 0.9 mm.

Finally, the metallic patch GRIN is designed at 200 GHz. Two different samples are designed and simulated in CST software. All samples have periodicity *p* of 0.6 mm. Samples #1, and #2 are rectangle patch of patch side *L* changes from 0.35 to 0.225 mm for sample #1 and changes from 0.35 to 0.3 mm for sample #2. The dispersion diagrams for all samples at the minimum and maximum allowable patch side *L* are plotted as shown in Fig. 7.6. All samples are mounted on RT/Duriod 5880 substrate of relative permittivity ε_r of 2.2 and height h of 0.127 mm. It is clear from Fig. 7.6 that, sample #1 and sample #2 have phase variations Δφ of 11.94° and 9.34°, respectively at 200 GHz.

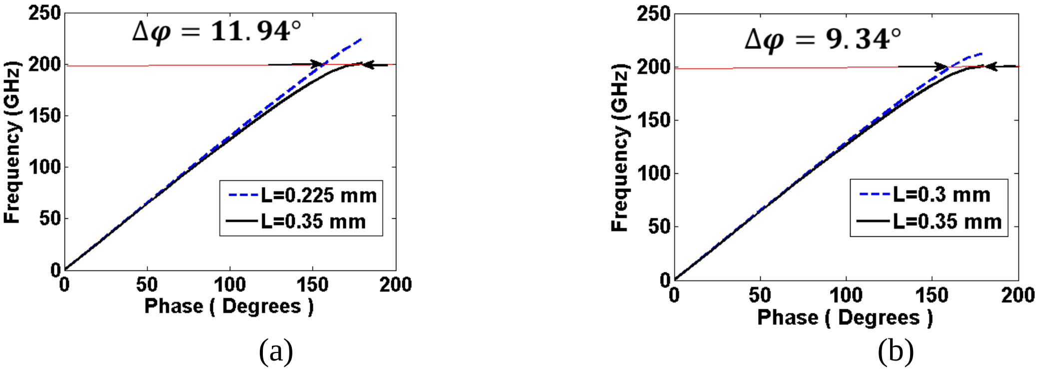

(a) (b)

Fig. 7.6. Dispersion diagram for the metallic patch GRIN MTS and its phase variation at 200 GHz for (a) sample #1 which is a rectangular patch of side L changes from 0.35 to 0.225 mm, and (b) sample #2 which is a rectangular patch of side L changes from 0.35 to 0.3 mm. All samples have unit cell size p of 0.6 mm.

7.3. Design and Simulation of 10 GHz Slotted Waveguide Antenna Incorporated with Metallic Patch MTS Employing GRIN Structure for Beam Focusing Purposes

Here, slotted waveguide antenna incorporated with two dimensional square or circular patch structures employing GRIN MTS is proposed, designed, simulated and optimized using CST EM solver. The function of the GRIN MTS structure is to improve the surface wave and hence focuses the radiation beam and as a result the antenna radiation parameters such as Gain, directivity and radiation efficiency are improved without significant change in the bandwidth. Figures 7.7 (a) and 7.7 (b) show the proposed antenna incorporated with square and circular patch GRIN MTS, respectively. The proposed antenna consists of the slotted waveguide antenna (shown in Figs 7.7 (c) through 7.7 (e)) and the GRIN MTS. The GRIN MTS structure is placed in front of the antenna slot with a horizontal separation distance d_z and vertical offset d_y measured from the centre of the slot as shown in Figs. 7.7 (f) and 7.7(g). The proposed antenna is designed at 10 GHz. The antenna is fed by rectangular waveguide WR-19 of dimensions a and b. The slot length and width are L_s and W_s, respectively. The waveguide length L_{wg} is 30 mm which equals the free space wavelength at 10 GHz. The waveguide side and top/bottom walls thicknesses are t_1 and t_2, respectively, while the slot wall thickness is t_3. The dimensions of the slotted waveguide antenna operating at 10 GHz are given in Table. 7.1. The impact of the GRIN MTS size, the horizontal distance d_z and vertical offset d_y on the 10 GHz proposed antenna performance are displayed in the next subsections.

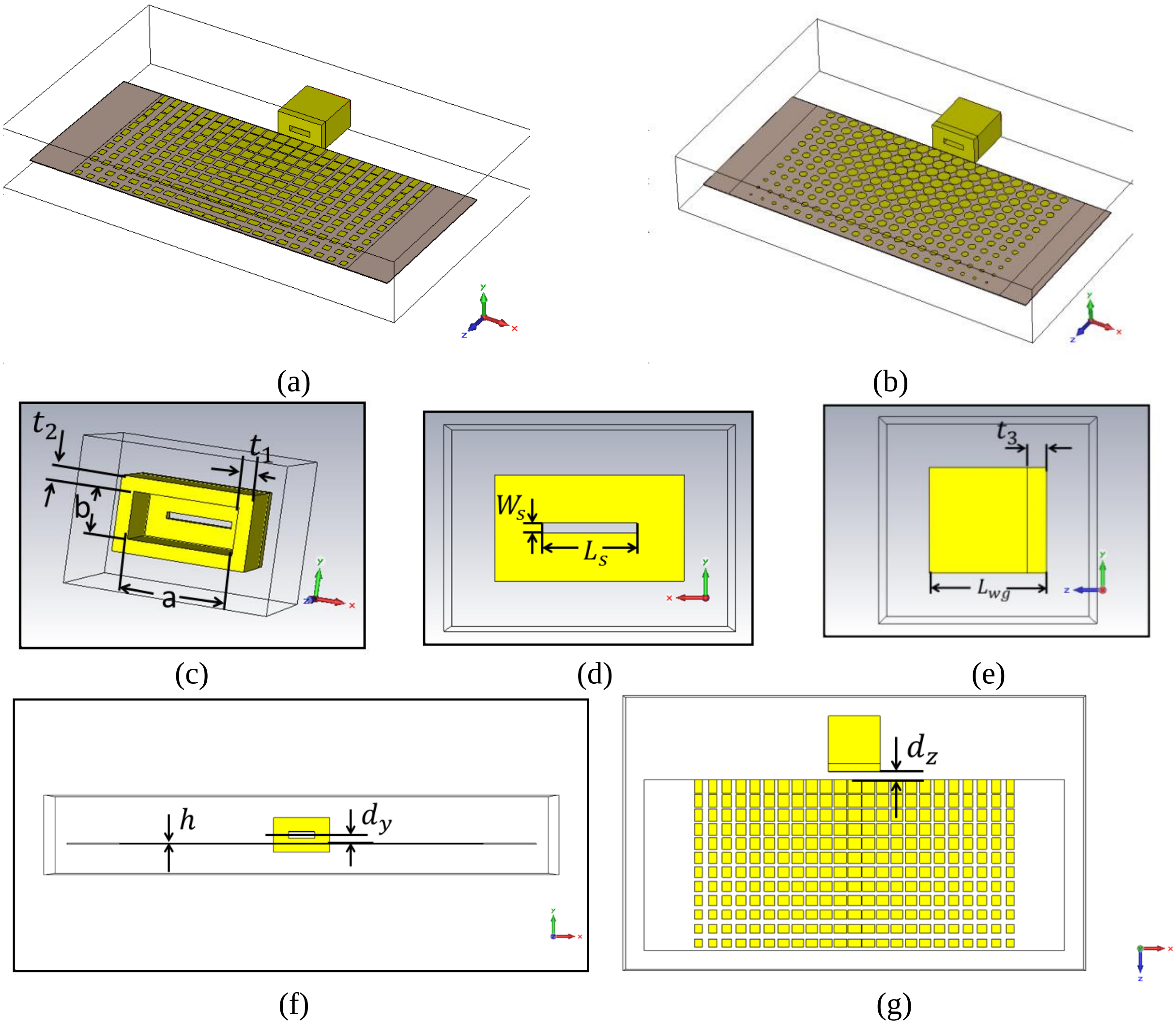

Fig. 7.7. The proposed 10 GHz slotted waveguide antenna incorporated with GRIN MTS constructed from (a) 2D rectangular patch metasurface and (b), 2D circular patch metasurface, (c), (d) and (e) are the slotted waveguide antenna, (f) and (g) are the side and top views of the proposed slotted waveguide antenna incorporated with 2D GRIN MTS structure.

Table 7.1 dimensions of the 10 GHz proposed antenna incorporated with MTS GRIN structure.

Parameter	a	b	L_{wg}	t_1	t_2	t_3	L_s	W_s	p	h	d_z	d_y
Dimensions (mm)	22.86	10.16	30	5	5	5	15.2	4	9	0.508	1:0.5:5	-1:-0.5:-7

7.3.1. Impact of Metallic Patch GRIN Metasurface Size on the Proposed Antenna Performance

Here, the impact of the GRIN MTS size on the proposed antenna performance is studied. The proposed antenna incorporated with three GRIN MTS samples of different sizes are modelled and simulated in CST software. The GRIN MTS samples are constructed from metallic rectangular and/or circular patches mounted on a grounded dielectric substrate. The dimensions of the samples are given in Table 7.2 and their phase variations $\Delta\varphi$ are presented in Fig. 7.3. It should be noted that, samples #1 and #2, are square patches and their GRIN profiles is linearly distributed while sample #3 is circular patch with parabolic distributed GRIN profile. The GRIN profiles distribution is linearly for square patches and parabolic for circular patches in both x and y directions. The horizontal distance d_z and the vertical offset d_y of the Metasurface with respect to the centre of the antenna slot are set at 2.5 mm and -5 mm, respectively. The impedance matching and the radiation parameters of the proposed antenna are calculated and extracted using CST software. The results of the proposed antenna incorporated with the different samples are plotted and compared as in Fig. 7.8. The antenna performance key parameters such as Fractional Bandwidth FBW, the reflection coefficient S_{11}, radiation efficiency η_{rad} , E and H planes gains and Half Power Beam Widths (HBPWs), main lobe directions and the side lobe level are reported in Table 7.2.

Table 7.2 Impact of GRIN MTS structure size and step size on the 10 GHz proposed antenna performance

Parameters	Sample #1	Sample #2	Sample #3
Periodicity *p*	9	9	9.2
GRIN structure profile	Square patches of L_x *and* L_y which are 2D linearly distributed of 8.5:-0.4:4.1	Square patches of L_x *and* L_y which are 2D linearly distributed of 8.5:-0.3:5.2	Circular patches of r=4.4 to 2 with parabolic 2D spatial distribution
Size ($N_x \times N_z$)	23×12	23×12	23×12
d_z	2.5	2.5	2.5
d_y	-5	-5	-5
FBW (%)	10.425	10.575	11.474
S_{11} at 10 GHz (dB)	-42.739, shifted to 10.084 GHz	-40.014, shifted to 10.079 GHz	-33.472, shifted to 10.081 GHz
η_{rad} (%)	98.86	99.69	97.47
η_{tot} (%)	98.52	99.35	97.19
E-plane HPBW (°) , Gain (dB), main lobe (°) direction (°), and side lobe level (°)	30, 10.6, 23, and -5.4	30.4, 10.6, 22, and -5.5	30.2, 10.3, 23, and -4.9
H-plane HPBW (°) , Gain (dB), main lobe (°) direction (°), and back lobe level (°)	74.7, 6.85, 2 and -14.4	74.9, 7, -1, and -14.6	75.6, 6.57, 0 and -13.4

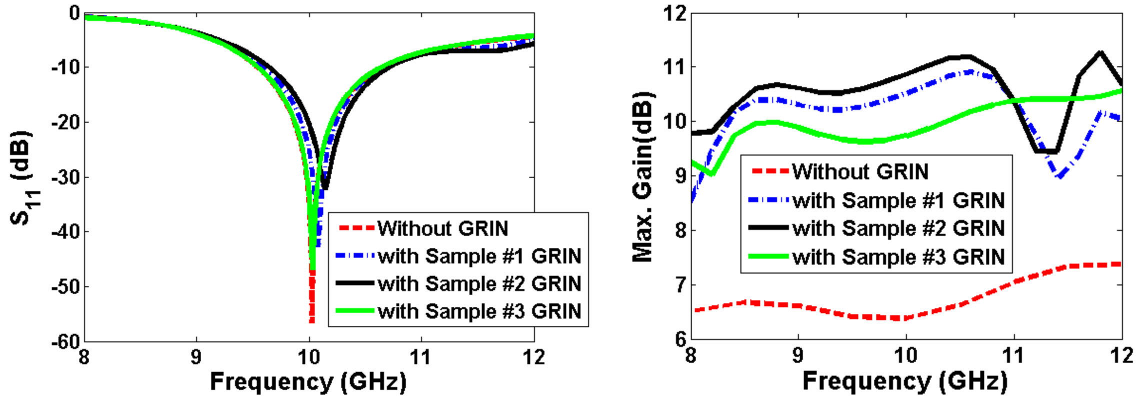

(a) (b)

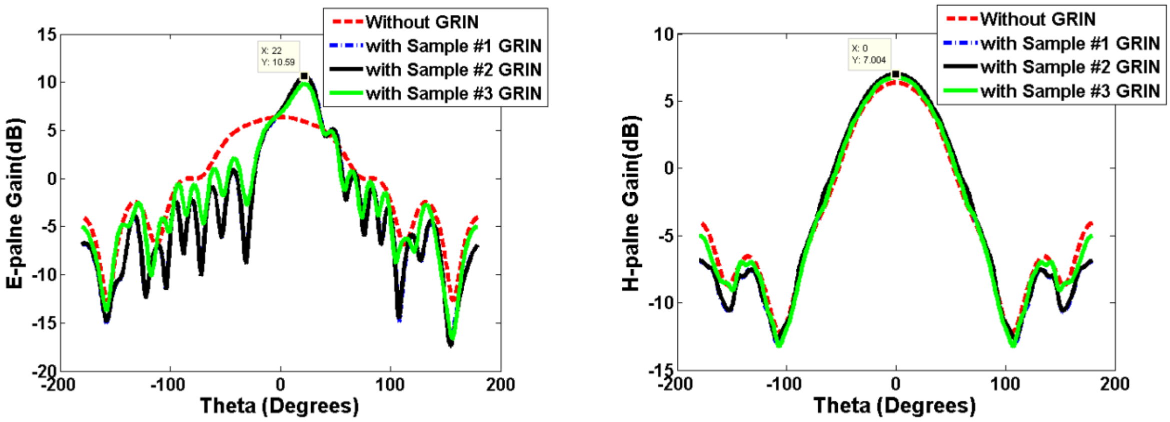

(c) (d)

Fig. 7.8. Impedance matching and radiation parameters of the proposed slotted waveguide antenna with and without GRIN MTS structure at different GRIN MTS sample sizes , (a) magnitude of S_{11}, (b) magnitude of maximum gain versus frequency, (c) *E*-pane gain and (d) *H*-plane gain. Samples #1 and #2 are GRIN structure of equal x and y direction periodicities of p=9. The rectangular patches GRIN profiles are linearly gradient distributed in x and y directions of patch dimensions Lx and Ly are changed from 8.5 to 4.1 with step 0.4 for sample 1 while the patch dimensions Lx and Ly are changed from 8.5 to 5.2 with step 0.3 for sample 2. For sample #3, GRIN profile is parabolic distributed in both x and y directions. The horizontal distance d_z and the vertical offset d_y of the Metasurface with respect to the centre of the antenna slot are set at 2.5 and -5, respectively. All dimensions are in mms.

It is clear from Fig. 7.8 and Table 7.2 that, the GRIN MTS structure improves the *E*-plane gain from 6.5 to 10.6 dB while the beam area is reduced from about 107 to 30 degrees. Also, as the aperture of the GRIN MTS increases, the beam becomes more focused and hence more improvement in the antenna gain is obtained. Samples #2 is considered as the optimal GRIN MTS size, since it provides the best antenna parameters compared to samples #1 and #3.

7.3.2. Impact of Horizontal Spacing between the Antenna Slot and Metallic Patch GRIN Metasurface on the Proposed Antenna Performance

Here, the effect of the horizontal spacing between the antenna slot and the GRIN MTS structure on the proposed antenna performance is studied. The slotted antenna is incorporated with sample #2 presented in the last subsection and then horizontal spacing d_z is changed from 2 to 5 mm with step size of 2.5 mm to optimize d_z while the vertical offset d_y is set at -

5 mm. The antenna performance parameters are computed in CST software for different horizontal spacing d_z and plotted as shown in Fig. 7.9.

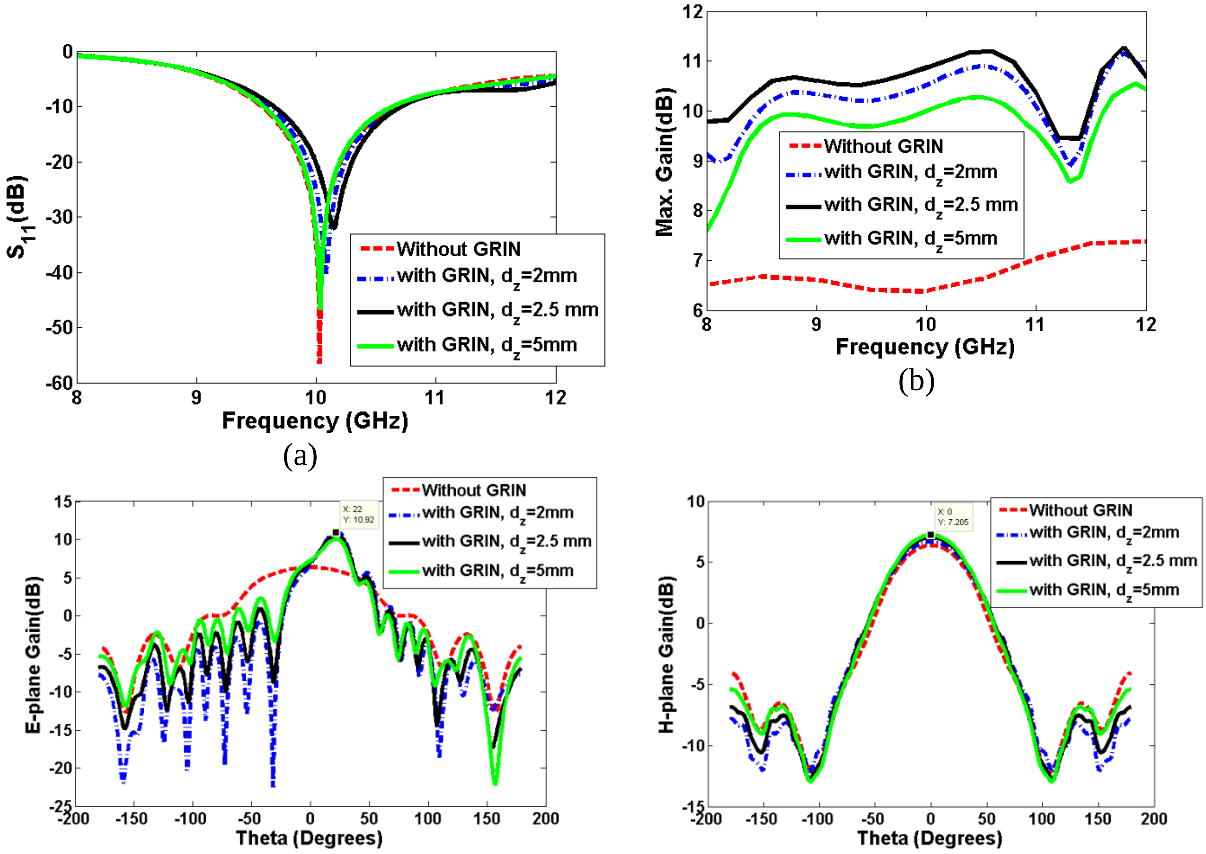

(a) (b)

(c) (d)

Fig. 7.9. Impedance matching and radiation parameters for the proposed slotted waveguide antenna with and without GRIN MTS structure of sample #2 size, at different horizontal spacing d_z, (a) magnitude of S_{11}, (b) magnitude of maximum gain versus frequency, (c) E-pane gain and (d) H-plane gain. The vertical offset d_y of the Metasurface with respect to the centre of the antenna slot is set at -5 mm.

It is clear from Fig. 7.9 that, the optimal E-plane gain of 10.92 dB is obtained at d_z spacing of 2.5 mm. Also, as d_z increases, the H-plane gain increases and the E-plane gain decreases. Furthermore, the antenna has good impedance matching mostly for all d_z spacing and the antenna bandwidth is slightly changed by changing d_z.

7.3.3. Impact of Vertical Offset between the Antenna Slot and Metallic Patch GRIN Metasurface on the Proposed Antenna Performance

Here, the impact of the vertical offset between the antenna slot and the GRIN MTS structure on the proposed antenna performance is studied. The proposed slotted antenna is incorporated with sample #2 presented in subsection 7.3.1, the vertical spacing d_z is set at 2.5 mm and the vertical offset d_y is optimized . The GRIN MTS is offset from the centre of the slot vertically with -2.5, -5 and -7 mm in the y-direction and for each offset distance; the antenna performance parameters are calculated and extracted using CST software. Figure 7.10 illustrates the reflection coefficient S_{11}, maximum gain versus frequency, and E and H planes gains for the proposed antenna with and without GRIN MTS at different vertical offset d_y.

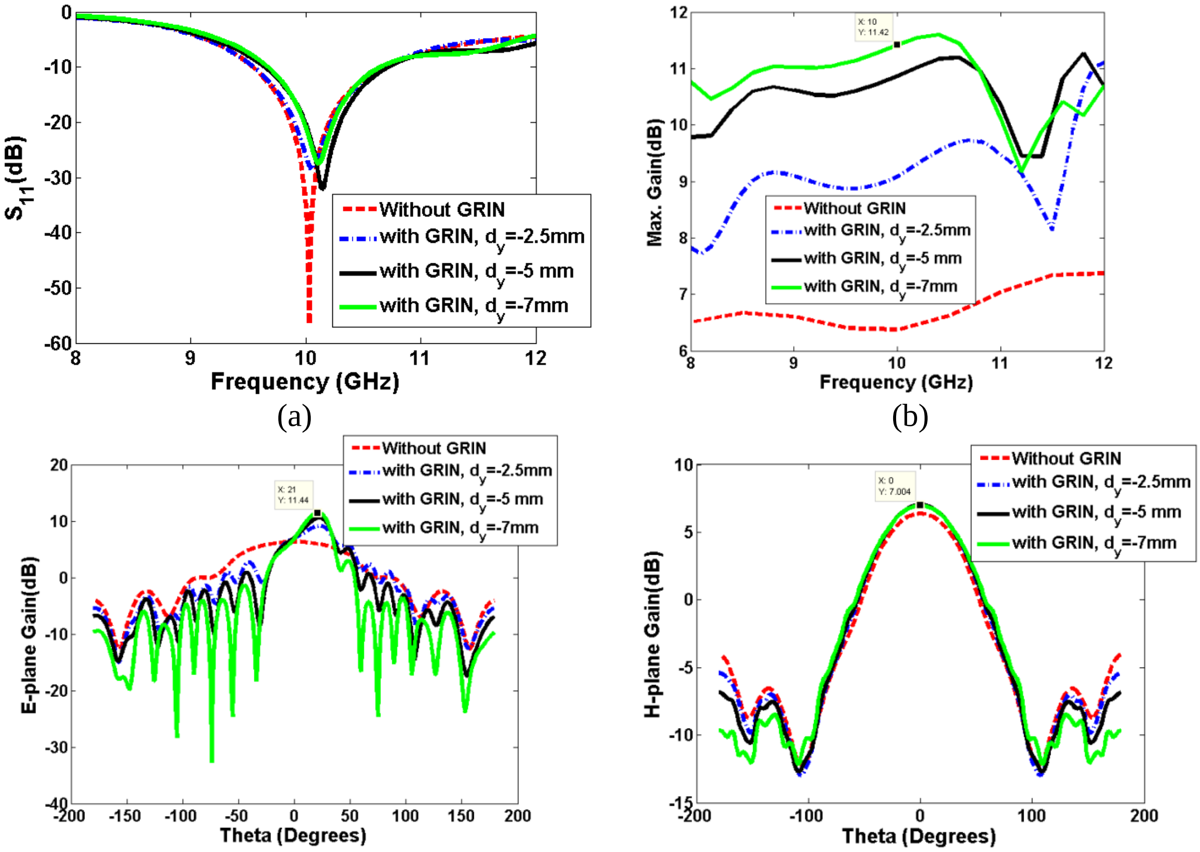

(a) (b)

(c) (d)

Fig. 7.10. Impedance matching and radiation parameters for the proposed slotted waveguide antenna with and without GRIN MTS structure of sample #2 size, at different vertical offset d_y, (a) magnitude of S_{11}, (b) magnitude of maximum gain versus frequency, (c) E-pane gain and (d) H-plane gain. The horizontal spacing d_z of the Metasurface with respect to the centre of the antenna slot is set at 2.5 mm.

It is clear from Fig. 7.10 that as d_y increases the side lobe level decreases and the E-plane gain increases too while the H-plane gain is slightly changed. The optimal E-plane and H-plane gains are 11.44 dB and 7 dB, respectively at d_y of -7 mm. the HPBW for E-plane and H-plane are 75° and 30°, respectively. This means d_y is optimized at -7 mm.

7.4. Design, Simulation and Optimization of 60 GHz Slotted Waveguide Antenna Incorporated with Patch GRIN MTS Structure

The proposed slotted waveguide antenna incorporated with GRIN MTS structure presented in section 7.3 is redesigned to operate at 60 GHz for millimetre waves wireless communication applications including WLAN and WPAN. The structure of the antenna is shown in Fig. 7.7 and the 60 GHz proposed antenna dimensions are given in Table. 7.3. The 60 GHz is excited by WR-15 waveguide with dimensions *a* and *b* presented in Table 7.3. The horizontal spacing d_z and the vertical offset d_y between the GRIM MTS structure and the centre of the slot are optimized using CST software. The optimal d_z and d_y are 1.5 and -1 mm, respectively. Three 2-D GRIN MTS samples of different sizes are designed with dimensions and GRIN profiles given in Table. 7.4. The dispersion diagrams of the three samples are given in Fig. 7.4. The impact of the 2-D GRIN MTS structure size on the antenna performance is studied and the proposed antenna is simulated in CST at different samples sizes and at optimal horizontal spacing d_z and vertical offset d_y of 1.5 and -1 mm, respectively. Figure 7.11 shows the proposed antenna performance key parameters including reflection coefficient S_{11}, maximum gain versus frequency, *E* and *H* planes gain.

Table 7.3 dimensions of the 60 GHz proposed antenna incorporated with GRIN MTS structure.

Parameter	a	b	L_{wg}	t_1	t_2	t_3	L_s	W_s	p	L	r	h	d_z	d_y
Dimensions (mm)	3.759	1.880	10	1	1	1	2.61	1	1.5	1.2:0.4	0.6:0.225	0.13	1	-0.75

Table 7.4 Impact of GRIN MTS structure size and step size on the 60 GHz proposed antenna performance

Parameters	Sample #1	Sample #2	Sample #3
Periodicity, p (mm)	1.5	1.5	1.5
Rectangle patch side, L (mm) or circular patch radius *r* (mm)	L=1.2:-0.1:0.4	L=1.2:-0.075:0.45	$r_{max} = 0.6$ and $r_{min} = 0.225$
Refractive index profile	Linearly distributed	Linearly distributed	Parabolic distributed
Size ($N_x \times N_z$)	17×9	21×11	21×11
d_z (mm)	1.5	1.5	1.5
d_y (mm)	-1	-1	-1

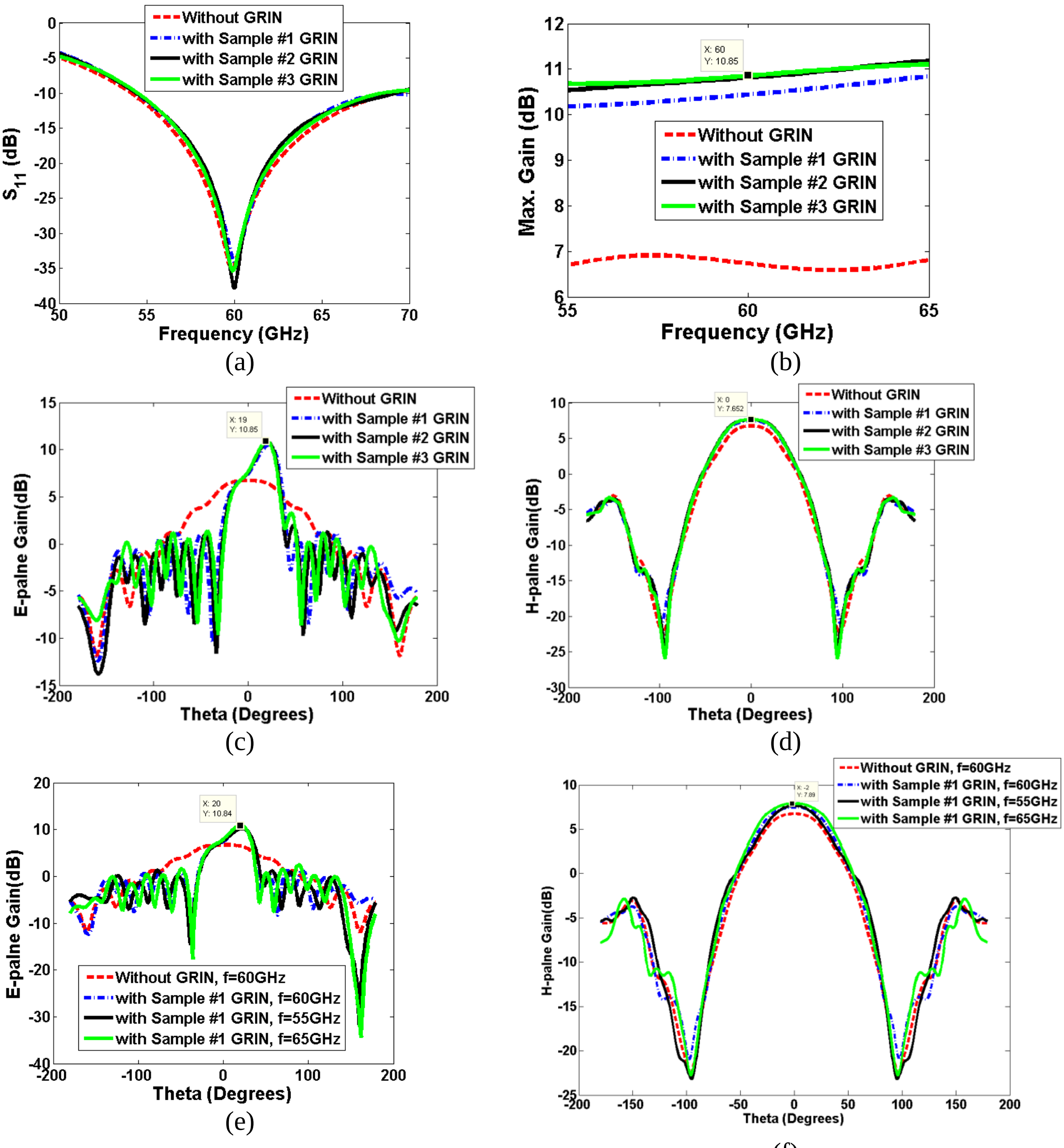

(a) (b) (c) (d) (e) (f)

Fig. 7.11. Impedance matching and radiation parameters for the proposed slotted waveguide antenna operating at 60 GHz with and without GRIN MTS structure at different GRIN MTS sample sizes, (a) magnitude of S_{11}, (b) magnitude of maximum gain versus frequency, (c) *E*-plane gain, (d) *H*-plane gain, (e) and (f) are *E* and *H* plane gains at three different frequencies inside the antenna bandwidth, respectively. The horizontal distance d_z and the vertical offset d_y of the Metasurface with respect to the centre of the antenna slot are set at 1.5 mm and -1 mm, respectively.

It is clear from Fig. 7.11 that, the optimal gain is obtained for samples #3 GRIN MTS of circular metallic patch with parabolic distributed index of refraction. The *E* and *H*-plane gains are improved from 6.7 dB (for both) to 10.85 dB and 7.67 dB, respectively. Also the impedance matching is good for all samples and the bandwidth is slightly reduced while the *E*-plane HPBW decreases from 106.8° and to 29° and the *H*-plane HPBW remains approximately the same at 65.8° . The improvement in the antenna gain and the reduction in the HPBW are due to beam focusing caused by spatially variation of the refractive index across the aperture near field area of the antenna. Such index of refraction spatially variation of GRIN profile of the MTS employing spatially surface impedance variation which enables the structure to work as a lens and in return it focuses the radiated waves in the far field and hence gain improvement occurs. Also, it is clear from Figs. 7.11 (e) and 7.11(f) that, *E* and *H* plane gains are slightly changed at the bandwidth edges and centre frequencies of 55, 65 and 60 GHz.

7.5. Design, Simulation and Optimization of 100 GHz Slotted Waveguide Antenna Incorporated with Patch GRIN MTS Structure

The proposed slotted waveguide antenna incorporated with GRIN MTS structure presented in section 7.3 is redesigned to operate at 100 GHz for millimetre waves wireless communication applications with high bit rate. Also it can be used for board to board communications to develop High Performance Computing (HPC). The structure of the antenna is shown in Fig. 7.7. The dimensions of the 100 GHz antenna incorporated with GRIN MTS are given in Table. 7.5. The 100 GHz is excited by WR-10 waveguide with dimensions a and b presented in Table 7.5. The impact of the 2-D GRIN MTS structure size on the antenna performance is studied and the proposed antenna is simulated in CST at horizontal spacing d_z and vertical offset d_y of 1 and -0.75 mm, respectively. Three 2-D GRIN MTS samples of different sizes are designed with dimensions given in Table. 7.6. The dispersion diagrams of the three samples are given in Fig. 7.5. the proposed antenna incorporated with GRIN MTS of different sizes is simulated in CST software and the results are plotted in Fig. 7.12 which shows the proposed 100 GHz antenna performance key parameters including reflection coefficient S_{11}, maximum gain versus frequency, E and H planes gain, 3-D maximum gain. Also, the E-field magnitude and surface current on the structure are plotted as in Figs. 7.12 (h) and 7.12 (i).

Table 7.5 dimensions of the 100 GHz proposed antenna incorporated with MTS GRIN structure.

Parameter	a	b	L_{wg}	t_1	t_2	t_3	L_s	W_s	p	L	r	h	d_z	d_y
Dimensions (mm)	2.54	1.27	9	2.5	0.2	0.2	1.5	0.5	1	samples #1, and #2	Sample #3	0.13	1	-0.75

Table 7.6 Impact of GRIN MTS structure size and step size on the 100 GHz proposed antenna performance

Parameters	Sample #1	Sample #2	Sample #3
Periodicity, P (mm)	1	1	1
Rectangle patch side, L (mm) or circular patch radius r (mm)	L=0.75:-0.025:0.425	L=0.75:-0.02:0.41	$r_{max} = 0.375$ and $r_{min} = 0.21$
Refractive index profile	Linearly distributed	Linearly distributed	Parabolic distributed
Size ($N_x \times N_z$)	27×14	35×18	19×10
d_z (mm)	1	1	1
d_y (mm)	-0.75	-0.75	-0.75

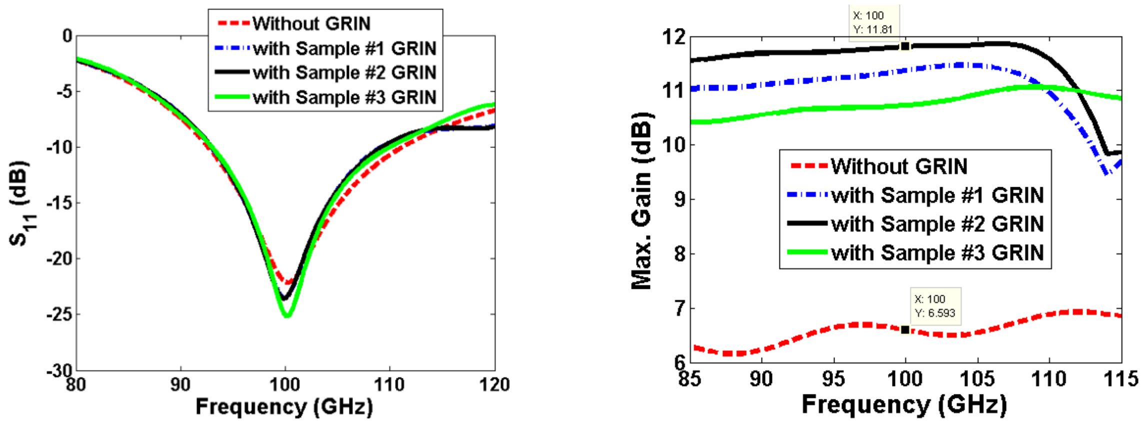

(a) (b)

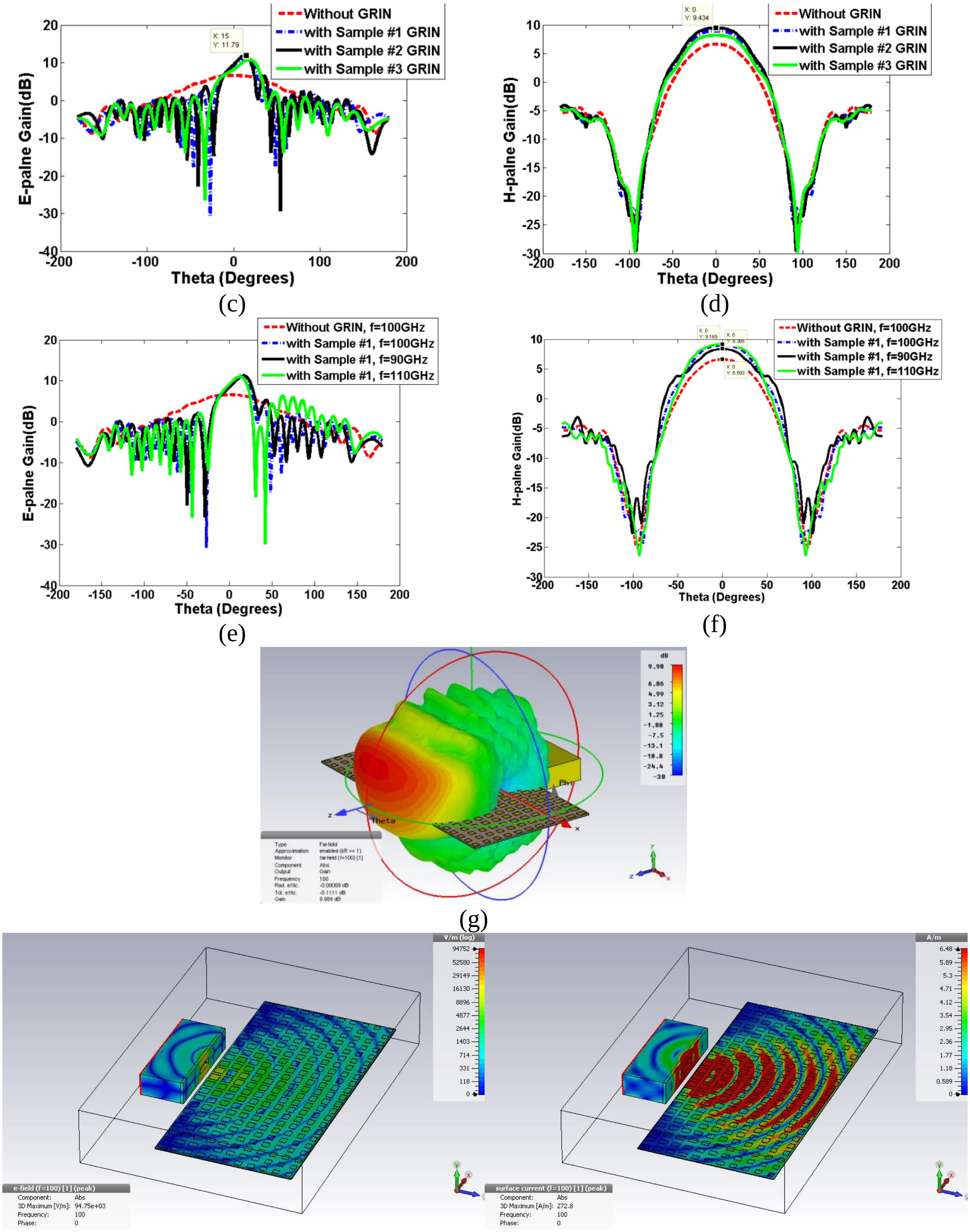

(c) (d)

(e) (f)

(g)

(h) (i)

Fig. 7.12. Impedance matching and radiation parameters for the proposed slotted waveguide antenna operating at 100 GHz with and without GRIN MTS structure at different GRIN MTS sample sizes, (a) magnitude of S_{11}, (b) magnitude of maximum gain versus frequency, (c) *E*-pane gain, (d) *H*-plane gain, (e) and (f) are *E* and *H* planes gains at three different frequencies inside the antenna bandwidth, respectively, (g) 3-D maximum gain, (h), and (i) are *E*-field magnitude and surface current on the structure, respectively at 100 GHz. The horizontal

distance d_z and the vertical offset d_y of the Metasurface with respect to the centre of the antenna slot are set at 1 mm and -0.75 mm, respectively.

It is clear from Fig. 7.12 that, as the size of the GRIN MTS structure increase, the gain increases too. For example sample #2 which has 2-D MTS periodic structure of size 35×18 unit cells provides the highest gain compared to the other two samples which have smaller sizes. The E and H plane gains are improved from 6.6 dB to 11.81 dB and 9.4 dB, respectively. While the E and H planes HPBW are reduced from 104.5° and 71.2° to 24.1 and 70.6°. The proposed antenna has a good impedance matching and the bandwidth does not change with the gain improvement. The FBW of the proposed 100 GHz antenna is 16.33 % and the radiation efficiency is about 97%. The improvement in the gain is due to E and H fields' improvement in the near field area cause by surface impedance modulation of the GRIN MTS structure as shown the near E-field and surface current given in Figs. 7.12 (h) and 7.12 (i). Such near field improvements verified that our proposed GRIN MTS works as a lens.

7.6. Design, Simulation and Optimization of 200 GHz Slotted Waveguide Antenna Incorporated with Patch GRIN MTS Structure

Here, the proposed slotted waveguide antenna incorporated with GRIN MTS structure presented in section 7.3 is redesigned to operate at 200 GHz for board to board communications to develop High Performance Computing (HPC). The dimensions of the 200 GHz proposed antenna and the WR-5 excitation waveguide are given Table. 7.7. The proposed antenna is simulated in CST and optimized by changing the horizontal spacing d_z and vertical offset d_y. After many parametric sweeps in CST, d_z and d_y are optimized at 0.5 and -0.25 mm, respectively. The proposed antenna is then simulated at the optimal d_z and d_y and at three different GRIN MTS samples presented in Table 7.8. The dispersion diagrams of such samples are given in Fig. 7.6. The proposed antenna performance key parameters are presented in Fig. 7.13.

Table 7.7 dimensions of the 200 GHz proposed antenna incorporated with GRIN MTS structure.

Parameters	a	b	L_{wg}	t_1	t_2	t_3	L_s	W_s	p	L	h	d_z	d_y
Dimensions (mm)	1.295	0.648	3 or 6	2.5	0.2	0.2	0.775	0.3	0.6		0.23	0.5	-0.25

Table 7.8 Impact of GRIN MTS structure size and step size on the 200 GHz proposed antenna performance

Parameters	Sample #1	Sample #2	Sample #3
Periodicity, P (mm)	0.6	0.6	0.6
Rectangular patch side, L (mm)	L=0.35:-0.025:0.225	L=0.35:-0.01:0.3	L=0.35:-0.025:0.15
Refractive index profile	Linearly	Linearly	Linearly
Size ($N_x \times N_z$)	11×6	11×6	17×9
d_z (mm)	0.5	0.5	0.5
d_y (mm)	-0.25	-0.25	-0.25

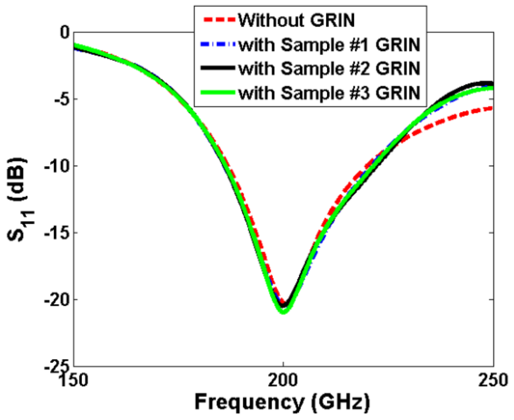

(a)

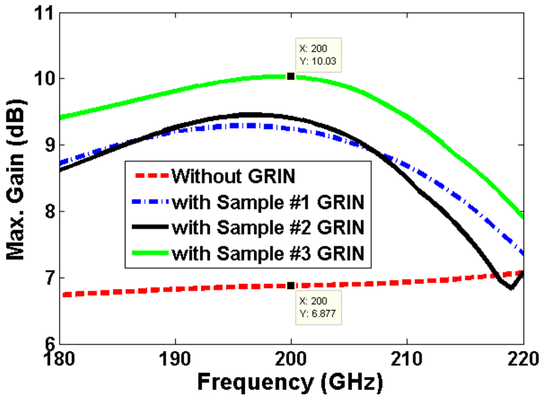

(b)

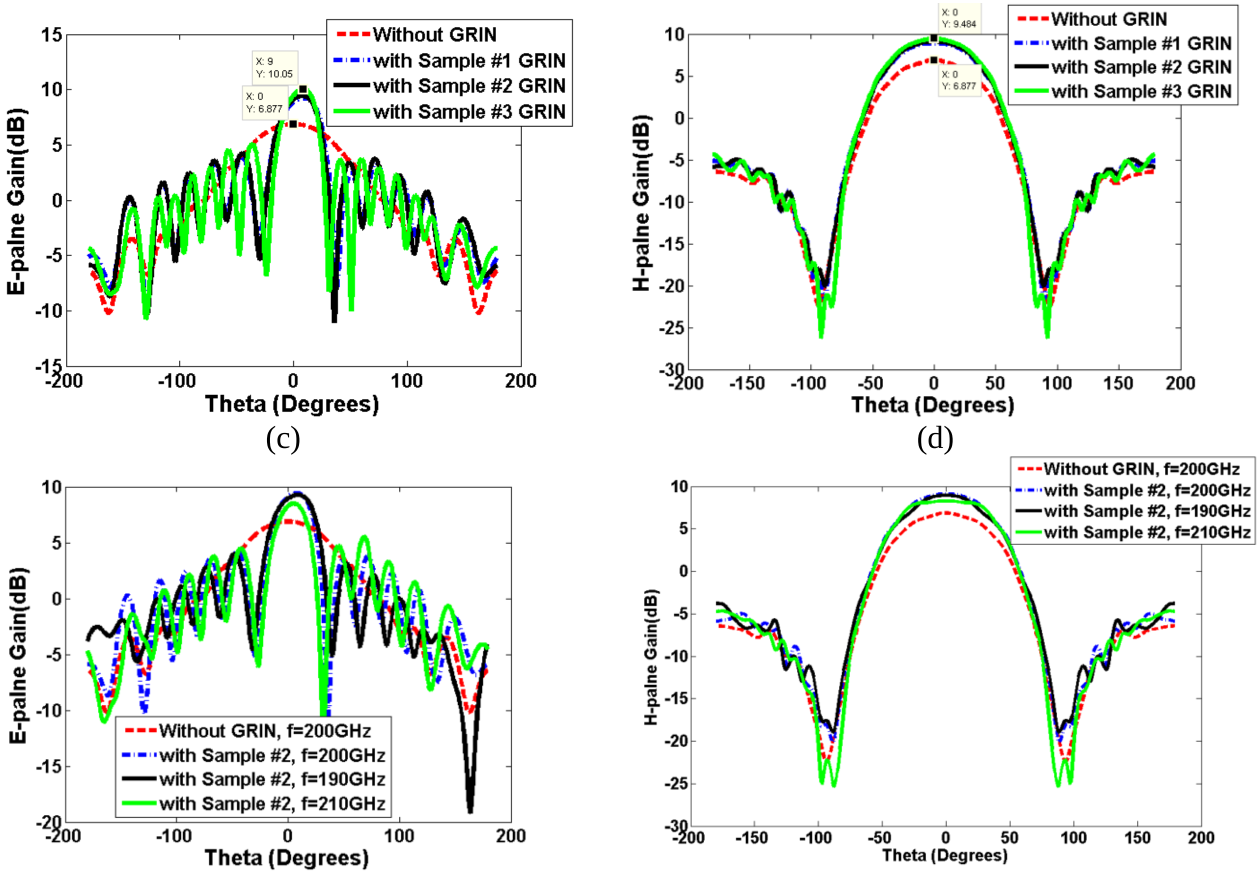

(c) (d)

(e) (f)

Fig. 7.13. Impedance matching and radiation parameters for the proposed slotted waveguide antenna operating at 200 GHz with and without GRIN MTS structure at different GRIN MTS sample sizes, (a) magnitude of S_{11}, (b) magnitude of maximum gain versus frequency, (c) *E*-pane gain, (d) *H*-plane gain, (e) and (f) are *E* and *H* planes gains at three different frequencies inside the antenna bandwidth, respectively. The horizontal distance d_z and the vertical offset d_y of the Metasurface with respect to the centre of the antenna slot are set at 0.5 mm and -0.25 mm, respectively.

It is clear from Fig. 7.13 that, as the GRIN MTS structure size increases, the radiation beam becomes more directive and hence the antenna gain increases. The optimal gain is obtained in case of sample #3. The *E* and *H* planes gains are improved from 6.9 dB to 10 dB and 9.48 dB, respectively. The *E* and *H* HPBW are reduced from 91.8° and 77.3° to 31.7° and 74.8°, respectively. However, the proposed antenna incorporated with GRIN MTS has good impedance matching and its bandwidth is slightly changed. Such gain improvement is due to beam focusing due to the gradient phase velocity affecting the index of refraction gradient which is spatially distributed in the near field aperture area of the antenna. Also, it should be noted that, the antenna has low side lobe level and high main lobe gain for all frequencies inside the antenna bandwidth as shown in Figs. 7.13 (e) and (f). The *E* and *H* plane gains are compared and plotted at 200, 190 and 210 GHz frequencies which are located at the antenna centre frequency and at frequencies close to the lower and higher antenna cut-off frequencies, respectively.

7.7. Design of 10 GHz Slotted Waveguide Antenna Incorporated with Slot Ring Metasurface Employing GRIN Structure

Here, a slotted waveguide antenna incorporated with multilayer 2D periodic structures of annular slots employing resonance GRIN MTS structure to focus the radiated wave is proposed, designed, simulated and optimized. Firstly, a unit cell with an annular slot is designed to exhibit a gradient index of refraction (GRIN) around 10 GHz. This can be achieved by changing the radius of the annular slot and extracting the crossponding refractive index by using the Effective Medium Theory (EMT) enabling the range of the GRIN to be computed. Then the annular slot unit cell is used to construct a 2D periodic structure employing linearly or parabolic spatially distributed index of refraction to focus the radiated wave when it is inserted in front of the conventional slotted waveguide antenna. Finally, the proposed antenna performance key parameters are calculated and extracted by using CST Microwave Studio.

7.7.1. Design of 10 GHz GRIN Structure Based on Annular Slotted Structure

Here, an annular slotted metasurface employing GRIN structure presented in [11] is designed on RT/Duroid substrate of effective permittivity of 2.2 and height *h* of 0.508 mm. The slot structure is single sided and the slot is etched in the copper cladding of thickness *t* of 17.5 µm as shown in Fig. 7.14. The structure has a unit cell of periodicity *p* in both *x* and *y* directions of 10 mm. The slot width *g* is set to 0.3 mm and the radius *r* of the inner circle is changed from 3.8 to 4.3 mm to design a GRIN structure operating at 10 GHz.

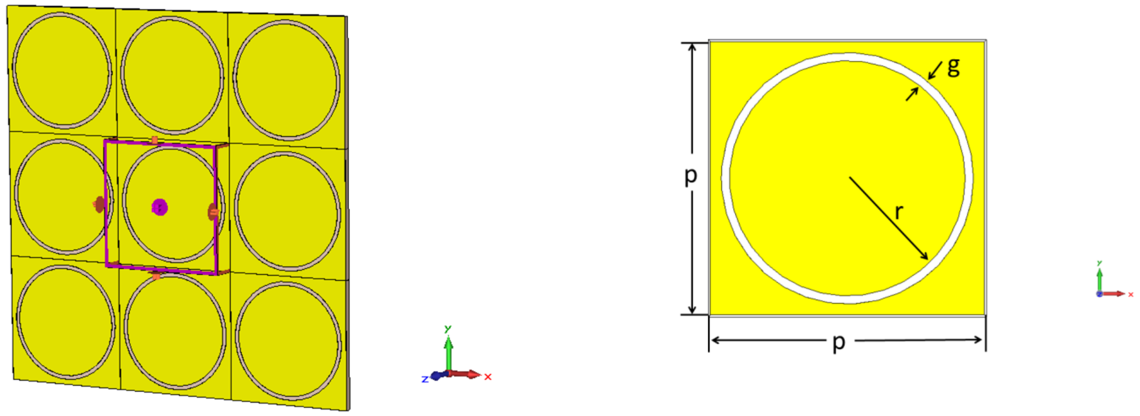

(a) (b)

Fig. 7.14. Metasurface circular slotted structure, (a) 3D view showing the unit cell boundary conditions, and (b) front view of one unit cell.

The annular slot unit cell is simulated in CST software using a frequency domain solver with unit cell 2D boundary conditions to ensure that the structure is infinite and homogenous. The magnitude and phase of the scattering parameters are extracted and plotted as shown in Fig. 7.15 (a) through 7.15 (d) which shows that, the structure has a good transmission and reflection characteristics around 10 GHz. Then the effective parameters of the structure are extracted and plotted from the scattering parameters using NRW algorithm [12-14] as shown in Figs. 7.15 (e) through 7.15 (j).

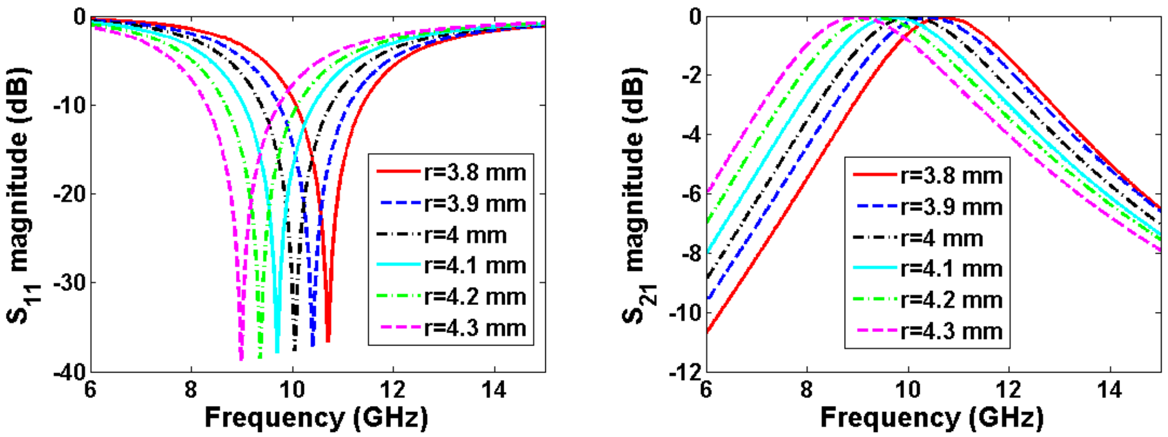

(a) (b)

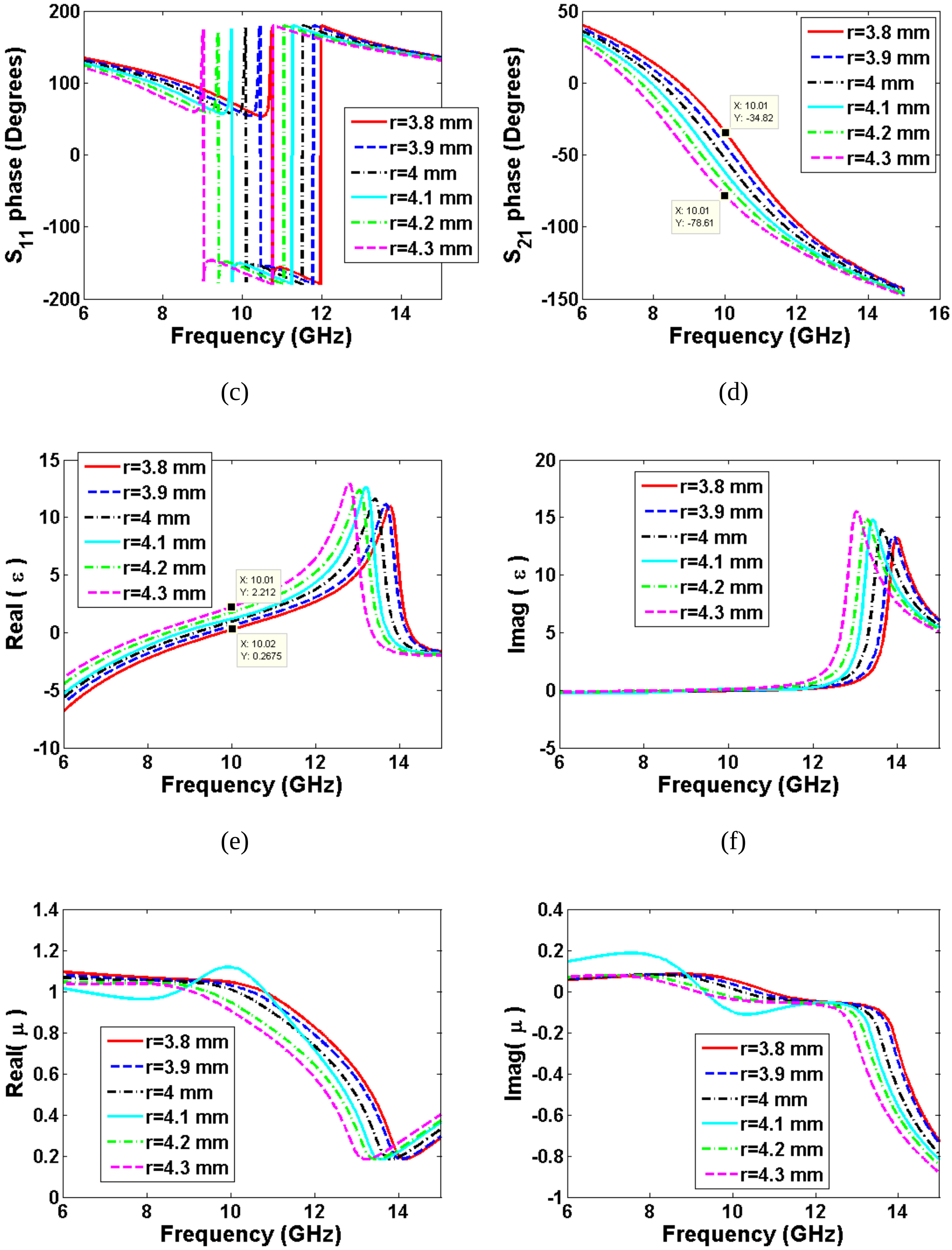
S11 phase (Degrees)
200
100
0
-100
-200
6
8
10
12
14
Frequency (GHz)
r=3.8 mm
r=3.9 mm
r=4 mm
r=4.1 mm
r=4.2 mm
r=4.3 mm
S21 phase (Degrees)
50
0
-50
-100
-150
16
X: 10.01
Y: -34.82
X: 10.01
Y: -78.61
Real (ε)
15
10
5
-5
-10
X: 10.01
Y: 2.212
X: 10.02
Y: 0.2675
Imag (ε)
20
Real(μ)
1.4
1.2
1
0.8
0.6
0.4
0.2
Imag(μ)
0.4
0.2
-0.2
-0.4
-0.6
-0.8
-1

(c) (d)

(e) (f)

(g) (h)

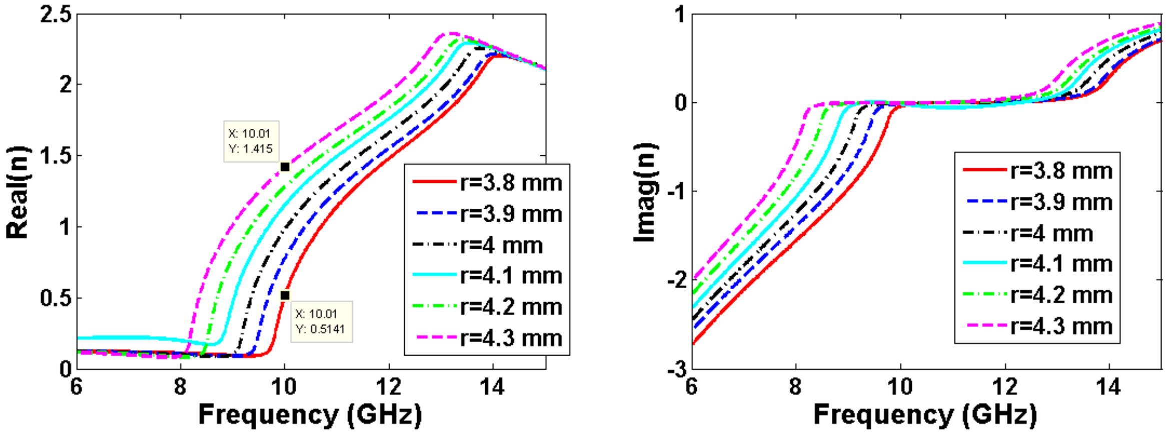

(i) (j)

Fig. 7.15. The scattering and the effective parameters of the annular slot unit cell at different radius *r* changes from 3.8 mm to 4.3 mm and periodicity *p* of 10 mm in both *x* and *y* directions, (a) magnitude of the reflection coefficient, (b) magnitude of the transmission coefficient, (c) phase of the reflection coefficient, (d) phase of the transmission coefficient, (e) and (f) real and imaginary part of effective permittivity, respectively, (g) and (h) real and imaginary part of effective permeability, (i) and (j) real and imaginary part of effective refractive index.

It is clear from Fig. 7.15 that, the minimum value of S_{21} is -0.854 dB at *r*=4.3 mm and the crossponding S_{11} is -7.73 dB, while the maximum value of S_{21} is -0.056 dB at *r*=3.8 mm and the crossponding S_{11} is -37.5 dB. The phase of S_{21} is changed by $\Delta\varphi = -44.458°$, the refractive index *n* changes from 0.5236 to 1.412 and also, the phase of the transmission is changed from -35.41 to -78.61 degrees as the radius *r* of the inner circle of the metasurface structure changes from 3.8 mm to 4.3 mm at 10 GHz. This means the index of refraction is changed by about 0.9 as the radius of the annular slot changes from 3.8 mm to 4.3 mm without affecting significantly the transmission and reflection coefficients.

7.7.2. Design, Simulation and Optimization of 10 GHz Incorporated with Linearly Distributed *E*-plane and *H*-plane GRIN Structures

In this section, the annular slot unit cell designed in the previous subsection is used to construct 2-D periodic structure of linearly spatially distributed index of refraction which employs GRIN MTS. The GRIN MTS is placed in front of the conventional slotted waveguide antenna with a separation distance d_z between the antenna slot and the first MTS layer and each two MTS layers are separated by distance d_{z1}. The proposed slotted waveguide antenna incorporated with multilayers of the GRIN MTS was constructed as shown in Fig. 7.16 and it was modelled and simulated using CST software.

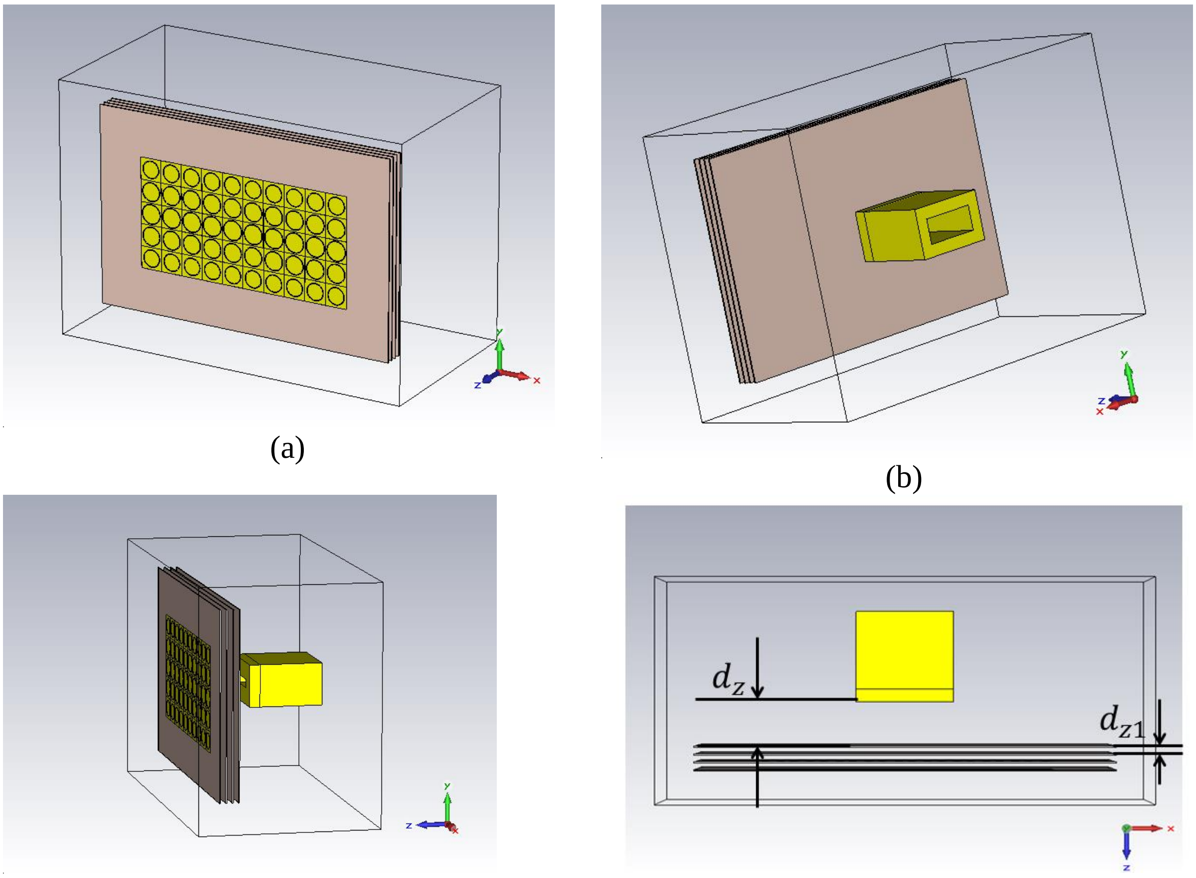

(a) (b) (c) (d)

Fig. 7.16. The proposed slotted waveguide antenna incorporated with multi layers 2D periodic structure of annular slot employing GRIN MTS, (a) 3D view showing the GRIN MTS structure, (b) 3D view showing the waveguide excitation port, (c) 3D view showing the antenna whole structure and the antenna radiating slot, and (d) top view showing the separation distance between the antenna slot and the first layer of the GRIN MTS and the intra separation distance between each two consecutive GRIN layers.

Since the main functionality of using GRIN MTS is to focus the radiated beam, so it can be designed to dominantly focus the *E* or *H* plane fields or both. For example if the antenna is incorporated with GRIN MTS with a profile distributed across the *E*-plane, so the radiated wave will be focused in the *E*-plane direction and similarly for the *H*-plane. However we can obtain both the *E* and *H* planes radiated wave focusing if different layers of *E* and *H* plane GRINs are used. Figure 7.17 illustrates the impact of GRIN MTS with *E* or/and *H* planes linearly distributed index of refraction on the proposed antenna performance. It should be noted that, 2D periodic structures of annular slot of sizes 5×6 and 6×5 in the *x* and *y* directions are used to construct GRIN MTS with *E* and *H* planes GRIN profiles, respectively. Such GRIN sizes provide the optimal antenna impedance matching. The antenna performance key parameters such as FBW, HPBWs, *E* and *H* plane gains, side lobe level and main lobe directions are given in Table 7.9.

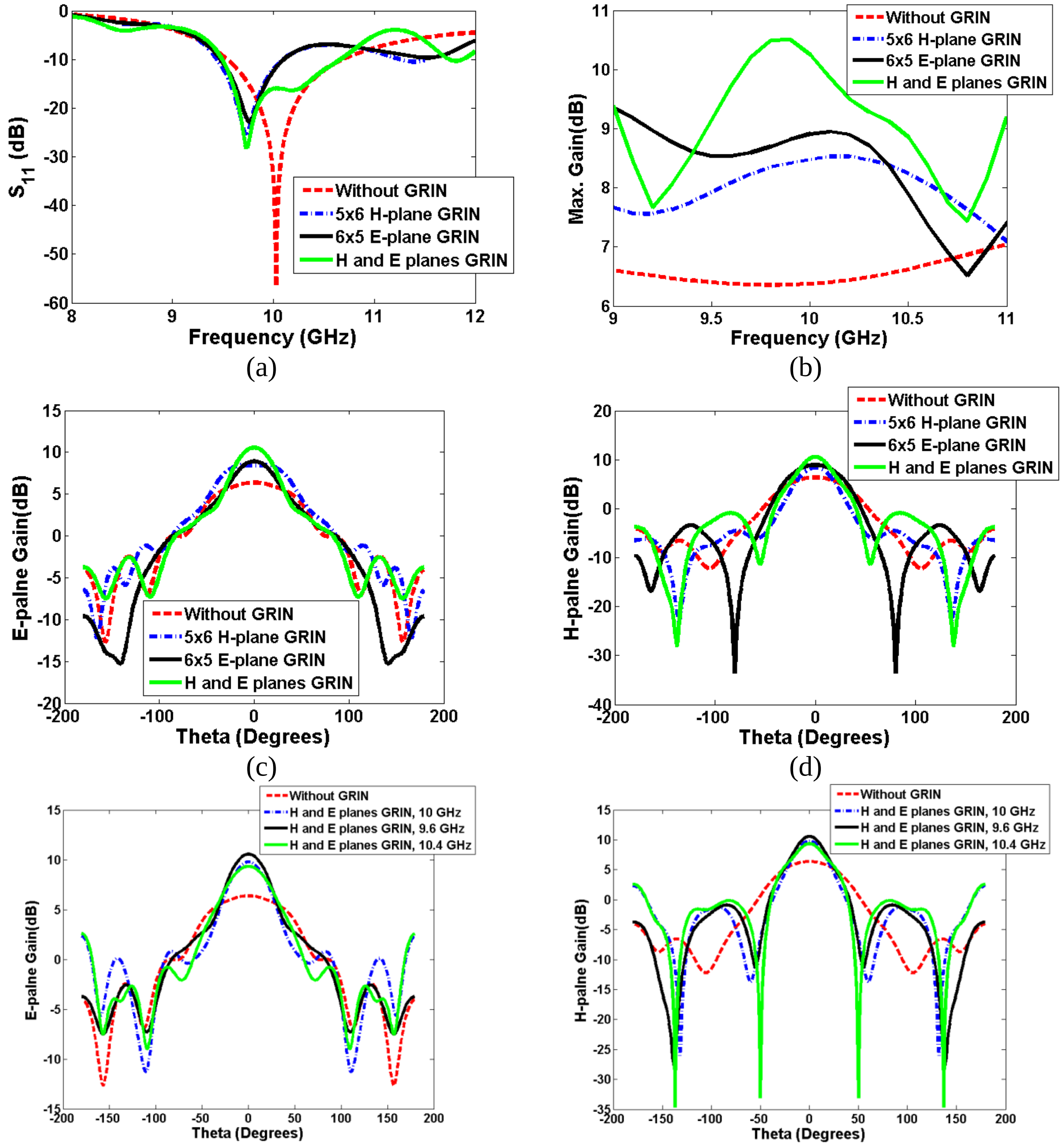

(a) (b)

(c) (d)

(e) (f)

Fig. 7.17. Impedance matching and radiation parameters for 10 GHz proposed slotted waveguide antenna with and without GRIN MTS distributed across different radiation planes. Three different samples are used, the first one is for only *E*-plane GRIN distributed, the second one for H-plane GRIN distributed and the third one uses both *E* and *H* plane GRIN distributed structures; (a) magnitude of S_{11}, (b) magnitude of maximum gain versus frequency, (c) *E*-plane gain, (d) *H*-plane gain, (e) and (f) are *E* and *H* planes gains at three different frequencies inside the antenna bandwidth, respectively.

It is clear from Fig. 7.17 that, the proposed antenna incorporated with GRIN of linear profile suffers from large back lobe levels particularly for frequencies outside the antenna bandwidth. The lower and the higher cut-off frequencies of the antenna which are 9.6 GHz and 10.4 GHz as shown in Fig. 7.17 (e) and 7.17 (f). One of the suggested solutions to mitigate the side lobe level is to use a parabolic GRIN profile instead of a linear GRIN profile which will be discussed in the coming subsection.

Table 7.9 The performance key parameters of the proposed antenna incorporated with linearly distributed GRIN MTS across *E* and *H* planes

Parameters	H-plane GRIN	E-plane GRIN	Cascaded *H*-plane and *E*-plane GRINs
Periodicity p (mm)	10	10	10
GRIN structure profile	Slotted ring with a Linear distribution of $r_{\min} = 3.8\,mm$ and $r_{\max} = 4.3\,mm$ and step size based on the structure size		
Size ($N_x \times N_z$)	5×6	6×5	5×6 and 6×5, one layer each, with 5 mm separation between each 2 layers
Slot- GRIN separation distance d_z(mm)	17	17	s_z =17mm and 5 mm between each 2 layers
Δn	0.9	0.9	0.9
FBW (%)	6.52	6.47	11.664
S_{11} at 10 GHz (dB)	-25.51, shifted to 9.738	-22.78, shifted to 9.768	-28.22, shifted to 9.736 GHz
η_{rad} (%)	98.36	98.2	96.8
η_{tot} (%)	92.26	92.4	94.4
E-plane HPBW (°) , Gain (dB), main lobe (°) direction (°), and side lobe level (°)	88.6, 8.48, 12, and -9.6	56.9, 8.91, 0, and -18.5	55, 10.3, 0, and -13.2
H-plane HPBW (°) , Gain (dB), main lobe (°)	38.6, 8.39, 0, and -12.9	56.9, 8.91, 0, and -12.3	33, 10.3, 0, and -10.3

direction (°), and side lobe level (°)			

It is clear from Table 7.9 that, the optimal gain as obtained for the antenna incorporated with both GRIN MTS across both the *E* and *H* planes. The gain is improved from about 6.7 dB to 10.3 dB and the beam area is reduced from about 107° to 55° for the *E*-plane and from 67° to 33° for the *H*-plane without significant change in the impedance matching and the antenna bandwidth.

7.7.3. Design, Simulation and Optimization of 10 GHz Antenna Incorporated with Parabolic Distributed *E*-plane and *H*-plane GRIN Structures

Here, the proposed slotted waveguide antenna operating at 10 GHz incorporated with parabolic spatially distributed GRIN across the antenna *E* and/or *H* planes was deigned, simulated and optimized in CST software. The proposed antenna is shown in Fig. 7.16. The main advantage of using a parabolic distributed GRIN over the linearly distributed one is it reduces the side lobe level. The designed *E* and *H* planes GRINs are of sizes, 6×5 and 5×6 in the *x* and *y* directions, respectively. Three different *E* plane GRINs of sizes 6×5, 10×5 and 15×7 in *x* and *y* directions as well as an *H* plane GRIN of size 5×6 were deigned which are exhibited the same range of index of refraction of 0.9. The impact of such GRIN MTS on the antenna performance were studied and calculated in CST software and the results are plotted in Fig. 7.18. Furthermore, the antenna performance key parameters are reported in Table 7.10.

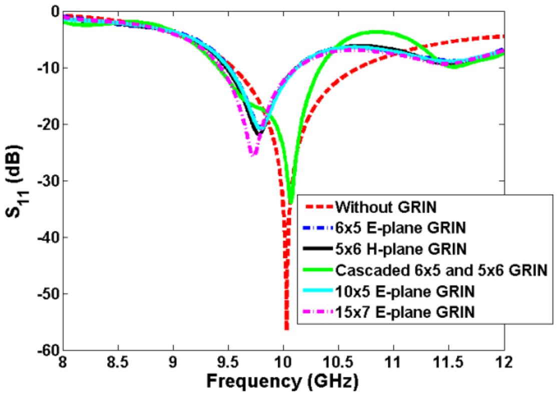
S11 (dB)
Frequency (GHz)
0
-10
-20
-30
-40
-50
-60
8
8.5
9
9.5
10
10.5
11
11.5
12
Without GRIN
6x5 E-plane GRIN
5x6 H-plane GRIN
Cascaded 6x5 and 5x6 GRIN
10x5 E-plane GRIN
15x7 E-plane GRIN

(a)

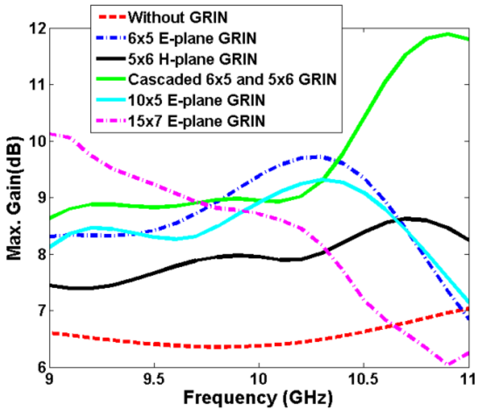
Max. Gain(dB)
Frequency (GHz)
12
11
10
9
8
7
6
9
9.5
10
10.5
11
Without GRIN
6x5 E-plane GRIN
5x6 H-plane GRIN
Cascaded 6x5 and 5x6 GRIN
10x5 E-plane GRIN
15x7 E-plane GRIN

(b)

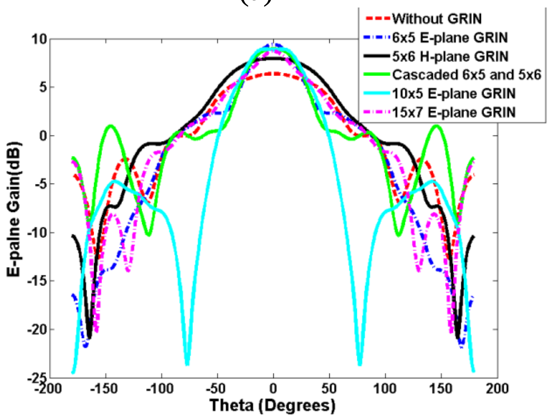
E-palne Gain(dB)
Theta (Degrees)
10
5
0
-5
-10
-15
-20
-25
-200
-150
-100
-50
0
50
100
150
200
Without GRIN
6x5 E-plane GRIN
5x6 H-plane GRIN
Cascaded 6x5 and 5x6
10x5 E-plane GRIN
15x7 E-plane GRIN

(c)

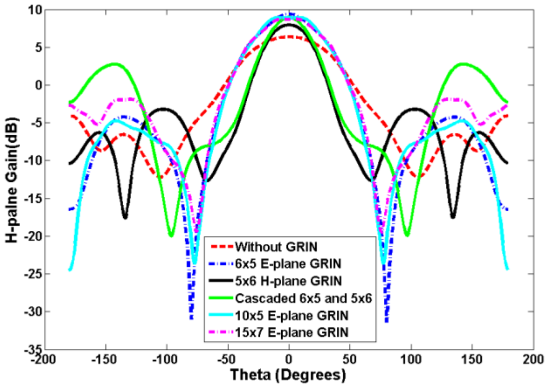
H-palne Gain(dB)
Theta (Degrees)
10
5
0
-5
-10
-15
-20
-25
-30
-35
-200
-150
-100
-50
0
50
100
150
200
Without GRIN
6x5 E-plane GRIN
5x6 H-plane GRIN
Cascaded 6x5 and 5x6
10x5 E-plane GRIN
15x7 E-plane GRIN

(d)

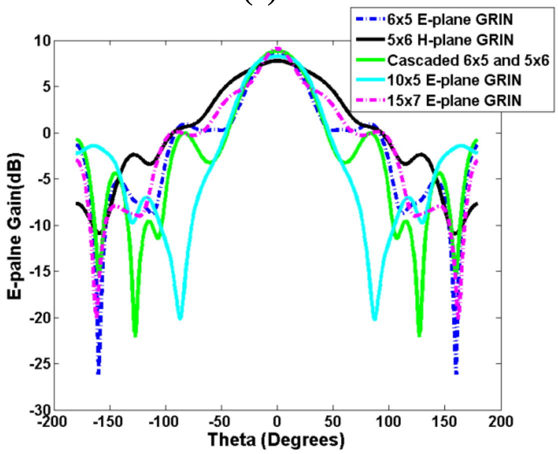
E-palne Gain(dB)
Theta (Degrees)
10
5
0
-5
-10
-15
-20
-25
-30
-200
-150
-100
-50
0
50
100
150
200
6x5 E-plane GRIN
5x6 H-plane GRIN
Cascaded 6x5 and 5x6
10x5 E-plane GRIN
15x7 E-plane GRIN

(e)

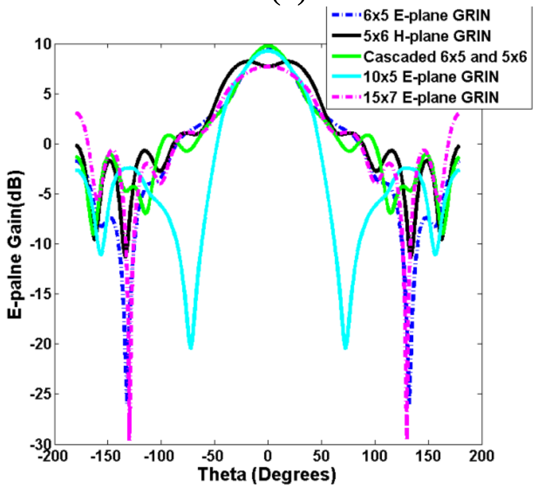
E-palne Gain(dB)
Theta (Degrees)
10
5
0
-5
-10
-15
-20
-25
-30
-200
-150
-100
-50
0
50
100
150
200
6x5 E-plane GRIN
5x6 H-plane GRIN
Cascaded 6x5 and 5x6
10x5 E-plane GRIN
15x7 E-plane GRIN

(f)

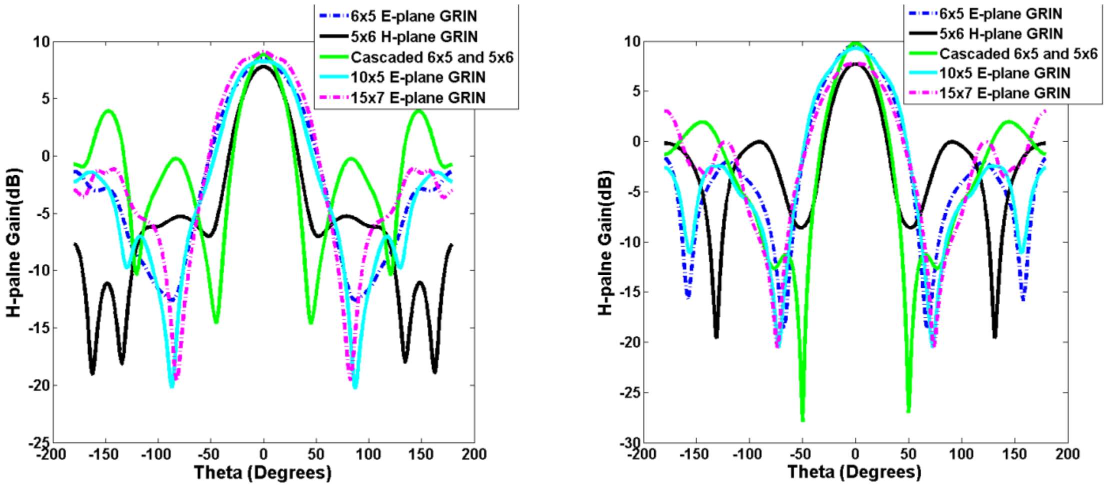

(g) (h)

Fig. 7.18. Impedance matching and radiation properties of the 10 GHz slotted waveguide antenna with and without parabolic distributed GRIN MTS across the *E* and *H* planes of different sizes, (a) S_{11} magnitude, (b) maximum gain versus frequency, (c) *E*-plane gain at 10 GHz, (d) *H*-plane gain at 10 GHz, (e) E-plane gain at 9.6 GHz, (f) E-plane gain at 10.4 GHz, (g) H-plane gain at 9.6 GHz, and (h) H-plane gain at 10.4 GHz.

Table 7.10 The key performance parameters of the 10 GHz proposed antenna incorporated with a parabolic distributed GRIN MTS across the *E* and *H* planes with different sizes and different configuration.

Parameters	6×5 E-plane GRIN	5×6 H-plane GRIN	Cascaded E-plane and H-plane GRINs	10×5 E-plane GRIN	15×7 E-plane GRIN
Periodicity p in x and y directions (mm)	10	10	10	10	10
GRIN structure profile	Slotted ring with a parabolic distribution of $r_{\min} = 3.8\,mm$ and $r_{\max} = 4.3\,mm$ and step size based on the structure size				
Size ($N_x \times N_z$)	6×5	5×6	5×6 and 6×5, one layer each, with 5 mm separation between each 2 layers	10×5	15×7
Slot- GRIN separation distance d_z(mm)	17	17	d_z =17 mm and 5 mm between each 2 layers	17	17
Δn	0.9	0.9	0.9	0.9	0.9
FBW (%)	0.6284/10	0.6471/10	0.938/10	0.635/10	0.715/10
S_{11} at 10 GHz (dB)	-20.514, shifted to	-21.774, shifted to	-33.7, shifted to 10.063 GHz	-20.85, shifted to	-25.8, shifted to

	9.802 GHz	9.7664 GHz		9.8 GHz	9.73 GHz
η_{rad} (%)	97.83	97.24	97.27	97.3	95.97
η_{tot} (%)	92.90	91.90	96.96	92.52	90.43
E-plane HPBW (°), Gain (dB), main lobe (°) direction (°), and side lobe level (°)	47.8, 9.38, 0, and -7.1	97.6, 7.95, 0, and -8.8	54.2, 8.95, 0, and -8	52.7, 8.89, 0, and -24.6	61.6, 8.68, 0, and -11.4
H-plane HPBW (°), Gain (dB), main lobe (°) direction (°), and side lobe level (°)	53.6, 9.38, 0, and -13.6	40.8, 7.95, 0, and -11.2	37.1, 8.95, 0, and -6.2	58.1, 8.92, -8, and -13.7	62.8, 8.71, 5, and -10.6

It is clear from Fig.7.18 and Table 7.10 that, when cascading the *E* and *H* plane GRINs the gain degrades and also the side lobe increases, this means it is better to use only whether an *E*-plane or an *H*-plane GRIN, referring to Fig. 7.18, the *E*-plane GRIN is the best candidate for improving all of the radiation pattern simultaneously including gain, beam width, and side lobe level. Furthermore at the two frequencies of 9.6 GHz and 10.4 GHz located inside the antenna bandwidth and close to its lower and the higher cut off frequencies, it is clear that as the size of the *E*-plane GRIN structure changed in the direction normal to the GRIN profile distribution, the back lobe level and the side lobe level changed. The optimal *E* plane GRIN size was 10×5 which provide the lowest side lobe level and the highest main lobe level.

After the *E* plane parabolic distributed GRIN is considered as the optimal one in terms of best antenna performance point of view, the impact of the number of layers of the GRIN MTS on the antenna performance was studied and reported. Six different sizes of the 3D GRIN MTS composed of multi-layered *E* plane parabolic distributed 2D GRINs were designed and integrated with the slotted waveguide antenna. The 2D GRIN MTS used to construct the 3D GRIN are of sizes 6×5 and 10×5, while the number of layers used was 1, 2 or 4 cascaded layers. The proposed antenna incorporated with 3D GRIN MTS of different sizes are designed and simulated in CST. The antenna performance is calculated and plotted in Fig. 7.19 and the antenna key parameters are reported in Table 7.11.

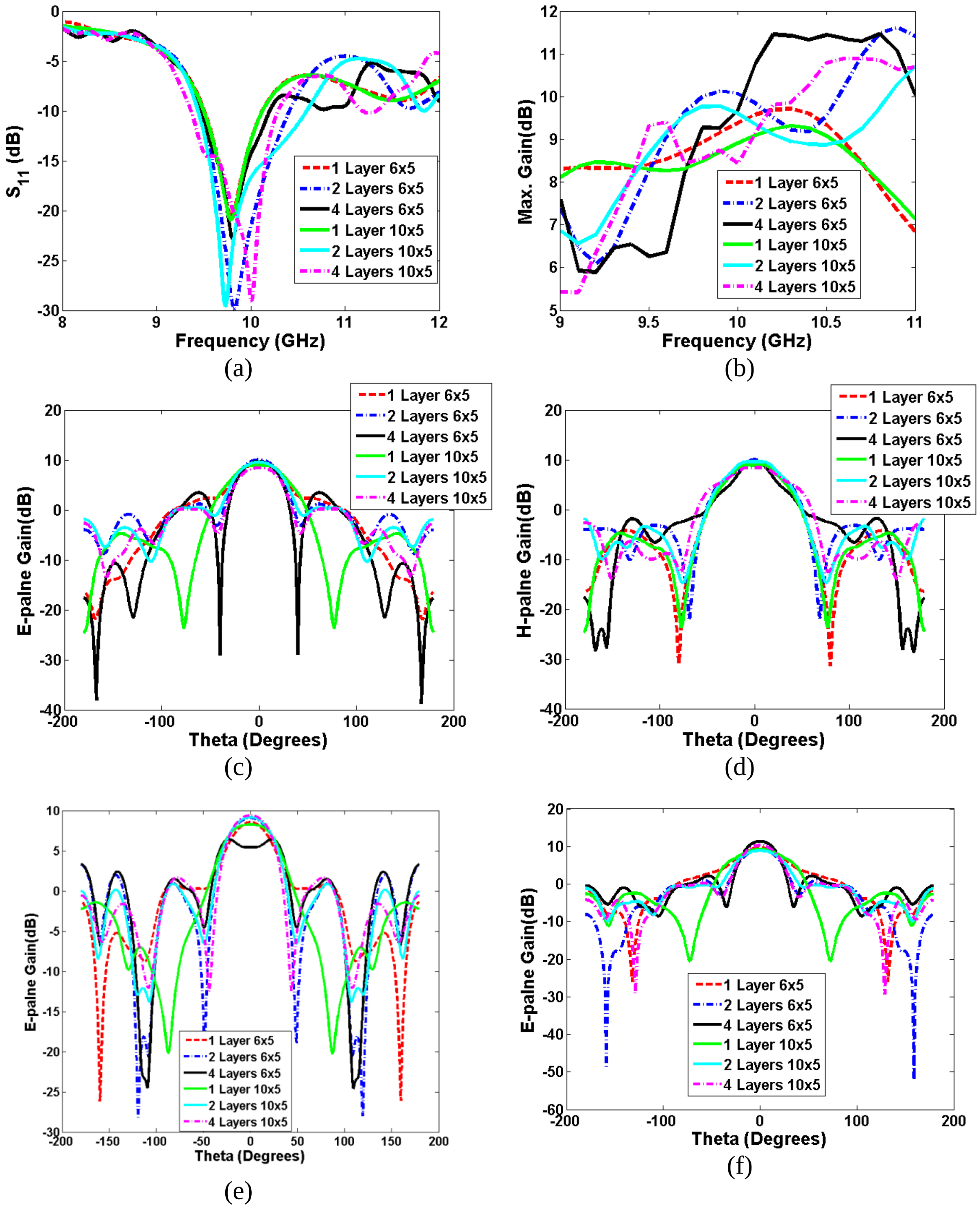

(a) (b)

(c) (d)

(e) (f)

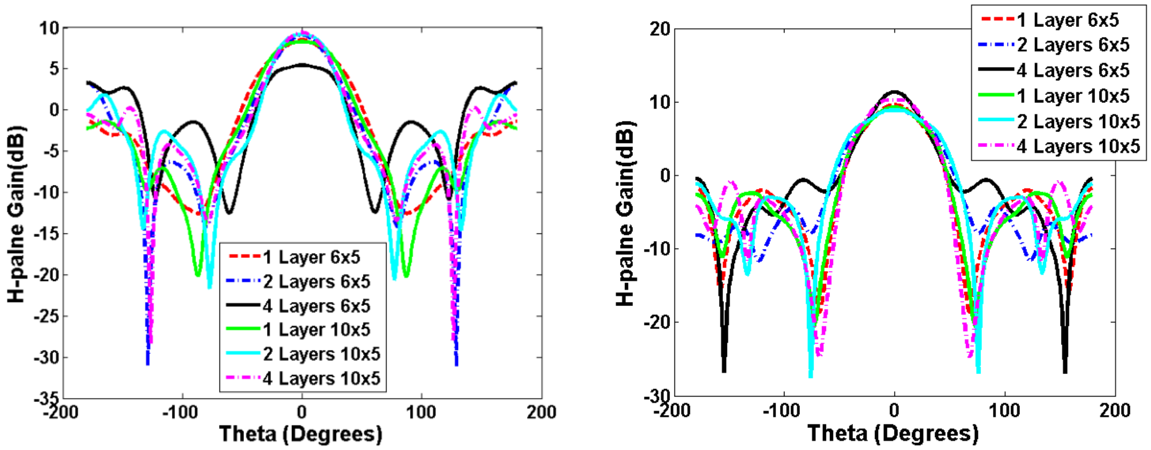

(g) (h)

Fig. 7.19. Impact of the number of layers of *E* plane parabolic distrusted GRIN MTS of different sizes on the 10 GHz proposed antenna performance; (a) S_{11} magnitude, (b) maximum gain versus frequency, (c) *E*-plane gain at 10 GHz, (d) *H*-plane gain at 10 GHz, (e) *E*-plane gain at 9.6 GHz, (f) *E*-plane gain at 10.4 GHz, (g) *H*-plane gain at 9.6 GHz, and (h) *H*-plane gain at 10.4 GHz.

Table 7.11 The performance key parameters of the 10 GHz proposed antenna incorporated with 3D GRIN structure composed of parabolic distributed GRIN MTS across the E-plane with different sizes and different number of layers.

Parameters	6×5 *E*-plane GRIN, 2 layers	6×5 *E*-plane GRIN, 4 layers	10×5 *E*-plane GRIN, 2 layers	10×5 *E*-plane GRIN, 4 layers
Periodicity p in x and y directions (mm)	10	10	10	10
GRIN structure profile	Slotted ring with a parabolic distribution of $r_{\min} = 3.8\,mm$ and $r_{\max} = 4.3\,mm$ and step size based on the structure size			
Size ($N_x \times N_z$)	6×5, with 5 mm separation between each 2 layers	6×5, with 3 mm separation between each 2 layers	10×5, with 4 mm separation between each 2 layers	10×5, with 2 mm separation between each 2 layers
Slot- GRIN separation distance d_z(mm)	17	17	17	17
Δn	0.9	0.9	0.9	0.9
FBW (%)	9.5	7.52	11.6	9.25
S_{11} at 10 GHz (dB)	-29.84, shifted to 9.828 GHz	-22.6 shifted to 9.82 GHz	-29.53, shifted to 9.73 GHz	-29.09
η_{rad} (%)	96.51	94.44	96.90	92.14
η_{tot} (%)	95.92	91	94.83	92.05
E-plane HPBW (°), Gain (dB), main lobe (°)	44.1, 10.1, 0, and -8.9	41.8, 9.68, 0, and -6.2	48.5, 9.57, 0, and -9.2	46.8, 8.43, 0, and -8.2

direction (°), and side lobe level (°)				
H-plane HPBW (°) , Gain (dB), main lobe (°) direction (°), and side lobe level (°)	44.8, 10.1, 0, and -13.3	37.9, 9.68, 0, and -11.5	58.6, 9.61, -6, and -13	70.4, 8.43, -3, and -11.1

It is clear from Fig. 7.19 and Table 7.11 that, the optimal antenna performance is obtained in case of 3D GRIN MTS structure composed of 4 layers of 6×5 *E* plane parabolic distributed 2D GRIN MTS. Since such 3D GRIN MTS provides the highest gain and reduces the side lobe level mostly for all frequencies inside the antenna bandwidth. The *E* and *H* planes gains are improved from 6.7 dB to 9.68 dB, respectively. The *E* and *H* planes HPBW are reduced from 107° and 67° to 41.8° and 37.9°, respectively. However the proposed antenna has a good impedance matching and good FBW of approximately 7.5 %.

7.7.4. 10 GHz Slotted Waveguide Antenna Incorporated with Annular Slot GRIN Structure Employing Luneburg Lens

Here, a Luneburg lens composed of a parabolic distributed annular slot 2D periodic structure is propose, designed and simulated. The lens was designed at 10 GHz and it has a GRIN parabolic profile in two directions (i.e. it is a planar lens). Then Luneburg lens is placed in front of conventional slotted waveguide antenna operating at 10 GHz with a separation distance d_z as shown in Fig. 7.20. The function of the Luneburg lens is to beam focus the EM waves in the near field aperture and hence the radiated beam becomes more focused as hence the antenna gain increases. To increase the gain dramatically, multilayers of the Luneburg lens are used as shown in Fig. 7.20 (c) and the layers are separated by distance d_{z1}. The antenna is excited by WR-19 standard waveguide.

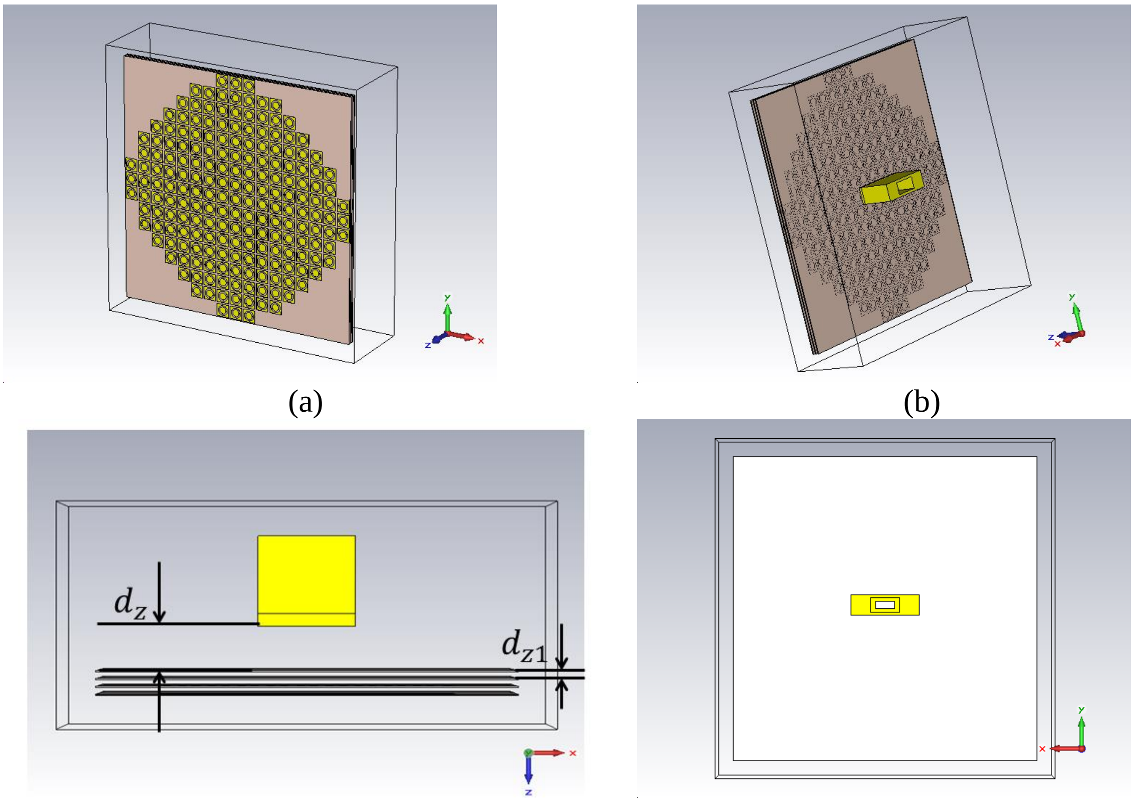

(a) (b)

(c) (d)

Fig. 7.20. The proposed slotted waveguide antenna incorporated with parabolic distributed GRIN in two directions employing a Luneburg lens, (a) 3D view showing the Luneburg lens, (b) 3D view showing the waveguide excitation port, (c) top view and (d) front view showing the antenna whole structure as well as the antenna radiating slot.

The proposed antenna was designed and optimized at 10 GHz with the aid of CST software. The optimal size of the proposed Luneburg lens at 10 GHz is 13×13 which can cover the aperture area and hence improve the antenna gain properly and also it provides good impedance matching. The dimensions of the annular slot unit cell are presented in subsection 7.7.1 and the index of refraction gradient range is 0.9. The optimization process is carried out using CST software. The optimal separation distance d_z between the antenna slot and the Luneburg lens is 17 mm and the optimal intra layer separation $d_{z1}$is 3 mm. The proposed antenna performance for different layers of the Luneburg lens was calculated and plotted in Fig. 7.21.

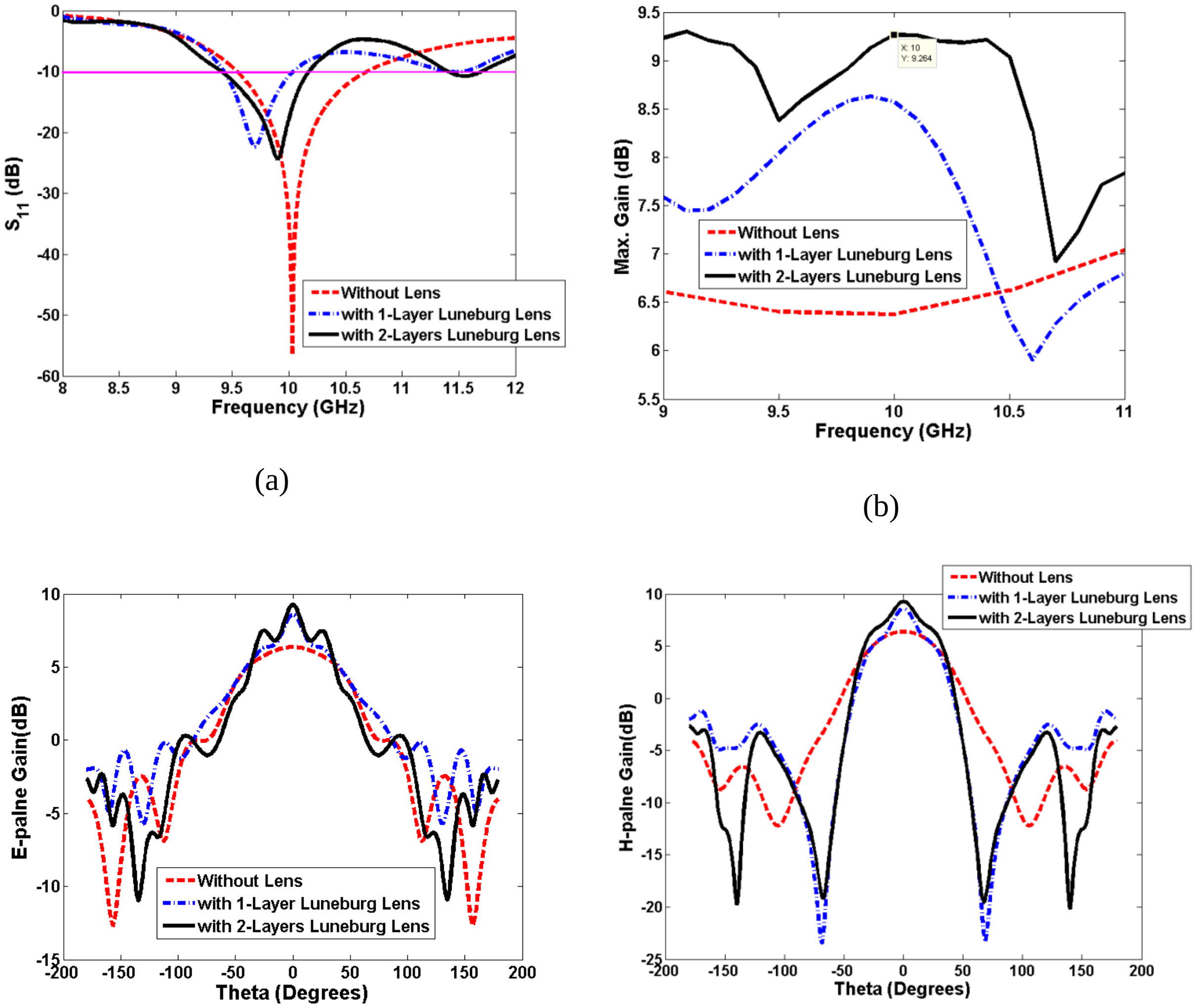

(a)

(b)

(a)

(b)

Fig. 7.21. Performance of the proposed 10 GHz antenna incorporated with multi-layered parabolic distributed GRIN MTS employing Luneburg lens; (a) S_{11} magnitude, (b) maximum gain versus frequency, (c) *E*-plane gain at 10 GHz, (d) *H*-plane gain at 10 GHz. The Luneburg lens has a size of 13×13 in *x* and *y* directions, the separation distance between the lens and the antenna slot is 17 mm and the intra layer separation is 3 mm.

It is clear from Fig. 7.21 that, as the number of layers of the GRIN MTS increases, the gain increases, the HPBW decreases and the impedance matching slightly decreases. The proposed antenna gain is increased from 6.7 dB to 9.25 dB when the proposed antenna is incorporated with 2 layers of GRIN MTS employing the Luneburg lens, while the HPBW is reduced from 107° and 67° to 32.6 ° and 30° for *E* and *H* planes, respectively. The 2 layers GRIN MTS provides the optimal gain improvement with good impedance mismatching compared with 1 layer and 3 layers (not shown in Fig. 7.21) GRIN MTS structures.

7.8. Design of 60 GHz Slotted Waveguide Antenna Incorporated with Slot Ring Metasurface Employing GRIN Structure

Here, the proposed slotted waveguide antenna presented in the previous section (shown in Figs. 7.16 and 7.20) was redesigned to operate at 60 GHz for millimetre wave WLAN and WPAN applications. Two different GRIN MTS based on annular slot 2D periodic structure were designed and integrated with the conventional slotted waveguide antenna for beam focusing purposes. The first annular slot 2D periodic structure employing a Luneburg lens and the second one employing the *E* and/or *H* planes parabolic distributed GRIN MTS for focusing the *E* and/or *H* planes radiation beam. The design of the two GRIN MTS topologies and their impact on the antenna performance are presented in the coming 3 subsections.

7.8.1. Design of Annular Slot Unit Cell Employing GRIN MTS around 60 GHz

Here, a unit cell of annular slot shown in Fig. 7.14 which exhibit spatially distributed gradient index of refraction around 60 GHz was designed, simulated and characterized based on the Effective Medium Theory (EMT). Figure 7.14 shows the structure of the annular slot unit cell. It is a slotted ring etched on a copper cladded RT/Duroid 5880 substrate of dielectric constant of 2.2 and height of 0.127 mm. The dimensions of the annular slot unit cell which exhibit GRIN around 60 GHz is given in Table 7.12. To optimize the GRIN around 60 GHz, the slot radius *r* was swept from 0.562 to 0.662 mm with step 0.02 mm. The annular slot unit cell is simulated in CST with unit cell boundary conditions in the frequency domain solver; the scattering parameters magnitude and phase were calculated and plotted as shown in Figs. 7.22 (a) through to 7.22 (d). Then the NRW algorithm was used to extract the effective parameters of the unit cell from the *S-parameters* as shown in Figs. 7.22 (e) to 7.22 (j).

Table 7.12 dimensions of annular slot unit cell employing 2-D GRIN medium at 60 GHz

Parameter	p	g	r	h	ε_r	t	Substrate	Metal cladding
Dimension (mm)	2	0.25	0.562:0.02:0.662	0.127	2.2	0.0175	RT/Duroid 5880	Copper

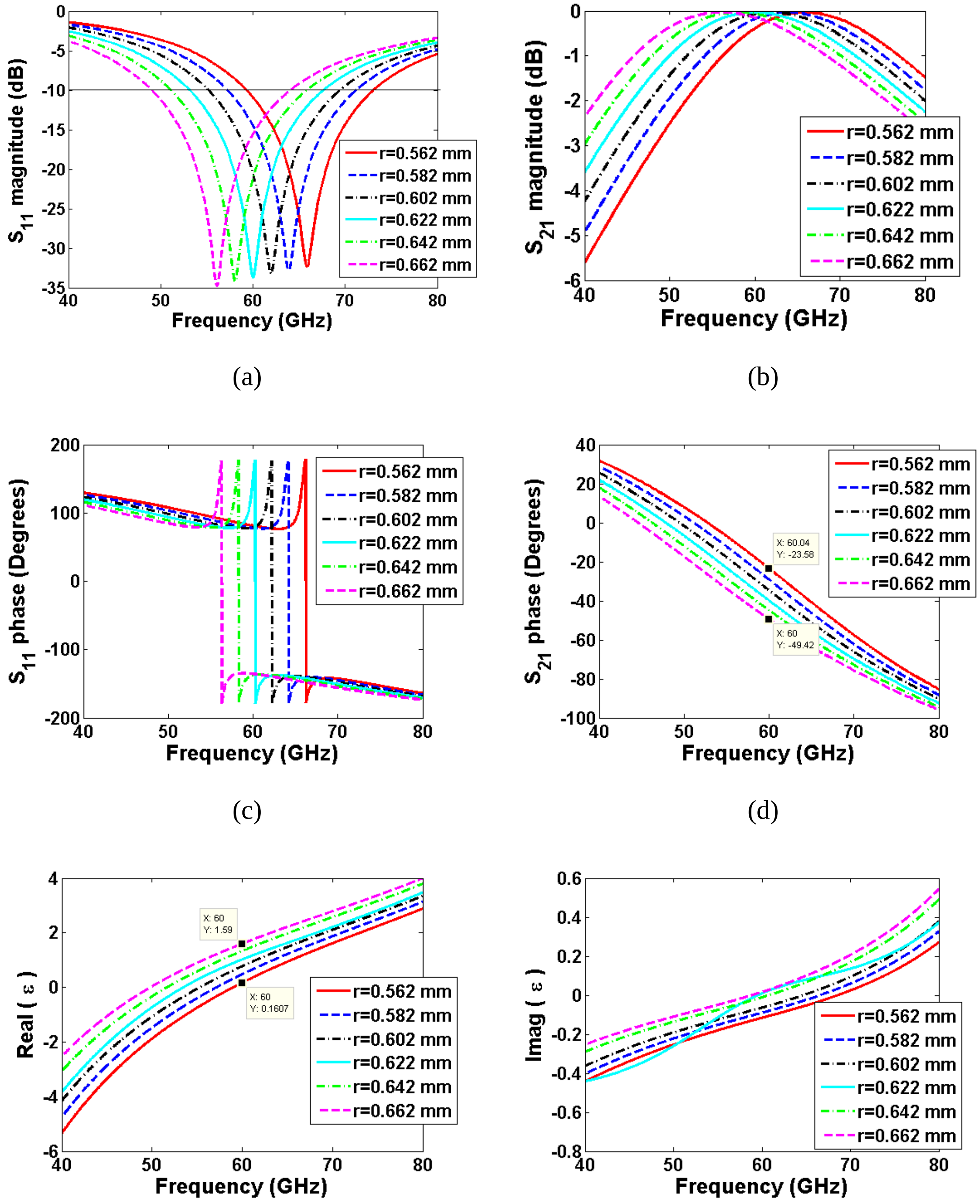

(a) (b)

(c) (d)

(e) (f)

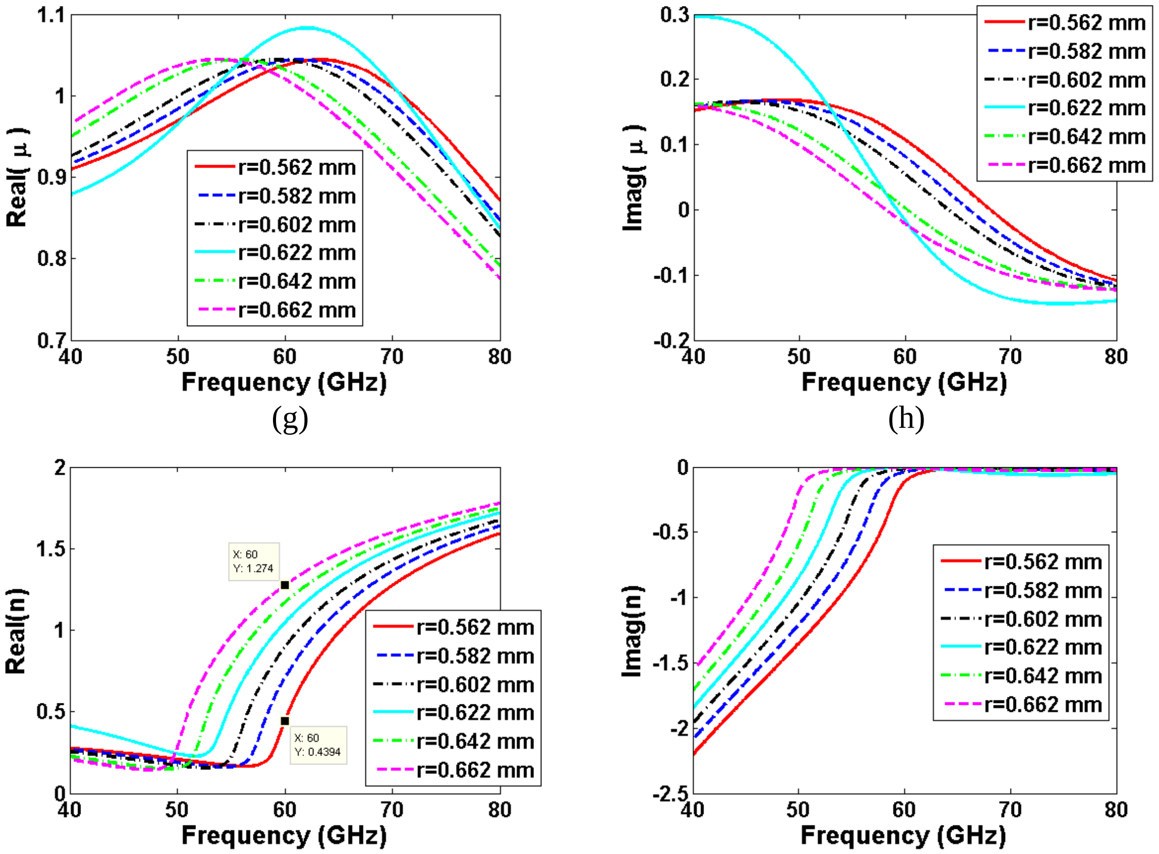

(g) (h)

(i) (j)

Fig. 7.22. The scattering and the effective parameters of the annular slot unit cell to construct GRIN medium around 60 GHz at different radius *r* changes from 0.562 mm to 0.662 mm and periodicity *p* of 2 mm in both *x* and *y* directions, (a) magnitude of the reflection coefficient, (b) magnitude of the transmission coefficient, (c) phase of the reflection coefficient, (d) phase of the transmission coefficient, (e) and (f) real and imaginary part of effective permittivity, respectively, (g) and (h) real and imaginary part of effective permeability, (i) and (j) real and imaginary part of effective refractive index.

It is clear from Fig. 7.22 that, inside the sweeping range of *r*, the annular slot provides a good transmission coefficient S_{21} ranges from -0.0287 to -0.2227 dB (which implies a good transmission) as *r* changes from 0.562 to 0.662 mm. Furthermore, the index of refraction is changed from 0.439 to 1.27, i.e. there is 0.831 gradient in the index of refraction around 60 GHz.

7.8.2. 60 GHz Slotted Waveguide Antenna Incorporated with Annular Slot GRIN Structure Employing Luneburg Lens.

Here, the proposed slotted waveguide antenna presented in Fig. 7.20 was redesigned to operate at 60 GHz. The proposed antenna was composed of a slotted waveguide antenna incorporated with annular slot GRIN MTS employing a Luneburg lens. Two different sized samples of the Luneburg lenses with the dimensions shown in Table. 7.13 were designed and the impact of each sample on the antenna performance studied and reported as in Fig. 7.23 and Table 7.13. The separation distance d_z between the Luneburg lens and the antenna slot was set at 3 mm and the intra layer separation d_{z1} was set at 1.5 mm. furthermore, the proposed antenna performance key parameters are displayed in Table 7.13.

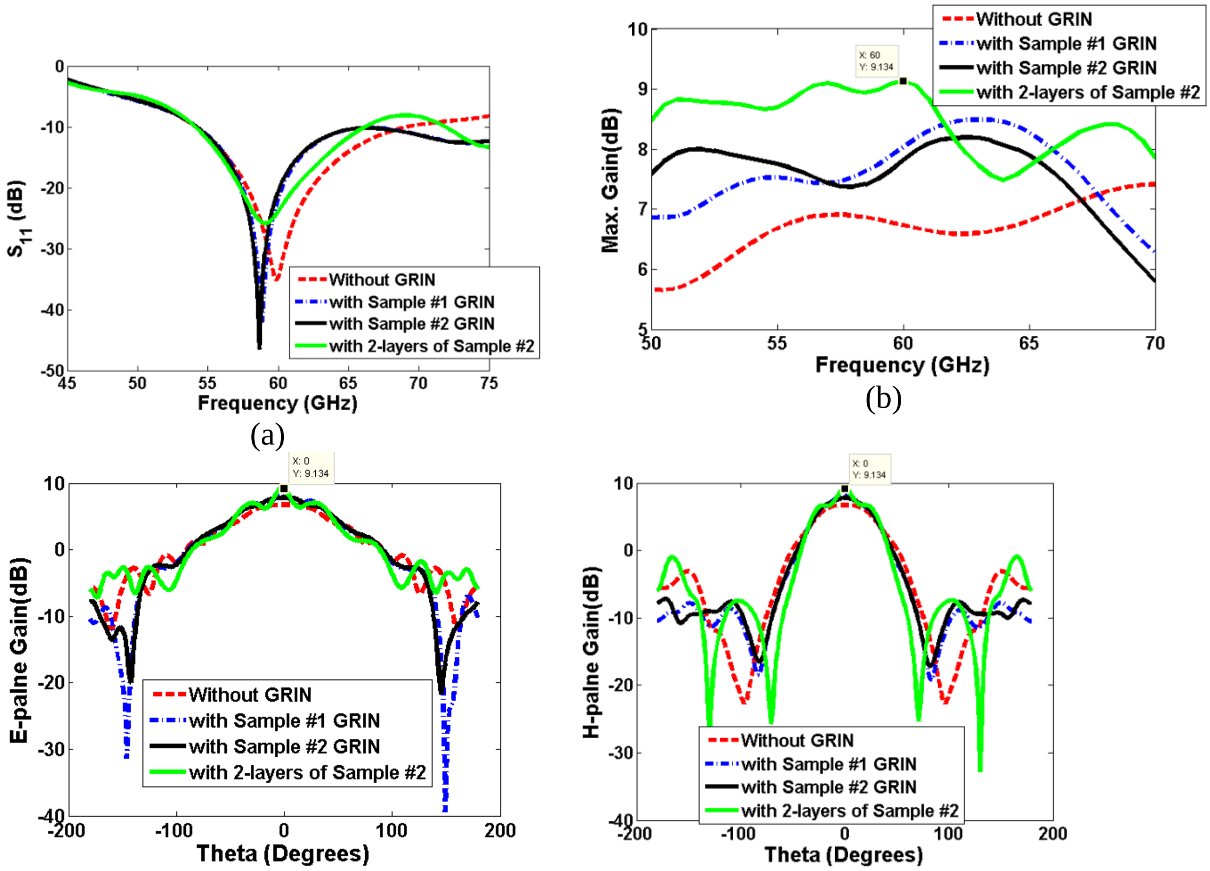

(a) (b) (c) (d)

Fig. 7.23. Impact of annular slot MTS GRIN structure size on the performance of the proposed antenna performance; a) S_{11} magnitude, (b) maximum gain versus frequency, (c) *E*-plane gain at 60 GHz, (d) *H*-plane gain at 60 GHz. The separation distance between the lens and the antenna slot is 3 mm and the intra layer separation is 1.5 mm.

Table 7.13 Impact of the GRIN MTS size employing Luneburg lens on the proposed antenna performance

Parameters	Sample 1	Sample 2	Sample 2, 2 layers
Periodicity p (mm)	2		
GRIN structure profile	Slotted ring with a parabolic distribution of $r_{\min} = 0.562\ mm$ And $r_{\max} = 0.682\ mm$		
Size ($N_x \times N_z$)	11×11	13×13	13×13, 2 layers with 1.5 mm separation between the 2 layers
Slot- GRIN separation distance d_z(mm)	3		
Δn	0.831	0.831	0.831
FBW (%)	12.828/60	12.96/60	11.85/60
S_{11} at 60 GHz (dB)	-41.55, shifted to 58.877 GHz	-46.303, shifted to 58.68 GHz	-25.8
η_{rad} (%)	98.90	98.96	98.90
η_{tot} (%)	98.16	98.45	98.04
E-plane HPBW (°) , Gain (dB), main lobe (°) direction (°), and side lobe level (°)	87.9, 8.09, -2, and -15.1	92.6, 7.82, 4, -10.1	53.3, 9.28, -2, -2.3
H-plane HPBW (°) , Gain (dB), main lobe (°) direction (°), and side lobe level (°)	57.3, 8.04, 0, and -15.8	58, 7.81, 1, and -15	53.4, 9.13, 0, and -10.1

It is clear from Fig. 7.23 and Table 7.13 that, as the number of GRIN MTS layers increases, the beam becomes more focused and hence the gain increases. Thus, the optimal gain is obtained when placing samples #1 and #2 together in front of the antenna. The gain is improved due to beam focusing caused by Luneburg lens from about 6.7 dB to 9.28 dB and 9.13 dB for the *E* and *H* planes, while the HPBW is reduced from 107° and 67° to 53.3° and 53.4° for *E* and *H* planes, respectively. However, the proposed antenna has good impedance matching and the bandwidth is slightly reduced.

Furthermore, to optimize the separation distance d_z between the antenna slot and the Luneburg lens, the proposed antenna incorporated with sample #2 GRIN MTS was simulated in CST for different separation distances and the proposed antenna performance parameters are calculated and plotted in Fig. 7.24.

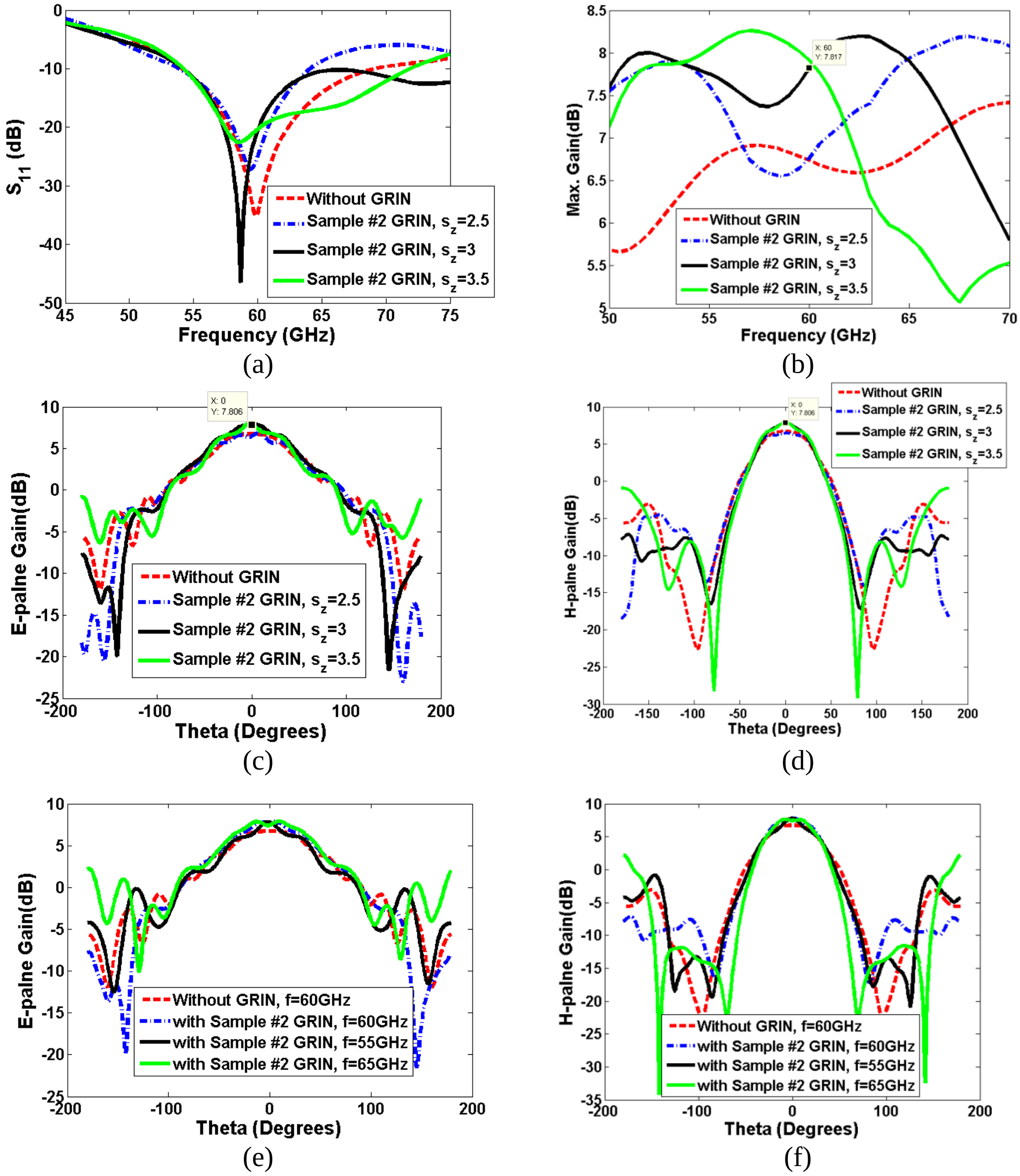

Fig. 7.24. Impact of separation distance d_z(or s_z) between the MTS GRIN and the antenna slot on the performance of the proposed antenna performance; a) S_{11} magnitude, (b) maximum gain versus frequency, (c) *E*-plane gain at 60 GHz, (d) *H*-plane gain at 60 GHz. sample #2 Luneburg lens was integrated with the slotted antenna to construct the proposed device.

It is clear from Fig. 7.24 that, the optimal separation distance between the slot and the MTS structure is 3 mm which gives a maximum gain of 7.8 dB at 60 GHz by using a single layer of size 13 by 13 unit cells. Also at d_z of 3 mm optimal impedance matching occurs.

7.8.3. Design, Simulation and Optimization of 60 GHz Incorporated with Parabolic Distributed *E*-plane and *H*- plane GRIN MTS Structures

Here, the proposed slotted waveguide antenna incorporated with *E*-plane and *H*- plane GRIN MTS shown in Fig. 7.16 was redesigned to operate at 60 GHz. The GRIN MTS structure was constructed from 2D periodic structure of annular slot unit cell with the dimensions given in Table 7.12. Three different samples (samples #1, #2, and #3) of GRIN MTS with parabolic spatial distribution were designed with the dimensions given in Table 7.14. Sample #1 is 5×6 unit cells with parabolic distributed GRIN across the *H*-plane. Samples #2 and #3 are of sizes 13×7 and 6×5, respectively with parabolic distributed GRIN across the *E*-plane. The impact of samples #1 and #2 on the proposed antenna performance were studied and the antenna parameters are plotted in Fig. 7.25.

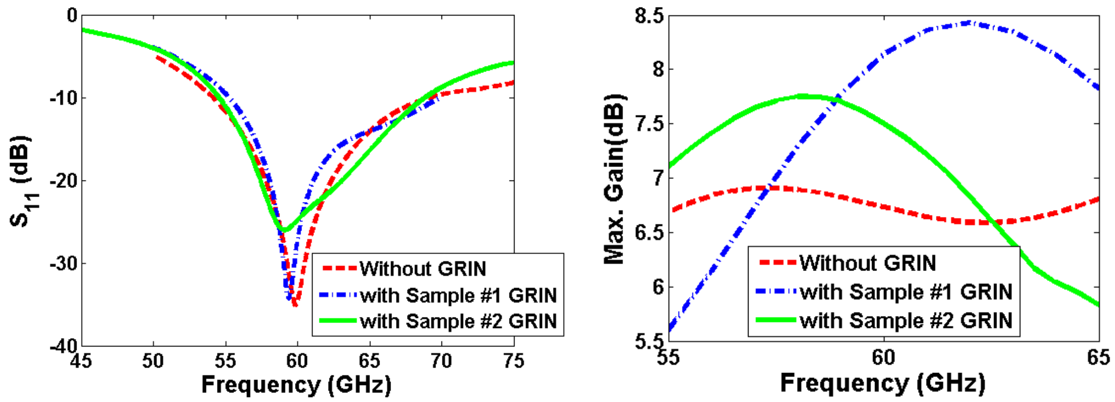

(a) (b)

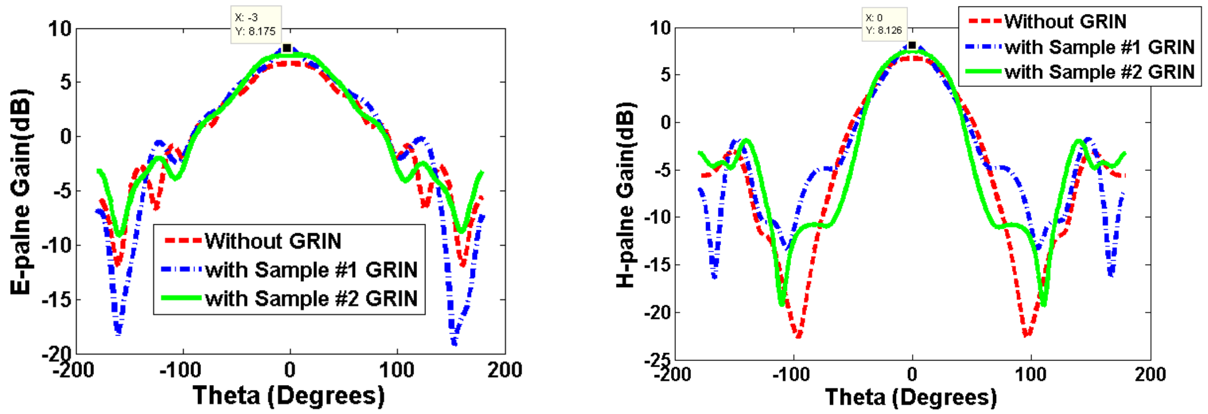

(c) (d)

Fig. 7.25. The Impact of parabolic distributed GRIN with different sizes on the proposed antenna performance; (a) S_{11} magnitude, (b) maximum gain versus frequency, (c) *E*-plane gain at 60 GHz, (d) *H*-plane gain at 60 GHz. The separation distance between the lens and the antenna slot is 3 mm.

It is clear from Fig. 7.25 that, sample #1 gives the best antenna performance, so it can be considered as the best candidate to focus the radiated waves and then if it is rotated by 90° to become 6×5 structure in the *x* and *y* directions, respectively, so the GRIN profile will be parabolic distributed along *y* axis and constant along *x* axis, so this sample (it is denoted as sample#3) can be used to improve the *E*-plane field. However samples #1 and #3 can be integrated to culminate both *E* and *H* fields and also multilayers from same or different samples can be used to obtain a more focused radiated beam. The impact of the different combination scenarios of parabolic spatially distrusted GRIN MTS samples on the proposed antenna performance were studied and plotted in Fig. 7.26. The separation distance between the antenna slot and the edge of the GRIN MTS and the intra separation distance between the different layers of the GRIN MTS are reported in Table 7.14. Also the antenna performance key parameters such as S_{11} , FBW, HPBW, gain, main lobe direction and side lobe level are reported in Table 7.14.

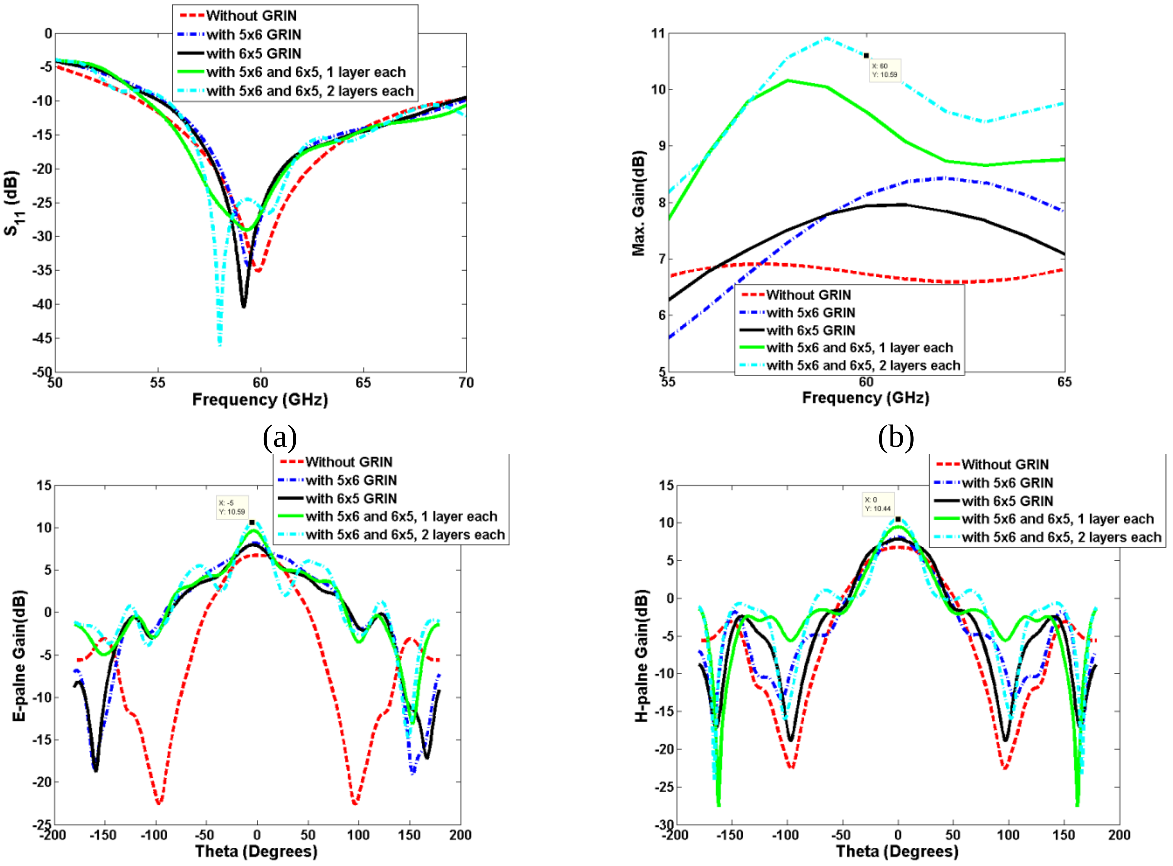

(a) (b)

(c) (d)

Fig. 7.26. Impact of the different combination scenarios of parabolic spatially distrusted GRIN MTS samples on the proposed antenna performance; (a) S_{11} magnitude, (b) maximum gain versus frequency, (c) *E*-plane gain at 60 GHz, (d) *H*-plane gain at 60 GHz. The separation distance between the lens and the antenna slot is 3 mm.

Table 7.14 Impact of the different combination scenarios of parabolic spatially distrusted GRIN MTS samples on the 60 GHz proposed antenna performance.

Parameters	Sample 1	Sample 2	90 degrees rotated Sample 1 or (Sample 3)	Cascaded samples 1 and 3, 1 layer of each	Cascaded samples 1 and 3, 2 layers of each
Periodicity p (mm)	2				
GRIN structure profile	Slotted ring with a Linear distribution of $r_{\min} = 0.562\ mm$ And $r_{\max} = 0.682\ mm$ and step size based on the structure size				
Size ($N_x \times N_z$)	5×6	13×7	6×5	5×6 and 6×5, one layer each, with 1.5 mm separation between each 2	5×6 and 6×5, two layers each, with 1.5 mm separation between

				layers	each 2 layers
Slot- GRIN separation distance d_z(mm)	4	4	4	d_z =4mm and 1.5 mm between each 2 layers	d_z =4mm
Δn	0.8346	0.8346	0.8346	0.8346	0.8346
FBW (%)	24.45	24.16	23.2	25.8	23.92
S_{11} at 60 GHz (dB)	-34.02, shifted to 59.46 GHz	-25.912, shifted to 59.334 GHz	-40.4, shifted to 59.20 GHz	-29.345 shifted to 59.34 GHz	-46.15, shifted to 58 GHz
η_{rad} (%)	99.26	99.15	98.98	98.60	97.96
η_{tot} (%)	99.07	98.83	98.69	98.38	97.714
E-plane HPBW (°) , Gain (dB), main lobe (°) direction (°), and side lobe level (°)	83.9, 8.17, -3, and -8.4	96.2, 7.5, 0, and -9.5	62.7, 7.94, -4 and -8.1	37.3, 9.62, -4, -5.3	29.1, 10.6, -3, and -4.6
H-plane HPBW (°) , Gain (dB), main lobe (°) direction (°), and side lobe level (°)	45.1, 8.13, 0, and -9.9	62.1, 7.49, 0, -9.4	62.6, 7.83, 0, and -10.2	39, 9.45, 0, and -10.9	31.6, 10.4, 0 and -9.4

It is clear from Fig. 7.26 and Table 7.14 that, GRIN MTS composed of 2 layers of sample #1 and 2 layers of sample #3 provides the optimal gain and narrower HPBW. The gain of the proposed 60 GHz antenna is improved from 6.7 dB to 10.6 dB and 10.4 dB for both *E* and *H* planes, respectively. Also the beam is reduced from 107° and 67° to 29.1° and 31.6°, for *E* and *H* planes, respectively. However, the proposed antenna has good impedance matching and the bandwidth is slightly reduced. The 60 GHz proposed antenna FBW is 25.38%.

7.9. Design of 100 GHz Slotted waveguide Antenna Incorporated with Annular Slot Metasurface Employing GRIN MTS Structure for Beam Focusing

Since one of the major motivations of this thesis is to design a THz high gain antenna to be used for high data bit rate communication system, the proposed antenna presented in Fig. 7.20 was redesigned to operate at 100 GHz. The proposed antenna was composed of a conventional slotted waveguide antenna incorporated with a multilayer annular slot 2D periodic structure employing a Luneburg lens. The design of annular slot unit cell exhibiting GRIN and also the design and characterization of the 100 GHz proposed slotted waveguide antenna will be presented in the coming subsections.

7.9.1. Design of Annular Slot Unit Cell Employing GRIN MTS around 100 GHz

Here, a unit cell of the annular slot is shown in Fig. 7.14 which exhibits a spatially distributed gradient index of refraction around 100 GHz was designed, simulated and characterized based on the Effective Medium Theory (EMT). The dimensions of the annular slot unit cell which exhibits GRIN around 100 GHz is given in Table 7.15. To exhibit GRIN around 100 GHz, the slot radius *r* was swept from 0.289 to 0.349 mm with a step of 0.01 mm. The *S-parameters* of the annular slot unit cell were calculated in CST frequency domain solver with unit cell Floquet's boundary conditions and plotted in Figs. 7.27 (a) to 7.27 (d). And then the effective parameters of the unit cell were extracted from the *S-parameters* using NRW algorithm and the results are reported in Figs. 7.27 (e) to 7.27 (j).

Table 7.15 dimensions of slotted ring employing 2-D GRIN medium at 100 GHz

Parameter	p	g	r	h	ε_r	t	Substrate	Metal cladding
Dimension (mm)	1.5	0.25	0.289:0.01:0.349	0.13	2.2	0.0175	RT/Duroid 5880	Copper

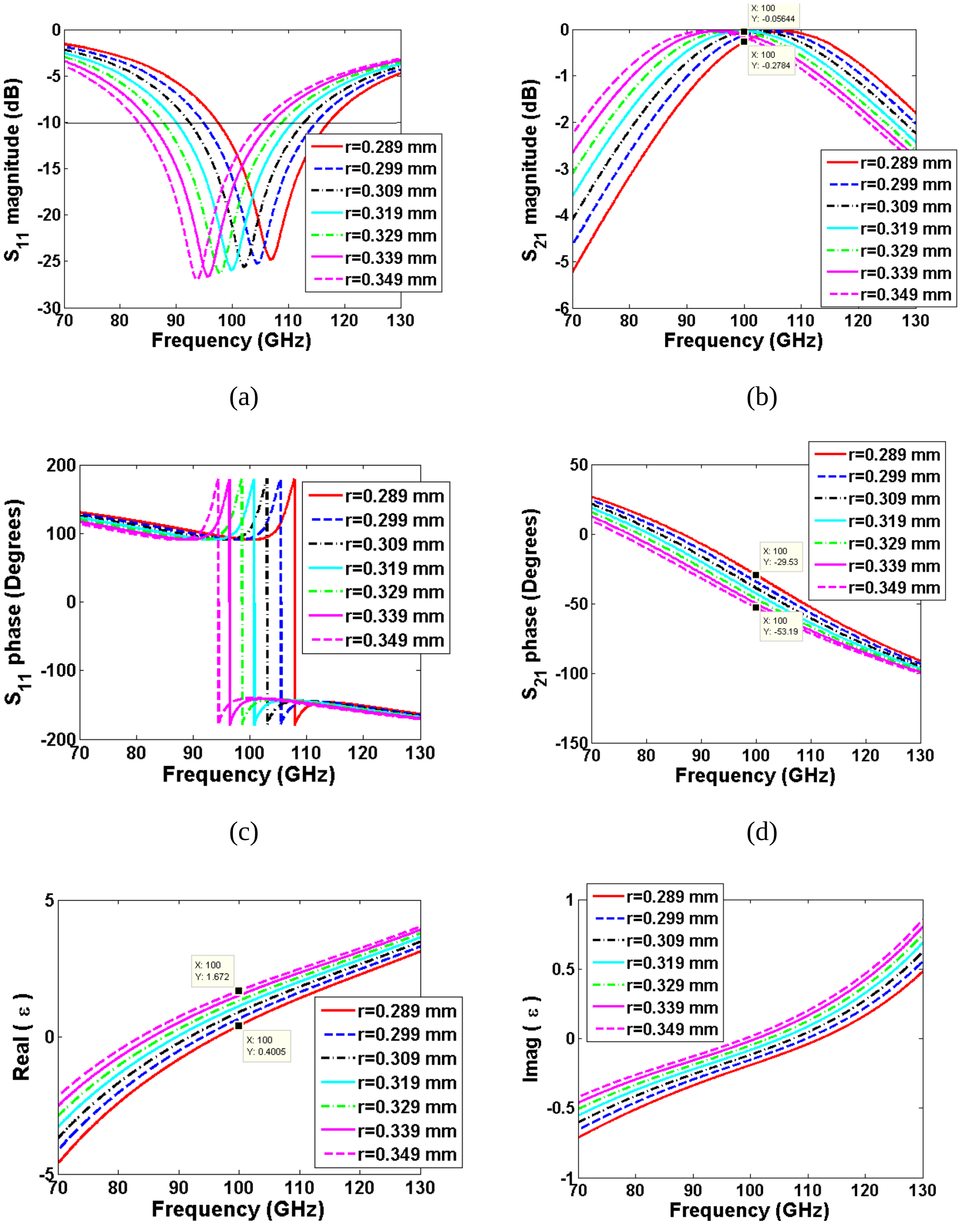

S11 magnitude (dB)
0
-5
-10
-15
-20
-25
-30
70
80
90
100
110
120
130
Frequency (GHz)
r=0.289 mm
r=0.299 mm
r=0.309 mm
r=0.319 mm
r=0.329 mm
r=0.339 mm
r=0.349 mm
S21 magnitude (dB)
0
-1
-2
-3
-4
-5
-6
X: 100
Y: -0.05644
X: 100
Y: -0.2784
S11 phase (Degrees)
200
100
0
-100
-200
S21 phase (Degrees)
50
0
-50
-100
-150
X: 100
Y: -29.53
X: 100
Y: -53.19
Real (ε)
5
0
-5
X: 100
Y: 1.672
X: 100
Y: 0.4005
Imag (ε)
1
0.5
0
-0.5
-1

(a)

(b)

(c)

(d)

(e)

(f)

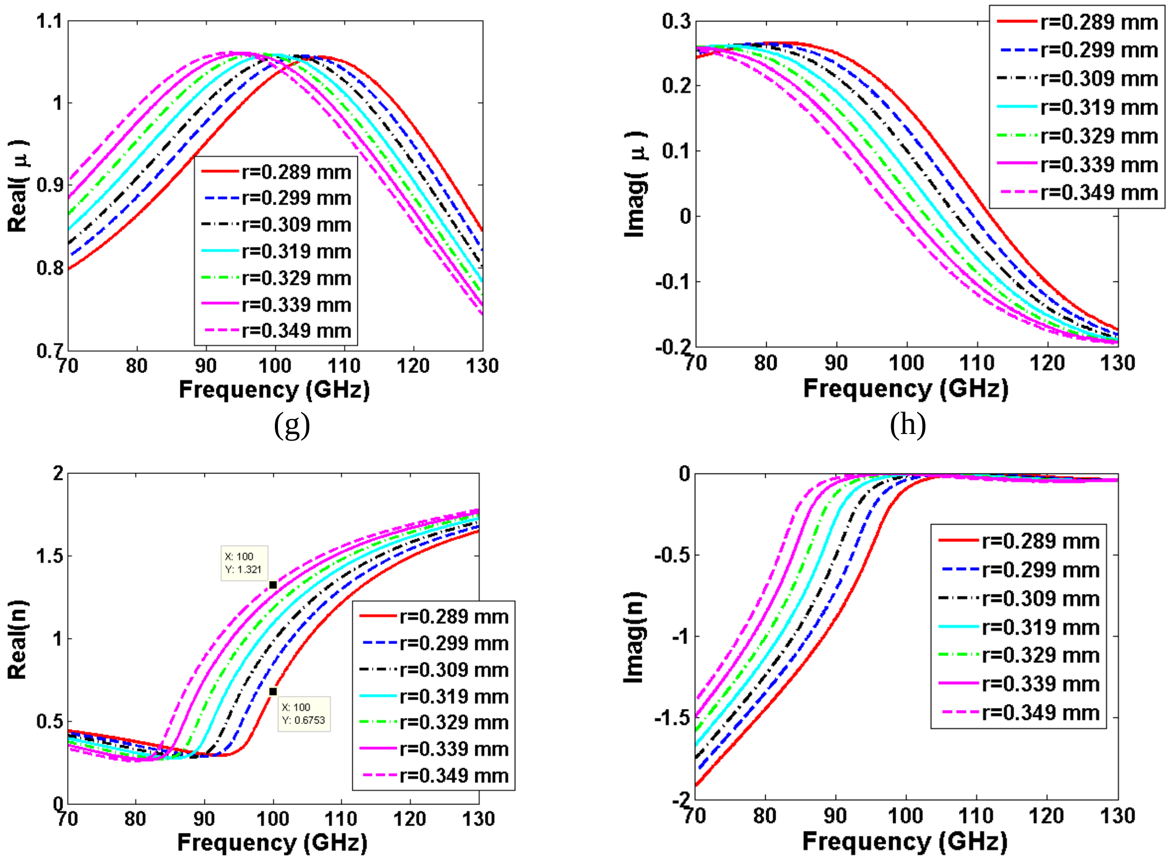

(g) (h)

(i) (j)

Fig. 7.27. The scattering and the effective parameters of the annualar slot unit cell to construct GRIN medium around 100 GHz at different radius *r* changes from 0.289 mm to 0.349 mm and periodicity p of 1.5 mm in both *x* and *y* directions, (a) magnitude of the reflection coefficient, (b) magnitude of the transmission coefficient, (c) phase of the reflection coefficient, (d) phase of the transmission coefficient, (e) and (f) real and imaginary part of effective permittivity, respectively, (g) and (h) real and imaginary part of effective permeability, (i) and (j) real and imaginary part of effective refractive index.

It is clear from Fig. 7.27 that, inside the sweeping range of *r* (i.e. 0.289 mm to 0.349), the annular slot provides a good transmission coefficient S_{21} in the range from -0.056 to -0.278 dB which implies good transmission. Furthermore, the index of refraction is changed from 0.675 to 1.32. This means the gradient in the index of refraction is 0.645.

7.9.2. 100 GHz Slotted Waveguide Antenna Incorporated with Annular Slot GRIN Structure Employing Luneburg Lens

Here, the designed annular slot unit cell which exhibits GRIN around 100 GHz was used to construct a 2D periodic structure of parabolic spatially distributed GRIN structure employing a Luneburg lens [11]. The Luneburg lens was placed in front of a 100 GHz slotted waveguide antenna as shown in Fig. 7.20. The antenna was excited by WR-10 waveguide. The separation distance between the antenna slot d_z and the Luneburg lens and the number of GRIN MTS layers was optimized using CST software to maximize the antenna gain. The optimal separation d_z was found to be 1.7 mm. The impact of the number of layers of the GRIN MTS employing Luneburg lens on antenna performance was studied and simulated in CST software. Figure 7.28 shows the performance of the 100 GHz proposed antenna incorporated with 1 and 2 layers of GRIN MTS structure.

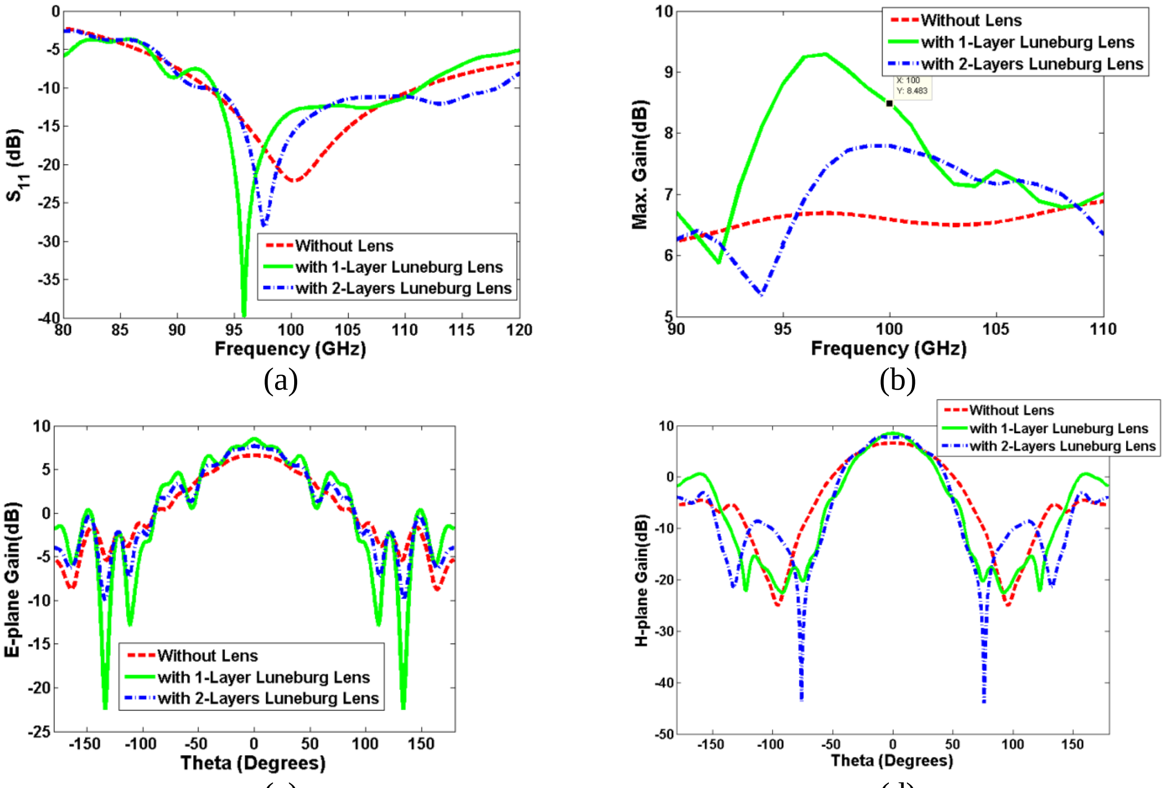

(a) (b)

(c) (d)

Fig. 7.28. Performance of 100 GHz proposed slotted waveguide antenna incorporated with multilayer annular slot GRIN MTS structure employing a Luneburg lens; a) S_{11} magnitude, (b) maximum gain versus frequency, (c) *E*-plane gain at 100 GHz, (d) *H*-plane gain at 100 GHz. The separation distance between the lens and the antenna slot is 1.7 mm and the intra GRIN MTS layers separation was 0.5 mm.

It is clear from Fig. 7.28 that, 2 layers of 13×13 unit cells 2D periodic structure of parabolic distributed GRIN MTS provides more beam focusing and gain improvement as compared to 1 layer of 2 D periodic structure of GRIN. As a result, the gain was improved from 6.6 dB to 8.5 dB and the beam area was reduced from 104.5° and 71.2° to 91.6° and

43.3° for the E and H planes, respectively, while the bandwidth and impedance matching was slightly changed. The 100 GHz proposed antenna FBW was 18.85 %.

7.10. Fabrication and Measurement

Here, the proposed slotted waveguide antennas incorporated with resonance and non-resonance GRIN MTS structure for beam focusing purposes were fabricated and tested. The proposed resonance GRIN MTS was composed of an annular slot MTS while the non-resonance GRIN MTS was composed of a metallic rectangular/circular patch 2-D periodic structure mounted on a dielectric substrate. The proposed antenna consists of a conventional slotted waveguide antenna and a GRIN MTS structure. The conventional slotted waveguide antenna had been fabricated by using milling technology, while the GRIN MTS had been fabricated by using wet etching PCB technology. The proposed antennas incorporated with resonance and non-resonance GRIN MTS were fabricated and tested at 10, and 60 GHz. For the 10 GHz antenna, the GRIN MTS structures were fabricated on 5880 RT/Duroid substrate of height 0.508 mm with copper cladding of 35 μm thickness and for 60 GHz, they were fabricated on 5880 RT/Duroid substrate of height 0.127 mm with copper cladding of 17.5 μm thickness. The following subsections presented the fabricated antenna and the measured results in comparison to the simulations results.

7.10.1. 10 GHz Slotted Waveguide Antenna Incorporated with Non-Resonance GRIN MTS Lens

Figure 7.29 shows the fabrication of the 10 GHz proposed slotted waveguide antenna incorporated with a metallic patch 2D periodic structure employing an non-resonance GRIN MTS. Three different samples were fabricated with the dimensions presented in Table 7.2. Samples #1 and #2 were constructed from a rectangular metallic patch 2D periodic structure with linearly spatially distributed GRIN while sample #3 was constructed from a circular metallic patch 2D periodic structure with parabolic spatially distributed GRIN. The GRIN MTS was placed in front of the antenna patch as shown in Fig. 7.27 with a horizontal separation d_z and vertical offset d_y with respect to the antenna slot centre of 2.5 mm and -7 mm, respectively. Then the antenna was excited by WR-19 standard waveguide.

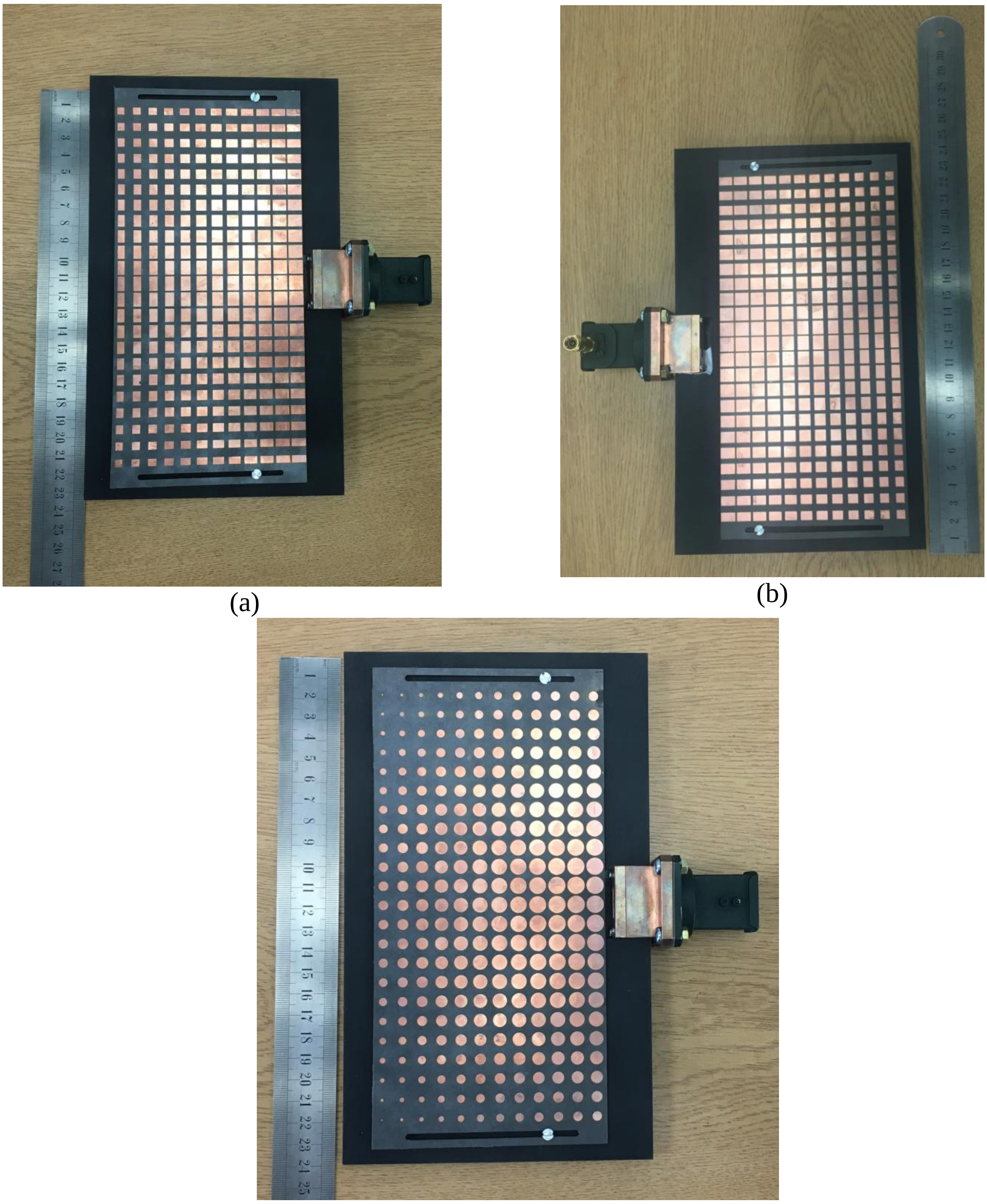

(a) (b)

(c)

Fig. 7.29. Fabricated 10 GHz slotted waveguide antenna incorporated with GRIN MTS based on rectangle /circular patches structure. The proposed antenna was connected with an SMA connector to waveguide adaptor; (a) sample #1, (b) sample #2 and (c) sample #3. The details of sample #1, #2 and #3 are given in Table 7.2.

The impedance matching parameters and the radiation pattern properties of the fabricated 10 GHz proposed antenna were measured and displayed as shown in Fig. 7.30. Figure 7.30 shows the magnitude of the S_{11}, maximum gain versus frequency, E and H plane gains for the simulated and measured antenna.

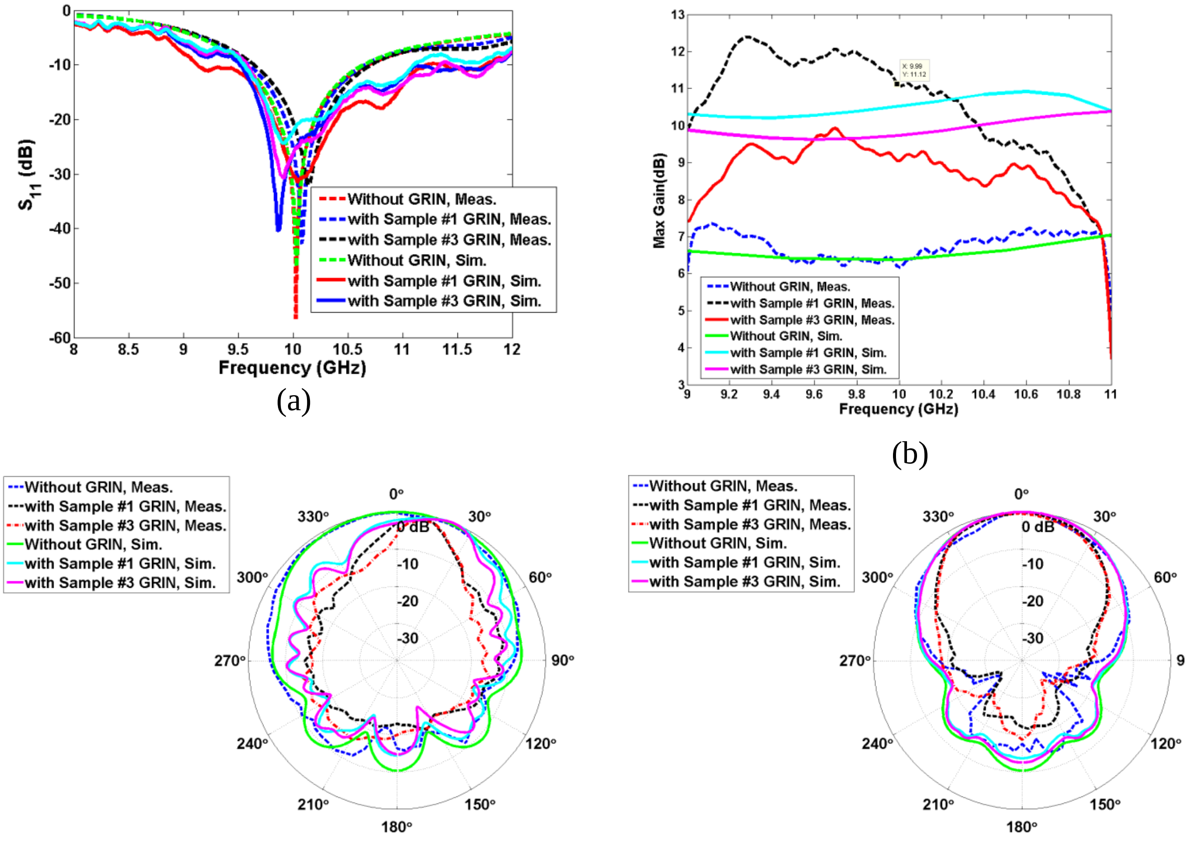

(a)

(b)

(c)

(d)

Fig. 7.30. Simulated and measured impedance matching parameters and radiation pattern properties of the 10 GHz proposed slotted waveguide antenna with and without GRIN MTS at different in both sample size and different index of refraction spatially distribution profiles. The horizontal separation distance d_z and the vertical offset d_y of the GRIN MTS with respect to the slot centre are 2.5 and -7 mm, respectively; (a) magnitude of S_{11}, (b) magnitude of the maximum gain, (c) E-plane gain and (d) H-plane gain.

It is clear from Fig. 7.30 that, there are nice agreements between the simulated and the measured results with a little bit deviation due to the non-accurate mechanical assembly between the slotted waveguide antenna fabricated by the milling technology and the GRIN MTS fabricated by wet etching PCB technology. The proposed antenna incorporated with sample #1 provides the optimal antenna performance. Figure 7.30 (a) shows that, the proposed antenna has a good S_{11} and the FBW was approximately 10.5 %. Figure 7.30 (b) shows that, sample #1 provides the optimal measured gain in the *E*-plane and it is about 11.12 dB. However, the measured HPBW for the *H*-plane and *E*-plane are about 70° and 25°, respectively as it is illustrated from Figs. 7.30 (c) and (d). The main beam directions are 22° and 0° for *E* and *H* planes, respectively.

7.10.2. 60 GHz Slotted Waveguide Antenna Incorporated with Non-Resonance GRIN MTS Lens

Figure 7.31 illustrates the fabricated 60 GHz antenna incorporated with 2D periodic structure of metallic patches employing non-resonance GRIN MTS structure. Two different samples of GRIN MTSs are fabricated (samples #2 and #3) with detailed dimensions given in Table 7.4. Samples #2 and #3 have a linearly and parabolic 2D spatially distributed GRIN profiles. The horizontal separation distance d_z and the vertical offset d_y of the GRIN MTS with respect to the antenna slot centre are set at 1.5 mm and -1 mm, respectively. The antenna was excited by WR-15 standard waveguide.

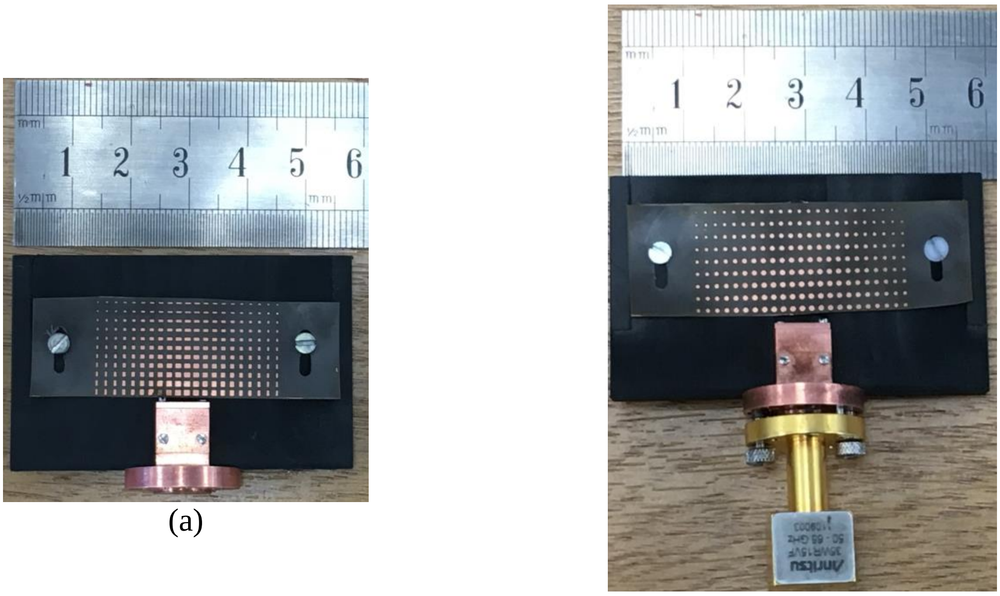

(a)

(b)

Fig. 7.31. Fabricated 60 GHz slotted waveguide antenna incorporated with GRIN MTS based on rectangle /circular metallic patches structure. The slot antenna was connected to an SMA to waveguide adaptor; (a) sample #2 and (b) sample #3. The details of samples #2 and #3 are given in Table 7.5.

The performance of the proposed antenna with and without GRIN MTS was measured as shown in Fig. 7.32 which illustrates the magnitude of the S_{11}, the maximum gain versus frequency, the *E* and *H* plane radiation patterns.

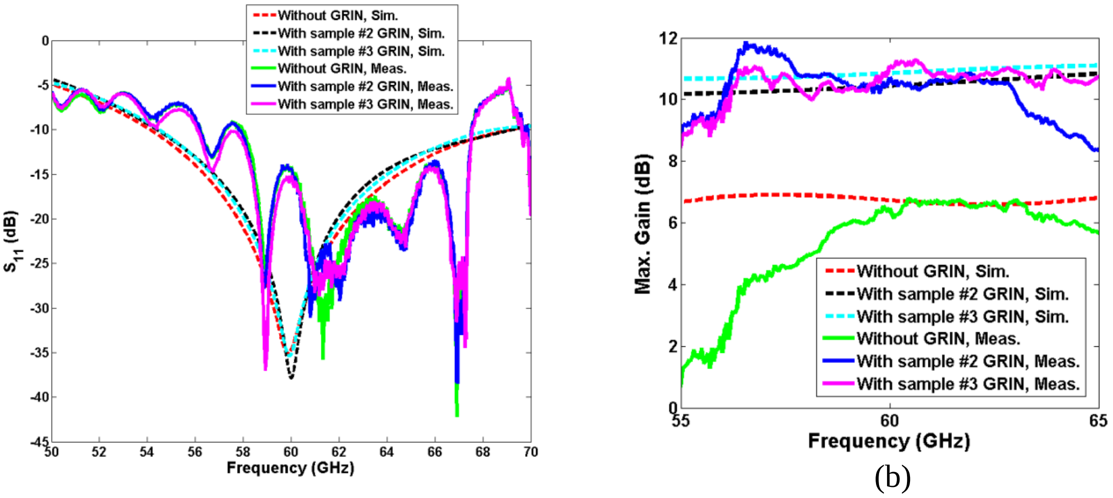

(a)

(b)

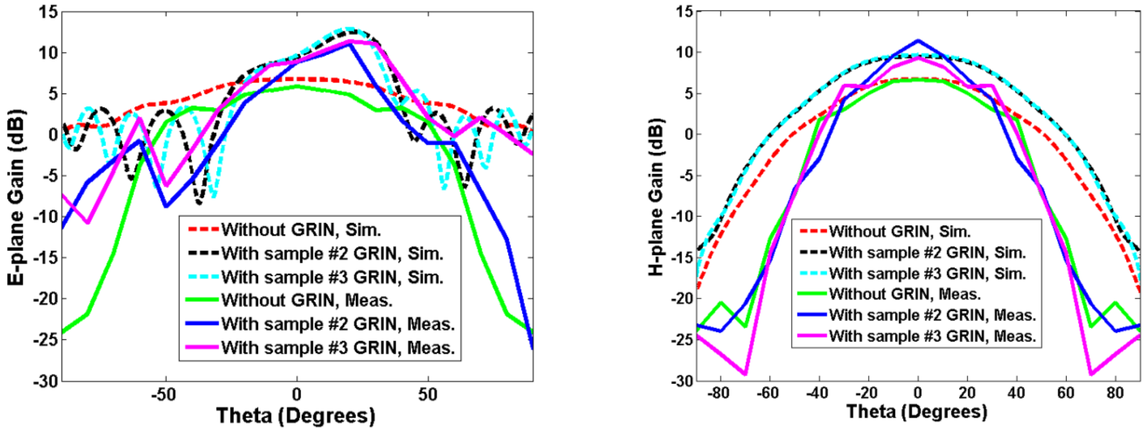

(c) (d)

Fig. 7.32. Simulated and measured impedance matching parameters and radiation pattern properties of the 60 GHz proposed slotted waveguide antenna with and without non-resonance GRIN MTS at different sample sizes and different index of refraction spatially distribution profiles. The horizontal separation distance d_z and the vertical offset d_y of the GRIN MTS with respect to the slot centre are 1.5 and -1 mm, respectively; (a) magnitude of S_{11}, (b) magnitude of the maximum gain, (c) E-plane gain and (d) H-plane gain.

It is clear from Fig. 7.32 that, there is nice agreement between the measured and the simulated results with a little bit of deviation due to the non-accuracy of mechanical assembly. The proposed antenna incorporated with sample #3 provides the optimal antenna performance. Figure 7.32 (a) shows that, the measured proposed antenna has S_{11} of about -20 dB at 60 GHz and it has a FBW of about 25%. Figures 7.32 (b) through 7.32 (d) show that, the optimal measured gain of the proposed antenna is about 11 dB at 60 GHz. The measured *E*-plane HPBW of the proposed antenna decrease from about 106° and to 29° and the *H*-plane HPBW remains approximately the same at 65°. The main radiation beam directions are 20° and 0° for the *E* and *H* planes without significantly affecting the antenna impedance matching and its bandwidth.

7.10.3. 10 GHz Slotted Waveguide Antenna Incorporated with Resonance GRIN MTS Lens

Here, 10 GHz proposed slotted waveguide antenna incorporated with 2D periodic structure of annular slot employing a parabolic distributed GRIN profile across the E-plane was fabricated and tested. Figure 7.33 illustrates the fabricated proposed antenna incorporated with 4 layers GRIN MTS of parabolic profile across the E-plane; the size of each layer was 6×5 unit cells of the annular slot with dimensions presented in subsection 7.7.1. The GRIN MTS layers behave as a lens and it can focus the radiated waves and hence the antenna gain can be improved. The GRIN MTS structure was placed in front of the antenna slot at a separation distance d_z of 17 mm and the GRIN MTS intra-layer separation d_{z1} was 5 mm.

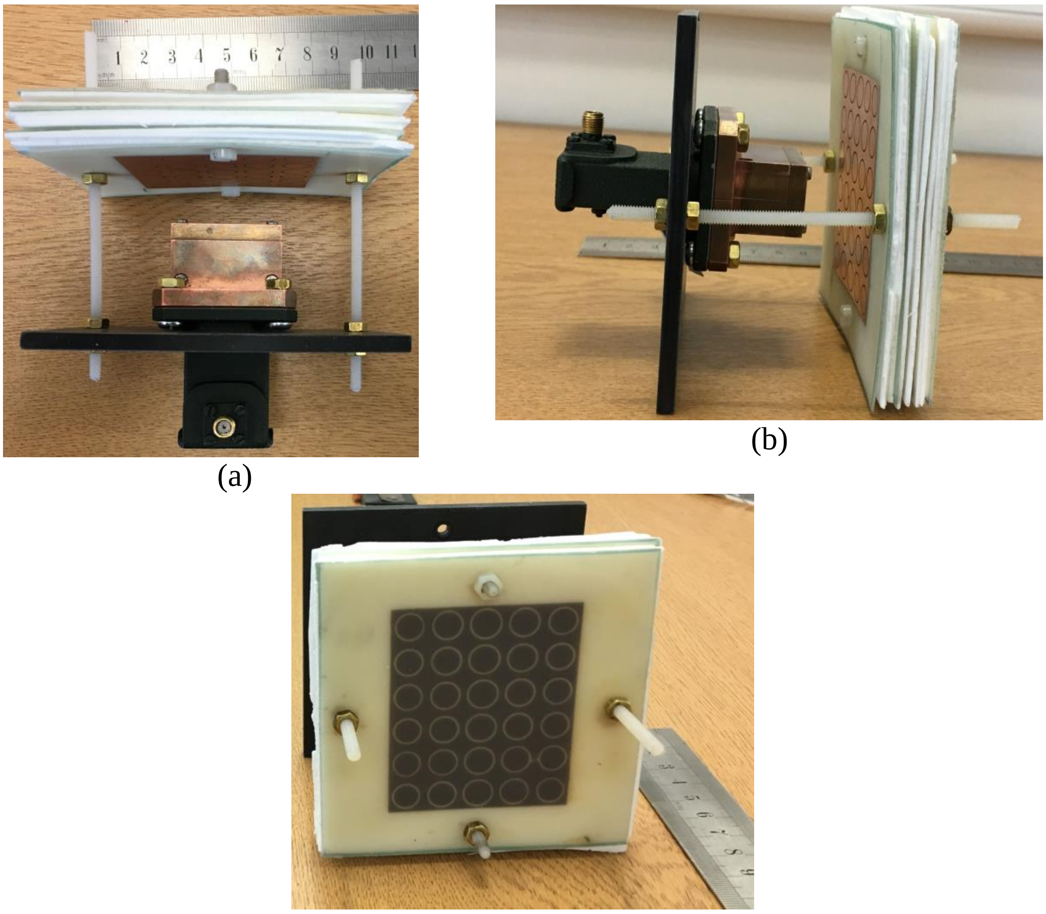
(b)

(a)

(c)

Fig. 7.33. Fabricated 10 GHz slotted waveguide antenna incorporated with parabolic spatially distributed GRIN medium based on annular slot MTS. (a), (b) and (c) are top, side and back views, respectively for the slotted antenna incorporated with parabolic spatially distributed GRIN medium in the E-plane direction only.

The impedance matching parameters including S_{11} magnitude and maximum gain and also the radiation properties including the *E* and *H* plane patterns for the proposed antenna were measured and compared with the simulation results as shown in Fig. 7.34.

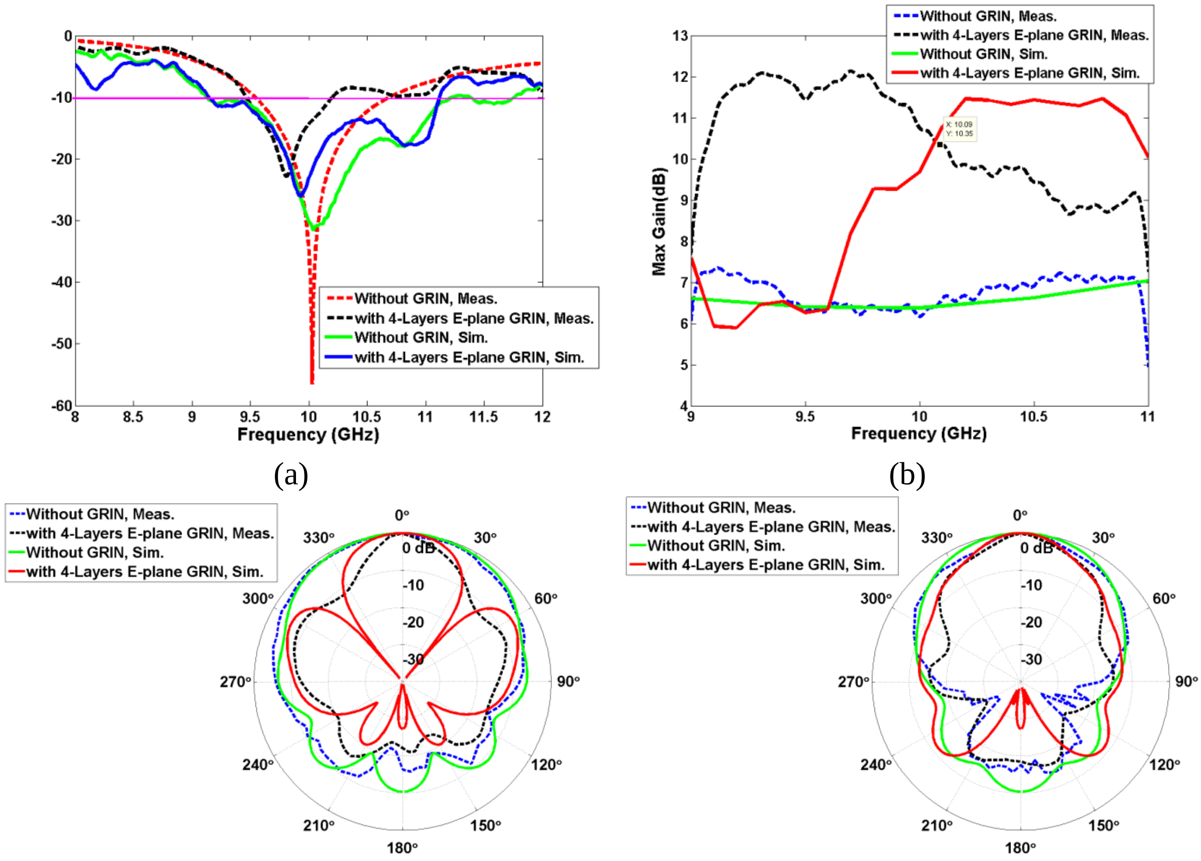

(a) (b)

(c) (d)

Fig. 7.34. Simulated and measured impedance matching parameters and radiation pattern properties of the 10 GHz proposed slotted wave guide antenna with and without 4 Layers annular slot GRIN MTS of the *E*-plane parabolic spatially distributed index of refraction. The separation distance d_z between the antenna slot and the GRIN MTS edge was 17 mm and the separation distance between each two GRIN layers was 5 mm; (a) magnitude of S_{11}, (b) magnitude of the maximum gain, (c) *E*-plane gain and (d) *H*-plane gain.

It is clear from Fig. 7.34 that, there is an agreement between the simulated and measured results with some deviation due to mechanical assembly. The proposed antenna incorporated with 4 layers of GRIN MTS with parabolic profile across the *E*-plane provides the optimal antenna performance. The obtained measured gain was 10.3 dB at 10 GHz. The measured *E* and *H* planes HPBW were reduced from 107° and 67° to about 40° and 35°, respectively. However the proposed antenna has a good impedance matching as well as good FBW of approximately 10%.

7.10.4. 60 GHz Slotted Waveguide Antenna Incorporated with Resonance GRIN MTS Lens

Figure 7.35 illustrates the fabricated 60 GHz slotted waveguide antenna incorporated with GRIN structure composed of 2 layers of parabolic distributed GRIN MTS across the *E*-plane and 2 layers of parabolic distributed GRIN MTS across the *H*-plane. The GRIN MTS layer was constructed from a 2D periodic structure of annular slot unit cells with the dimensions presented in Table. 7.12. The separation distance between the antenna slot and the GRIN medium is 3 mm and the intra-layer separation was 1 mm. The proposed 60 GHz antenna was excited by WR-15 standard waveguide. The antenna parameters were measured and plotted as shown in Fig. 7.36.

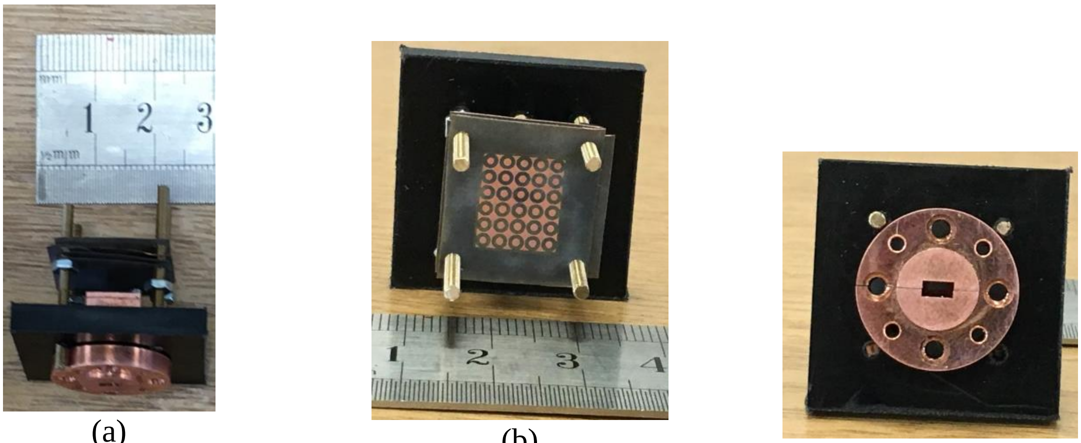

(a) (b) (c)

Fig. 7.35. Fabricated 60 GHz slotted waveguide antenna incorporated with parabolic spatially distributed GRIN medium based on slotted ring MTS. (a), (b) and (c) are top, back and front views, respectively. The GRIN medium was composed of 2 layers of *E*-plane and 2 layers of *H*-plane parabolic distributed GRIN profiles. The separation distance between the antenna slot and the GRIN medium was 3 mm and the intra-layer separation was 1 mm.

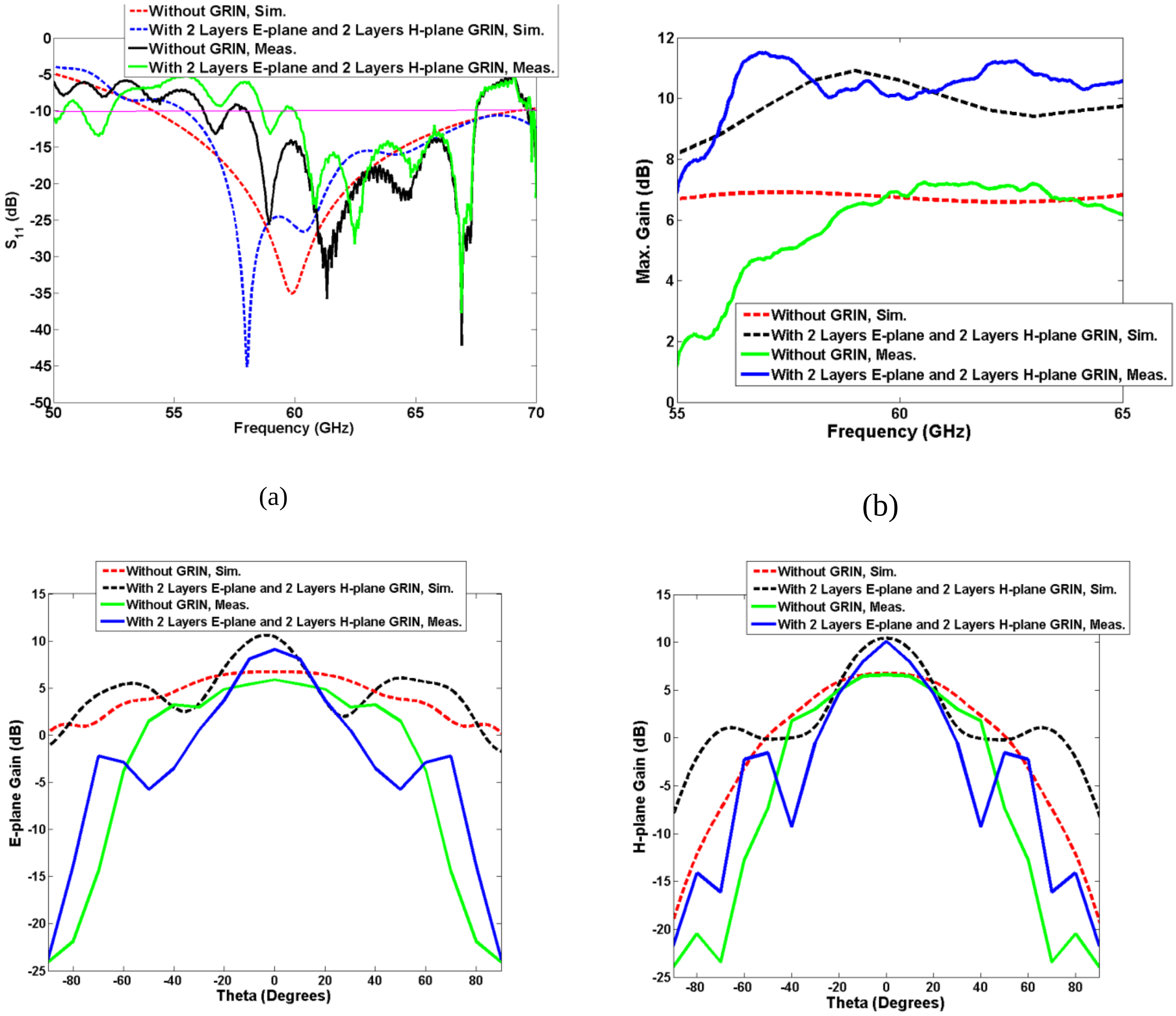

(a) (b)

(a) (b)

Fig. 7.36. Simulated and measured impedance matching parameters and radiation properties of the 60 GHz proposed slotted waveguide antenna incorporated with GRIN MTS composed of 2 layers of *E*-plane and 2 layers of *H*-plane parabolic spatially distributed annular slot GRIN MTS. The separation distance between the antenna slot and the first GRIN layer was 3 mm and the intra layer to layer separation was 1 mm; (a) magnitude of S_{11}, (b) magnitude of the maximum gain, (c) *E*-plane gain and (d) *H*-plane gain.

It is clear from Fig. 7.36 that, there is a nice agreement between the measured and the simulated results with small deviation due to mechanical assembly. Figure 7.36 (a) shows that measured proposed antenna has S_{11} of about -15 dB at 60 GHz and the FBW was about 16%. Figures 7.36 (b) through 7.36 (d) illustrate that, the measured gain was improved from about 6.7 dB to 10.1 dB for both the *E* and *H* planes. Furthermore, the measured HPBW was reduced from 107° and 67° to 28° and 30°, for the *E* and *H* plane, respectively. However, the measured 60 GHz proposed antenna has good impedance matching and the bandwidth is slightly reduced.

7.11. Summary

In this chapter two different structures for high performance slotted waveguide antennas incorporated with GRIN medium are proposed, designed, simulated, fabricated and measured. The proposed antennas were designed, simulated and optimized at 10, 60, 100 and 200 GHz. For verification purposes, 10 and 60 GHz antennas were fabricated and measured. The proposed antennas provide a high gain without significantly affecting the impedance matching and the antenna bandwidth. The gain improvement was obtained due to beam focusing caused by the GRIN structure. The GRIN structure was implemented from one layer or multilayers of the 2D periodic structure of resonance or non-resonance, parabolic or linear spatially distributed GRIN MTSs. The resonance GRIN MTS was composed of annular slot 2D periodic structure with linear or parabolic GRIN profile. The non-resonance GRIN MTS was composed of metallic patches of 2D periodic structure with linear or parabolic GRIN profile. Also, the GRIN profile can be spatially distributed across the antenna *E*-plane or *H* plane or both. In addition, a Luneburg lens has been constructed based on parabolic distributed annular slot 2D periodic structure in both the *E* and *H* planes.

The non-resonance metallic patch GRIN MTS has been designed at 10, 60, 100 and 200 GHz frequencies based on dispersion-diagram with the aid of Eigen mode CST solver. While the resonance annular slot GRIN MTS has been designed based on Effective Medium Theory (EMT) by extracting the effective parameters from the *S-parameters* using NRW algorithm. The antennas were fabricated by using low structured milling technology to fabricate the slot antenna, in addition to the wet etching PCB technology to fabricate the

GRIN MTS. The antennas were tested in the lab, S_{11} magnitude, maximum gain, *E* and *H* planes radiation patterns were measured and compared to the simulation results.

For the proposed 10 GHz slotted waveguide antenna incorporated with metallic patch GRIN MTS, the gain improvement occurs in the *E*-plane and it is about 11.12 dB while the *H* plane gain is about 7.5 dB. However, the measured HPBW for the *H*-plane and *E*-plane are about 70° and 25°, respectively. The main beam directions are 22° and 0° for *E* and *H* planes, respectively. Also, the proposed 60 GHz slotted waveguide antenna incorporated with a metallic patch GRIN MTS, the measured gain is about 11 dB at 60 GHz. The measured *E* plane HPBW decrease from about 106° and to 29° and the *H*-plane HPBW remains approximately the same at 65°. The main radiation beam directions are 20° and 0° for *E* and *H* planes, respectively, without significantly affecting the antenna impedance matching and its bandwidth. The 10 and 60 GHz proposed antennas have FBW of 10.5 and 25%, respectively.

For the 10 GHz proposed antenna incorporated with an annular slot based employing a resonance GRIN medium, the obtained measured gain is 10.3 dB at 10 GHz. The measured *E* and *H* planes HPBW are reduced from 107° and 67° to about 40° and 35°, respectively. However the proposed antenna has a good impedance matching and good FBW of approximately 10 %. For the 60 GHz proposed antenna incorporated with annular slot based GRIN medium, the measured gain was improved from about 6.7 dB to 10.1 dB for both the *E* and *H* planes. Furthermore, the measured HPBW was reduced from 107° and 67° to 28° and 30°, for *E* and *H* plane, respectively. However, the measured 60 GHz proposed antenna has good impedance matching and the bandwidth is slightly reduced. The 60 GHz proposed antenna FBW is 16%. It is clear from chapter 7 that, the optimal antenna incorporated with GRIN MTS is the one based on annular slot 2D periodic structure with multilayers of both E and H planes parabolic distributed GRIN structure. The typical gain of a single element of the proposed antenna is about 11.12 dB.

7.12. References

[1] Ziolkowski, Richard W. "Special issue on metamaterials." IEEE Trans. Antennas & Propag. 51, no. 10 (2003): 2546-2765.

[2] Kildal, Per-Simon. "Special issue on artificial magnetic conductors, soft/hard surfaces, and other complex surfaces." IEEE Trans. Antennas and Propagation 53, no. 1 (2005): 2-7.

[3] D. Sievenpiper, L. Zhang, F. J. Broas, N. G. Alexopulos, and E. Yablanovitch, "High-impedance electromagnetic surfaces with a forbidden frequency band," *IEEE Trans. Microwave Theory Tech.*, vol. 47, no. 11, pp. 2059–2074, Nov. 1999.

[4] P.-S. Kildal, "Definition of artificially soft and hard surfaces for electromagnetic waves," *Electronics Letters*, vol. 24, no. 3, pp. 168–170, 1998.

[5] S. Maci and P.-S. Kildal, "Hard and soft surfaces realized by FSS printed on a grounded dielectric slab," in *Proc. URSI-IEEE AP-S Symp.*, Monterrey, CA, Jun. 2004, pp. 285–288.

[6] B. Fong, J. S. Colburn, J. J. Ottusch, J. L. Visher, and D. F. Sievenpiper, "Scalar and tensor holographic artificial impedance surfaces," *IEEE Trans. Antennas Propag.*, vol. 58, no. 10, pp. 3212–3221, Oct. 2010.

[7] C. H.Walter, "Surface-wave Luneburg lens antennas," *IRE Trans. Antennas Propag.*, vol. 8, pp. 508–515, 1960.

[8] S.Maci,G.Minatti,M.Casaletti, andM.Bosiljevac, "Metasurfing: Addressing waves on impenetrable metasurfaces," *IEEE Antennas Wireless Propag. Lett.*, vol. 10, pp. 1499–1502, 2011.

[9] G. D. M. Peeler and H. P. Coleman, "Microwave stepped-index Luneburg lenses," *IRE Trans. Antennas Propag.*, vol. 6, no. 2, pp. 202–207, Apr. 1958.

[10] Bosiljevac, Marko, Massimiliano Casaletti, Francesco Caminita, Zvonimir Sipus, and Stefano Maci. "Non-uniform metasurface Luneburg lens antenna design." IEEE transactions on antennas and propagation 60, no. 9 (2012): 4065-4073.

[11] Paul, O., Reinhard, B., Krolla, B., Beigang, R. and Rahm, M., 2010. Gradient index metamaterial based on slot elements. *Applied Physics Letters*, *96*(24), p.241110.

[12] X. Chen, T. Grzegorczyk, B. Wu, J. Pacheco and J. Kong, 'Robust method to retrieve the constitutive effective parameters of metamaterials', Physical Review E, vol. 70, no. 1, 2004.

[13] Arslanagić, S., Troels Vejle Hansen, N. Asger Mortensen, Anders Heidemann Gregersen, Ole Sigmund, Richard W. Ziolkowski, and Olav Breinbjerg. "A review of the scattering-parameter extraction method with clarification of ambiguity issues in relation to metamaterial homogenization." IEEE Antennas and Propagation Magazine 55, no. 2 (2013): 91-106.

[14] Nicolson, A. M., & Ross, G. F. "Measurement of the intrinsic properties of materials by time-domain techniques. Instrumentation and Measurement", IEEE Transactions on, 19(4), 377-382, 1970.

Chapter 8 Conclusion and Future Work

8.1. Final Conclusion

In this thesis, new high performance microwaves, millimetres and terahertz antennas have been proposed, designed, simulated and verified experimentally. The developed antennas are based on Metatronics. Metatronics combine electronics, plasmonics, metamaterials, photonics and magnetics together in one electromagnetic paradigm. Metatronics exhibit new properties which are not found in nature such as medium with; negative effective parameters, near to zero effective parameters or gradient index of refraction. This thesis is focused on improving the gain of the antenna without affecting the antenna bandwidth by beam focusing based on negative index of refraction, low epsilon medium and gradient index of refraction. This thesis added the following contributions to the scientific world;

Firstly, the performance of a patch antenna is greatly improved by beam focusing when it is integrated with a 3-D SRRs/TWs periodic structure employing a MTM lens. The MTM lens was suspended above the patch antenna; the MTM lens focused the radiated EM waves of the patch antenna in a narrow area. As results, the antenna gain and directivity have improved. The optimized radiation properties of the proposed patch antenna have been obtained through the justification of the patch-MTM lens separation and the dimensions of the 3-D MTM periodic structure employing the MTM lens. As an example for terahertz application, the proposed antenna has been designed to operate at 303 GHz which can be used for heart beat rate measurement. The terahertz antenna simulation results demonstrated enhancements of 1.1dB, 14.73 GHz and 12.62 dB in the antenna gain, bandwidth and return loss as compared with the patch antenna without a MTM lens. These improvements in the antenna parameters validate the proposed concept of beam focusing using a 3-D periodic structure of SRRs/TWs, which employ the MTM lens, without modifying significantly in the matching methodology of the patch antenna. Furthermore, we have demonstrated the validity of the above properties. At 10 GHz by fabricating and measuring an antenna to verify the design concept. The results showed that at this frequency the antenna gain, bandwidth and return loss have improved by 1.5 dB, 10.15 MHz and 2 dB, respectively with minimal change in the antenna beam width. The challenges of SRRs/TWs NRI medium is its mechanical stability and difficulty incorporating it with a patch antenna.

Secondly, the performance of a 10 GHz patch antenna is greatly improved by beam focusing when it is integrated with a 3-D CSRRs/TWs periodic structure employing an MTM lens. The MTM lens was suspended above the patch antenna through bears made of foam. The 2-D infinite periodicity CSRR/TWs MTM structure was designed and simulated using CST software and the effective parameters extracted. The results illustrated that the MTM structure has negative values for the real part of the effective parameters. Furthermore, the angular independence of the CSRR/TWs MTM structure with infinite 2-D periodicity has been verified by rotating the MTM structure from 0 to 180 degrees with respect to the excitation probe of the TEM waves. The results showed that the MTM structure has negative effective parameters and good reflection and transmission characteristics in a wide band of angles around 10 GHz which proved that, the MTM acts as a lens. In addition, the infinite periodicity truncation of the MTM structure was also studied by designing and simulating 3-D MTM structures with finite sizes of 2×2×2, 3×3×2, and 4×2×2. The results showed that, the MTM structure truncation has no impacts on both the MTM lens negative effective parameters and homogeneity. The proposed antenna has been designed and optimized in CST software, the antenna bandwidth was improved and the return loss generally increased, although it might be improved if the MTM lens size is further optimized. Furthermore, we have demonstrated the validity of the above properties by CST software EM simulator and experimentally at 10 GHz and showed that at this frequency the antenna gain, has improved by 4.6 dB, while the beam width is reduced from 75 degrees to 41 degrees which validate the concept of beam focusing using CSRR/TWs MTM lens. The measured and the simulated results showed an improvement in the return loss by about -20 dB for the antenna incorporated with the MTM lens of size 2×2×2 although it increases further when 3×3×2 and 4×2×2 MTM lens sizes are used. This improvement is due to the reactance coming out from the electric and the magnetic coupling between the patch and the MTM lens and the coupling between the different parts of the MTM lens itself which result in a reactance term added to the antenna input impedance.

Thirdly, slotted waveguide antennas incorporated with eSRR metasurface structure employing anisotropic LEM medium in the direction of the radiated wave propagation was designed and fabricated. The eSRR metasurface structure is placed in front of the slotted waveguide antenna. Due to the anisotropy LEM property of the MTS; the radiated spherical waves are converted to quasi-planar waves in the direction of the *E*-plane. As a result, the beam becomes more focused; the gain and the directivity of the *E*-plane are improved, while the beam area is reduced. The proposed antenna operating at 10 GHz was designed and optimized by using the CST software. The eSRR metasurface unit cell which has a transmission peak and the LEM MTS around 10 GHz was designed and simulated using the frequency domain solver with unit cell boundary conditions, the *S-parameters* were calculated and then the effective parameters of the metasurface extracted from the *S*-parameters, the simulation results of the metasurface unit cell with infinite periodicity showed that, the eSRR structure exhibits LEM in the direction of the *E*-field polarization and has unity effective permittivity and permeability in the other two directions. The effect of periodicity truncation and the number of eSRR MS layers on the scattering parameters and the effective parameters were studied. For experimental verification, the proposed antenna slotted waveguide antenna incorporated with anisotropic LEM MS eSRR structure was fabricated and measured. The measured results showed that, the *E*-plane gain of the proposed antenna is improved from 6.5 dB to 9.5 dB, while the beam area reduced from 94.1 degrees to 45.1 degrees. The return loss and the bandwidth remains approximately the same. In addition, the proposed antenna operating at 303 GHz was designed and optimized by using the CST software. The eSRR metasurface unit cell which has a transmission peak and the LEM around 303 GHz was designed and simulated using the frequency domain solver with unit cell boundary conditions, the *S-parameters* are calculated and then the effective parameters of the metasurface are extracted from the *S*-parameters. The simulated results showed that, the *E*-plane gain of the proposed antenna was improved from 6.5 dB to 10.1 dB, while the beam area reduced from 94.1 degrees to 47 degrees. The return loss and the bandwidth and the total efficiency were slightly changed.

Fourthly, two different structures for high performance slotted waveguide antennas incorporated with GRIN medium were proposed, designed, simulated, fabricated and measured. The proposed antennas were designed, simulated and optimized at 10, 60, 100 and 200 GHz. For verification purposes, 10 and 60 GHz antennas were fabricated and measured. The proposed antennas provide a high gain without significantly affecting the impedance matching and the antenna bandwidth. The gain improvement was obtained due to beam focusing caused by the GRIN structure. The GRIN structure was implemented from one layer or multilayers of 2D periodic structures that were resonance or non-resonance and parabolic or linear spatially distributed GRIN MTSs. The resonance GRIN MTS was composed of annular slot 2D periodic structure with linear or parabolic GRIN profile. The non-resonance GRIN MTS was composed of metallic patches 2D periodic structure with linear or parabolic GRIN profile. Also, the GRIN profile can be spatially distributed across the antenna *E*-plane or *H* plane or both. In addition, a Luneburg lens has been constructed based on parabolic distributed annular slot 2D periodic structure in both the *E* and *H* planes. The non-resonance metallic patch GRIN MTS has been designed at 10, 60, 100 and 200 GHz frequencies based on the dispersion-diagram with the aid of the Eigen mode CST solver. While the resonance annular slot GRIN MTS has been designed based on the Effective Medium Theory (EMT) by extracting the effective parameters from the *S-parameters* using the NRW algorithm. The antennas were fabricated by using milling technology to construct the slot antenna, in addition to the wet etching PCB technology to fabricate the GRIN MTS. The antennas were tested in the lab, with the S_{11} magnitude, maximum gain for both the E and H planes radiation patterns were measured and compared to the simulation results.

For the proposed 10 GHz slotted waveguide antenna incorporated with metallic patch GRIN MTS, the gain improvement occurs in the E-plane and it is about 11.12 dB while the H plane gain is about 7.5 dB. However, the measured HPBW for the H-plane and E-plane are about 70° and 25°, respectively. The main beam directions are 22° and 0° for E and H planes, respectively. Also, the proposed 60 GHz slotted waveguide antenna incorporated with metallic patch GRIN MTS, the measured gain is about 11 dB at 60 GHz. The measured E plane HPBW decreases from about 106° and to 29° and the H-plane HPBW remains approximately the same at 65°. The main radiation beam directions are 20° and 0° for E and H planes, respectively, without significantly affecting the antenna impedance matching and its bandwidth. The 10 and 60 GHz proposed antennas have FBW of 10.5 and 25%, respectively.

For the 10 GHz proposed antenna incorporated with annular slot based employing resonance GRIN medium, the obtained measured gain is 10.3 dB at 10 GHz. The measured E and H planes HPBW are reduced from 107° and 67° to about 40° and 35°, respectively. However the proposed antenna has a good impedance matching and good FBW of approximately 10 %. For the 60 GHz proposed antenna incorporated with annular slot based

GRIN medium, the measured gain is improved from about 6.7 dB to 10.1 dB for both *E* and *H* planes. Furthermore, the measured HPBW is reduced from 107° and 67° to 28° and 30°, for *E* and *H* plane, respectively. However, the measured 60 GHz proposed antenna has good impedance matching and the bandwidth is slightly reduced. The 60 GHz proposed antenna FBW is 16%.

Finally, a semi analytical model based on the transfer function is developed to facilitate the design and analysis methodology of PCA using the EM solver such as CST Microwave Studio (see the appendix B). Since the PCA is composed of optoelectronic and EM models, CST software was used to solve the EM model and the optoelectronic model of the PCA dipole antenna had been solved numerically. Then the convolution theory was used to combine the two modes and extract the transfer function for the antenna system. It should be noted that, the solution of the optoelectronic model of the PCA includes the calculation of the photoconductive current generated from the excitation of the PCA by femtosecond pulse laser. In addition, the PCA proposed model has been verified by studying the impact of the pulse laser parameters and the PCA geometry on the antenna performance. The results showed that, the PCA performance parameters derived by the semi analytical model are matched with that of experimental results presented in many publications. In addition, a 300 GHz GRIN MTS lens based on annual slot 2D periodic structure is proposed and designed to focus the radiated waves from the PCA. A unit cell of the annular slot was modelled and simulated using the CST software; the radius of the annular slot is swept in CST such that the structure exhibits GRIN around 300 GHz. Then the effective parameters of the annual slot are extracted from the *S-parameters* by using effective medium theory. The designed GRIN MTS can be used to construct GRIN lens to focus the radiated waves from the PCA if it is placed at the back side of the antenna substrate and hence the generated *E*-Feld at the transmitting antenna and the detected current at the receiving antenna are improved.

8.2. Future work

The following hot research topics can be considered as a motivating for future work to contribute the scientific activity in this area of research.

1- Development of a THz 3D anisotropic structure employing simultaneously ENZ and MNZ Lenses to focus both the radiated *E* and *H* fields for situating in construction of high gain and high power THz antennas excited by waveguide feeds for high resolution imaging systems.

2- Development of a high power and high gain THz antenna excited by a waveguide and incorporated with a micro-machined GRIN MTS structure with a high fabrication tolerance and easy assembly processes.

3- Development of active GRIN, NRI, Anisotropic Lens to compensate the high losses of the passive Metamaterials particularly at THz frequencies.

4- Proposed, design, simulation, fabrication and measurement of a complex structure of THz PCA incorporated with plasmonic electrodes, GRIN MTS lenses and vertical electrodes with high quantum, matching and radiation efficiencies and high radiation power and wide bandwidth to be used for THz applications.

5- Development of high performance THz antennas based on Metatronics with switchable beam to be used for board to board communication for High Performance Computing (HPC) applications.

8.3. List of Publications

[1] Abdelrehim, A.A. and Ghafouri-Shiraz, H., 2016. High performance terahertz antennas based on split ring resonator and thin wire metamaterial structures. Microwave and Optical Technology Letters, 58(2), pp.382-389.

[2] Abdelrehim, A.A. and Ghafouri-Shiraz, H., 2016. High performance patch antenna using circular split ring resonators and thin wires employing electromagnetic coupling improvement. Photonics and Nanostructures-Fundamentals and Applications, 21, pp.19-31.

[3] Abdelrehim, A.A. and Ghafouri-Shiraz, H., 2016. Performance improvement of patch antenna using circular split ring resonators and thin wires employing metamaterials lens. Progress In Electromagnetics Research, 69, pp.137-155.

[4] Abdelrehim, A.A. and Ghafouri-Shiraz, H., 2017. High Gain Slotted Waveguide Antenna Based on Beam Focusing Using Electrically Split Ring Resonator Metasurface Employing Negative Refractive Index Medium. Progress In Electromagnetics Research, 79, pp.115-126.

[5] Abdelrehim, A.A. and Ghafouri-Shiraz, H., 2017. Design of high performance slotted wave guide antenna based on electrically split ring resonator metasurface employing anaisotropic low epsilon meaduim for E plane beam focusing. Submitted to IET journal.

[6] Abdelrehim, A.A. and Ghafouri-Shiraz, H., 2017. High performance terahertz slotted waveguide antenna based on electrically split ring resonator metasurface employing low epsilon medium for E-plane beam focusing. Microwave and Optical Technology Letters, 59(7), pp.1507-1517.

[7] Abdelrehim, A.A., Gardner, P. and Ghafouri-Shiraz, H., 2018. Development of High Performance and High Fabrication Tolerance THz Antenna Based on Non-resonance GRIN MTS. Prepared to be Submitted as IEEE transaction journal.

Appendix A: Nicolson-Ross-Weir (NRW) Algorithm

The effective parameters of MTM unit cell with infinite periodicity in *x* and *y* directions, including effective permittivity *ε*, effective permeability μ, and refractive index *n*, have been extracted from the *S-parameters* using Nicolson-Ross-Weir (NRW) approach. In [1], the authors proved that, the MTM effective parameters extraction based on the *S-parameters* method has no ambiguity related to the sign of the wavenumber $k_s$and the intrinsic impedance η_s of the metamaterials layer, while it has ambiguities related to the branch of the complex logarithm. Based on this method, the effective permittivity ε_s and the effective permeability μ_s are given as follow:

$$\varepsilon_s = \frac{k_s}{\omega \eta_s} \tag{A.10}$$

$$\varepsilon = \varepsilon' + j\,\varepsilon'' = \frac{\varepsilon_s}{\varepsilon_0} \tag{A.2}$$

Where ε' , and ε'' are the real and imaginary parts of the relative (effective) permittivity of the MTM slab, respectively, ε is the MTM slab relative permeability and ε_0 is the free space permittivity.

$$\mu_s = \frac{k_s \eta_s}{\omega} \tag{A.3}$$

$$\mu = \mu' + j\,\mu'' = \frac{\mu_s}{\mu_0} \tag{A.4}$$

Where μ' , and μ'' are the real and imaginary parts of the relative (effective) permeability of the MTM slab, respectively, μ is the MTM slab relative permeability and μ_0 is the free space permeability.

The intrinsic impedance in the MTM layer η_s can be calculated from the free space intrinsic impedance η_0 which is 120π Ω and the MTM *S-parameters* as follow:

$$\eta_s = \pm\,\eta_0 \sqrt{\frac{(S_{11}+1)^2 - S_{21}^2}{(S_{11}-1)^2 - S_{21}^2}} \tag{A.5}$$

The wavenumber k_s inside the MTM layer of thickness d can be expressed as follow:

Where

$$k_s = \frac{j}{d}\log(Z) = \frac{1}{d}\big(-(Arg(Z) + 2\pi p) + j\,log(Z)\big) \tag{A.6}$$

$$Z = \frac{S_{21}(\eta_s + \eta_0)}{(\eta_s + \eta_0) - S_{11}(\eta_s - \eta_0)} \tag{A.7}$$

The term $2\pi p$ (where p is an integer number) defines the branches of log Z, there is a specific value of p which gives the branch ambiguity in the real part of k_s which is k_s' it has been noticed that, there is no branch ambiguity in the imaginary part of k_s which is k_s''.The branch ambiguity factor p is determined based on the geometry of the MTM slab, whether it is thin, thick or multi-layered.

[1] Arslanagic, S., Hansen, T. V., Mortensen, N. A., Gregersen, A. H., Sigmund, O., Ziolkowski, R. W., & Breinbjerg, O. (2013). A review of the scattering-parameter extraction method with clarification of ambiguity issues in relation to metamaterial homogenization. Antennas and Propagation Magazine, IEEE, 55(2), 91-106.

Appendix B: Development of THz GRIN MTS Lens for Beam Focusing of THz Photoconductive Antenna Radiation Waves

In this Appendix, a semi analytical model based on transfer function is developed to facilitate the design and simulation of Photoconductive Antenna (PCA). The PCA is used as THz transmitter and receiver; it is excited by a pulsed laser and it is biased by a DC voltage. The developed model combines both optoelectronic and EM models. The EM model of the PCA can be solved by an EM solver incorporated in CST software and the optoelectronic model can be solved mathematically or by an optoelectronic solver presented in Comsol software. The optoelectronic model solves the carrier dynamic model of the semiconductor substrates on which the PCA is mounted. Also, it computes the photoconductive current generated by the excited pulsed laser in the gap of the PCA dipole antenna. The EM model is used to probe the *E*-field at specific location in the PCA substrate side. Then from the generated photoconductive current and the probed *E*-field, the actual *E*-field generated from the THz PCA can be calculated. In addition a 300 GHz GRIN MTS lens based on an annular slot was designed to focus the radiated waves from the conventional PCA when was placed at the back of PCA substrate and hence the generated E-field from the PCA can be improved. The simulation of the complex structure of the conventional THz PCA incorporated with a GRIN MTS lens is left as future work, since it needs high performance computation units because of the size of GRIN MTS lens.

B.1. Photoconductive Antenna Characterization based on Transfer Function Model

The performance of the THz PCA can be improved by integrating a PCA dipole antenna mounted on a LT-GaAs substrate [1-4] with a GRIN MTS Lens (GML) instead of Hemispherical Lens (HSL). The photoconductive antenna is a multilayer physics structure which requires the solution of the optoelectronic energy balance equation and the solution of the EM Maxwell's equations since it is a pulsed laser excited device [5, 6]. Thus we have three methods to design and develop the THz PCA. The first method is to use multilayer physics software such as Comsol multilayer physics to solve both the EM and the optoelectronics features of the PCA and this method is used when we want to improve the quantum, radiation and impedance matching efficiencies of the PCA [7]. This method can solve more complicated structures and it takes time to optimize bulky structures. The major challenge of the first method is long computation time particularly when the antenna electrodes and/or the EM structure are complicated. The complexity of antenna electrodes helps to improve the quantum efficiency while the complex EM structure helps to improve the radiation properties of the antenna. In the second method of modelling and simulating the PCA, the optoelectronic problem is firstly solved and the photoconductive current generated by exciting the PCA by a pulsed laser beam in the antenna gap which then computed. The photoconductive current can be computed by using software such as Silvio or Comsol software and also this method can solve the complicated optoelectronic model. Then the photoconductive current is used as an input signal to and EM solver such as CST to obtain the radiation properties of the PCA. But unfortunately the second method suffers from the stability problem because when exciting the EM structure in CST by a photoconductive current, it may cause stability problems and the solver results may be not correct or may be correct with big error bars.

To overcome the challenges of the two aforementioned methods, a third method is proposed which will be addressed in this chapter. In this method, the EM characteristics of the PCA antenna is obtained by using the EM commercial software such as CST Microwave Studio for any arbitrary input current $i_1(t)$ and the E-field $E(t)$ is probed at any distance in the near field of the antenna as shown in Fig. B.1(a). Then the actual photoconductive current

$i_{pc}(t)$ of the PCA is obtained by solving the carrier dynamic optoelectronic equations (B.1) to (B.4) for a PCA illuminated with a pulsed 800 nm laser source using the numerical methods [5, 6]. The specifications of the photoconductive material, the antenna physical parameters and the pulsed laser source are given in Table. B.1. After the photoconductive current $i_{pc}(t)$ is calculated analytically, the crossponding photoconductive E-field $E_{pc}(t)$ is computed as shown in Fig. B.1 (b) based on Fast Fourier Transform (FFT) and convolution/multiplication properties presented in Eqs. (B.5) to (B.9)

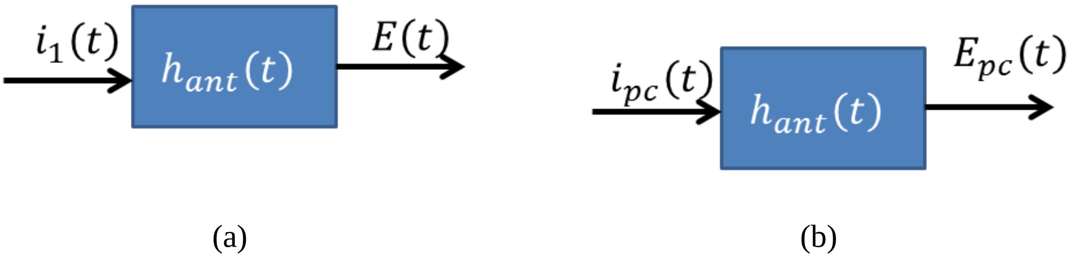

Fig. B.1. Transfer function based model to superposition the PCA analysis theoretically and by using CST EM solver (a) model of PCA excited by arbitrary signal $\mathrm{i}_1(\mathrm{t})$ and (b) model of PCA excited by actual photoconductive current $\mathrm{i}_{\mathrm{pc}}(\mathrm{t})$

Table B.1 Laser, photoconductive material and antenna parameters

Parameter	Notation	Value
Electron mobility for LT-GaAs	μ_e	200 $cm^2/(v.s)$
Reflection coefficient in air-photoconductive material interface	R	(for GaAs) 0.318
Optical absorption coefficient	α	6000 cm^{-1}
Laser frequency /(laser	f_{opt}/λ_{opt}	375 THz /(800 nm)

wavelength)		
Laser repetition rate	f_{rep}	80 MHz
Laser pulse duration	τ_l	100 fs
Carrier lifetime	τ_c	1 ps
Carrier recombination time	τ_r	100ps
Screening factor	ζ	900
Antenna gap length	L	10μm
Antenna gap width	W	10μm
Antenna length	H	100 μm
Depth of excitation region	$T_{LT-GaAs}$	1μm
Bias voltage	V_{bias}	30 V
Laser average power	P_{av}	1 W
Laser spot radius	r	10μms

To calculate the photoconductive E-field $E_{pc}(t)$ from any arbitrary excitation current $i_1(t)$ as it has been described by the transfer function based model for PCA (method 3), the following procedure is processed

Firstly, the photoconductive current $i_{pc}(t)$ is calculated by solving numerically the following carrier dynamic equations (Eqs. (B.1) through (B.4)) of the photoconductive substrate when it is illuminated by a pulsed laser. The specifications of the photoconductive substrate and the pulsed laser beam is given in Table (B.1)

$$\frac{dN(t)}{dt} = -\frac{N(t)}{\tau_c} + \frac{\alpha I_1(t)}{hf} \qquad (B.1)$$

$$\frac{dv(t)}{dt} = -\frac{v(t)}{\tau_s} + \frac{e}{m^*}\left(\frac{V_{bais}}{L} - \frac{P_{SC}}{\zeta\varepsilon}\right) \qquad (B.2)$$

$$\frac{dP_{SC}(t)}{dt} = -\frac{P_{SC}(t)}{\tau_r} + J(t) \qquad (B.3)$$

$$J(t) = e.N(t).v(t) \qquad (B.4)$$

The generated photoconductive current $i_{pc}(t)$, is plotted as in Fig. B.2

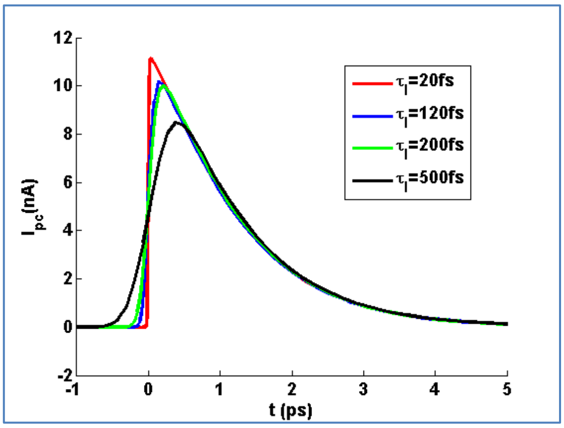

Fig. B.2. Photoconductive current generated from LT-GaAs substrate of thickness 1μm and with the parameters provided in Table 8.1

Secondly, the EM model of the PCA shown in Fig. (B.3) was modelled, simulated and solved using CST by exciting the structure by an arbitrary current $i_1(t)$ as shown in Fig. B.4 (a). The parameters of laser pulse excitation signal, the PCA geometry and the semiconductor substrate are given in Table B.1. The crossponding E-field is probed in the substrate side at location of (0, 0, 1000 μm) and plotted as shown in Fig. B.4 (b).

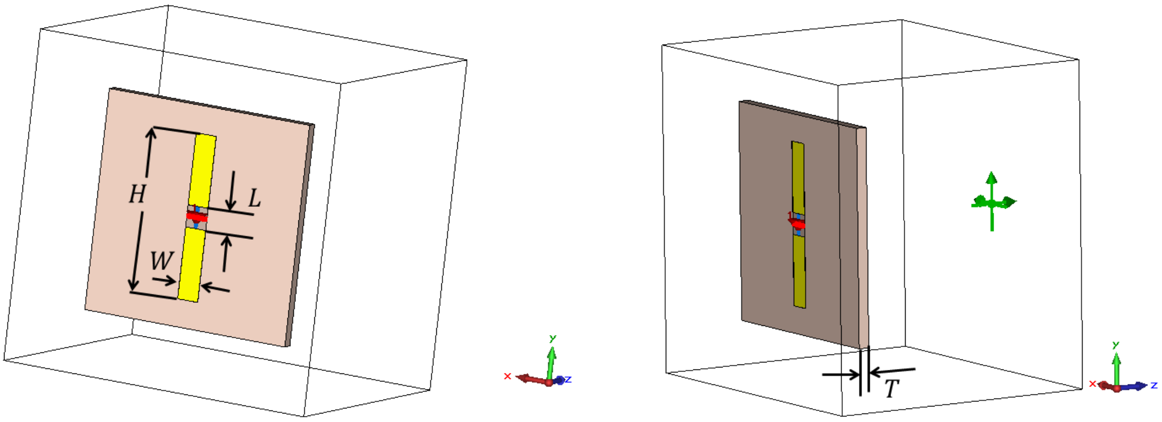

(a) (b)

Fig. B.3. The EM model of the PCA mounted on LT-GaAs substrate (a) 3D view of the PCA with the antenna physical parameters, and (b) 3D view of the PCA with *E*-filed probe located at (0, 0, 1000 μm).

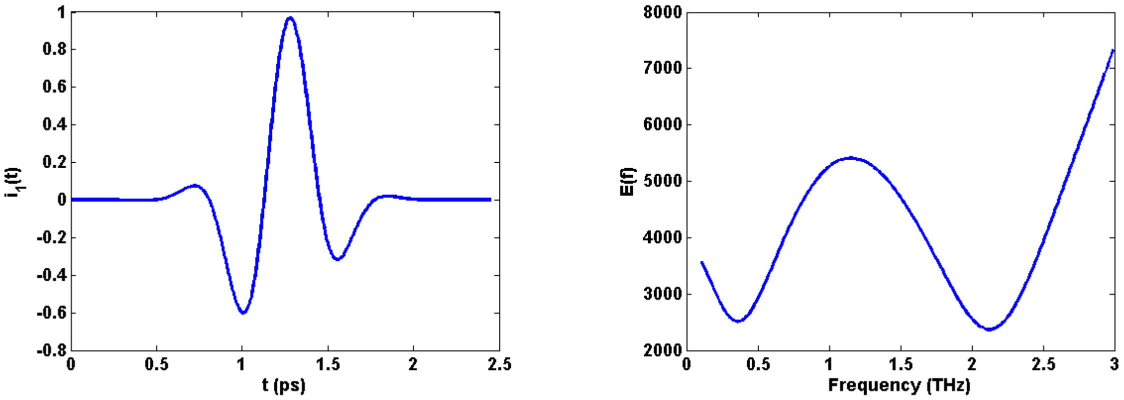

(a) (b)

Fig. B.4. Time domain of (a) an arbitrary excitation current $i_1(t)$ used in excitation of the EM model of the PCA which satisfies stability of the EM CST simulator, (b) the crossponding generated E-field probed at (0,0,1000 μm).

Thirdly, the system model shown in Fig. B.1 (a) is analyzed and the photoconductive *E*-field can be calculated as follows

$$E(t) = i_1(t) * h_{ant}(t) \tag{B.5}$$

By taking the FFT for Eq. (B.5)

$$E(f) = I_1(f). H_{ant}(f) \tag{B.6}$$

So, the transfer function of the PCA can be calculated as follows and plotted as shown in Fig. B.5

$$H_{ant}(f) = \frac{E(f)}{I_1(f)} \qquad (B.7)$$

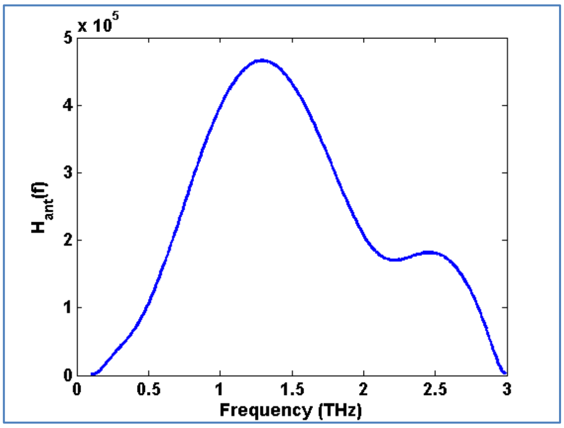

Fig. B.5. The extracted transfer function of the EM model of the PCA with the specification presented in Table B.1

Then, when the PCA is excited by photoconductive current as shown in Fig. B.1 (b), the probed photoconductive E-field will be $E_{pc}(t)$ and can be computed as follows

$$E_{pc}(t) = i_{pc}(t) * h_{ant}(t) \qquad (B.8)$$

By taking the FFT for Eq. (B.8), the photoconductive E-field can be calculated in the frequency domain using Eq. (B.9)

$$E_{pc}(f) = I_{pc}(f).H_{ant}(f) \qquad (B.9)$$

For verification purposes, the photoconductive current $i_{pc}(f)$, E-field $E_{pc}(f)$ and the detected current density $J_{det}(f)$ at the receiver side assuming identical transmitting and receiving antennas are computed and plotted at different laser pulse duration τ_l as shown in Fig. B.6.

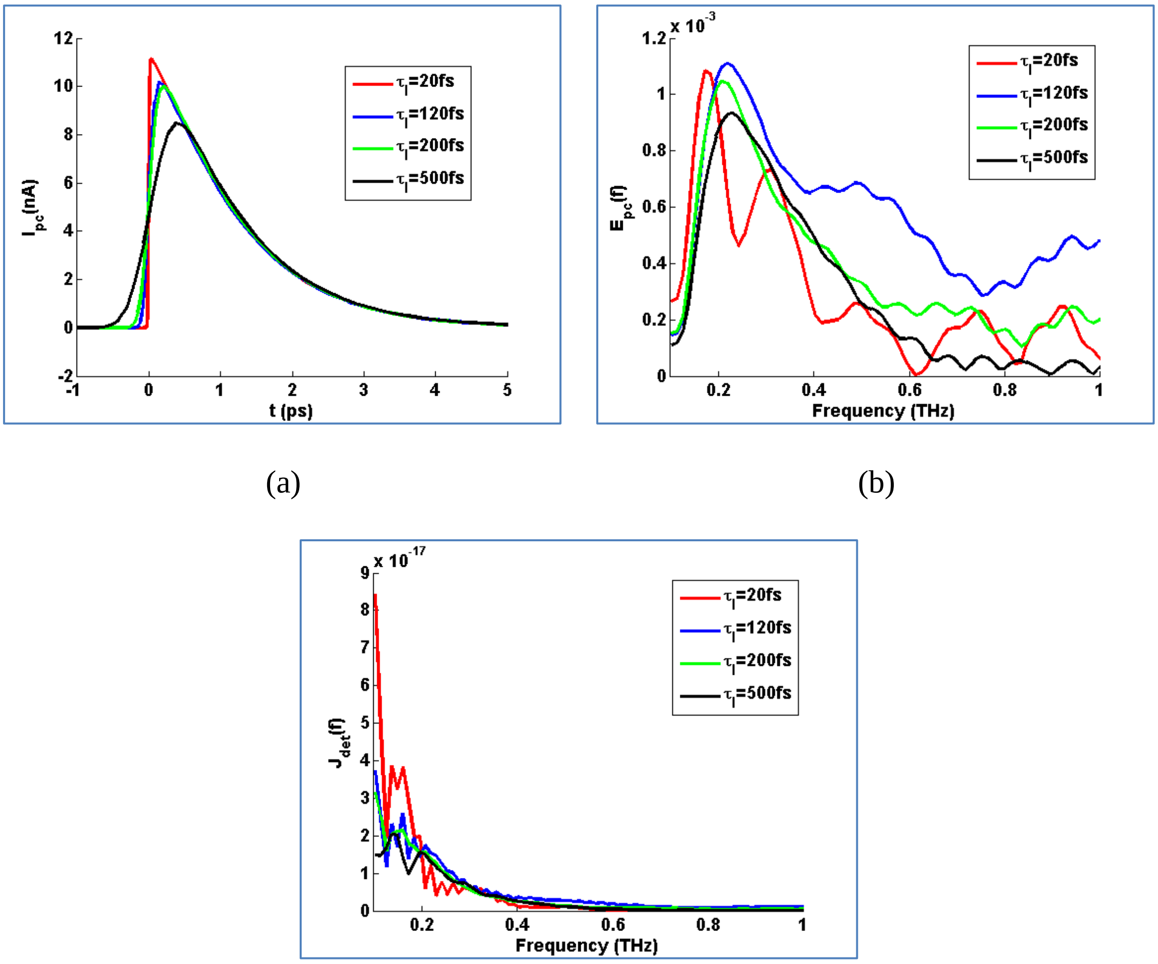

(a) (b)

(c)

Fig. B.6. The performance of THz PCA antenna at different the laser pulse duration τ_l ; (a) photoconductive current $i_{pc}(f)$, (b) photoconductive E-field $E_{pc}(f)$ and (c) detected current density $J_{det}(f)$.

It is clear from Fig. B.6 that, as the laser pulse duration τ_l increases, $i_{pc}(f)$, $E_{pc}(f)$ and $J_{det}(f)$ decease which agrees with the published work in the literature [2, 8].

Also, the impact of laser average power P_{av} and laser carrier life time τ_c on the PCA antenna performance are given in Figs. B.7 and B.8, respectively.

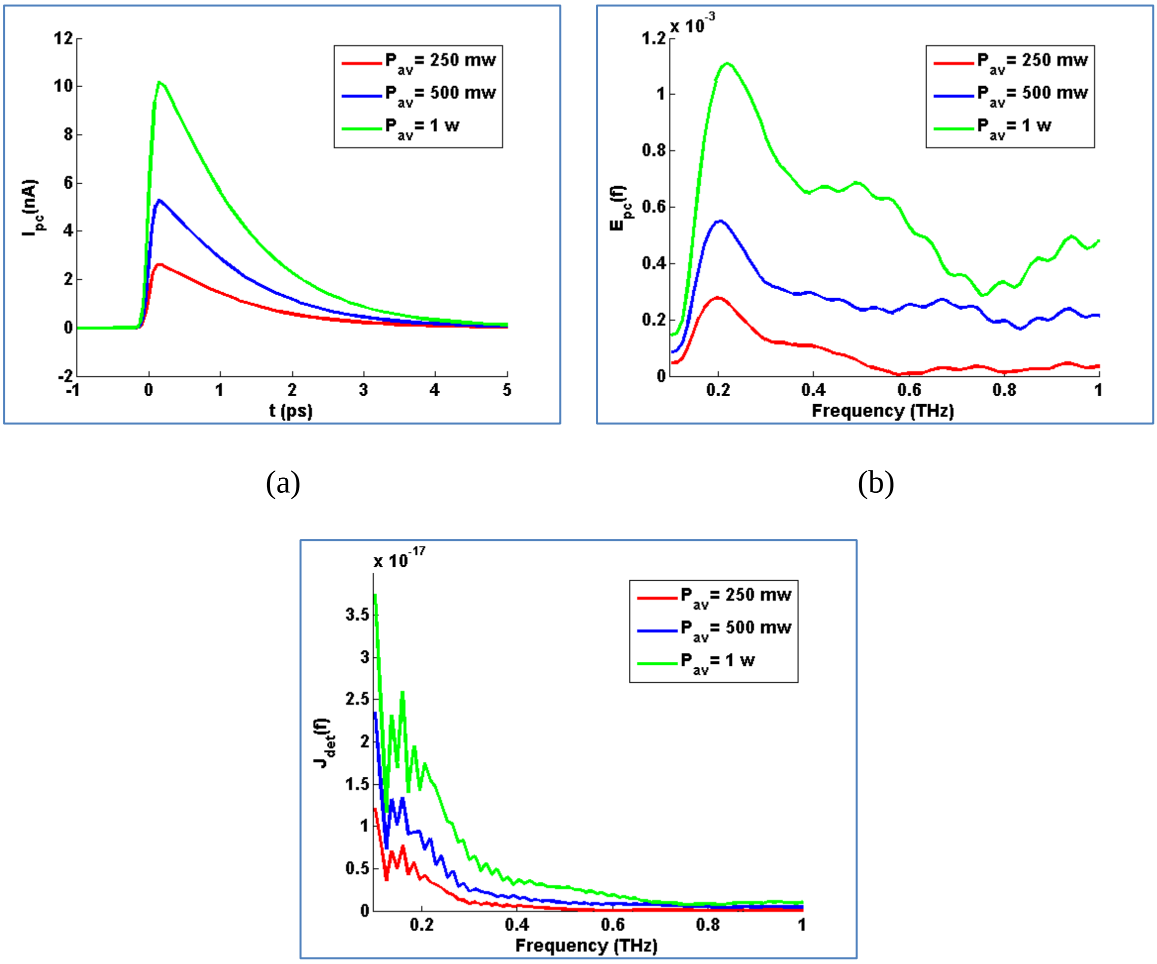

(a) (b)

(c)

Fig. B.7. The performance of THz PCA antenna at different laser average power P_{av}; (a) photoconductive current $i_{pc}(f)$, (b) photoconductive E-field $E_{pc}(f)$ and (c) detected current density $J_{det}(f)$.

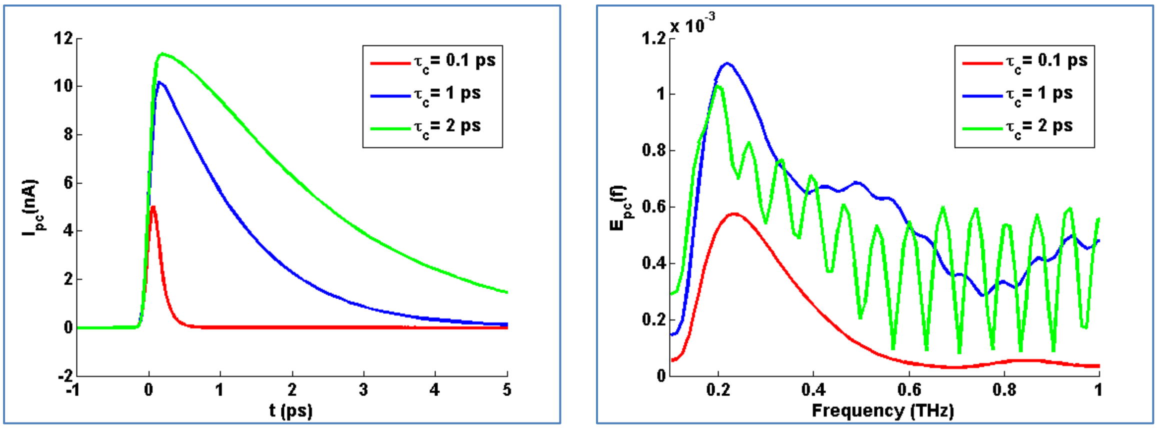

(a) (b)

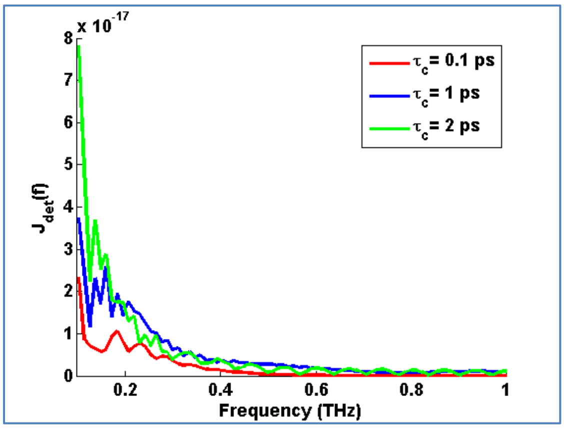

(c)

Fig. B.8. The performance of THz PCA antenna at different laser carrier life time τ_c ; (a) photoconductive current $i_{pc}(f)$, (b) photoconductive E-field $E_{pc}(f)$ and (c) detected current density $J_{det}(f)$.

It is clear from Figs. B.7 and B.8 that, as the laser average power P_{av} increases, $i_{pc}(f)$, $E_{pc}(f)$ and $J_{det}(f)$ increase too. Also, as different laser carrier life time τ_c increases, the PCA parameters $i_{pc}(f)$, $E_{pc}(f)$ and $J_{det}(f)$ increase also.

Furthermore, the impact of PCA antenna dimensions such as the dipole length L and the dipole width W on the PCA antenna performance were studied, simulated and plotted as given in Figs. 8.9 and 8.10, respectively.

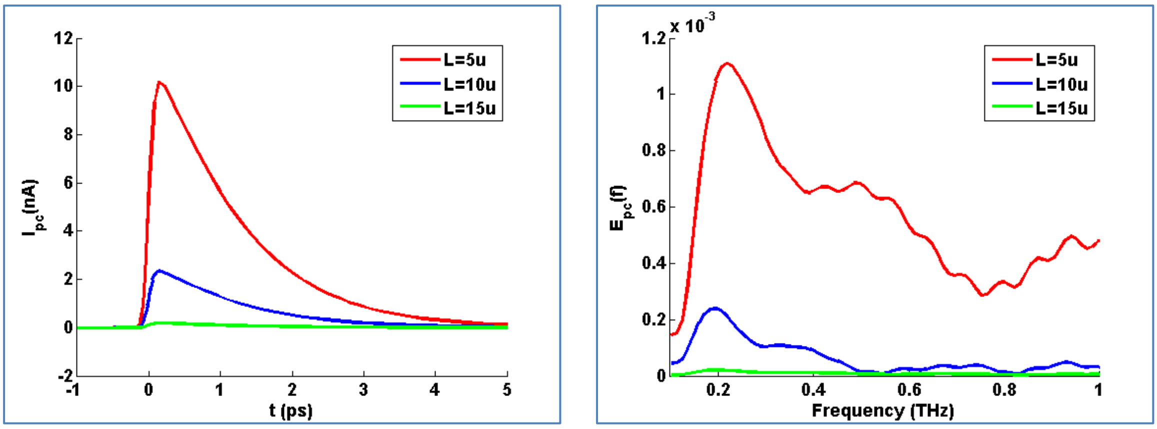

(a) (b)

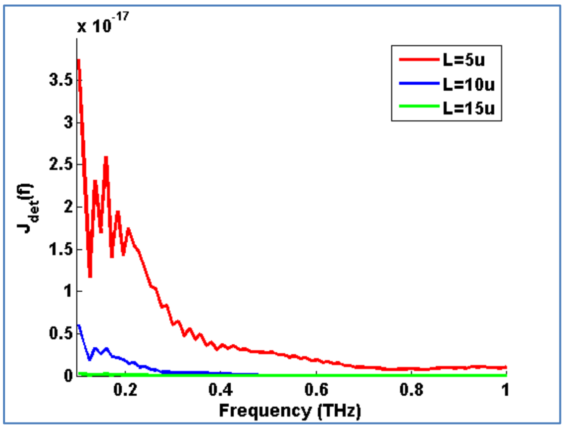

(c)

Fig. B.9. The performance of THz PCA antenna at dipole length L ; (a) photoconductive current $i_{pc}(f)$, (b) photoconductive E-field $E_{pc}(f)$ and (c) detected current density $J_{det}(f)$.

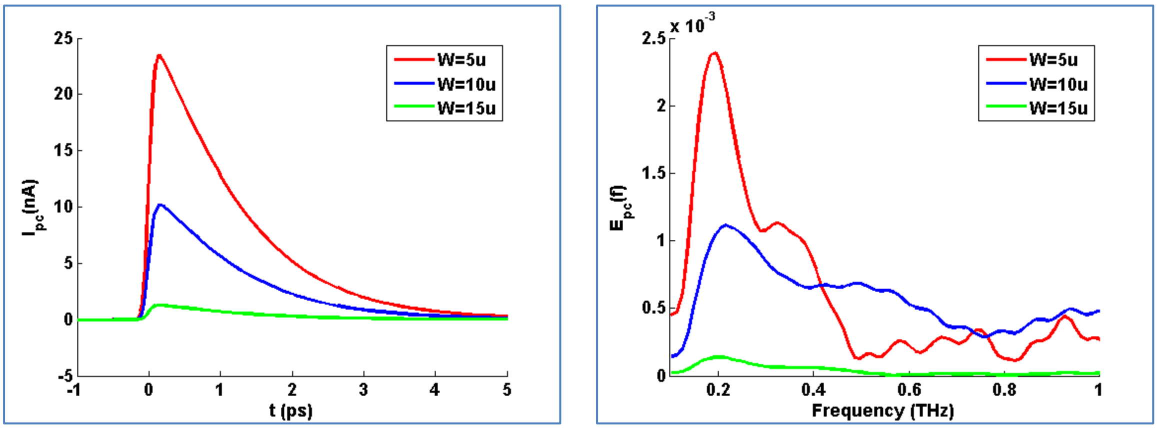

(a) (b)

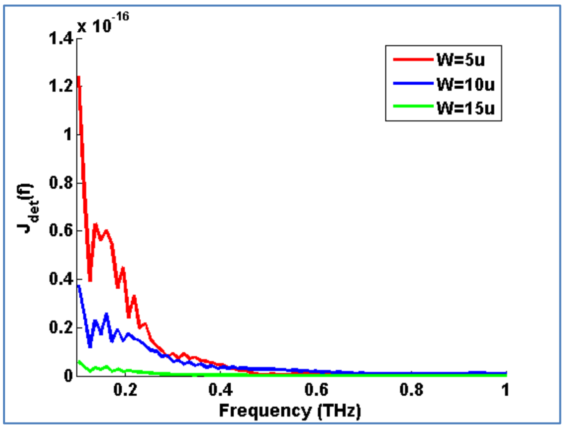

(c)

Fig. B.10. The performance of THz PCA antenna at dipole length W ; (a) photoconductive current $i_{pc}(f)$, (b) photoconductive E-field $E_{pc}(f)$ and (c) detected current density $J_{det}(f)$.

Figures B.9 and B.10 illustrate that as the antenna dipole length L increases, the $i_{pc}(f)$, $E_{pc}(f)$ and $J_{det}(f)$ decrease and as antenna dipole width W increases, the PCA parameters $i_{pc}(f)$, $E_{pc}(f)$ and $J_{det}(f)$ decrease.

B.2. Design, Simulation and Characterization of 0.3 THz GRIN MTS Lens Based on Annular Slot Metasurface

Here, a unit cell of annular slot shown in Fig. 7.14 was redesigned to construct the 2D periodic structure of spatially distributed gradient index of refraction (GRIN) around 300 GHz. The unit cell was designed, simulated and characterized based on the Effective Medium Theory (EMT). The dimensions of the annular slot unit cell which exhibit GRIN around 300 GHz is given in Table 8.2. It is clear that, to obtain GRIN at 300 GHz, the slot radius r is swept from 0.1 to 0.14 mm with a step size of 0.01 mm. The *S-parameters* of the annular slot unit cell are calculated in the CST frequency domain solver with unit cell Floquet's boundary conditions and the results are plotted in Figs. B.11 (a) to B.11 (d). And then the effective parameters of the unit cell are extracted from the *S-parameters* using NRW algorithm and the results are reported in Figs. B.11 (e) to B.11 (j).

Table B.2 dimensions of annular slot unit cell employing 2-D GRIN medium at 300 GHz

Parameter	p	g	r	h	ε_r	t	Substrate	Metal cladding
Dimension (mm)	0.5	0.05	0.10:0.01:0.14	0.127	2.2	0.0175	RT/Duroid 5880	Copper

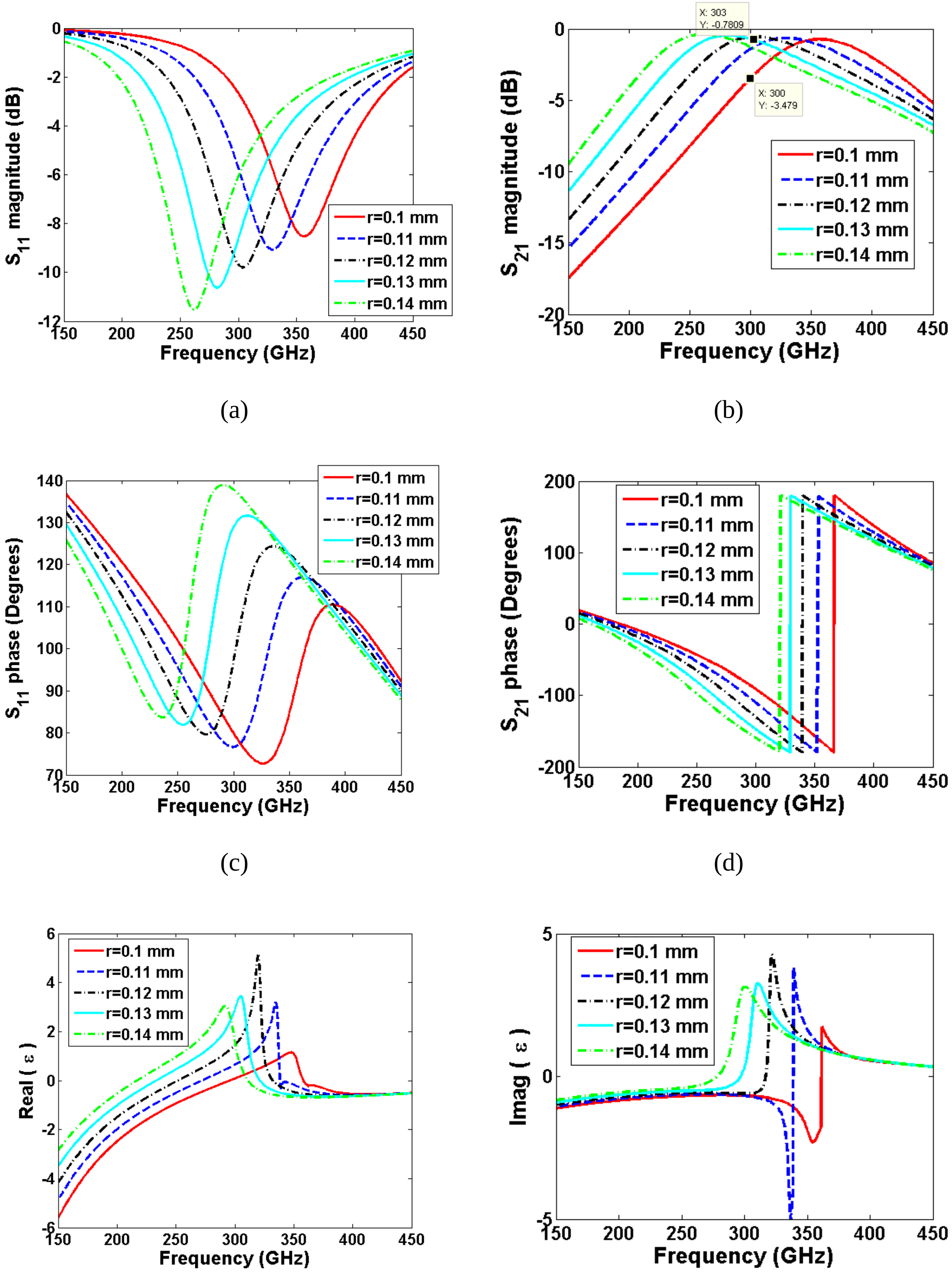
S11 magnitude (dB)
Frequency (GHz)
S21 magnitude (dB)
X: 303
Y: -0.7809
X: 300
Y: -3.479
S11 phase (Degrees)
S21 phase (Degrees)
Real (ε)
Imag (ε)
r=0.1 mm
r=0.11 mm
r=0.12 mm
r=0.13 mm
r=0.14 mm

(a) (b)

(c) (d)

(e) (f)

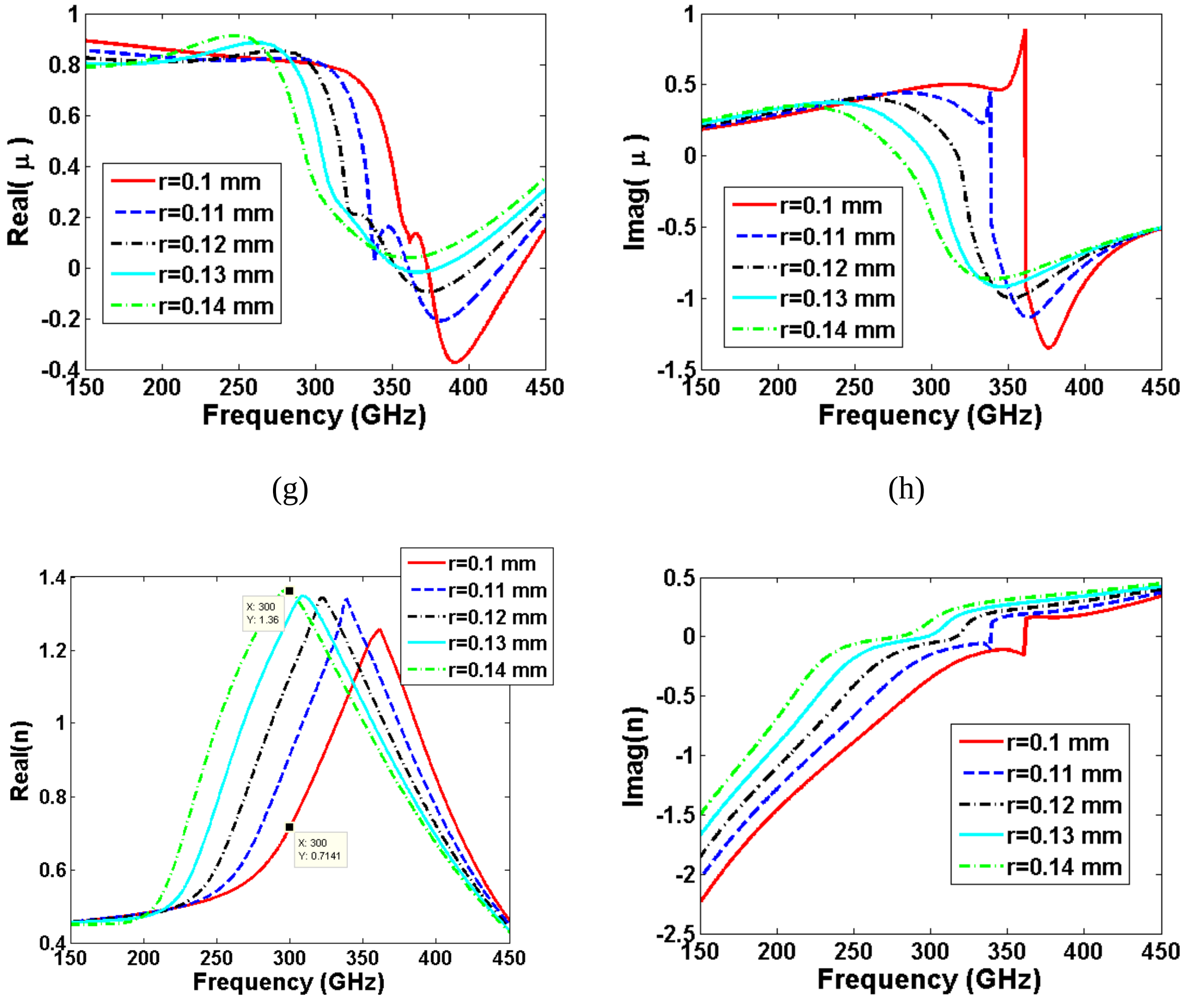

(g) (h)

(i) (j)

Fig. B.11. The scattering and the effective parameters of the annualar slot unit cell to construct GRIN medium around 300 GHz at different radius *r* changes from 0.1 mm to 0.14 mm and periodicity p of 0.5 mm in both *x* and *y* directions, (a) magnitude of the reflection coefficient, (b) magnitude of the transmission coefficient, (c) phase of the reflection coefficient, (d) phase of the transmission coefficient, (e) and (f) real and imaginary part of effective permittivity, respectively, (g) and (h) real and imaginary part of effective permeability, (i) and (j) real and imaginary part of effective refractive index.

It is clear from Fig. B.11 that, as the slot radius is changed from 0.1 mm to 0.14 mm, the index of refraction is changed from 0.714 to 1.36 at 300 GHz and the crossponding S_{21} magnitude is in the range from -3.47 dB to -0.78 dB. The designed annular slot unit cell was used to construct a 2D periodic structure employing GRIN MTS which can be placed at the side of PCA substrate to focus the radiated waves from the PCA. Since the simulation and the calculation of the proposed PCA incorporated with GRIN MTS needs significant computer resources the size of the GRIN MTS lens was limited to a few millimetres while the size of the conventional PCA was a few micrometres, thus the simulation of the complex structure of the proposed PCA will be considered as a future work.

B.3. Summary

In this Appendix, a semi analytical model based on the transfer function was developed to facilitate the design and analysis methodology of a PCA using the EM solver such as CST Microwave Studio. Since the PCA is composed of optoelectronic and EM models, CST software is used to solve the EM model and the optoelectronic model of the PCA dipole antenna had been solved numerically. Then the convolution theory is used to combine the two modes and extract the transfer function for the antenna system. It should be noted that, the solution of the optoelectronic model of the PCA includes the calculation of the photoconductive current generated from the excitation of the PCA by femtosecond pulse laser. In addition, the PCA proposed model has been verified by studying the impact of pulse laser parameters and the PCA geometry on the antenna performance. The results showed that, the PCA performance parameters derived by the semi analytical model are matched with that of experimental results presented in many publications.

Furthermore, 300 GHz GRIN MTS lens based on an annular slot 2D periodic structure is proposed and designed to focus the radiated waves from the PCA. A unit cell of the annular slot was modelled and simulated in CST software; the radius of the annular slot was swept in CST such that the structure exhibits GRIN around 300 GHz. Then the effective parameters of the annular slot are extracted from the *S-parameters* by using effective medium theory. The designed GRIN MTS can be used to construct GRIN lens to focus the radiated waves from the PCA if it is placed at the back side of the antenna substrate and hence the generated *E*-

field at the transmitting antenna and the detected current at the receiving antenna are improved.

B.4. References

[1] P. R. Smith, D. H. Auston, and M. C. Nuss, "Subpicosecond photoconducting dipole antennas," Quantum Electronics, IEEE Journal of, vol. 24, pp. 255-260, 1988.

[2] F. Miyamaru, Y. Saito, K. Yamamoto, T. Furuya, S. Nishizawa, and M. Tani, "Dependence of emission of terahertz radiation on geometrical parameters of dipole photoconductive antennas," Applied Physics Letters, vol. 96, p. 211104, 2010.

[3] M. Tani, S. Matsuura, K. Sakai, and S.-i. Nakashima, "Emission characteristics of photoconductive antennas based on low-temperature-grown GaAs and semi-insulating GaAs," Appl. Opt., vol. 36, pp. 7853-7859, 1997.

[4] Y. C. Shen, P. C. Upadhya, H. E. Beere, E. H. Linfield, A. G. Davies, I. S. Gregory, C. Baker, W. R. Tribe, and M. J. Evans, "Generation and detection of ultrabroadband terahertz radiation using photoconductive emitters and receivers," Applied Physics Letters, vol. 85, pp. 164-166, 2004.

[5] S. Hughes, M. Tani, and K. Sakai, "Vector analysis of terahertz transients generated by photoconductive antennas in near- and far-field regimes," Journal of Applied Physics, vol. 93, pp. 4880-4884, 2003.

[6] P. U. Jepsen, R. H. Jacobsen, and S. R. Keiding, "Generation and detection of terahertz pulses from biased semiconductor antennas," J. Opt. Soc. Am. B, vol. 13, pp. 2424-2436, 1996.

[7] Burford, N.M. and El-Shenawee, M., September. Multiphysics modeling of THz photoconductive antennas. In Infrared, Millimeter, and Terahertz waves (IRMMW-THz), 2014 39th International Conference on (pp. 1-2). IEEE, 2014.

[8] M. Tani, K. Yamamoto, E. Estacio, C. Que, H. Nakajima, M. Hibi, F. Miyamaru, S. Nishizawa, and M. Hangyo, "Photoconductive Emission and Detection of Terahertz Pulsed Radiation Using Semiconductors and Semiconductor Devices," Journal of Infrared, Millimeter and Terahertz Waves, vol. 33, pp. 393-404, 2012.